Contributions au développement de méta modèles pour la simulation et le recalage en dynamique d'ensemble

Francesco d'Alessandro

THÈSE DE DOCTORAT DE L'ÉTABLISSEMENT UNIVERSITÉ BOURGOGNE FRANCHE-COMTÉ

PRÉPARÉE À L'UNIVERSITÉ DE FRANCHE-COMTÉ

École doctorale n° ED37

ED SPIM

Doctorat de Mécanique

Par

Mr. Francesco D'ALESSANDRO

Contributions to the development of surrogate models for the simulation and calibration of global aeroengine dynamics

Contributions au développement de métamodèles pour la simulation et le recalage en dynamique d'ensemble

Thèse présentée et soutenue à Besançon, le 7 Septembre 2023

Composition du Jury :

Pr. BOUCARD Pierre-Alain	Professeur des universités, ENS Paris-Saclay, LMPS	Président
Pr. THOUVEREZ Fabrice	Professeur des universités, École centrale de Lyon, LTDS	Rapporteur
Pr. BALMES Étienne	Professeur des universités, ENSAM ParisTech, PIMM	Rapporteur
Pr. CHEVALLIER Gaël	Professeur des universités, UBFC, FEMTO-ST	Directeur de thèse
Dr. COGAN Scott	Chargé de recherche CNRS, HDR, UBFC, FEMTO-ST	Codirecteur de thèse
Dr. BENAMARA Tariq	Ingénieur de recherche, CENAERO	Examinateur
Dr. SAINVITU Caroline	Ingénieur de recherche, CENAERO	Examinateur
Dr. FESTJENS Hugo	Ingénieur, SAFRAN AE	Examinateur

I would like to dedicate this thesis to:
my mother, Lucia,
my father, Nicola,
my brother, Vincenzo.

Remerciements

À fin de cette aventure de recherche, il me semble naturel et fondamental de remercier toute personne qui a participé à la bonne réussite de ce travail.

En premier lieu, je souhaite remercier de manière particulière tout mon encadrement académique et industriel, ce travail n'aurait pas pu être possible sans leur énergie, engagement, passion et surtout sans leurs conseils précieux. J'ai eu la chance d'avoir un encadrement avec des incroyables dotes scientifiques et humaines. Travailler avec un tel encadrement a été un honneur et une grande chance pour moi. J'ai pris quelque chose de vous tous et je porterai avec moi pour toujours vos conseils et vos idées.

Merci à mon directeur de thèse Gaël CHEVALLIER de m'avoir fait confiance depuis le début de ce projet et de m'avoir conduit jusqu'à la fin de ce travail de recherche sans hésitation. Grâce à ses conseils, j'ai pu grandir scientifiquement et apprendre beaucoup de choses du point de vue humaine. Je ne regretterai jamais d'avoir assisté à la soutenance de thèse de Marco, ou on a pu se rencontrer et jeter les bases de ces travaux de recherche.

Merci à mon encadrant Hugo FESTJENS qui m'a inspiré, motivé et guidé dans l'univers de la dynamique des rotors. Nos échanges ont été fondamentaux pour ma formation et pour relever mes qualités scientifiques. Merci de m'avoir donné la vision du haut des choses et appris à prendre le recul nécessaire à comprendre les vraies problématiques qu'on affronte. Hugo a su m'apprendre la rigueur nécessaire pour m'exprimer dans le monde académique et à défendre mes idées avec vigueur et ténacité comme lui-même fait.

Merci à mon directeur de thèse Scott COGAN de m'avoir transmis sa vision philosophique et pragmatique de la science, merci de m'avoir appris le rôle fondamental de la communication et du partage dans le monde de la science. Je conserverai jalousement les beaux souvenirs du voyage en Floride qu'on a pu partager en 2022 pour l'IMAC XL.

Merci à Tariq BENAMARA et a sa grande patience, merci d'avoir lu mes travaux toujours

à la dernière minute, merci de m'avoir rassuré les nombreuses fois où je me sentais perdu dans les difficultés du sujet, merci d'avoir apporté toujours le mot amical qui m'a poussé et encouragé. Je me rappellerai toujours des longues balades à Boston en occasion de TurboExpo 2023.

Merci à Caroline SAINVITU qui a pu me guider dans le monde de la méta-modélisation et des mathématiques appliquées, merci de m'avoir supporté et de m'avoir permis de développer mes idées dans un domaine qui ne m'appartenait pas.

Je tiens à remercier chaleureusement les membres de mon jury de thèse pour avoir accepté d'évaluer mes travaux et pour les nombreuses questions passionnantes, pour les discussions sur les résultats présentés et pour le magnifique moment d'échange qu'ils m'ont offert lors de la soutenance.

Merci à l'équipe de dynamique d'ensemble de SAFRAN AIRCRAFT ENGINES de m'avoir accueilli et permis de découvrir le fabuleux monde des moteurs d'avion. Merci spécialement à mes chefs Alexandre et Francois de m'avoir donné le temps et la sérénité nécessaires pour réussir à porter à terme ces travaux fondamentaux pour ma réussite personnelle.

Je souhaite aussi remercier les membres du FEMTO-ST qui m'ont conseillé et supporté dans ces trois ans de travail, merci à Émeline REBOUL pour sa patience et son écoute, merci à tous mes collègues doctorants avec qui on a pu partager inquiétudes et sérénité. Merci à Robin pour les belles escalades dans les monts du Jura, merci à Manu, Svenja, Ludo (et son énorme plante) et Margaux d'avoir partagé le bureau 42H avec moi pendant ma permanence au FEMTO.

Merci à ma famille, que même à 2000 Km de distance a su m'accompagner et supporter dans ces travaux. Les paroles gentilles et rassurantes de ma mère Lucia m'ont permis d'affronter la distance, la solitude, la fatigue et de combattre contre moi-même. La force de mon père Nicola m'a inspiré et m'a donné la résilience pour réussir. Mon frère Vincenzo et son énergie représentent un modèle à atteindre pour moi.

Merci à toi, *mi amor* Giorgia, de m'avoir offert beaucoup de beaux moments et de légèreté pendant la dernière période de ma thèse.

Merci à vous tous, d'avoir donné une contribution fondamentale à la réalisation de ces travaux et surtout à forger les traits de la personne que je suis devenue aujourd'hui.

Résumé

Les ingénieurs utilisent aujourd'hui des modèles numériques dans toutes les phases de vie d'un propulseur aéronautique, de la conception à l'exploitation, pour identifier leur réponse dynamique. Ces jumeaux numériques ont vocation à être utilisés dans des plans d'expériences (DoE) de grande taille, il est donc nécessaire d'évaluer rapidement le comportement dynamique d'un grand nombre de configurations différentes. Ce travail repose aujourd'hui sur l'exploitation directe des modèles Eléments Finis (EF) des machines. Pour être représentatifs du comportement réel, ces modèles numériques doivent intégrer un haut niveau de description géométrique du système, du comportement des matériaux et des liaisons entre les composantes. Certaines liaisons présentent des comportements non-linéaires (contact rotor-stator principalement). Le coût de calcul prohibitif et le nombre élevé des paramètres de conception ne permettent pourtant pas d'évaluer la dynamique de l'ensemble des configurations potentielles. C'est pourquoi aujourd'hui, seule la sensibilité locale à un nombre assez limité de paramètres clefs est évaluée. L'objectif de ce travail de recherche est de fournir des outils d'évaluation rapide de l'espace de conception, à utiliser comme support pour des opérations d'optimisation, de recalage et de diagnostic.

Les travaux se concentrent initialement sur l'accélération des calculs de réponse à balourd, avec prise en compte des nonlinéarités aux supports palier, aujourd'hui réalisés par intégration temporelle en balayage lent sur toute la plage de fonctionnement du moteur. Pour cela une méthode de Balance Harmonique (HBM) a été développée et adaptée au cas des machines tournantes.

Pour le traitement des modèles EF de taille industrielle, une méthode de réduction de modèle dédiée aux machines tournantes a été développée. Il s'agit d'une réduction sur base de Ritz qui adopte une base de modes de la structure excités au passage des vitesses critiques. Ces bases des vitesses critiques présentent des propriétés dynamiques invariantes avec l'évolution de la vitesse de rotation et permettent une réduction du modèle particulièrement adaptée aux calculs de réponse à balourd. Une comparaison avec les méthodes de réduction classiques est proposée dans ces travaux et l'efficience de cette ap-

proche est montrée sur un modèle de taille industrielle. La méthode est adaptée aux cas de systèmes linéaires, nonlinéaires et aux simulations en domaine temporel et fréquentiel.

Toutefois, ces méthodes de réduction présentent des limites théoriques liées au nombre de modes présents dans la plage de fonctionnement de la machine. Le coût de simulation reste donc élevé par rapport au besoin dans un cas d'étude de type many-query. Dans ces travaux, on propose d'introduire des méthodes *data-driven* pour dépasser ces limites. Des méta-modèles sont adoptés pour l'approximation directe des réponses à balourd non linéaires d'un ensemble propulsif en une configuration quelconque dans son espace de conception. Plusieurs stratégies de méta-modélisation ont été étudiées et comparées pour identifier celle qui s'adapte le plus au besoin industriel.

Mots clés : Dynamique des rotors non linéaires, HBM, réduction de modèles, vitesses critiques, métamodèles, RBNN, POD.

Abstract

Engineers nowadays use numerical models in any phases of the life-cycle of an aeronautical engine, from the design to the exploitation, to identify their dynamical response. These numerical twins are intended to be used in large-scale Designs of Experiments (DoE), so it is necessary to quickly evaluate the dynamical behaviour of a large number of different configurations. This work is based nowadays on the direct exploitation of Finite Element (FE) models of turbomachines. To be realistic and reliable, these numerical models have to represent in detail the geometry of the system, the mechanical behaviour of materials and the mechanical connections between components. Materials, geometries and mechanical connections can introduce nonlinearities to be more representative. The prohibitive computational burden and the high number of design parameters, make unaffordable to perform an exhaustive study of the dynamics of any potential configuration of the turbomachine in the whole design space. For this reason, only the local sensitivity to a rather limited number of key parameters is directly evaluated trough FE simulations. This work seeks to provide numerical tools for rapid evaluation of multiple configurations of an aeroengine in its design space to support optimisation, calibration, diagnosis operations or any other sort of many-query study.

The work is initially focused on accelerating unbalanced response simulations taking into account nonlinearities due to the rotor/stator interaction, performed nowadays using time marching algorithms over the whole operating frequency range of the engine. An Harmonic Balance (HB) algorithm has been developed and adapted to rotating machines.

A model reduction approach dedicated to rotating machines has been developed to deal with industrial size FE models and to reduce the computational effort of numerical simulations. The proposed Ritz-based reduction technique adopts a basis composed by the mode shapes of the structure excited at critical speeds. These bases have invariant dynamical properties, which are particularly interesting for the evaluation of unbalance responses of rotating systems. The efficiency of this model reduction approach is demonstrated on an industrial scale FE model, in time and frequency domains, and in linear and nonlinear

frameworks.

However, these reduction methods have theoretical limitations related to the amount of modes excited in the operating frequency range of the machine, the majority of them have to be included in the reduction basis in order to produce a reliable reduced order model (ROM). The computational burden is still too important to the meet the industrial exigences in a many-query framework. In this work, we propose data-driven methods to overcome these limitations. Surrogate models are adopted for the approximation of the nonlinear unbalance responses of an aeroengine in any configuration included in its design space. Multiple surrogate modeling strategies have been investigated and compared to identify the one that best suits the industrial exigences.

Keywords : Nonlinear rotordynamics, HBM, model reduction, critical speeds, surrgoate modeling, RBNN, POD.

Contents

List of Figures

List of Tables

Glossary

AFT *Alternating Frequency-Time*

AI *Artificial Intelligence*

BPR *ByPass Ratio*

BWM *Backward Whirling Modes*

CFD *Computational Fluid Mechanics*

CM *Computational Mechanics*

CMS *Component Mode Synthesis*

CPU *Central Processing Unit*

CROR *Counter-Rotating Open Rotor*

CS *Critical Speed*

DoE *Design of Experiments*

DOF *Degree Of Freedom*

DOFs *Degrees Of Freedom*

EEARTH *Enhanced Error Assessment of Response Time Histories*

FE *Finite Element*

FEM *Finite Element Model*

FFT *Fast Fourier Transformation*

FOM *Full Order Model*

FRF *Frequency Response Function*

FWM *Forward Whirling Modes*

GE *General Electric*

GU *Gap Usage*

HB *Harmonic Balance*

HBM *Harmonic Balance Method*

HBPR *High ByPass Ratio*

HP *High Pressure*

HPC *High Performance Computing*

HPOTP *High Pressure Oxygen Turbopump*

iFFT *Inverse Fast Fourier Transformation*

IHB *Incremental Harmonic Balance*

KLM *Karhunen-Loève Method*

LCVT *Latin Centroidal Voronoi Tessellations*

LP *Low Pressure*

MA *Modal Analysis*

MFSM *Multi-Fidelity Surrogate Modeling*

NM *Normal Mode*

NN *Neural Networks*

NNM *Nonlinear Normal Modes*

PCA *Principal Component Analysis*

PGD *Proper Generalized Decomposition*

POD *Proper Orthogonal Decomposition*

RBF *Radial Basis Functions*

RBNN *Radial Basis Neural Networks*

RGB *Reduction Gear Box*

RL *Redline*

RMSE *Root Mean Square Error*

ROM *Reduced Order Model*

SAE *Safran Aircraft Engines*

SBO *Surrogate Based Optimisation*

SE *Super-Element*

SFD *Squeeze Film Dampers*

SM *Surrogate Model*

SVD *Singular Values Decomposition*

SVM *Support Vector Machines*

SVR *Support Vector Regression*

TI *Time Integration*

TRBF *Tuned Radial Basis Functions*

UDF *UnDucted Fan*

UHBR *Ultra High ByPass Ratio*

Chapter 1

Industrial context and Introduction

"L'avion a dévoilé pour nous le vrai visage de la terre."
"The airplane has unveiled for us the true face of the earth."

Antoine de Saint-Exupery: French writer, poet, journalist and aviator (1900-1944)

Objectives

For more than 50 years, the twin spool turbofan has remained the standard in civil aviation aeroengines. An historical transition phase is currently going on towards the architectures that will characterize the aeronautical propulsion for the next decades. In this first chapter, this architectural transition is presented with a focus on the role of numerical simulation for mechanical design in this technological breakthrough context.

Contents

1 Aircraft engines in a technological breakthrough

In the early 20th century, the aircraft propulsion was assured by multiple forms of piston engines. In 1921, the French engineer Maxime Guillaume patented a new way to propel aircrafts using turbogas systems: "*Thruster by reaction on air*" (*"Propulseur par réaction sur l'air"*) [Guillaume, 1921]. The patented system is reported in Figure 1.1.

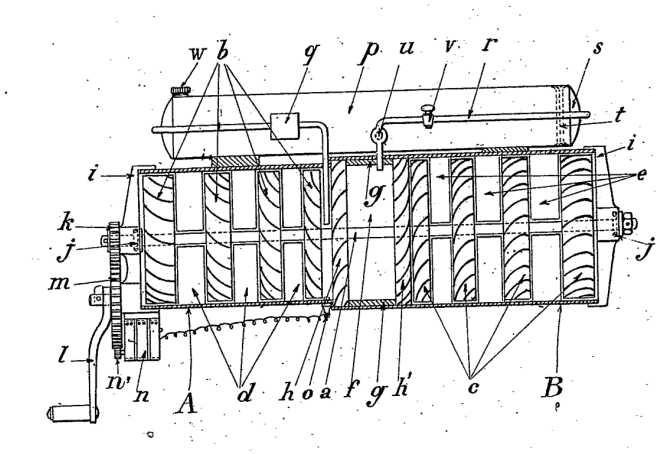

Figure 1.1: *"Propulseur par réaction sur l'air"* adapted from [Guillaume, 1921].

In early turboengines, a multi-stage compressor and a multi-stage turbine are mounted on a unique rotating shaft (e.g. *General Electric* (GE) GE-J47 [Janes, 2022]), this architecture is known as *single spool* [Royce, 2015] (see Figure 1.2a). In *multiple spools* (multiple shaft) architectures, multiple independent segments are working at different regimes, using a system of concentric drive-shafts connecting each compressor with its relative turbine (See Figure 1.2a). Each compressor-turbine set is free to rotate at a different rotational speed appropriate to the desired performance characteristics, leading to the improvement of the overall turbomachine performance. The first twin spool architectures were developed between 1950 and 1960, representing a revolution in aeronautical propulsion systems, we can cite the Pratt & Whitney J57 engine or the SNECMA/Rolls-Royce Olympus 593 designed for the French-British supersonic civil aircraft *Concorde* [Janes, 2022]. The British aircraft engine manufacturer Rolls-Royce presented at the same time the first triple spool configuration, characterised by three independent segments: low, intermediate and high pressure modules, the first example of a triple spool engine is the Rolls-Royce RB-203 Trent. This architecture is characterised by more components (more bearings, seals, shafts and sumps) and higher mechanical complexity and maintenance costs than the twin spool variant [Kauser, 1994]. Nevertheless, the triple spool architecture is still adopted by aircraft engine manufacturers such as Rolls-Royce Trent 900 [RR-Trent900, 2009], for its higher compression pressure ratio obtained as result of higher rotational speeds of the high pressure module leading to higher thermal efficiencies [Kauser, 2001].

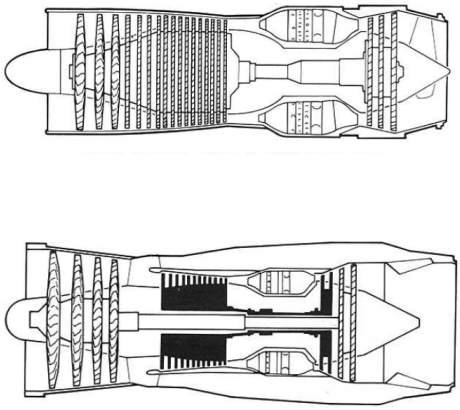

(a) Single spool (top) and Twin spool (bottom) architectures. Adapted from [Royce, 2015].

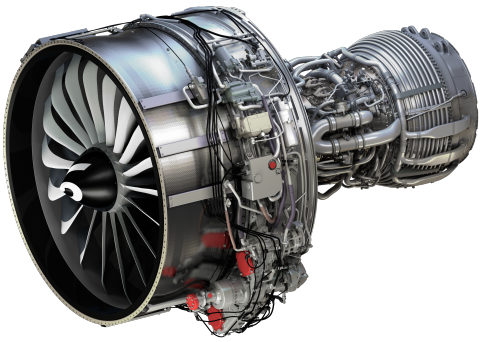

(b) Twin-spool double flux - CFM LEAP 1A [CFM-LEAP-1A, 2022].

Figure 1.2: Aeroengine's architectures.

Another important improvement of turbo-gas thrusters is the development of the *double flux* architecture between 1970 and 1980 increasing the efficiency of the machines. In this architecture, the airflow is compressed by a large fan and split into two channels: the largest portion is used to thrust the aircraft *by-passing* the core, the remaining portion is delivered to the combustion system in the usual way to generate the mechanical energy necessary to supply the fan, compressors and the other aircraft's accessories [Gorla, 2003]. The fan can be connected directly (e.g. CFM-LEAP 1A reported in Figure 1.2b) or through an epicyclic *Reduction Gear Box* (RGB) to the low pressure module (e.g. Pratt & Whitney GTF engine [PW-GTF, 2023]), referred respectively to as *turbofan* and *geared turbofan*. Another largely released engine type is the *turboprop*, which uses a propeller instead of a fan. In this case the propeller is always connected to the low pressure module through an asymmetric or epicyclic gearbox (e.g. the triple spool engine Europrop intl. TP-400). With the development of the double flux architecture, the concept of *ByPass Ratio* (BPR) β has been introduced, measuring the ratio between the cold airflow and the hot airflow processed respectively by the fan and the core of the engine. Figure 1.3 shows that the bypass ratio of the turbofan makes this architecture more efficient than the turbojet at the same cruise speed. The turboprop is even more efficient than the turbofan but only in a limited range of speeds. Sweeping the blades of the turboprop, the speed limit of this technology can be extended.

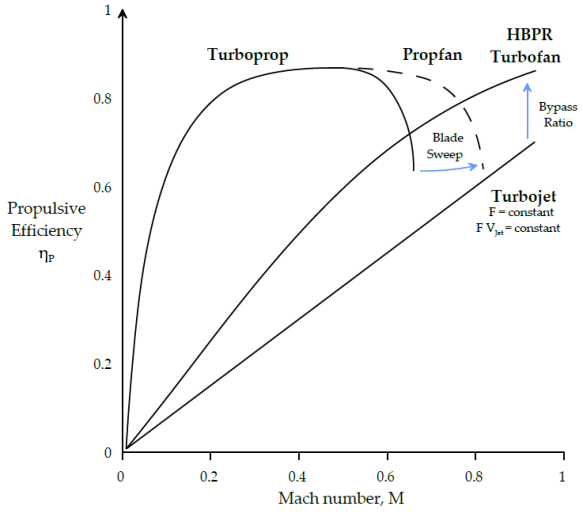

Figure 1.3: Propulsive efficiency for different engine types. Adapted from [Alves, 2020].

The historical evolution of the civil aircraft engines is mainly driven by the engine's propulsive efficiency improvement. The energetic performances of aeroengines are related to their BPR. As the BPR increases, the specific fuel consumption S_{fc} decreases and this represents a relevant advantage of high bypass turbofan engines in a high fuel cost environment : $S_{fc} \propto {}^{1}/_{\beta}$ [Sforza, 2016].

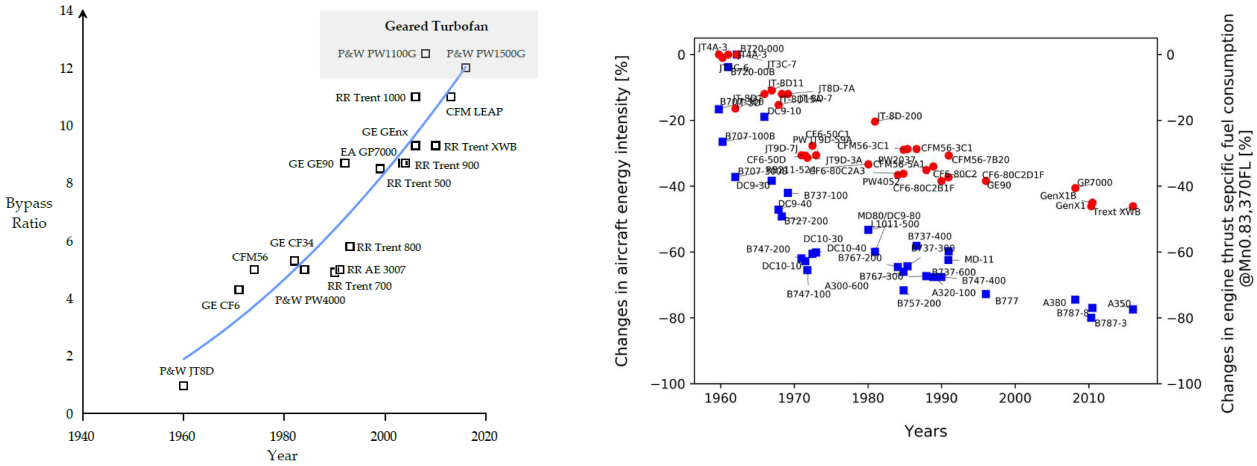

(a) Turbofan BPR evolution over the years. Adapted from [Alves, 2020].

(b) Trends in aircraft engine efficiency. Adapted from [Koff, 1991].

Figure 1.4: Turbo-fan performances over the years.

Since the 1960's, the BPR increased almost linearly over the years (see Figure 1.4a). Increasing the BPR, engines have become more and more efficient reducing their specific fuel consumption (see Figure 1.4b) [Yin, 2020; Alves, 2020]. This trend opens to a new generation of aircraft engines, propelled by larger fans and without the engine duct: the *UnDucted Fan* (UDF) [Koff, 1991] (see Figure 1.5), promising an increase in thermal and

propulsive efficiencies with a reduction of $25 - 35\%$ in fuel consumption and environmental impact [Schimming, 2003; Langston, 2018]. UDFs are also known as *open-rotor* and are part of a family of engines referred to as *Ultra High ByPass Ratio* (UHBR). An example of open-rotor architecture is reported in Figure 1.6a. The first concept of UDF was developed around 1980 by NASA in collaboration with GE aviation with the GE36 program. The engine was never developed industrially because the drop in oil price in mid-eighties caused a loss of interest in the project. Nowadays, the energy crisis and the new ecological challenges made this type of architecture interesting again.

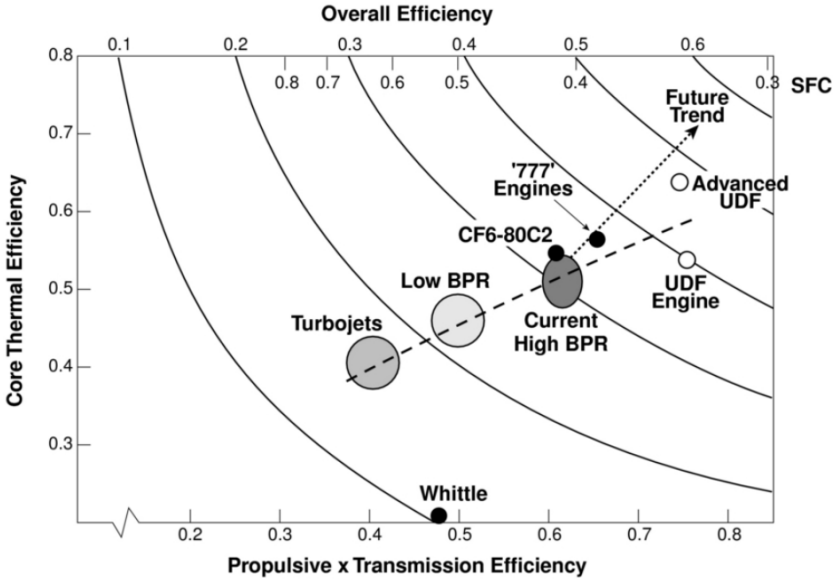

Figure 1.5: Trends in aircraft engine efficiency. Adapted from [Koff, 1991].

The fuel price is a fundamental variable in civil aviation and the environmental impact of the engines has to meet challenging goals of modern regulation organisms such as the Advisory Council for Aeronautics Research and Innovation in Europe (ACARE). According to the Flightpath 2050 Europe's vision for aviation report, aircraft engines have to reduce their CO_2 emissions by 75% and NO_x by 80% by year 2050 in comparison to the same technology of the year 2000 [Darecki, 2011]. Aircraft and aircraft engines manufacturers are involved in the ecological transition. To meet the European Union's goals for aeronautical transportation, the aircraft engines manufacturer *Safran Aircraft Engines* (SAE) in collaboration with GE aviation is engaged in the *RISE* program (Revolutionary Innovation for Sustainable Engines) promising a next generation engine that could reduce CO_2 emissions by more than 20% in comparison to the CFM-LEAP engines by 2035, using the open rotor technology [SAE-carbon, 2021].

The classical double flux architecture is physically limited in terms of BPR to 10-12

[Sforza, 2016; Alves, 2020], because at this point the weight of the duct and the drag force impact negatively the engine's performances. The UDF is basically a double flux engine, with an UHBR without the duct. This architecture is generally associated to a gearbox in order to optimize the rotational speeds of the low pressure shaft and the engine's core. The engine's core improves its performances increasing rotational speed. On the other hand, the rotational speed of the fan has to be regulated properly to avoid supersonic phenomena and instabilities at the extremities of the blades as they are particularly large.
Two configurations can be cited concerning this type of engine:

- Pusher configuration: using a couple of counter rotating fans positioned on the rear of the engine (see Figure 1.6a) as presented in NASA/GE-GE36 engine or in SAE *Counter-Rotating Open Rotor* (CROR) demonstrator reported in Figure 1.6b. The two counter rotating fans are chosen for aerodynamical and acoustic reasons connected to the low pressure shaft through the RGB.

- Puller configuration: using only one fan positioned at the front of the engine, with a non-rotating set of variable-pitch 'stators' (*rectifier*) allowing to redirect the thrust airflow generated by the rotating front set. The gearbox is still employed in this architecture allowing the fan to reach the optimal working regime. This configuration is being developed in RISE program, a 3D model of the RISE engine is reported in Figure 1.7.

The main advantages of this architecture are related to the absence of the nacelle, so there are no bypass duct losses, significantly lower external nacelle drag and a higher BPR (can reach $\beta = 30$ or more according to Langston [Langston, 2018]).

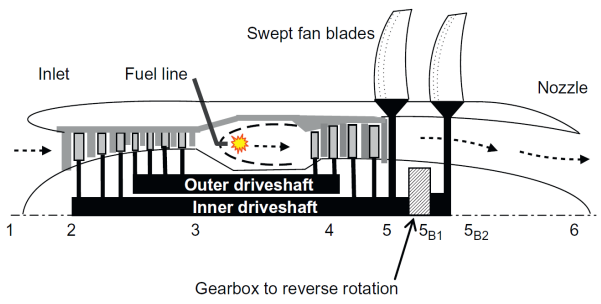

(a) Schematic diagram of an open rotor. Adapted from [Sforza, 2016].

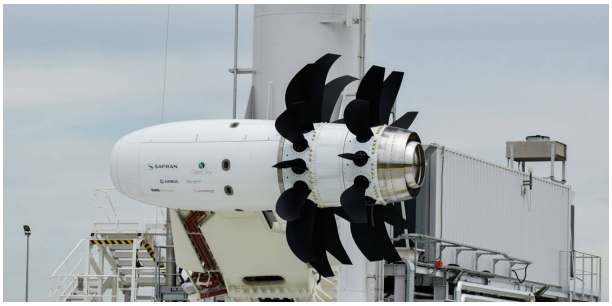

(b) SAE CROR demonstrator [CROR, 2019].

Figure 1.6: UDF schematic representation and SAE CROR demonstrator.

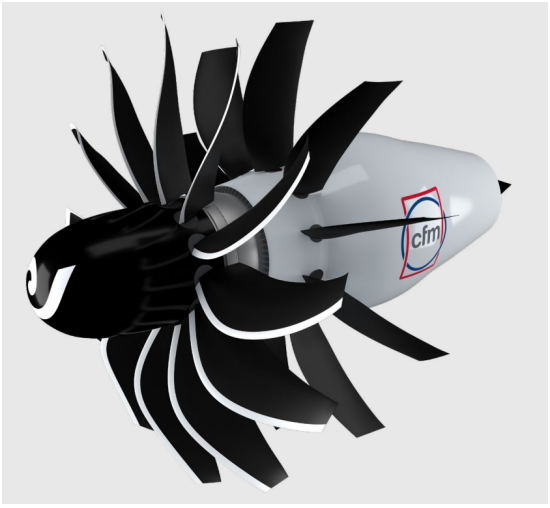

Figure 1.7: CFM-RISE engine 3D model, adapted from [CFM-RISE, 2021].

The multiple advantages of this new technology are not coming without technical challenges. Among other challenges, one can cite the noise generated by the fan without the acoustic shield of a duct. Adopting such a large fan the engine's installation on the aircraft is not trivial as well, multiple possibilities are still open, some of them can be cited: design high wing aircrafts to manage the fan's diameter or positioning the engine on the rear of the aircraft integrated to the fuselage (see Figure 1.8).

Figure 1.8: UDF engine installation [SAE-GE, 2021].

In this work, we are mainly interested in rotordynamics, it is thus essential to cite some of the technological challenges appeared with the introduction of these new architectures regarding directly this field of study:

- In UDF architectures the gearbox allows to reach higher rotational speeds on the low-pressure segment which implies the possibility of a low pressure rotor working

in supercritical regimes. The study of the stability of supercritical rotors requires to master the damping sources of the system.

- Another relevant challenge consists in the integration of the gearbox with the UDF architectures.
- The hybridisation of the engine is considered as well in this historical period and the integration of an electrical power system to the thermal one represents another relevant matter. The electrical power system can be connected directly on the low pressure shaft or through a transmission system.
- UDFs are UHBR engines and by definition the diameter of the fan is larger than common HBPR engines (e.g. in RISE program is proposed a fan diameter of 365-396cm [CFM-web, 2021] while the CFM-LEAP has a fan diameter of 176-198 cm [CFM-ad, 2017]). Classically, the whole engine's dynamics is decoupled from the fan's dynamics. This hypothesis could be questioned taking into account the new fan's dimensions.
- The unducted architectures are subject to an aero-elastic excitation referred to as *whirl-flutter* [Stapelfeldt, 2016], consisting in an excitation of the whole body of the engine arising from the interaction between the airflow and the engine's propeller and casing. This phenomenon is detailed in the case of UDFs in [Van Zante, 2014].
- Fans in UDFs architectures are generally characterised by blades with variable pitch angles, the balancing of the fan in this configuration and the pitch angle mechanisms themselves are fundamental technologies being studied and developed nowadays.
- Concerning the aeroengine's safety, the extreme event of *fan blade-off* is studied in depth: without the duct there is no protection for the fuselage in case of high speed blade ejection.

These fundamental changes in new aeroengine's architectures disrupt the classical design paradigms. New experiences, design process and numerical tools are necessary to design robust engines and master these new technological challenges.

2 The role of numerical simulation in a technological breakthrough

In the development of new engineering products, three key elements may be identified to support the design process and the decision making: simulation, physical prototyping

and know-how. The engineering expert masters the *know-how (savoir-faire)* and the empirical knowledge: complex industrial products are developed combining human intuition with a large pre-existing experience managing data, knowledge and models [Ball, 1997; Ullman, 2001].

In the specific case of the technological breakthrough which the aeronautics is facing nowadays, the empirical knowledge and the expert's *know-how* acquired on the classical multiple spool turbofan, cannot always be extrapolated to the UHBR architectures. This means that the experimental and numerical frameworks have to produce new knowledge to assure the design of robust products.
The exploration of the design space [Roux, 1998; Koch, 2002; Dasari, 2019], the sensitivity analysis [Guedri, 2012; Kuczkowiak, 2020], the robustness analysis [Atamturktur, 2015] or the model calibration [Bi, 2017] demand to perform multiple simulations in multiple configurations of the system to acquire knowledge on the system's behaviour, these type of studies are referred to as *many-query frameworks*.
Detailed and accurate simulations are nevertheless prohibitive and the simulation's cost only allows a partial exploration of the design space and a partial understanding of the impact of the parameters on the behaviour of the system. It is thus essential to be able to simulate efficiently the responses of the system in the interesting design space. Reducing the computational burden and increasing the number of simulations in the desing space, it is possible to better understand the system's behaviour in the whole design space and master the uncertain parameters.

This work investigates the problem of nonlinear rotordynamics simulation on industrial scale aeroengines FEMs for many-query studies: their important size ($\propto 10^6$ DOFs) and the presence of nonlinearities make the simulations unaffordable to perform many-query analyses (sensitivity, robustness analyse or model calibration). For this reason, either a low number of simulations are performed producing quite limited results in many-query frameworks or if the study demands an higher accuracy the higher volume of simulations performed makes the many-query study very expensive. With this work we seek to provide numerical tools to reduce the computational burden with no or negligible degradation of the solution's quality.
Towards this end, multiple techniques are studied and developed from classical *Computational Mechanics* (CM). Time integration solvers are generally accurate in the evaluation of steady state responses but at the same time they are demanding in terms of computational burden. For this reason, a dedicated *Harmonic Balance* (HB) solver is developed to evaluate efficiently nonlinear responses of industrial scale FEM.
To work with large FEMs, the employment of model reduction techniques is essential. In structural mechanics, model reduction is generally associated to the Ritz projection, in

this research a Ritz reduction dedicated to rotating machines is developed and applied to industrial scale FEMs.
The dedicated Ritz reduction and the HB solver are coupled to reduce the overall computational burden of numerical simulations. Nevertheless, this research shows that the gain in computational burden obtained with the combination of classical CM approaches is still insufficient in a many-query framework since theoretical limits remain. A new paradigm of model order reduction is thus adapted from computational fluid mechanics [Sainvitu, 2010; Benamara, 2017b], allowing to strongly reduce the computational burden of simulations using data-based surrogate models. The mathematical limitations in CM methods have been removed with the introduction of a machine learning technique in the simulation process.

This research is mainly focused on the three research areas cited above (nonlinear HB, dynamic model order reduction and data-based surrogate modeling) applied to rotordynamics for modeling industrial scale turbomachines. In Section 2 of Chapter 2, the FEM of an industrial scale turbomachine is used to present the modeling choices adopted in this work. The details of numerical techniques adopted or developed in this work are given in a preliminary way in Sections 4.3.2, 5, 6 of Chapter 2, the work outline and the contributions of this research are resumed in Section 7 of Chapter 2.

Chapter 2

Numerical modeling of turbomachines

"Heavier-than-air flying machines are impossible."
Lord Kelvin: British physicist (1824-1907)

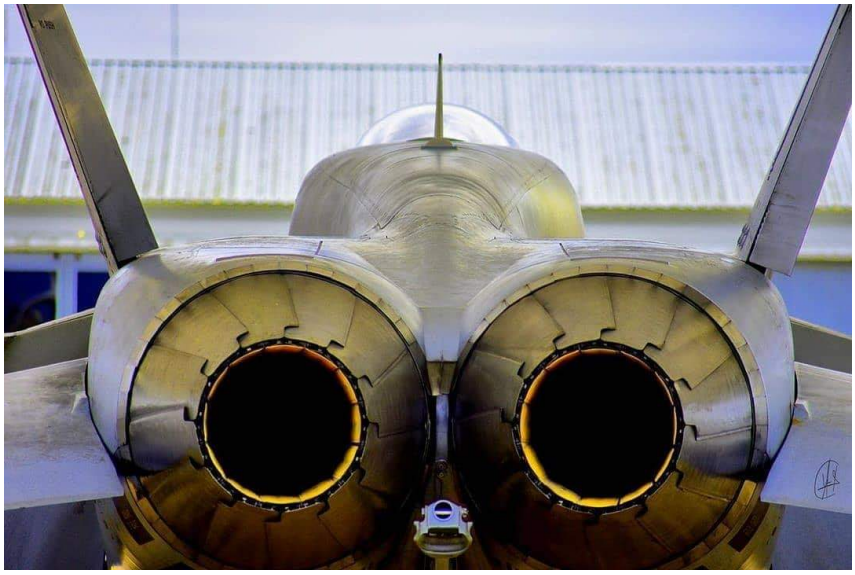

Objectives

In this chapter we present the literature related to the development of finite elements models representing rotating systems for industrial applications. The principles of rotordynamics are introduced in the case of whole shaft and bladed discs. Numerical analyses in rotordynamics are introduced as well focusing on nonlinear unbalance responses with rotor-stator contact. Classical reduction methods based on Ritz projections are presented and new paradigms of data-based model reduction are introduced. Finally, the contributions and the outline of the work are given.

Contents

1 Introduction to numerical modeling in rotordynamics

Rotordynamics has been studied from the beginning of the 20^{th} century by Jeffcott and Laval, developing the so-called *Jeffcott-Laval rotor*, composed of a rigid disc on a flexible shaft mounted on a pair of rigid symmetrical supports [Jeffcott, 1919]. Later, Stodola and Green [Stodola, 1927; Green, 1948] presented a more realistic model than the Jeffcot-Laval one: a rigid disc on a rigid shaft mounted on a pair of flexible viscoelastic supports, including the gyroscopic effect with a description of the physics of the disc by 4 DOFs. These works displayed for the first time the phenomenology of rotating shafts defining the relevance of critical speeds and of the steady-state response of the rotor over its operating frequency range. These models are still adopted for educational purposes [Lalanne M, 1998; Genta, 2007] and to study complex phenomena on simple systems [Choi, 1994; Chu, 1998].

In the early sixties, the numerical simulation revolution and the first FE analyses in rotordynamics arrived: Ruhl presented a study about the dynamics of a turborotor [Ruhl, 1970; Ruhl, 1972], Nelson and McVaugh proposed the first FE model including gyroscopic terms [Nelson, 1976]. In 1977 Zorzi and Nelson introduced viscous and structural damping in FE rotating beams [Zorzi, 1977] and finally in 1980 Nelson used for the first time a sequence of Timoshenko's beams to model rotating shafts [Nelson, 1980].

These first numerical models allowed to simulate the response of rotating systems over their operating frequency range and their modal situation. The unbalance response of real rotating machines is generally impacted by nonlinear phenomena. Classical sources of nonlinearities are related to the presence of nonlinear journal bearings such as SFDs [Adiletta, 2002; Della Pietra, 2002] or others (e.g. hydrodynamic supports, etc.) and to the rotor-stator contact phenomena [Muszynska, 1989; Ahmad, 2010; Jacquet-Richardet, 2013]. These phenomena were studied initially by direct experiments or through elementary analytical model as shown by Gunter in 1966 [Gunter Jr, 1966]. The first FE models with nonlinear journals and rub phenomena were published between 1975 and 1980 [Childs, 1975; Adams, 1980]. Before the early eighties, direct time integration methods were the only options to evaluate the response of nonlinear rotor-bearing systems. New frequency-based solvers for the evaluation of the steady-state response of a nonlinear system were proposed by Choi et al. in 1987 [Choi, 1987] using the Galerkin method associated with the *Fast Fourier Transformation* (FFT). Natraj et al. in 1989 proposed an alternative to the Choi's method using *trigonometric collocation* [Nataraj, 1989]. The HBM presented in an early form on a Jeffcott rotor by Yamauchi [Yamauchi, 1983], then

by Choi and Noah [Choi, 1987] and by Kim and Noah [Kim, 1990; Kim, 1996], have become a recognised alternative to the direct time marching methods and today is adopted for nonlinear rotordynamics by multiple research teams [Von Groll, 2001; Guskov, 2007; Bonello, 2009].

These works show how to model a rotating system using beam elements taking into account any relevant characteristic of the system to describe its dynamical behaviour (rotating damping, gyroscopic effect, nonlinearities, etc.). Moreover, the main numerical methods used to simulate the response of a complex rotating system in the time or frequency domain and in a linear or nonlinear configuration are given for the FE framework. These elements are observed in detail in the body of the present chapter introducing as well the elements of model order reduction allowing to deal with large scale FEMs. Surrogate modeling techniques are then presented in order to define a new paradigm of model order reduction in structural mechanics. In this work we seek to mix the classical elements of rotordynamics with new model order reduction and surrogate modeling approaches to define a new way to deal with industrial scale rotordynamical FEMs. The purposes of this work are defined in this chapter with a section dedicated to the contributions and the outline of the present thesis.

2 Rotating systems modeling

This section presents the techniques to model a modern aeroengine in a whole engine dynamics framework. The cross section of the industrial aeroengine Rolls-Royce Trent-900 [RR-Trent900, 2009] reported in the upper part of Figure 2.1, is used to present the main rotordynamical elements of the machine. It is a triple-spool double flux engine (BPR of 8.5), powering the so-called *Super-Jumbo Jet* AIRBUS A380.
This architecture consists in three independent and concentric shafts: low, middle and high pressure modules, represented respectively in blue, yellow and red in the upper part of Figure 2.1. On the bottom of the figure the modeling elements necessary to simulate the dynamical behaviour of the system are illustrated. Several groups of modeling elements are highlighted:

- **Grey elements**: rotating shafts represent the main structural element of rotors. They can be modeled using mono-dimensional beam elements, bi-dimensional Fourier representation or three-dimensional elements.
- **Blue elements**: bladed discs represent the elementary component of a multi stage compressor/turbine. Depending on the type of analysis to perform they can be modeled using a lumped mass representation, a bi-dimensional or a three-dimensional detailed representation.

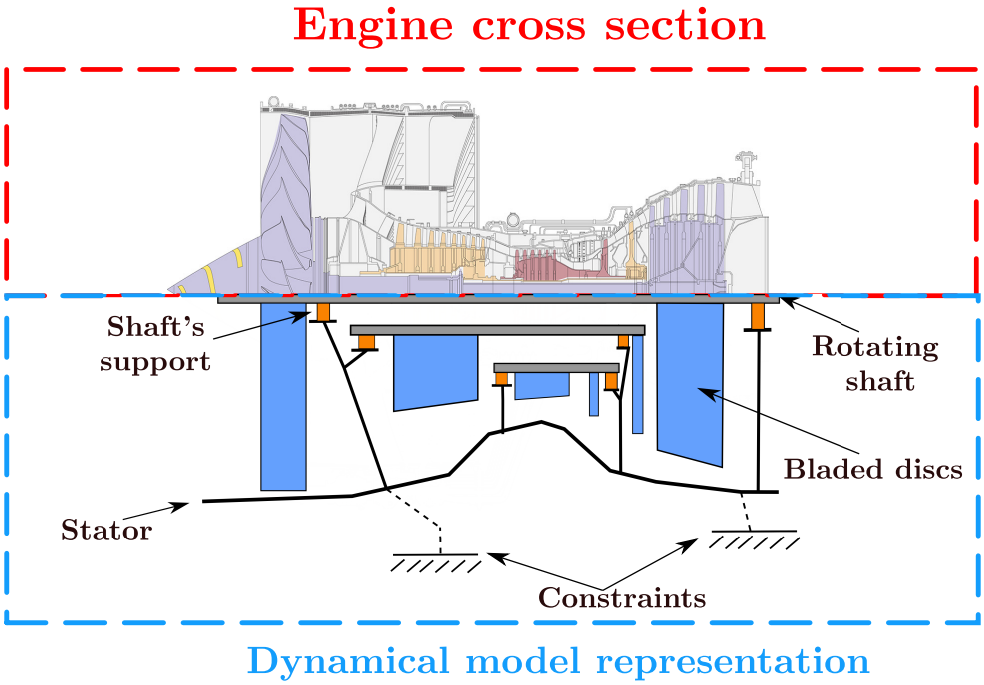

Figure 2.1: Mechanical modeling of an industrial scale aeroengine. Rolls-Royce Trent 900 [RollsRoyce-Trent, 2022].

- **Orange elements**: shaft supports make the mechanical connection between the stator and the rotor. They can be purely elastic or viscoelastic (also known as SFDs). These components have a fundamental role in the definition of the whole engine dynamics, characterizing critical speeds, the shape of vibration modes and their modal damping ratios.

- **Black elements**: stator or casing. Any rotor is supported by the casing, representing the fundamental mechanical element of the turbomachine and assuring its mechanical integrity.

Two different modeling approaches are employed to study the dynamical behaviour of complex rotating systems:

1. The *whole engine dynamics* approach: dedicated to the study of the dynamical behaviour of the whole turbomachine, identifying the position of critical speeds and their unbalanced responses. In this approach, if the system is characterised by axisymmetrical rotors and stators, it can be represented indifferently in the inertial or rotating reference frames. If only the rotor is axisymmetrical it is preferred to express the system in the inertial reference frame, in order to have invariant dynamical matrices [Geradin, 1984; Genta, 2007; Kirchgäßner, 2016]. Dynamical operators become time-dependent if the rotors are not perfectly axisymmetrical and in this case special solution methods are required (e.g. multi-body dynamics) [Genta, 1988].

In whole engine dynamics studies, the hypothesis of rigid discs is generally assumed, neglecting the detailed geometry and physics of the bladed discs. The shafts are generally represented using mono-dimensional beam elements [Bonello, 2010; Petrov, 2012; Parent, 2014], but not only.

2. The *dynamics of the bladed disk*: dedicated to the study of dynamical phenomena regarding singular discs. A detailed representation of the disc geometry is generally adopted, while the shaft dynamics are neglected, generally the operators are expressed in a rotating reference frame [Jacquet-Richardet, 1996; Laxalde, 2007; Yuan, 2017].

In this work we focus on the whole engine dynamics, the aspects regarding the dynamics of the bladed discs are introduced in this chapter but they are not studied in depth in the following chapters of this work.

2.1 Shaft modeling

In this section the bibliographical elements motivating the modeling choices of the rotating shafts (**grey elements** in Figure 2.1) assumed in later chapters of this work are given. Multiple modeling approaches can be adopted in FE framework to simulate the dynamical behaviour of rotating shafts. The choice of the modeling approach is generally dependent on the shaft's symmetry properties and on the accuracy needed for the study: mono-dimensional (1D), bi-dimensional (2D) and three-dimensional (3D) modeling approaches are possible for rotating shafts modeling, these three approaches are presented in this section.

The simplest modeling approach for rotating shafts is the mono-dimensional one using beam elements. From the late seventies, beam elements have been employed to study the dynamical behaviour of rotating shafts in FE frameworks. The first works were presented by Ruhl in 1970 and by Ruhl et al. in 1972, using Euler-Bernoulli beam formulation neglecting the gyroscopic effect and shear deformations [Ruhl, 1970; Ruhl, 1972]. Nelson and MacVaugh in 1976 used the Rayleigh's beam to model rotating shafts, including the effect of the rotational inertia [Nelson, 1976]. Later works have been enriched by Zorzi and Nelson by introducing the viscous damping effect in 1977 [Zorzi, 1977]. In 1980, the Timoshenko beam has been used by Nelson for rotor modeling, taking into account the gyroscopic effect, shear efforts, planar flexion effects, torsional efforts and the rotational inertia [Nelson, 1980]. In last work, the Timoshenko beam element is compared with the two other aforementioned beam elements (Euler-Bernoulli and Rayleigh beams), demonstrating that it is the most accurate option for shafts modeling. Other works extend this result to rotating beams [Yokoyama, 1988; Katz, 1988; Genta, 2013].

Nowadays, the employment of Timoshenko beam for shafts modeling is recognised and widely used (e.g. [Vance, 1991; Lalanne M, 1998; Genta, 2007]). An example of rotating shafts modeling using Timoshenko beam elements is given in Figure 2.2.
This mono-dimensional modeling approach is employed in aeroengine's design to study the whole engine dynamics which demands a simplified representation of the rotating shafts. When both rotors and stators are symmetrical with respect to the rotation axis, the dynamical operators can be expressed with similarity in the inertial or rotating reference frames, as they are in any case invariant with the rotation of the shaft. On the contrary, with non-symmetrical stator and symmetrical rotors the use of the inertial reference frame is recommended since it allows to represent both the stator and rotor with invariant operators. The employment of the rotating reference frame in this last case would generate periodic operators for the representation of the non-symmetrical stator. Some aeronautical applications of this approach are presented by Bonello et al., Sinou et al. adopting Timoshenko beam elements [Bonello, 2010; Sinou, 2005] or by Parent et al. adopting Eulero-Bernoulli's beams [Parent, 2014].

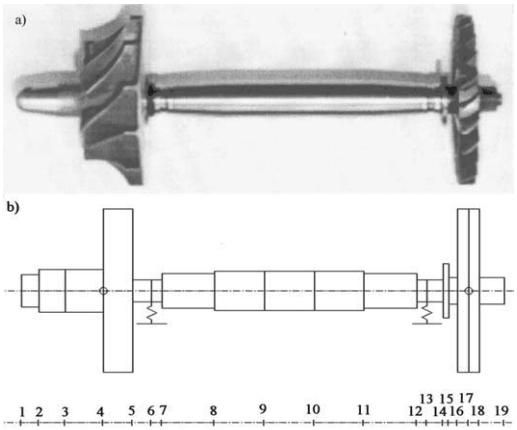

Figure 2.2: Rotor of a small turbojet engine. a) Picture of the rotor b) Beam FE model [Genta, 2007].

The mono-dimensional representation generally yields results that are accurate enough for low frequency dynamics (left side of Campbell diagram). However, high frequency modes are generally poorly represented. If the shafts are too stub or the cross section is too thin to be modeled with beam elements a two or three dimensional representation of the shaft is required to predict properly the dynamics of the system. Both these types of approaches are more expensive than the first one cited as FEMs have higher nodal density and the solution methods are not the same as these adopted in the mono-dimensional case.
The most widely used bi-dimensional modeling approach in rotordynamics was introduced for the fist time by Geradin in 1984 [Geradin, 1984], also known as *2D Fourier*

multi-harmonic modeling or *2D Fourier finite elements modeling* [Combescure, 2008], is employed to study the dynamical behaviour of axisymmetrical rotors or rotors with *cyclic symmetry* (consisting of N identical radial sectors). This approach allows to obtain more detailed results than the 1D modeling approach using models with a limited nodal density. Rotating shafts, multi-stage turbomachines or propellers, are cyclic symmetric structures and this modeling approach can be adapted to these systems.
Finally, the three-dimensional modeling approach is generally associated to non-axisymmetrical rotors, the dynamical operators in this case are expressed in the rotating reference frame and time integration solvers are generally employed to take into account the time dependent nature of dynamical operators (e.g. multi-body dynamics solvers) [Tian, 2011]. Tannous et al. studied the impact of modeling rotating shafts with 1D and 3D elements for rotor-stator contact problems, proving that the three-dimensional predictions are more accurate than the mono-dimensional ones, with an higher computational burden [Tannous, 2015b]. To reduce the computational effort related to this kind of simulation, Tannous et al. presented an original technique consisting in switching from 1D to 3D representation of the shaft in a direct time integration procedure [Tannous, 2013; Tannous, 2015a].

In this work we are interested in the study of the whole engine dynamics, a mono-dimensional modeling of the shaft is chosen, adopting the Timoshenko's beam element. The equations of motion are expressed in the inertial reference frame since the rotors are considered as perfectly symmetrical with symmetrical and non-symmetrical supports in some applications.

2.2 Bladed discs: turbine and compressor stages modeling techniques

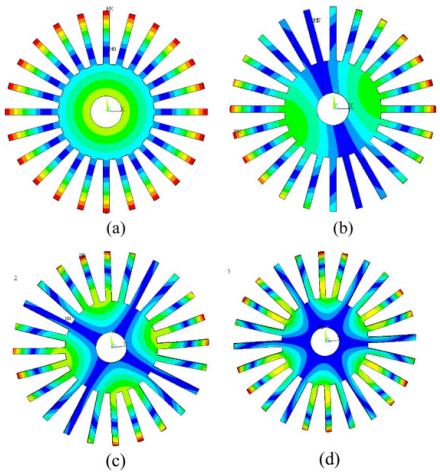

(a) Example of the bladed disc dynamics [Yuan, 2017]

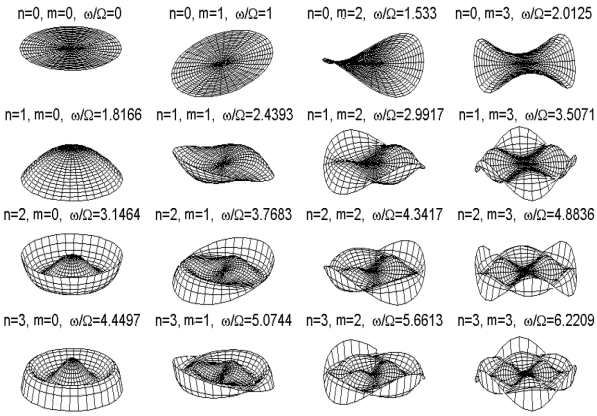

(b) Example of rotating membranes dynamics [Genta, 2007]

Figure 2.3: Rotating discs dynamics.

The representation of the compressor and turbine stages (**blue elements** in Figure 2.1) depends on the type of analysis to be performed. When the system is studied from a global point of view, the bladed disc dynamics is neglected since the shaft and the bladed disc dynamics are generally not strongly coupled. In whole engine dynamics studies, the bladed discs are considered as perfectly rigid, with no energy dissipation in the solid body due to disc deformations. As only the kinetic energy of the single disc impacts the dynamics of the whole engine, they are represented as lumped masses and inertias. This approach has been employed in the past (e.g. [Geradin, 1984; Genta, 1996a]) and it is still adopted nowadays to study the dynamics of rotating machines with symmetrical rotors (e.g. [Guskov, 2007; Chen, 2015], etc).

In the design phase of an aeroengine's bladed disc, the study of its dynamical behaviour is relevant and can't be neglected. In these cases the rigid-disc hypothesis is limiting and a three-dimensional representation of the disc's geometry is required to predict its vibrating behaviour correctly [Genta, 1996b; Laxalde, 2007]. In particular, in a bladed disc the internal section of the disc can display vibrating phenomena interesting different sectors of the disc's fleece periodically (see Figure 2.3 b) and dynamical effects related to vibration of the disc's blades (see Figure 2.3 a).
Bladed discs are perfect examples of cyclically periodic structures, this property can be widely employed to model this type of body. Yuan et al. [Yuan, 2017] presented a review showing two different modeling approaches to represent bladed discs in a fixed reference

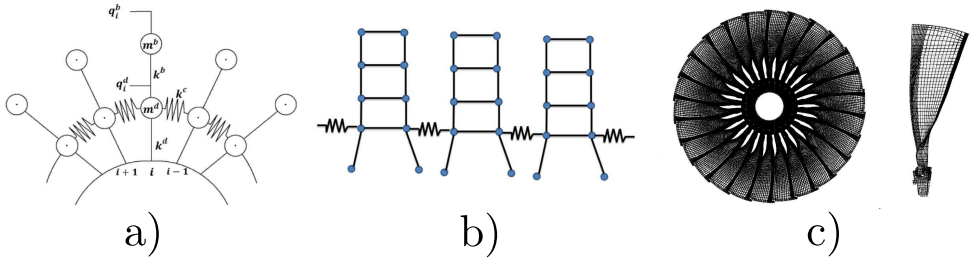

Figure 2.4: Disc modeling a) Mass-spring [Yuan, 2017]. b) Beam frame assembly [Yuan, 2017]. c) Three-dimensional modeling with cyclic symmetry [Petrov, 2004].

frame using their cyclic symmetry properties. The simplest way is to use a combination of lumped masses and springs to represent any blade connected to the rotor (see Figure 2.4a). A more complex approach is to use a beam frame assembly, allowing to increase the accuracy of the model (see Figure 2.4b). A three-dimensional representation of the disc can be adopted increasing the complexity of the simulation and the computational effort [Jacquet-Richardet, 1996; Laxalde, 2007]. Petrov presented multiple works using the cyclic symmetry of bladed discs taking into account nonlinear phenomena as well [Petrov, 2004; Petrov, 2006]. Colaitis adopted the same three-dimensional approach with an HBM solver to study the blade-tip/casing contact in the framework of aircraft engines, with a focus on the stability of the response [Colaitis, 2021].

As seen in some of the cited works, the dynamics of bladed discs and the whole shaft dynamics are different [Loewy, 1984] and thus a dynamical coupling between them is not trivial. It is fundamental at this point to understand the possible interactions between the dynamics of the bladed discs and the shaft dynamics. This matter has been studied for a longtime, according to multiple authors, a coupling can exist between the vibration modes of bladed discs (or fan) and shafts [Parent, 2015; Khader, 1990; Turhan, 2006]. The flexibility of the rotor can impact the shaft dynamics but only low modal diameter vibration modes (k=0 or k=1) are compatible with the shaft dynamics [Crawley, 1984; Crawley, 1986]. Thus the shaft and disc dynamics can be coupled at low frequencies as stated by Chun et al. [Chun, 1996].

One can conclude that if the dynamics of bladed discs is not essential in the study and since there is not a strong coupling between the disc and the shaft dynamics in any operating regime of the machine, it is possible to neglect the disc dynamics in a whole engine dynamics framework. This hypothesis is going to be adopted for the rest of this work.

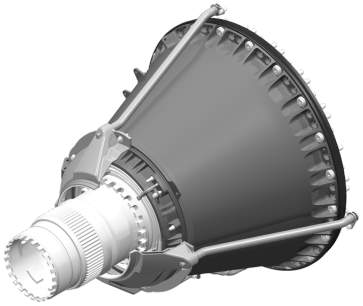

(a) Industrial front shaft support for aeronautical turbofan engines. [SAE-SP, 2019].

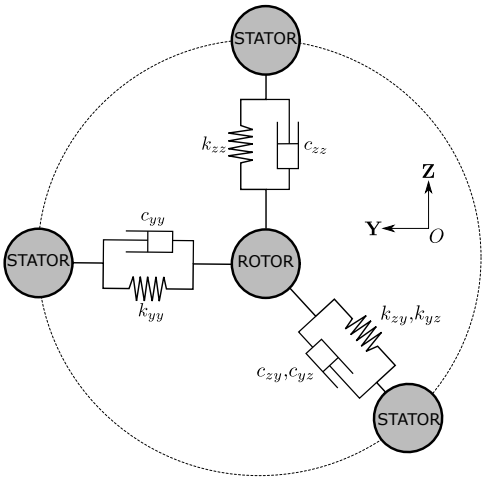

(b) Viscoelastic shaft support modeling.

Figure 2.5: Shaft support. a) Realistic shaft support assembly. b) Lumped stiffness/damping modeling approach.

2.3 Shaft support modeling

The shaft supports (**orange elements** in Figure 2.1) are fixed elements rigidly connected to the engine casing, supporting rotating shafts and generating radial and tangential forces in the plan perpendicular to the shaft (in Figure 2.5a is reported an example of industrial front shaft support assembly).
Shaft supports can be modeled without taking into account the detailed geometry of the linking element: using radial and angular lumped stiffnesses or a combination of lumped stifnesses and dampers (see Figure 2.5b).

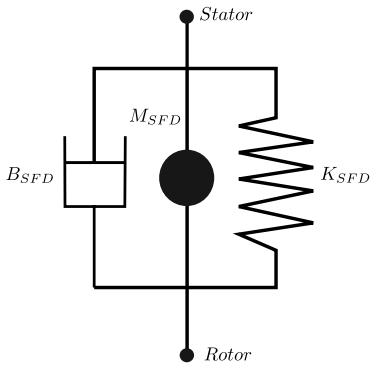

Figure 2.6: Linearised SFD according to [Zeidan, 1996].

For some specific types of support such as SFDs, a scalar mass is generally affected to the link [Vance, 1991; Zeidan, 1996] (see Figure 2.6).
The first experimental works on SFDs have been presented by Griffit in 1966 [Griffin, 1966]. In 1974 Mohan et al. published a first numerical study of a simple rotor including

a short SFD, no cavitation effect is considered in this work. In 1977, Gunter et al. presented a FE model including a model of nonlinear SFD, taking into account the cavitation effect generated in the fluid film [Gunter, 1977]. San Andres, Zeidan and Vance, investigated in depth the design and phenomena characterising different types of SFDs [San Andres, 1986; Zeidan, 1989; Zeidan, 1990; Zeidan, 1996]. In early 2000, Bonello showed for the first time the employment of an harmonic balance approach to identify the nonlinear frequency response of aircraft engines with SFDs [Bonello, 2002; Bonello, 2009]. Multiple works have been conducted using fluid mechanics to evaluate the dynamical forces generated by the whirling motion of a rotating shaft in a SFD [Guo, 2005; Defaye, 2006; Gehannin, 2009a; Gehannin, 2009b]. For more details concerning the design and the experimental works about SFDs, it is interesting to report a large overview produced by the Neapolitan scientists Adiletta and Della Pietra in 2002 [Adiletta, 2002; Della Pietra, 2002].

There are two types of SFDs: *classical* SFD (see Figure 2.7a) and the *integrated* variant (see Figure 2.7b). The first one is mainly employed in aeronautical turbomachines, with a separate *squirrel cage* ensuring the elastic function of the device and a cavity containing the fluid film, the second configuration is mainly employed for energy generation turbomachines, characterised by a unique component providing damping and elastic forces.

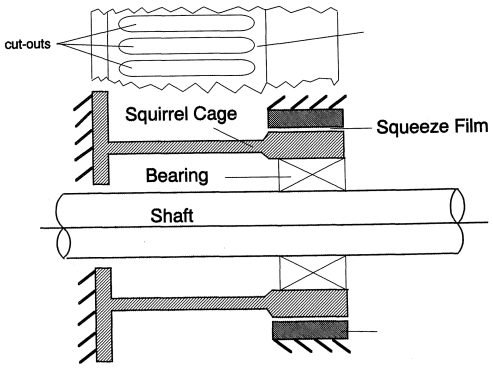

(a) Simplified representation of a *Classical* SFD [Zeidan, 1996].

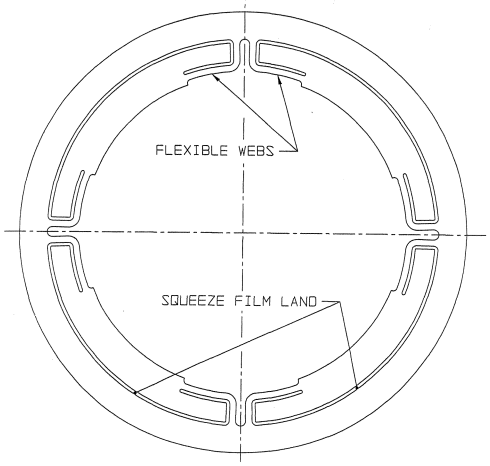

(b) *Integrated* SFD [Zeidan, 1996].

Figure 2.7: Classical and Integrated SFD architectures.

3 Finite element modeling

Adopting the modeling techniques presented in the above sections, two FE models are presented here. First of all, a modified Jeffcott-Laval rotor, counting a small number of DOFs, to simply present the concepts developed in the further parts of this work. Then, an industrial scale FE model representing a modern aeroengine ($\propto 10^6$ DOFs) is studied in order to prove the scalability of the numerical techniques developed.

3.1 Modified Jeffcott-Laval rotor

The considered modified Jeffcott-Laval model is defined in an inertial reference frame $\mathcal{R}_0(0, \mathbf{X}, \mathbf{Y}, \mathbf{Z})$ (see Figure 2.8a). In this model, we are not interested in torsional dynamics, the displacements field is defined in any node of the model as reported in Equation 2.1.

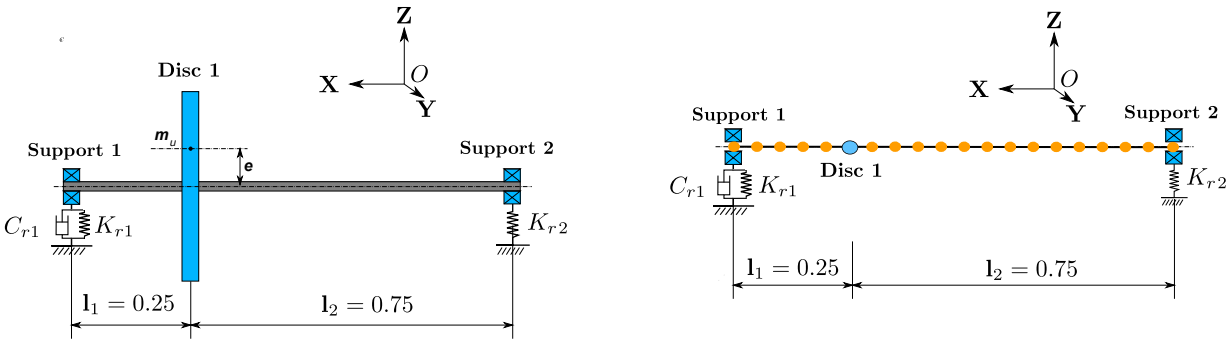

(a) Modified Jeffcott-Laval rotor. (b) Modified Jeffcott-Laval rotor FE model.

Figure 2.8: Modified Jeffcott-Laval rotor.

Property	Value
Beam's thickness $[m]$	0.003
External ray $[m]$	0.03
Material density $[kg/m^3]$	7900
Young's module $[N/m^2]$	2.1e11
Poisson ratio	0.3
Beam's length $[m]$	0.05
hysteretic damping factor	10%

Table 2.1: Mechanical properties of the Timoshenko beam used to model the shaft.

$$\mathbf{q}_f = \begin{bmatrix} u & v & \phi & \psi \end{bmatrix}^T_{\mathcal{R}_0} \tag{2.1}$$

u and v represent the displacements in the transversal plan of the rotor along the two directions $\mathbf{Y}$ and $\mathbf{Z}$, ϕ and ψ are respectively the rotations along the axis $\mathbf{Y}$ and $\mathbf{Z}$. The

considered Jeffcott-Laval rotor is presented in Figure 2.8a. It is characterised by a rigid disc, positioned on an elastic shaft with two radial supports at the extremities. The shaft is modeled using Timoshenko beams [Nelson, 1980] representing hollow cylinders, the details of their geometry are reported in Table 2.1.
20 beam elements have been used to model the whole shaft, each one of them is characterised by two nodes, when assembled, 24 independent nodes characterize the FE model of the rotor. Considering 4 DOFs per node, the model contains 92 DOFs. The stator is simply represented by 2 constrained nodes at the extremities of the rotor connected with the rotor by two supports: the support #1 represents a linearised SFD (see Figure 2.6), while the support #2 is purely elastic (see Figure 2.8b). The two supports are symmetrical, they have the same elastic behaviour along the two directions $\mathbf{Y}$ and $\mathbf{Z}$. The radial stiffness of the supports #1 and #2 are equal.

As specified in the previous sections, the disc is modeled using a lumped mass of $m = 50\,kg$ acting in the plan perpendicular to the rotation axis, the diametral and polar inertias of the disc are respectively: $I_d = 0.5kgm^2$, $I_p = 1kgm^2$. The matrices containing the mechanical properties of the Timoshenko beam and the matrices allowing to affect the lumped mass to the node representing the disc, are largely described in the scientific literature, nevertheless they are reported for completeness in Appendix 1.

This system is studied in linear and nonlinear frameworks, in particular in the case of a rotor-stator contact. To simulate the response of the system in nonlinear cases, a conditional nonlinear force is applied on the disc if the contact between the rotor and the stator is established, more details concerning the mathematical formulation of this nonlinear force are reported in the following.

3.2 Industrial scale model

In this work, the presented numerical methods are applied as well on an industrial scale FE model, discretised with about $\approx 10^6$ DOFs. The FE model is developed using the FE software MSC NASTRAN 2018 and it represents a realistic industrial scale aeroengine. For confidentiality reasons no pictures of this system are reported and the results concerning the numerical simulations performed are adimensionalised. A simplified representation of the system under study is given in Figure 2.9.

In this case, the displacements field is defined along the three axis of the inertial reference $\mathcal{R}_0(0, \mathbf{X}, \mathbf{Y}, \mathbf{Z})$ as seen in Equation 2.2.

$$\mathbf{q}_f = \begin{bmatrix} u & v & w & \phi & \psi & \xi \end{bmatrix}^T_{\mathcal{R}_0} \tag{2.2}$$

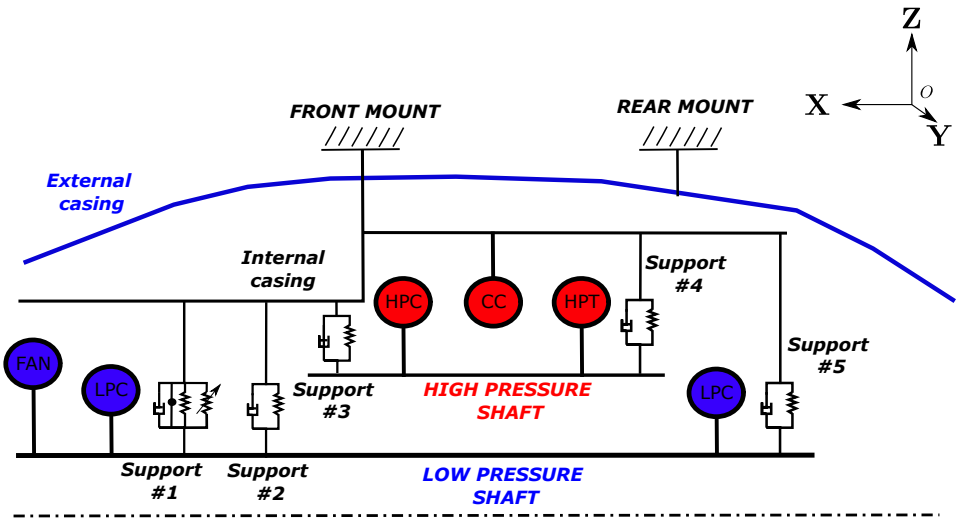

Figure 2.9: Simplified representation of the industrial system employed in this study.

The system reported here is a twin spool aeroengine, with a *Low Pressure* (LP) shaft and an *High Pressure* (HP) shaft. Five mechanical supports ensure the structural connection between the shafts and the stator, there is no physical connection between the two shafts. The support #1 contains a source of nonlinearity due to the contact between the rotor and the stator. This form of nonlinearity could appear at any point of the shaft, especially at the other supports where clearances are particularly small. Nevertheless, they are not considered in this work. Supports #1 is a SFD, modeled as seen in Section 2.3. Other supports are purely viscoelastic without nonlinear effects. It is known that the SFDs introduce important nonlinear effects because of the complex behaviour of the fluid film and of the cavitation effects appearing commonly in these devices [Gehannin, 2009a]. Nevertheless, these phenomena are not taken into account in this work.
The stator is represented using shell elements positioned at the neutral surface of the real casing, while the shaft is once again represented using a series of Timoshenko's beams, similar to the ones detailed for the modified Jeffcott-Laval rotor.

4 Numerical simulation in rotordynamics

In this section the most widely used analyses in rotordynamics are presented in order to define the numerical framework adopted in further parts of this work. The governing equations of motion expressed in an inertial reference frame and in the time domain have the following form:

$$\mathbf{M}\ddot{\mathbf{q}}_f + (\mathbf{D_v} + \Omega\mathbf{G})\dot{\mathbf{q}}_f + \mathbf{K}\mathbf{q}_f = m\,e\,\Omega^2\mathbf{f}(t) \tag{2.3}$$

with $\mathbf{M}$, $\mathbf{D_v}$,$\mathbf{G}$ and $\mathbf{K}$ representing respectively mass, viscous damping, gyroscopic and stiffness matrices expressed in an inertial reference frame $\mathcal{R}_f$. $\mathbf{q}_f$ and $\mathbf{f}(t)$ are respectively the physical displacement field of the system and the excitation vector expressed in the time domain. The scalar value e represents the distance of the unbalance mass to the rotation axis and m represents the value of the unbalance. The rotational speed of the rotor is Ω. Assuming an harmonic response, Equation 2.3 becomes Equation 2.4 expressed in frequency domain:

$$(-\omega^2\mathbf{M} + j\omega(\mathbf{D_v} + \Omega\mathbf{G}) + \mathbf{K})\hat{\mathbf{q}}_f = m\,e\,\Omega^2\,\hat{\mathbf{f}}, \tag{2.4}$$

with $\hat{\mathbf{q}}_f$ and $\hat{\mathbf{f}}$ representing respectively the displacements and the excitation in the Fourier space. In this last equation it is possible to include the hysteretic damping term $\mathbf{K}\eta_h$ as well, which cannot be expressed trivially in time domain [Genta, 2004]:

$$(-\omega^2\mathbf{M} + j\omega(\mathbf{D_v} + \Omega\mathbf{G}) + \mathbf{K} + j\mathbf{K}\eta_h)\hat{\mathbf{q}}_f = m\,e\,\Omega^2\,\hat{\mathbf{f}} \tag{2.5}$$

The third chapter is entirely dedicated to a discussion of the effects of viscous and hysteretic damping in rotating shafts and for this reason this subject is not studied in depth in this chapter.

4.1 Modal Analysis

In this section the linear modal analysis is presented in both conservative and non-conservative cases as they are essential to model order reduction approaches for structural dynamics. The nonlinear modal analysis is considered out of the scope of this work and will not be studied in depth.

4.1.1 Real modal Analysis

The *real modal analysis* in a linear framework is performed adopting the *real part* of Equation 2.4, including only the mass and stiffness matrices and neglecting any sort of damping effect. The modal properties of a dynamical system are defined by the solution of the following eigenvalue problem:

$$\left(\mathbf{K} + \lambda_j^2\mathbf{M}\right)\phi_j = 0 \rightarrow \left(\mathbf{K} + \lambda^2\mathbf{M}\right)\Phi = 0 \tag{2.6}$$

Where $\lambda/2\pi$ represents the natural frequencies of the vibration modes and Φ the mode shapes. Any mode shape ϕ_j has a corresponding natural frequency $\omega_j : \lambda_j = \pm i\omega_j$. Mode

shapes respect the following orthogonality relationship with mass and stiffness matrices:

$$\begin{cases} \Phi^T \mathbf{M} \Phi = diag(m_j) \\ \Phi^T \mathbf{K} \Phi = diag(k_j) = diag(m_j \omega_j^2) \end{cases} \tag{2.7}$$

Where m_j and k_j are respectively the *modal mass* and *modal stiffness* of the j-th mode, with $m_j \omega_j^2 = k_j$. Generally the modes shapes are normalised with respect to the mass, obtaining:

$$\begin{cases} \Phi^T \mathbf{M} \Phi = [I] \\ \Phi^T \mathbf{K} \Phi = diag(\omega_j^2) \end{cases} \tag{2.8}$$

The real modal analysis so described is employed in further sections and compared to the complex modal analysis to highlight the main differences between them.

4.1.2 Complex modal analysis

The complex modal analysis includes the damping effects. In this case, it is necessary to express the dynamical problem (Eq. 2.4) in the state space to produce normal modes respecting orthogonality properties. The state space representation is formulated by adding to Equation 2.4 the trivial Equation 2.9:

$$\mathbf{K}\, j\omega\, \hat{\mathbf{q}}_f - \mathbf{K}\, j\omega\, \hat{\mathbf{q}}_f = 0 \tag{2.9}$$

The passage to the state space is employed to solve this problem, yielding:

$$j\omega\, \mathbf{U}\, \hat{\mathbf{z}}_f - \mathbf{A}(\Omega^s)\, \hat{\mathbf{z}}_f = 0 \tag{2.10}$$

with :

$$\begin{aligned} \mathbf{U} &= \begin{pmatrix} \mathbf{M} & 0 \\ 0 & -\mathbf{K} \end{pmatrix} \\ \mathbf{A}(\Omega^s) &= \begin{pmatrix} -\mathbf{B} - \Omega^s \mathbf{G} & -\mathbf{K} \\ -\mathbf{K} & 0 \end{pmatrix} \\ \hat{\mathbf{z}}_f &= \begin{pmatrix} j\omega\, \hat{\mathbf{q}}_f \\ \hat{\mathbf{q}}_f \end{pmatrix} \end{aligned} \tag{2.11}$$

Other formulations of this operation are possible, producing similar results [Ljung, 1987; Balmès, 1996a]. In this case, the $\mathbf{U}$ matrix is symmetrical while the $\mathbf{A}(\Omega^s)$ matrix is anti-symmetrical (since $\mathbf{G} = -\mathbf{G}^T$). One can notice that the modal properties of the problem depend on the rotational speed of the system Ω^s (see Eq. 5.8). This is a peculiar characteristic of rotating systems since the rotational speed can indeed influence the position of natural frequencies and the shape of normal modes.

In eigenvalue analyses, *Basile's hypothesis* is a mathematical property of the eigenvectors which is verified if the real normal modes can diagonalise the damping matrix too:

$$\Phi^T \mathbf{D_v} \Phi = diag(\xi_j) \tag{2.12}$$

Where ξ_j represents the *modal damping ratio* of the j-th mode. This condition is verified if a form of proportional damping is employed such as the *Rayleigh proportional damping* ($\mathbf{D_v} = \alpha\mathbf{M} + \beta\mathbf{K}$) or the *Rayleigh generalised damping* ($\mathbf{D_v} = \mathbf{M}\sum_j \alpha_j \left(\mathbf{M}^{-1}\mathbf{K}\right)^{j-1}$) [Renaud, 2011; Festjens, 2012]. Caughey et al. [Caughey, 1965] have published the condition to satisfy so that the dynamics of a damped systems can be described by the undamped normal modes: $\mathbf{K}\mathbf{M}^{-1}\mathbf{D_v} = \mathbf{D_v}\mathbf{M}^{-1}\mathbf{K}$. Other variants of this condition can be formulated as seen in [Adhikari, 2006]. If this condition is verified, the modes shapes of the conservative model are the same as the non-conservative ones, the eigenvalues on the contrary are impacted by the damping effect.

In rotor dynamics, since the damping takes into account the gyroscopic effect (expressed by an anti-symmetrical matrix), the *Caughey's* condition is not verified. Nevertheless, at $\Omega = 0$, if the damping matrix has a proportional form, Caughey's condition is verified only for this specific regime.
Generally ($\Omega \neq 0\,rpm$), since the matrix $\mathbf{A}(\Omega^s)$ is anti-symmetrical the problem expressed in Equation 2.10 has two different eigenvectors sets: from the left and from the right [Wagner, 2010].

$$[\lambda\mathbf{U} - \mathbf{A}]\,\Psi_R = 0 \qquad and \qquad [\lambda\mathbf{U} - \mathbf{A}]^T\,\Psi_L = 0 \tag{2.13}$$

With:

$$\Psi_R = \begin{bmatrix} \theta_R \\ \lambda\theta_R \end{bmatrix} \qquad and \qquad \Psi_L = \begin{bmatrix} \theta_L \\ \lambda\theta_L \end{bmatrix} \tag{2.14}$$

Where θ_R and θ_L are sets of normal modes in the original physical space from the right and from the left. The two basis $\lambda\Psi_R$ and $\lambda\Psi_L$ represent the time derivative of Ψ_R and Ψ_L, λ contains the complex eigenvalues of the system. The complex j-th eigenvalue is written as follows:

$$\lambda_j = -\xi_j\omega_{0_j} \pm i\omega_{0_j}\sqrt{1-\xi_j^2} = -\xi_j\omega_{0_j} \pm i\omega_{r_j} \tag{2.15}$$

The j-th natural frequency in the complex modal analysis is $\omega_{r_j} = \omega_{0_j}\sqrt{1-\xi_j^2}$, with ω_{0_j} representing the natural frequency of the corresponding undamped mode. The j-th modal damping ratio is defined in Equation 2.16 and in mechanical structures it is

generally $0 < \xi_j << 1$.

$$\xi_j = \frac{1}{2}\sqrt{\frac{\left(\lambda_j + \bar{\lambda}_j\right)^2}{\left(\lambda_j \bar{\lambda}_j\right)}} \tag{2.16}$$

The orthogonality relations for a non-symmetrical eigenvalues problem are reported in Equation 2.17, with the arbitrary set of values γ_j.

$$\begin{cases} \Psi_L^T \mathbf{U} \Psi_R = diag(\gamma_j) \\ \Psi_L^L \mathbf{A} \Psi_R = \begin{bmatrix} diag(\Lambda\gamma_j) & 0 \\ 0 & diag(\bar{\Lambda}\gamma_j) \end{bmatrix} \end{cases} \tag{2.17}$$

Papadrakakis et al. express multiple relationships existing between these two modal basis, such as: $\Psi_R = (\Psi_L^{-1})^T$ [Papadrakakis, 2017]. The mathematical properties of the right and left bases of modes have been observed in depth by Ouisse and Foltete, Zhang et al and Mikota et al. [Zhang, 1988; Ouisse, 2011; Mikota, 2017].

4.1.3 Real and complex modal analysis comparison

It is interesting to visualise the shapes of the first 4 vibration modes of the conservative and dissipative configurations of the modified Jeffcott-Laval rotor presented in the above sections and compare them (see Figure 2.10). Table 2.2 reports the natural frequencies of the modes produced with real and complex modal analysis and for the complex modal analysis only, the relative damping ratios.
First of all, one can notice that the vibration modes come in pairs (Modes #1 and #2) and (Modes #3 and #4) in both the real and complex modal analyses. This is true because the considered system has symmetrical supports. In systems with non-isotropic supports, the modes are decoupled at $\Omega^s = 0\,rpm$ with different mode shapes.
Comparing real and complex modal analyses, one can notice that the mode shapes of the system are the same with a difference in the phase due to the presence of the damping effect in the complex modal analysis. Even if the complex modal analysis has been performed at $\Omega^s = 0\,rpm$ and the matrix $\mathbf{A}(\Omega^s)$ is symmetrical (no gyroscopic effect), Caughey's condition is not verified because the system damping is not perfectly proportional since the viscous damping is present only on the support #1. Moreover, the natural frequencies are overestimated in real modal analysis (see Table 2.2).

To sum up, even if the modes shapes of a damped structure can be approximated by the mode shapes of the associated conservative system, the error on the natural frequency make this tool less reliable than the complex approach [Khulief, 1997].

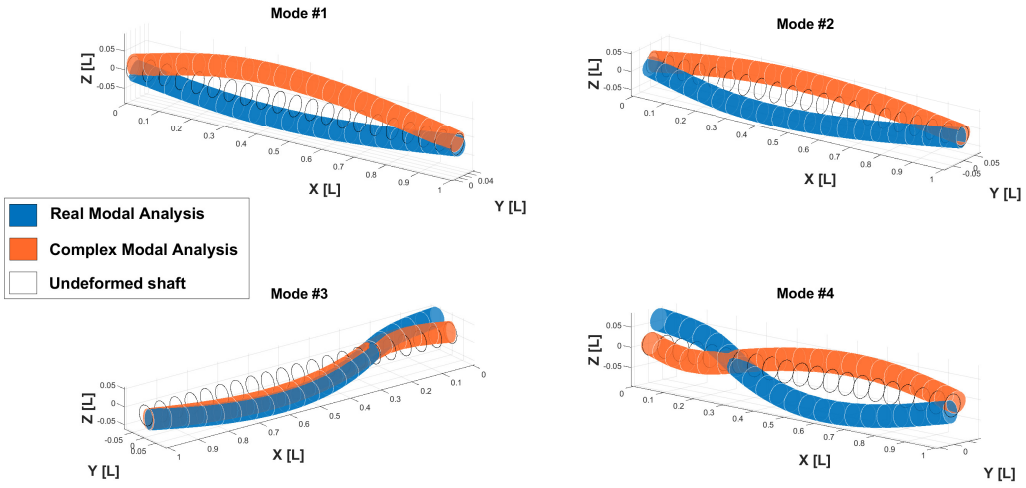

Figure 2.10: Real and complex modal analysis - first 4 modes shape of the modified Jeffcott-Laval rotor.

Vibration Mode	Nat. frequencies real MA (hz)	Nat. frequencies complex MA (hz)	Damping ratio complex MA (%)
Mode#1	36.8	36.6	0.13
Mode#2	36.8	36.6	0.13
Mode#3	73.2	74.7	3.2
Mode#4	73.2	74.7	3.2

Table 2.2: Real and Complex modal analysis - natural frequencies of the modified Jeffcott-Laval rotor.

4.2 Campbell analysis

As seen in above sections, the rotational speed of the system defines its mechanical properties such as the natural frequencies, shapes of the vibration modes and modal damping ratios. The Campbell analysis allows to study the evolution of the natural frequencies of the system with the variation of the rotational speed. It consists in solving the eigenvalue problem reported in Equation 2.10, for multiple regimes Ω_k. The Campbell analysis including the first 4 vibration modes of the modified Jeffcott-Laval rotor presented in the above sections is reported in Figure 2.11. Since these modes are complex they are characterised by an angle between their real and imaginary parts, they are rotating in the three-dimensional space with a specific direction: *Forward Whirling Modes* (FWM) if they rotate in the same direction as the rotor or *Backward Whirling Modes* (BWM) otherwise [Lalanne, 1996; Genta, 2007]. In the case reported in Figure 2.11, the modes #2 and #4 are whirling forward and the #1 and #3 are whirling backward.
In complex structures *mixed whirling modes* have been observed too, with some portions

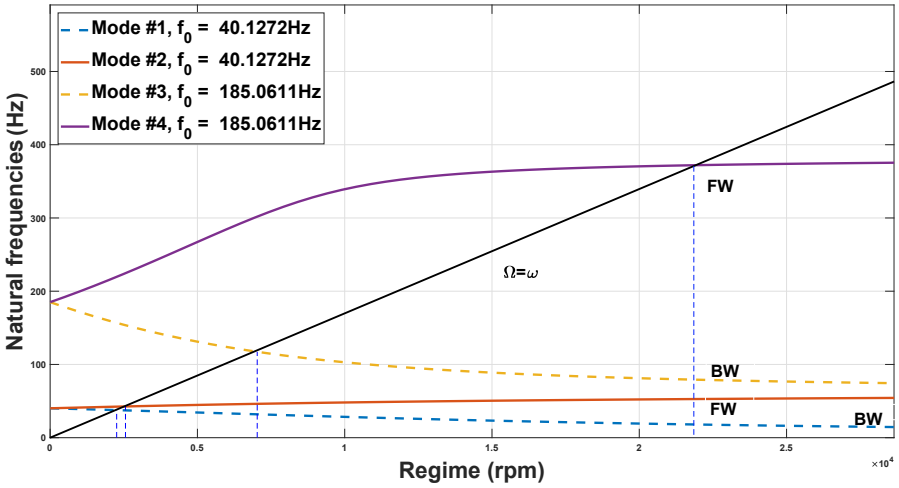

Figure 2.11: Campbell analysis of the first 4 modes of the system.

of the rotor whirling forward and some others whirling in the other direction [Shaw, 1989; Juethner, 2022].

4.3 Unbalance response

In this section, the unbalance response and critical speed analyses are presented with practical examples of the modified Jeffcott-Laval rotor. First of all, the unbalance response and the critical speed analyses are presented in the linear case, then the nonlinear unbalance response is presented with a focus on nonlinear supports and rotor-stator contact.

4.3.1 Linear unbalance response and critical speeds

Nowadays, it is physically impossible to manufacture a perfectly balanced rotor. The unbalance is the result of an uneven distribution of mass, causing vibrations and noise when the system operates. Three types of unbalances are defined in literature: static unbalance, torque unbalance and the dynamic unbalance (consisting in the combination of the first two effects) [Genta, 2007].
The static unbalance is defined by an unbalance mass m positioned off the rotation axis with a distance e (eccentricity) (see 2.8). This unbalance mass generates a rotating centrifugal force, expressed in Equation 2.18. Since the frequency of this type of excitation is always the same as the rotational speed, it is defined as *synchronous excitation*.

$$\mathbf{f}_{st}(t) = m\,e\,\Omega^2 \begin{bmatrix} cos(\Omega t) \\ sin(\Omega t) \\ 0 \\ 0 \end{bmatrix} \tag{2.18}$$

On the other hand, the torque unbalance generates a torque on the rotor along the axis **Y** and **Z**, it is represented by a pair of masses m positioned in two plans perpendicular to the rotation axis, with a distance b between them along the rotation axis. This type of excitation in mainly used on long rotors, and less so on thin rotors like discs.

$$\mathbf{f}_{tor}(t) = m\, e\, b\, \Omega^2 \begin{bmatrix} 0 \\ 0 \\ cos(\Omega t) \\ sin(\Omega t) \end{bmatrix} \tag{2.19}$$

Since the rotational speed changes the natural frequencies, the resonance is generated when the frequency of the excitation force is equal to a natural frequency: $\Omega = \omega_i$. These specific rotational speeds are known as *critical speeds*. In Figure 2.12 the Campbell diagram is associated to the unbalance response (static unbalance) of the modified Jeffcott-Laval rotor presented in the above sections, with an unbalance mass positioned on the disc. The response in displacements along the **Y** directions of the disc and the two supports are reported in the bottom of Figure 2.12. The black line in the Campbell diagram represents the relation $\Omega = a\omega + b$ (using a general linear relation), the critical speeds are identified by the intersections of this line with the curves representing the evolution of the natural frequencies of the system. Otherwise, the critical speeds can be calculated directly solving the modified eigenvalues problem presented in Equation 2.20, adopting the relation $\Omega = a\omega + b$ in Equation 2.3.

$$j\omega\, \mathbf{U}_{cs}\, \hat{\mathbf{z}}_f - \mathbf{A}_{cs}\, \hat{\mathbf{z}}_f = 0 \tag{2.20}$$

with :

$$\begin{aligned} \mathbf{U}_{cs} &= \begin{pmatrix} \mathbf{M} - j\,\mathbf{G}\; a & 0 \\ 0 & -\mathbf{K} \end{pmatrix} \\ \mathbf{A}_{cs} &= \begin{pmatrix} -\mathbf{B} - \mathbf{G}\, b & -\mathbf{K} \\ -\mathbf{K} & 0 \end{pmatrix} \\ \hat{\mathbf{z}}_f &= \begin{pmatrix} j\omega\, \hat{\mathbf{q}}_f \\ \hat{\mathbf{q}}_f \end{pmatrix} \end{aligned} \tag{2.21}$$

From Figure 2.12, we can notice that the system should have 4 critical speeds (4 intersection of the regime line with the natural frequency curves), while only 2 of them are displayed in the unbalance response. This is true because in rotating systems with symmetrical supports and synchronous driving excitations, the backward modes are not excited [DAlessandro, 2022b]. Only the forward modes are excited in this case at the critical speeds $\Omega_{CS1} = 2500\, rpm$ and $\Omega_{CS2} = 22000\, rpm$. One can notice that at the first critical speed, the shaft is bending with higher displacements on the disc. At the second

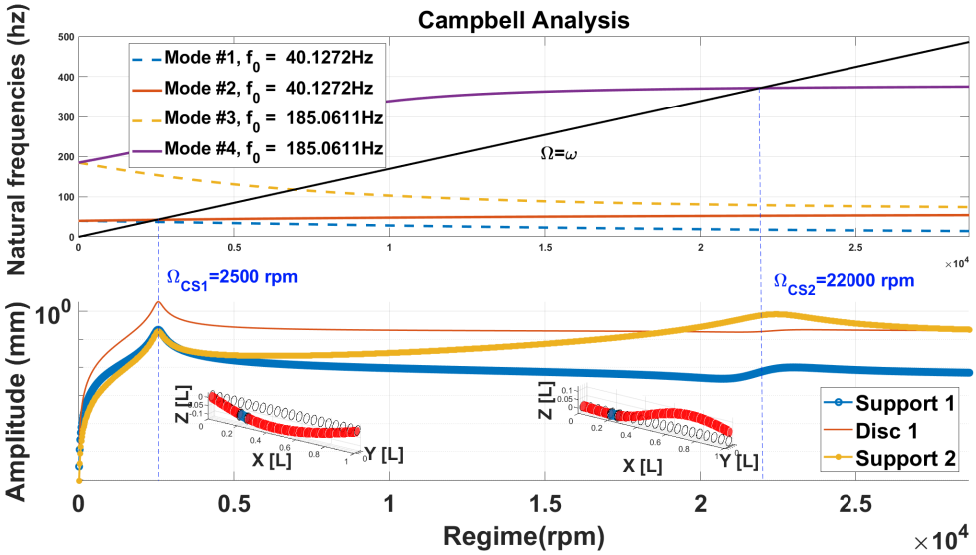

Figure 2.12: Campbell Diagram with critical speed evaluation and unbalance response

critical speed, only the long portion of the shaft close to the support #2 is involved in the motion (see Figure 2.12). More considerations concerning the critical speeds and the vibration modes associated to these regimes are presented in Chapter 5.

4.3.2 Nonlinear unbalance response

Nature is almost always nonlinear and linear behaviours are exceptions in the real world. In order to better represent the dynamical behaviour of real systems it is essential to include nonlinearities in numerical models. In whole engine dynamics it is important to cite two different sources of nonlinearities: supports with fluid films (SFDs) and rotor-stator contact. The classical unbalance response in Equation 2.4 sees the introduction of a new term $\hat{\mathbf{f}}_{\mathbf{nl}}(\hat{\mathbf{q}}_f, \omega, \Omega)$ to take into account the nonlinear effects, generally dependent on $\hat{\mathbf{q}}_f$, ω and Ω:

$$(-\omega^2\mathbf{M} + j\omega(\mathbf{D_v} + \Omega\,\mathbf{G}) + \mathbf{K} + j\mathbf{K}\eta_h)\,\hat{\mathbf{q}}_f + \hat{\mathbf{f}}_{\mathbf{nl}}(\hat{\mathbf{q}}_f, \omega, \Omega) = m\,u\,\Omega^2\,\hat{\mathbf{f}} \tag{2.22}$$

This equation cannot be solved directly since the nonlinear terms are unknown and dependent on displacements. It is thus necessary to adopt iterative approaches to find solutions approximating the equilibrium. As already introduced in Section 2.3, one of the most discussed sources of nonlinearity in rotordynamics is related to the SFDs and other types of nonlinear journal bearings.

Another common problem treated in rotordynamics is the rotor-stator contact. Indeed, in turbomachines the gap between fixed and rotating parts have to be as small as possible

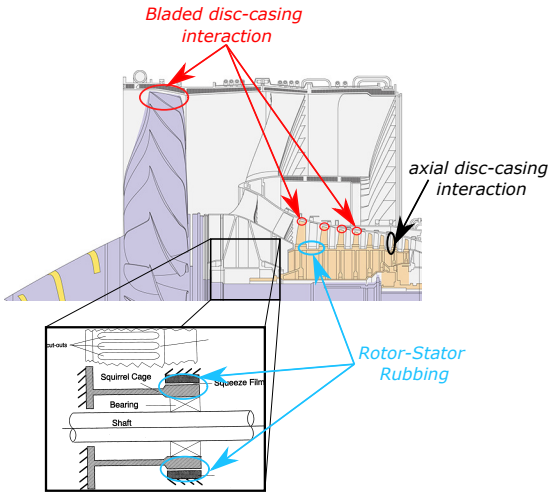

(a) Rotor-stator interactions.

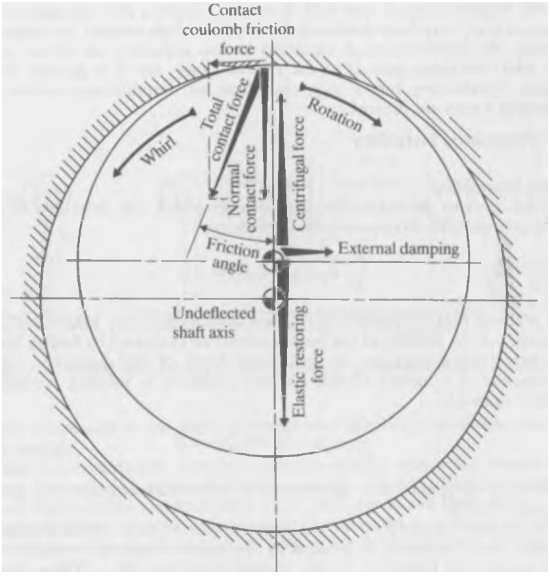

(b) Backward rotor-stator rub, adapted from [Ehrich, 1992].

Figure 2.13: Rotor-stator interactions and backward whirling motion with rotor-stator rub.

to increase their performances. The rotor-stator contact can be induced by multiple phenomena: vibrations generated by unbalance (residual or accidental), thermal deformation of the casing, accelerations generated by aircraft manoeuvres, cavitation in SFDs etc. Three classical forms of rotor-stator contact can be cited:(1) the rotor-stator contact between smooth surfaces (SFDs, shaft-support or similar, represented in blue in Figure 2.13a), (2) the bladed discs contact with the casing (represented in red in Figure 2.13a), and (3) the axial contact (represented in black in Figure 2.13a). Reviews of these phenomena can be found in [Choy, 1987; Jacquet-Richardet, 1996; Ahmad, 2010].

The most classical and simple contact condition is the *synchronous full annular rub* [Muszynska, 1995; Muszynska, 2005]. In this condition, a synchronous forward whirling motion of the rotor establishes a continuous contact with the stator. It is generally developed between smooth surfaces [Ehrich, 1992]. Another more complex scenario exists with backward whirling motion of the shaft. In this case, the tangential component of the friction force has a destabilizing effect and promotes the whirling motion (see Figure 2.13b). Two different regimes can be established in this case: *dry whirl*, a stable phenomenon with no sliding, and *dry whip*, an unstable phenomenon consisting in a permanent sliding of the rotor on the contact surface [Ehrich, 1992]. Choi, demonstrated that a transition from dry whirl to dry whip is mainly controlled by the friction coefficient between the rotor and the stator [Choi, 2002]. Cole described a condition in which the direct whirling motion can generate an intermittent rub annular whirl (*bouncing whirl*) transitioning afterwards

to the dry whip [Cole, 2008]. Bently et al. studied the influence of the stiffness of the rotor's supports on the occurrence of the dry whip phenomenon [Bently, 2002]. Their experience shows that the higher is the stiffness of the supports the easier is to reach the dry whip condition. Moreover, non-symmetrical supports can limit the occurrence of a permanent dry whip. Peletan simulated transitions from full annular rub to dry whip using an HB algorithm [Peletan, 2012a].
It is also possible to have a form of intermittent contact known as *partial rub* [Choi, 2002], where the rotor is not in stable contact with the stator. This sort of phenomena can be transient, periodic, semi-periodic or chaotic [Popprath, 2007]. The prediction of this type of regime is not trivial and multiple unstable behaviours can co-exist in the same regimes [Wilkes, 2008; Jiang, 2009].

Numerical simulations radically changed the way the nonlinear responses are studied. Nonlinear dynamics can be studied using linearised models (e.g. linearised SFDs [Zeidan, 1996]) or through nonlinear solvers integrating iterative tools. Numerical simulations represented a revolution for the treatment of nonlinear systems because there is no other way to predict their responses. Historically, nonlinear responses were calculated through time integration algorithms as shown by [Adams, 1980]. Nowadays, with the improvement of the computational tools, nonlinear simulations are also performed using nonlinear frequency based solvers such as the HBM [Guskov, 2007; Krack, 2019]. An example of steady-state nonlinear response evaluated with a HBM and a time marching approaches is reported in Figure 2.14.

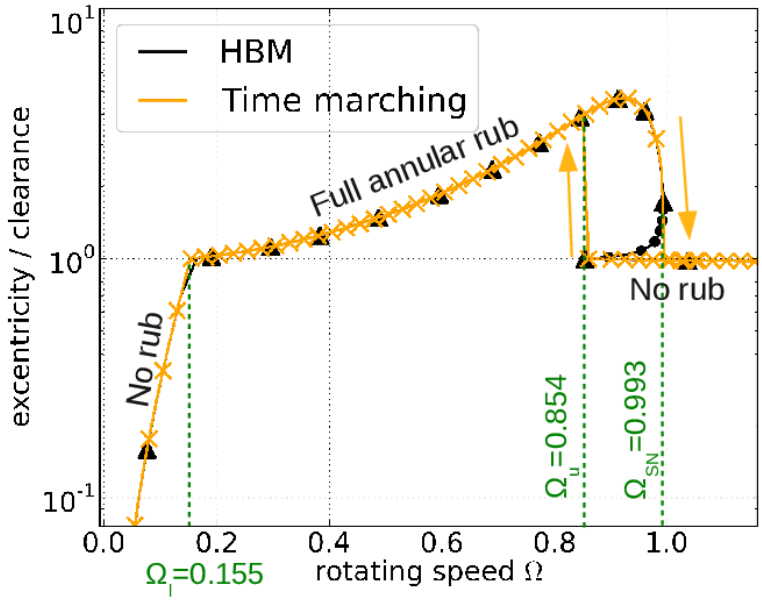

Figure 2.14: Rotor-stator rub, adapted from [Peletan, 2014].

5 Model reduction in rotordynamics

The dynamics of a mechanical system is described by a linear or a nonlinear combination of its vibration modes. A FE model contains a number of modes which is equal to the number of its DOFs, excited over a specific frequency range. Nevertheless, the system is generally studied over a working frequency range which is limited and a large spectrum of its vibration modes are not excited in a relevant manner. Most of these unexcited modes do not contribute significantly to the response in the operating frequency range, and they only represent an additive cost in terms of computational effort. It is worthwhile to use *dynamical model reduction* to reduce the size and the complexity of FE models in order to reduce the computational burden of simulations. Mathematically, the *Full Order Model* (FOM) is projected onto a reduced subspace which is intelligently chosen and which is able to generate the relevant portion of the solution with a negligible error.

The field of model reduction is broad and rich, and any methods allowing to simplify the complexity of a numerical model can be considered as a model reduction method. Model reduction in structural dynamics is generally associated to the Ritz projection presented in 1909 by the Swiss scientist Walter Ritz [Ritz, 1909b; Ritz, 1909a]. This method is also known as *Rayleigh-Ritz method* since Rayleigh accused Ritz of plagiarism claiming that the method was already employed in his own prior works [Lord Rayleigh, 1877; Rayleigh, 1911]. Leissa in 2005 showed that this claim was not justified [Leissa, 2005], Ilanko supported Leissa's study in 2009 [Ilanko, 2009]. The author shares Leissa's and Ilanko's points of view and for the rest of this work, this method is referred to as *the Ritz method*.

Many variants of this method have been developed from 1960 to nowadays, introducing intelligent approaches to identify the most relevant modes in the system response.
A breakthrough in structural model reduction was proposed firstly by Guyan in 1965 with the so called *static condensation* [Guyan, 1965] and then by Craig and Bampton in 1968 with the so called *dynamic condensation* [Craig Jr, 1968]. Both are variants of the Ritz reduction, allowing to describe the components of a system by their boundary nodes (master nodes) and a group of constrained internal modes of the component (slave nodes). In 1971, MacNeal proposed a generalisation of the Craig-Bampton condensation using free or constrained interfaces for the evaluation of the slave modes, this last method is employed in this work for the generation of the so called *Super-Element* (SE)s. In 1975 Rubin proposed an improved version of the MacNeal reduction, introducing experimental data in the numerical *Reduced Order Model* (ROM) [Rubin, 1975]. A further reduction of the size of the model can be produced by a modal reduction of the interfaces as showed by Farhat and Geradin in 1991 [Farhat, 1991] or by expressing the physics of the in-

terfaces in a weak form before the model reduction as seen in [Bourquin, 1992]. Rixen investigated this last form of *dual* approaches: the interfaces are not represented in nodal form but expressed in weak formulation (*dual Craig Bampton*) [Rixen, 2004; Allen, 2020]. The approaches cited here from the Guyan reduction, are known as *Component Mode Synthesis* (CMS) methods and they are generally applied with linear normal modes. It is interesting to cite as well the first works using *Nonlinear Normal Modes* (NNM) for model reduction purposes [Vakakis, 1997; Krysl, 2001; Legrand, 2004]. NNMs allow to observe the different components of the response of a nonlinear system. In contrast to linear normal modes, they are neither mutually independent, superposable, nor invariant, and their amplitude depend on the frequency as can be seen in Figure 2.15 [Hill, 2017; Kerschen, 2009]. Nevertheless, this topic is beyond the scope of this research.

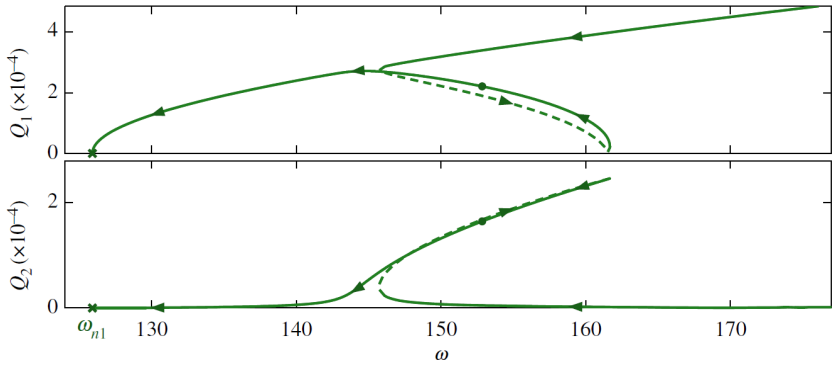

Figure 2.15: Maximum amplitude of displacement of two NNM against the frequency ω. Adapted from [Hill, 2017].

Classical model reduction approaches are particularly worthwhile for many-query studies and to study the behaviour of systems in multiple configurations. Balmès investigated the subject of model reduction using Ritz-based approaches taking into account the variation of the physical properties of mechanical systems [Balmès, 1996b]. In this framework, Sterenchuss and Balmès studied as well the parametric model reduction in bladed discs with cyclic and quasi-cyclic periodic geometries [Sternchüss, 2006; Sternchüss, 2009b]. The dynamics of the whole shaft is nevertheless excluded and a model reduction technique dedicated to rotating shafts appear to be absent in literature. Meanwhile, it is quite common to find rotating systems reduced using the classical Craig-Bampton method or the MacNeal reduction approaches [Seshu, 1997; Peletan, 2012a]. This doctoral work seeks to propose an innovative approach of modal reduction dedicated to rotating shafts.

All these methods, aside from the NNM approaches, are based in some way on linear eigenvalue analysis, but other types of linear decomposition can been employed in order to reduce the size of the dynamical systems. A widely employed variant is the *Proper*

Orthogonal Decomposition (POD) also known as *Karhunen-Loève Method* (KLM) in the field of structural dynamics [Kim, 1998; Liang, 2002; Kim, 2015; Lu, 2019]. In this case, the reduction bases are developed from the responses of the FOM evaluated preliminarily, the POD basis is thus calculated *a posteriori*. This approach is quite general and has been adopted in multiple scientific fields, it has been presented for the first time by Lumley in 1976 to study turbulent flows [Lumley, 1967], it is also defined by Jolliffe as *Principal Component Analysis* (PCA) in 1990 [Jolliffe, 1990].
As already said, the POD bases are developed *a posteriori* using responses obtained from preliminary experiments referred to as *snapshots* [Sirovich, 1987]. Another decomposition approach is the *Proper Generalized Decomposition* (PGD), in this case the PGD basis is evaluated *a priori* with no previous experience, exactly as done in classical modal reduction. Chinesta et al. and Ammar et al., studied the application of PGD in model order reduction [Ammar, 2010; Chinesta, 2011b; Chinesta, 2011a; Chinesta, 2013; Dumon, 2011]. This method consists in computing the solution of a numerical problem by enriching iteratively a partial solution improving its quality until reaching a predefined level of accuracy. Additional iterations increase the size of the PGD by adding a vector. The vectors of the PGD basis are not orthogonal and some of them may not be essential for the solution, hence the model can be reduced by removing them. It is essential to couple this approach with an intelligent algorithm to search for simulation points otherwise it may become counterproductive and computationally expensive.
For this reason, the POD approach is preferred in this work and it is studied in depth for model reduction purposes in further sections.

6 Machine learning for many-query frameworks

Model reduction is employed in many physical-based disciplines such as *Computational Fluid Mechanics* (CFD) [Rowley, 2005; Benamara, 2017a] or structural dynamics [Balmès, 1996b; Allen, 2020], but not only. Model reduction can be employed in any sort of numerical simulation in order to reduce the complexity or the size of a numerical model. Generally speaking, ROMs can be seen as fast-running *quasi-equivalent* surrogate for FOMs and they can have any numerical form able to reproduce accurately the desired results [Schilders, 2008b].

Model reduction in structural dynamics is classically associated with a form of Ritz projection, but in this work we want to propose another paradigm of model reduction in structural dynamics using surrogate models. A surrogate model able to reproduce accurately the responses of a dynamical system with a reduced computational effort can be defined as a ROM in a less classical way: *Surrogate model ROMs* [Guenot, 2013; Yondo,

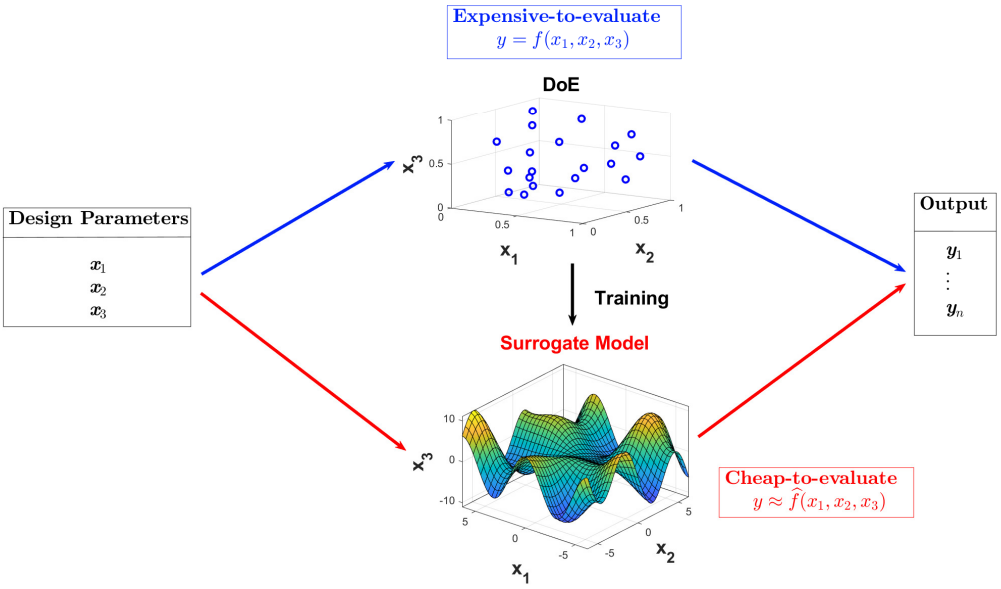

Figure 2.16: Surrogate modeling framework

2018]. Classical model reduction approaches allow to obtain extremely accurate ROMs, running faster than FOMs but still limited in many-query applications because of their evaluation time. Junge in 2009 obtained a speedup factor of ≈ 10 using Craig-Bampton and Rubin reductions approaches [Junge, 2009; Craig Jr, 1968; Rubin, 1975], in further parts of this work it is shown that using a dedicated approach for rotating systems it is possible to speed up the simulation by a factor ≈ 100 on an industrial scale model [DAlessandro, 2022b], see more references in [Wagner, 2010]. It seems quite hard to exceed this speedup limit because the classical modal reduction must include in the reduction basis any modes of the structure participating in the response of the system in the interesting frequency range, which is a theoretical limitation of the methods based on Ritz reduction [Dickens, 1997]. This limitation can be circumvented by changing the model reduction paradigm and moving to methods based on experiments and data.

Recent scientific methods such as *Artificial Intelligence* (AI) and machine learning, allow the development of fast-to-evaluate surrogate models from experimental and numerical outcomes (*Design of Experiments* (DoE)) and can be used for decision making, optimisation, sensitivity analysis and other many-query frameworks. In order to make this type of approach affordable, it is important to reduce to a minimum the computational effort associated to the DoE evaluation and to the training phase. A classical framework for surrogate model development is represented in Figure 2.16. The challenge is to keep as low as possible the size of DoEs and to obtain a surrogate which is as accurate as possible. In a model reduction perspective, one can consider a parallelism between Ritz-based ROMs and surrogate model ROMs: both of them are constrained by an *offline* preparation phase

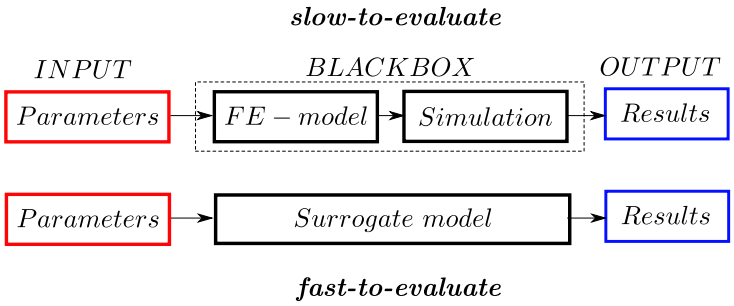

Figure 2.17: Surrogate modeling workflow

[Ramasso, 2022; Khatouri, 2022]. The offline phase in Ritz-based reduction consists in developing the reduction bases or in building the *Super-Element* (SE)s. As observed in [Donders, 2010], the development of the SEs with a classical MacNeal reduction approach [MacNeal, 1971] could take more than 26 hours for an industrial scale FE model. This offline phase exists in surrogate modeling too and consists in DoE evaluation and surrogate model training phases. Both of these approaches can be expensive in their offline phases, but the advantage of the surrogate model ROMs is their evaluation time which is almost instantaneous.

To give a definition of surrogate model, one can consider a generic black-box function, representing a numerical simulation or a physical experiment, with input parameters and results. A complex relation exists between the input and the results which is represented by this black-box function. A surrogate model (also known as *metamodel* or *emulator* [Dubourg, 2014]) approximates this relation with a mathematical function more or less complex which is fast to evaluate [Sobester, 2008]. In FE simulations, the black box function is represented by the FE model which can be substituted by the surrogate model (see Figure 2.17).

With these considerations in mind, we will provide below an overview of the most widely used type of surrogate modeling techniques adopted in engineering applications.

Two recent overviews can be cited: in 2018, Yondo et al. presented a review of the surrogate modeling works in aeronautical applications for many-query aerodynamical analyses (e.g. in design optimization, optimal control or uncertainty analysis) [Yondo, 2018], with a special attention to the DoEs. In 2022, Khatouri published an overview on surrogate modeling techniques for model-based design [Khatouri, 2022], identifying the three main objectives in machine learning: classification (*clustering*), interpolation (numerical model interpolating training data) and regression (numerical model best fitting training data). Different methods available in literature can be more or less adapted for these objectives. A first interesting family of surrogate models for prediction purposes has been presented

by Dyn, Rippa et al. in 1986 with the *Radial Basis Functions* (RBF) [Dyn, 1986], also defined as *Radial Basis Neural Networks* (RBNN) in the following years [Karayiannis, 1997; Spooner, 1999]. This class of surrogate models is mainly employed for interpolation but they have been adopted sometimes for regression purposes too [Walczak, 1996]. After the RBF, the Kriging interpolation appeared in 1989 and it is still studied and adopted today [Cressie, 1988; Kleijnen, 2009]. Kriging appears more efficient than RBFs for predictions, but at the same time more expensive in terms of computational burden during training and exploitation phases. Appearing at the same time as Kriging, we can cite the polynomial regression method presented by Sacks et al. in 1989 [Sacks, 1989] and multivariate adaptive regression splines presented by Friedman in 1991 [Friedman, 1991], best adapted for regression purposes and not interpolating the training points. In the nineties, there appeared the first artificial *Neural Networks* (NN) [Cheng, 1994; Papadrakakis, 1998] which proved more flexible and adapted to work with complex or nonlinear data but at the same time highly demanding in terms of quantity of training data [Bishop, 1995]. In 1992 a first classification algorithm has been published by Boser et al. [Boser, 1992] to group the training data in *clusters*, lately defined as *Support Vector Machines* (SVM) [Hearst, 1998]. A variant of SVMs has been presented in 2004 by Smola et al. and then by Clarck et al., the so-called *Support Vector Regression* (SVR) approach, for clustering and regression purposes [Smola, 2004; Clarke, 2005]. This work is focused around the model order reduction which is mainly related to the interpolation techniques (Kriging, RBF, etc.) which is investigated and applied in further chapters of this work.

Out of the scope of this work are the *Surrogate Based Optimisation* (SBO) and the *Multi-Fidelity Surrogate Modeling* (MFSM), for more details concerning these subjects see [Benamara, 2017a; Benamara, 2017b; Yondo, 2018; Khatouri, 2022].

7 Contributions and work outline

In this section it is presented an overview of the most relevant contributions of this research and a presentation of its structure.

A first contribution of this work is the development of a new mathematical formulation to study the hysteretic (or structural) damping in rotating shafts. Multiple papers in the past generated misunderstandings about the effect of the hysteretic damping in rotating structures [Lund, 1974; Melanson, 1998]. The stabilising effect of the hysteretic damping has been clarified by Genta in 2004 [Genta, 2004] using a classical *equivalent formulation* to treat the hysteretic damping which will be considered here as proportional to the instantaneous speed of the system. In the present study we want to propose a more

general formulation of the hysteretic damping in rotating beams taking into account the circulation of the forces acting on the rotor. Viscous damping is studied as well in detail for rotating beams and a pedagogical representation of the hysteretic and viscous damping forces in rotating system are proposed as well. The details of the model are given in Chapter 3.

In this work, the HBM have been adopted to solve nonlinear problems in the field of rotor-dynamics. We are focused on the full annular rub phenomenon and the physical behaviour of a rotating machine in this working condition is studied using the HBM. The details on the algorithm are given in Chapter 4, defining the hypothesis adopted in further parts of this work.

A second relevant contribution of this work lies in the model reduction of rotating systems. It is quite common to see classical modal reduction or CMS approaches in the literature to reduce the complexity of FE models representing rotating machines [Kane, 1991; Peletan, 2012a; Mitra, 2016; Joannin, 2017], but to the author's best knowledge, a method dedicated to rotating shafts and unbalance responses is lacking. In this work a model reduction approach is proposed, based on the fact that rotating systems have resonances at critical speeds and not at natural frequencies.
The efficiency of this approach is demonstrated in linear and nonlinear cases and in frequency and time domains. First of all, the proposed model reduction approach is studied in an academic framework on a simple model in order to allow the results of this research easily reproducible. Afterwards, the critical speeds reduction is applied on an industrial scale model, with nonlinearities to demonstrate the scalability of the method in an industrial framework. This subject is presented in Chapter 5.

Finally, the last and major contribution of this research concerns the proposition of a new paradigm of model order reduction for rotating systems using surrogate model ROMs [Khatouri, 2022]. Classical model reduction methods based on Ritz projection are limited by the fact that the ROMs must contain a minimum number of vectors to correctly represent the response of the system in the frequency range of interest [Kane, 1991; Dickens, 1997; Junge, 2009; Festjens, 2014]. This limitation can be circumvented using surrogate modeling techniques thus allowing to produce fast-to-evaluate ROMs from previous outcomes. In this study scalar and vectorial surrogate modeling approaches are studied on an industrial scale finite element model and their performances are compared, all of this is presented in Chapter 6.

In chapter 7 the conclusions of this work are drawn and the perspectives on future works are given.

Chapter 3

Formulation and interpretation of hysteretic damping models for rotating machines

"On ne fait jamais attention à ce qui a été fait. On ne voit que ce qui reste à faire"

"We never pay attention to what has been done; we only see what remains to be done."

Marie Curie: French physicist, Nobel prize (1867-1934)

Objectives

Damping modeling is crucial for predicting machine vibrations. In the case of rotating parts, damping can be responsible for instability phenomena coming from the circulating forces. Until the work of Genta [Genta, 2004], errors of interpretation and modeling have been propagated in analyses. This work proposes a mathematical model to represent the hysteretic damping in fixed and rotating coordinate models. The proposed mathematical models can be used in frequency and time domains. The effect of the hysteretic and viscous damping are discussed in forward and backward whirling modes. An original graphical post-processing highlights the main components of viscous and hysteretic damping forces and allows to compare the two considered damping models.

Contents

1 Introduction

Numerical simulation of rotating systems requires good damping modeling to be predictive in terms of vibration levels. Because the physical phenomena involved in damping are very diverse, and because some mathematical assumptions simplify the solution of equations, there are different mathematical formulations. This article brings elements of discussion about these mathematical choices and in particular about their effects on the stability of rotating machines.

Damping modeling has been the subject of thousands of publications for decades. The authors of these publications are looking for a compromise between the simplicity of mathematical and numerical models and the relevance of the results. For example, Caughey's [Caughey, 1965] and Rayleigh's [Hall, 2006] damping models are very convenient because they allow to work in a real mode basis but lead to artifacts such as frequency dependence and lead to sources of energy dissipation in geographical areas where there is none. Proportional damping is therefore an assumption that is less and less used by engineers. Similarly, viscous damping is a simplifying assumption that corresponds to relatively few real structural situations. Engineers prefer the use of hysteretic damping which is more realistic for structural applications. When faced with visco-elastic media, engineers use variants of hysteretic damping such as generalised Maxwell's models [Renaud, 2011; Festjens, 2012] which are very realistic but more expensive in simulation time.

The circulation of damping forces in rotating machines or strongly coupled systems (aeroelasticity, squeal, active control) can lead to paradoxical effects: damping can lead to vibratory instabilities, especially when the machine rotates beyond the critical speed [Muszynska, 1986]. Here again, many studies have addressed this subject [Dimarogonas, 2013; Puthanpurayil, 2011; Kounadis, 1992]. Genta [Genta, 2004] has clarified the occurrence of instabilities in the presence of hysteretic damping questioning the fact that stability was always acquired in the presence of hysteretic damping [Melanson, 1998]. In machines, damping can also come from localised dissipation in joints [Festjens, 2013] or in bearings [Della Pietra, 2002; Zeidan, 1996]. Genta [Genta, 2004] also showed that sources of damping should be considered in terms of whether they originate from rotating or fixed parts. Starting from this famous publication, recent works have addressed the case of composite shafts [Ri, 2020; Arab, 2018; Montagnier, 2007], cracked rotors [Roy, 2019], rotors including viscoelastic materials [Ganguly, 2022] or rotors with non-linear dissipative bearings [Kumar, 2019]. The employment of the hysteretic damping adopted in classical structural dynamics [Crandall, 1991] has led in the past to misunderstand the role of the hysteretic damping in rotating machines [Zorzi, 1977; Melanson, 1998]. A first clarification was proposed by Genta in 2004 [Genta, 2004]. The hysteretic damping force has a stabilizing role in sub-critical regimes and a destabilizing role in super-critical regimes for a direct whirling motion. In the case of a backward whirling motion, the hysteretic damping has

always a stabilizing role [Genta, 2010].

From the mathematical point of view, it is well known that the hysteretic damping can be applied on systems harmonically excited, with a representation of the damping force in the frequency domain. But, it is difficult to model mathematically the hysteretic damping in the time domain [Genta, 2010]. According to several works [Crandall, 1970; Genta, 2010], the hysteretic damping force is not defined if the excitation frequency is equal to zero. This is generally not an issue in non rotating systems because the excitation frequencies are always positive, but it is in rotor-dynamical applications since the excitation frequencies can have both positive and negative signs depending on the relation between the rotating speed of the system and the whirling speed [Genta, 2004]. Montagnier [Montagnier, 2007], studied an Euler-Bernoulli elastic shaft mounted on visco-elastic supports with hysteretic damping in the shaft. Nevertheless, a direct formulation of the hysteretic damping force in the frequency domain was missing.
First of all, the purpose of this article is to re-discuss this important subject for which few fundamental articles have been published and almost none in the last ten years. Starting from the formulation of the hysteretic damping proposed by Genta in 2010, this work wants firstly propose and justify a formulation of the hysteretic damping dedicated to rotating systems in a stationary reference frame and in a rotating reference frame. From a didactic point of view, this article proposes an original graphic representation of the circulation of damping forces. Finally, to illustrate the point, an example is treated on a symmetrical Jeffcot-like rotor in which a viscous damping and a hysteretic damping are used for the shaft modeling. Results are presented to illustrate the theory.

2 Theoretical background

In this section, the mathematical model to simulate the vibrations of a rotating shaft is recalled. The context is that of linear elastodynamics approximated by the finite element method (FEM). Two different damping models are discussed: hysteretic damping (HD) and viscous damping (VD) applied to the rotating shaft.

2.1 Kinematics

In rotor dynamics, equations can be written in a fixed reference frame ($\mathcal{R}_f$) or in a moving reference frame ($\mathcal{R}_m$), see Figure 3.1. The choice of the reference frame depends on the axial symmetry of the rotor and the stator, see [Shen, 2021]. If this symmetry is not respected, time-dependent terms may appear in operators, resulting in an increase of the computational burden. Several methods have been developed to take into account these terms using multibody dynamics [Genta, 1999] or the well know Floquet theory

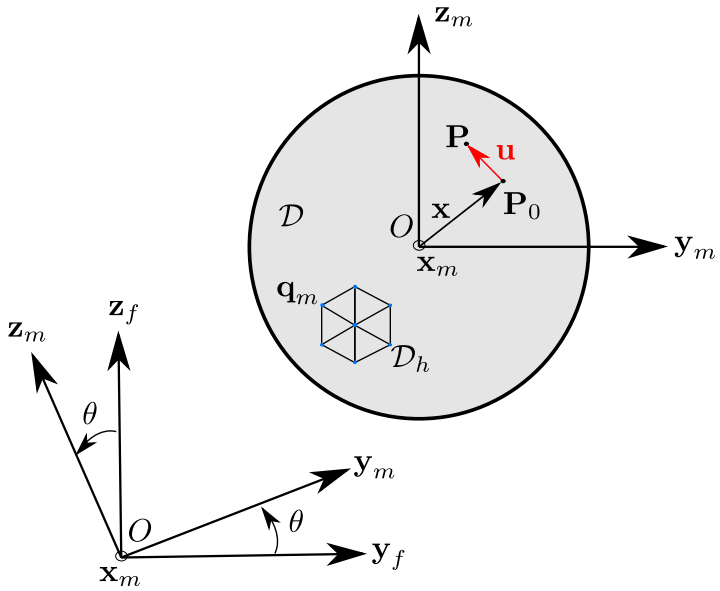

Figure 3.1: Fixed and rotating reference frames $\mathcal{R}_f$ and $\mathcal{R}_m$. Parameterization of the rotation and deformation movements.

[Lazarus, 2010; Floquet, 1879]. The stiffness or damping forces of the rotor are naturally calculated in $\mathcal{R}_m$ which is attached to the shaft. Nevertheless, since the stator of rotating machines is generally non-axisymmetrical and rotors are considered axisymmetrical, these systems are studied in the inertial reference frame attached to the stator. The present chapter deals with equations written in $\mathcal{R}_f$. Compared to the general framework [Gmür, 1997], in the present chapter, rigid body translations are neglected in parameterization.

A point P which belongs to the shaft can be defined by its coordinates in $\mathcal{R}_m$, $\{\mathbf{OP}\}_{\mathcal{R}_m} = \mathbf{x} + \mathbf{u}(\mathbf{x}, t)$ or in $\mathcal{R}_f$, $\{\mathbf{OP}\}_{\mathcal{R}_f} = \mathbf{R}_u(\mathbf{x} + \mathbf{u})$. Where $\mathbf{x}$ is the position of P in the Lagrangian configuration and $\mathbf{u}$ the displacements of P due to elastic deformations. Only the displacement along axis $\mathbf{Y}_m$ and $\mathbf{Z}_m$ are observed in this study thus the change of reference frame is realised by the following orthonormal matrix $\mathbf{R}_u$:

$$\mathbf{R}_u = \begin{bmatrix} cos(\theta) & -sin(\theta) \\ sin(\theta) & cos(\theta) \end{bmatrix} \tag{3.1}$$

The velocity in $\mathcal{R}_f$ is directly given by the derivative of the later:

$$\{\mathbf{v}_{\mathbf{P}/\mathcal{R}_\mathbf{f}}\}_{\mathcal{R}_f} = \mathbf{R}_u\dot{\mathbf{u}} + \dot{\mathbf{R}}_u(\mathbf{x} + \mathbf{u}) = \mathbf{R}_u\dot{\mathbf{u}} - \boldsymbol{\Omega}\mathbf{R}_u\mathbf{J}_u(\mathbf{x} + \mathbf{u}) \tag{3.2}$$

with:

$$\mathbf{J}_u = \begin{bmatrix} 0 & 1 \\ -1 & 0 \end{bmatrix} \tag{3.3}$$

and considering $\mathbf{\Omega} = \dot{\theta}$ as a constant. Moreover, from the previous equation, the relative velocity in $\mathcal{R}_m$ is defined by:

$$\{\mathbf{v_{P/\mathcal{R}_m}}\}_{\mathcal{R}_m} = \mathbf{R}_u^T\{\mathbf{v_{P/\mathcal{R}_f}}\}_{\mathcal{R}_f} + \Omega\mathbf{R}_u^T\mathbf{J}_u\{\mathbf{v_{P/\mathcal{R}_f}}\}_{\mathcal{R}_f} \tag{3.4}$$

2.2 Elastodynamics framework

The equilibrium equations of elastodynamics are established from the equations of linear elasticity by adding the contributions of inertial forces. This law is written here in the reference configuration, in $\mathcal{R}_m$, neglecting the volumetric forces such as the weight, considering axisymmetry. For more information, see for instance Gmur [Gmür, 1997].

$$\nabla^T\sigma(\mathbf{x},t) = \rho(\mathbf{x})\{\ddot{\mathbf{u}}(\mathbf{x},t) - 2\mathbf{\Omega}\mathbf{J}_u\dot{\mathbf{u}} + \mathbf{\Omega}^2(\mathbf{x}+\mathbf{u})\} \tag{3.5}$$

Where σ denotes the sum of the elastic σ_e and damping stress σ_d. ∇^T denotes the divergence operator. The elastic stress are naturally expressed by the constitutive law:

$$\sigma_e(\mathbf{x},t) = \mathbf{E}(\mathbf{x})\varepsilon(\mathbf{x},t) \tag{3.6}$$

where $\mathbf{E}$ denotes the Hooke's tensor and $\varepsilon(\mathbf{x},t)$ denotes the linearised strain tensor. The damping stresses are naturally added in the constitutive law and are proportional to the strain or to the strain rate depending on whether they are hysteretic or viscous. They have been written here in the frequency domain which is the most suitable for hysteretic damping.

$$\hat{\sigma}_d(\mathbf{x},\omega) = j\omega\eta_v\mathbf{E}(\mathbf{x})\hat{\varepsilon}(\mathbf{x},\omega) + j\eta_h\mathbf{E}(\mathbf{x})\hat{\varepsilon}(\mathbf{x},\omega) \tag{3.7}$$

The FEM can then be used to approximate the solution. This approximation is of course based on the discretization of the domain $\mathcal{D}$ with finite element $\mathcal{D}_h$ such that $\mathcal{D} = \cup_{h=1}^{N}\mathcal{D}_h$ and the use of interpolation functions such as $\mathbf{u} = \mathbf{H}(\mathbf{x})\mathbf{q}_m$. After processing the approximation, the Partial Differential Equations (PDEs) are transformed into a set of ordinary differential equations (ODEs).

$$\mathbf{M}\ddot{\mathbf{q}}_m + \Omega\mathbf{G}_m\dot{\mathbf{q}}_m + \{\mathbf{N}+\mathbf{K}\}\mathbf{q}_m + \mathbf{f_{dv}} + \mathbf{f_{dh}} = \mathbf{f_c} \tag{3.8}$$

where $\mathbf{q}_m$ denotes the discrete displacement field in $\mathcal{R}_m$, $\mathbf{M}$, $\mathbf{G}_m$, $\mathbf{K}$, $\mathbf{N}$ denote respectively the mass, gyroscopic (expressed in $\mathcal{R}_m$), stiffness and centrifugal softening matrices, $\mathbf{f_{dv}}$ denotes the viscous damping forces and $\mathbf{f_{dh}}$ denotes the hysteretic damping forces, $\mathbf{f_c}$ denotes the centrifugal forces linked to an unbalanced rotor for instance. The equation can also be written in $\mathcal{R}_f$:

$$\mathbf{M}\ddot{\mathbf{q}}_f + \Omega\mathbf{G}_f\dot{\mathbf{q}}_f + \mathbf{K}\mathbf{q}_f + \mathbf{R}\mathbf{f}_{\mathbf{dv}} + \mathbf{R}\mathbf{f}_{\mathbf{dh}} = \mathbf{R}\mathbf{f}_{\mathbf{c}} \tag{3.9}$$

where $\mathbf{q}_f$ denotes the discrete displacement field in $\mathcal{R}_f$. Since the shaft is axisymmetric, $\mathbf{M}$, $\mathbf{K}$, are the same, $\mathbf{G}_m$ denotes the gyroscopic matrix expressed in $\mathcal{R}_f$ and the damping and centrifugal forces must be projected onto $\mathcal{R}_f$ through the use of the matrix $\mathbf{R}$ that operates the change between the reference frames in the FEM displacement subspaces, introducing by this way some circulating forces which are going to be discussed further in the next sections. Details about the operators are given in Appendix 2 and they are more detailed in [Gmür, 1997].

2.3 Stability analysis on a Jeffcott-Laval rotor

In this section an analytical Jeffcott-Laval rotor is studied to observe the stability of the system at different regimes with different sources of damping in the rotating shaft. The free motion of the system is managed by Equation 3.10. First of all the rotor with viscous damping is considered:

$$\mathbf{M}\ddot{\mathbf{q}}_f + \mathbf{D}_\mathbf{v}\dot{\mathbf{q}}_f + \{\Omega\mathbf{D}_\mathbf{v}\mathbf{J} + \mathbf{K}\}\mathbf{q}_f = \mathbf{0} \tag{3.10}$$

The application to the Jeffcott-Laval rotor allows a simplification of this very general framework while not removing any generality. In this example the disc's rotations are not considered and the gyroscopic effect neglected.
Expanding the Equation 3.10 on the first two modes of the structure arriving at the same frequency ω_0 (symmetrical supports), with q_1 and q_2, representing the modal displacements.

$$\begin{bmatrix} m & 0 \\ 0 & m \end{bmatrix}\begin{bmatrix} \ddot{q}_1 \\ \ddot{q}_2 \end{bmatrix} + \begin{bmatrix} c & 0 \\ 0 & c \end{bmatrix}\begin{bmatrix} \dot{q}_1 \\ \dot{q}_2 \end{bmatrix} + \begin{bmatrix} k & \Omega c \\ -\Omega c & k \end{bmatrix}\begin{bmatrix} q_1 \\ q_2 \end{bmatrix} = \mathbf{0} \tag{3.11}$$

Assuming that the response of the system is a damped whirling motion with a circular centred orbit and with the whirling frequency of ω_0:

$$\mathbf{q}_f = \begin{bmatrix} e^{-\sigma t}cos(\omega_0 t) \\ e^{-\sigma t} \pm sin(\omega_0 t) \end{bmatrix}_{\mathcal{R}_f} \tag{3.12}$$

One can obtain analytically the value of the decay rate σ of the structure, the analytical solution of a similar system has been developed by Genta [Genta, 2004]. The decay rate σ of the structure with viscous damping is given by:

$$\sigma = \frac{c}{2m\omega_0}(\omega_0 \pm \Omega) = \zeta_v(\omega_0 \pm \Omega) = \zeta_v\omega_0 \pm \zeta_v\Omega = \zeta_F \pm \zeta_v\Omega \tag{3.13}$$

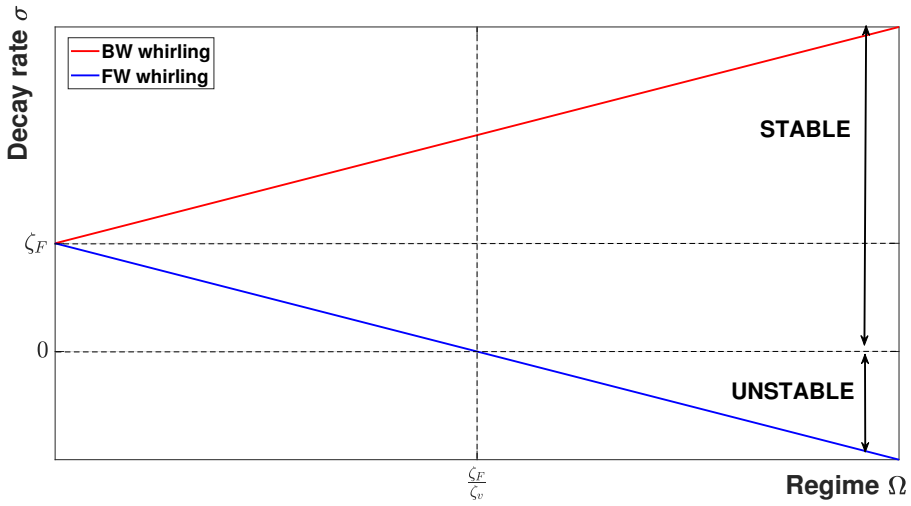

Figure 3.2: Stability of a Jeffcott-Laval rotor with viscous damping.

The system is stable if the value of σ is positive. The sign $\pm$ employed in Equations 3.12 and 3.13, depends on the type of whirling motion of the rotor: '+' for a backward motion and '-' for a forward motion. ζ_F represents the constant contribution of the decay rate and ζ_v is the damping ratio of the considered mode. In the case of a forward whirling motion, the system becomes unstable after the specific rotational speed $\Omega = \frac{\zeta_F}{\zeta_v} = \omega_0$, as reported in Figure 3.2.

- If $\Omega < \omega_0$ the system is in a **sub-critical** regime. The sign of σ is negative, the system is **stable**.
- If $\Omega > \omega_0$ the system is in a **super-critical** regime. The sign of σ is positive, the system is **unstable**.
- In the case of a backward whirling motion $\sigma = \zeta_F + \zeta_v \cdot \Omega$, σ is always positive and the system is unconditionally stable.

Considering the case of a pure hysteretic damping in the rotor, assuming

$$c_{eq} = k\eta_h/|\Omega - \omega| \tag{3.14}$$

and using it in Equation 3.13, the decay rate is given by:

$$\sigma = \frac{c_{eq}}{2m\omega_0}(\omega_0 \pm \Omega) = \frac{\omega_0\eta_h}{2} sign(\omega_0 \pm \Omega) \tag{3.15}$$

The sign $\pm$ employed in Equation 3.15 depends on the type of whirling motion of the rotor: '+' for a backward motion and '-' for a forward motion. In the case of a forward whirling motion, the stability of the system depends on the sign of $(\omega_0 - \Omega)$, it is stable

in sub-critical regimes ($\Omega < \omega$) and unstable in super-critical regimes ($\Omega > \omega$), showing a discontinuity in $\Omega = \omega$.
In the case of a backward whirling motion, the decay rate is $\sigma = \zeta_{hyst} \cdot sign(\omega_0 + \Omega)$, defining a system which is unconditionally stable. The decay rate for a Jeffcott-Laval rotor with hysteretic damping is represented in the frequency domain in Figure 3.3 for both forward and backward whirling motions.

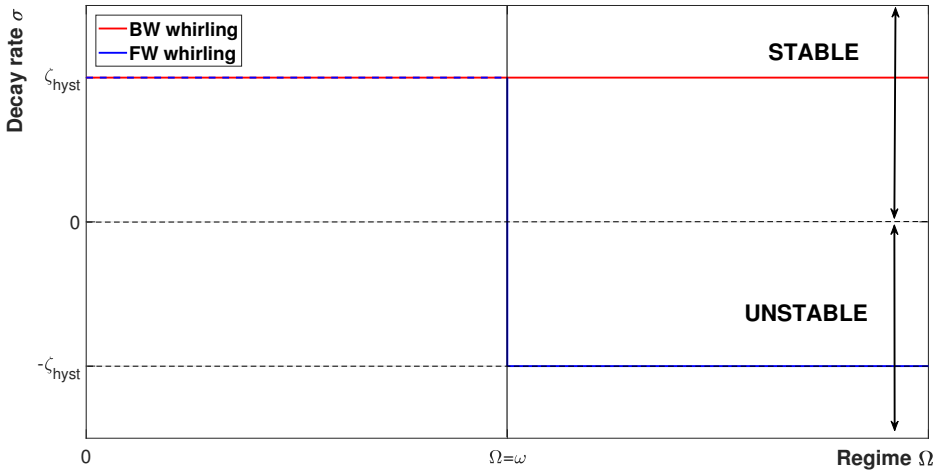

Figure 3.3: Stability of a Jeffcott-Laval rotor with hysteretic damping.

One can observe the difference between the evolution of the hysteretic damping and the viscous damping decay rates in the cases of forward and backward whirling motions: the viscous damping ratio is proportional to the rotating speed in both forward and backward whirling motions. On the other hand, the damping ratio of the hysteretic damping is constant in backward whirling motions and always positive, while is constant with a discontinuous variation in the critical speed of the mode for the forward whirling. It is interesting to notice that usually the viscous damping is present in the supports while the structural damping is employed for the material of the rotating shafts, so a combination of viscous and hysteretic damping effects can be seen in complex systems.

In this section the effect of viscous and hysteretic damping have been presented analytically on a simplified Jefccott-Laval rotor. In the following sections viscous and hysteretic damping are presented in a more general way adaptable to the FE framework.

3 Focus on viscous damping theory

The elementary viscous damping force $\mathbf{f_{dv}}$ is naturally evaluated in $\mathcal{R}_m$ as proportional to the instantaneous velocity:

$$\{\mathbf{f_{dv}}\}_{\mathcal{R}_m} = \mathbf{D_v}\dot{\mathbf{q}}_m \tag{3.16}$$

with $\mathbf{D_v}$ representing the viscous damping elementary matrix. We wish to express this force as a function of the velocity and displacement components in $\mathcal{R}_f$. Using the expression for the velocity in the moving reference frame given in equation 3.4, we have:

$$\dot{\mathbf{q}}_m = \mathbf{R}_u^T\dot{\mathbf{q}}_f + \Omega\mathbf{R}_u^T\mathbf{J}\mathbf{q}_f \tag{3.17}$$

Considering the axial symmetry of the rotor ($\mathbf{D_v}$ is symmetrical), we have equation 3.18.

$$\{\mathbf{f_{dv}}\}_{\mathcal{R}_f} = \mathbf{D_v}\dot{\mathbf{q}}_f + \Omega\mathbf{D_v}\mathbf{J}\mathbf{q}_f \tag{3.18}$$

In the case of an harmonic movement, equation 3.18 expressed in the frequency domain becomes:

$$\{\hat{\mathbf{f}}_{\mathbf{dv}}\}_{\mathcal{R}_f} = \mathbf{D_v}j\omega\hat{\mathbf{q}}_f + \Omega\mathbf{D_v}\mathbf{J}\hat{\mathbf{q}}_f \tag{3.19}$$

When the damping force is projected in the moving reference frame $\mathcal{R}_m$, the two components of the viscous damping force appear (see Figure 3.4). The first term $j\omega\hat{\mathbf{q}}_f$ of equation 3.19 is proportional to the instantaneous velocity of the system and thus to the whirling frequency ω. The instantaneous speed is always in quadrature with the displacements, generating a force which is opposed to the movement leading to a stabilising effect on the rotating shaft (see blue component in Figure 3.4 in the inertial reference frame side).
The second term $\Omega\mathbf{D}_v\mathbf{J}\mathbf{q}_f$, known as *circulatory damping force* [Nelson, 2007; Hetzler, 2013], is proportional to the rotational speed of the shaft Ω and to the displacements. It can assume different roles depending on the type of whirling motion of the shaft:

- **In the case of a forward whirling motion**: this component is oriented in the same direction as the displacements. Thus, increasing the rotational speed Ω and the dispalcement's amplitude, the second term increases generating an increasing destabilising force on the rotating shaft (see Figure 3.4). The viscous damping force in forward whirling rotating shafts is stabilising in subcritical regimes because the first term of equation 3.19 dominates and destabilising in supercritical regimes because the second term of 3.19 becomes governing (see Figure 3.4).
  We can also propose a physical interpretation of this phenomenon: the frequency of the displacements observed from the rotating reference frame is $(\Omega - \omega)$. In subcritical regimes, the whirling direction is the same as the whirling direction observed from the inertial reference frame. At the critical speed, the rotor is seen

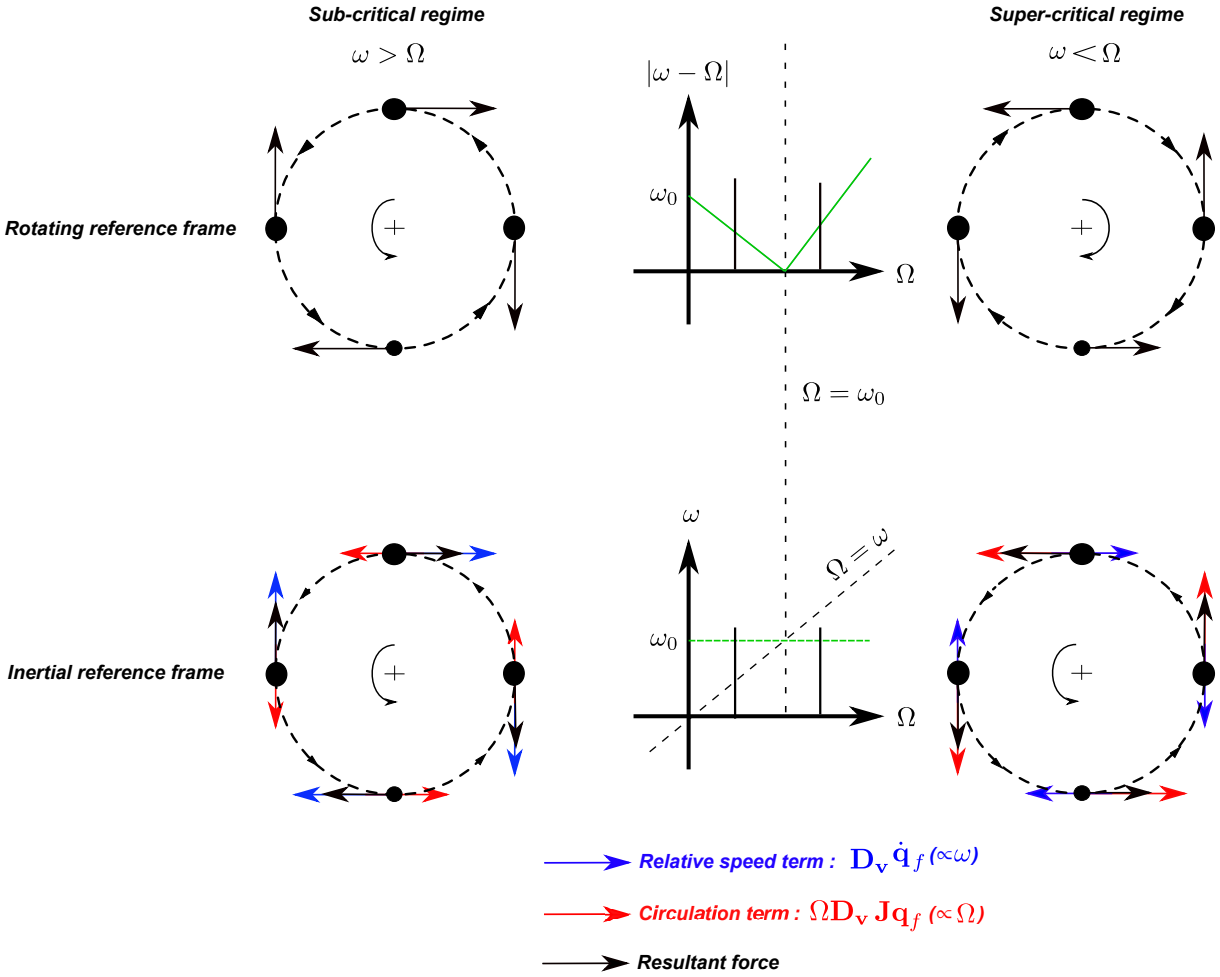

Figure 3.4: Viscous damping force representation in inertial and rotating reference frames, forward (direct) whirling motion.

as static from the point of view of the rotating reference frame ($\Omega - \omega = 0$). In supercritical regimes the whirling motion changes its whirling direction. The damping force is always opposed to the movement in the rotating reference frame, thus it changes its direction as the whirling motion does.
Reporting the damping force in the inertial reference frame, two components appear ($j\omega\hat{\mathbf{q}}_f$ and $\Omega\mathbf{D}_v\mathbf{J}\mathbf{q}_f$) and the resulting force is promoting the movement.

- **In the case of a backward whirling motion**: this term is oriented against the displacement, in accord with the first term of equation 3.18. Thus the viscous damping force is always stabilising (see figure 3.5).

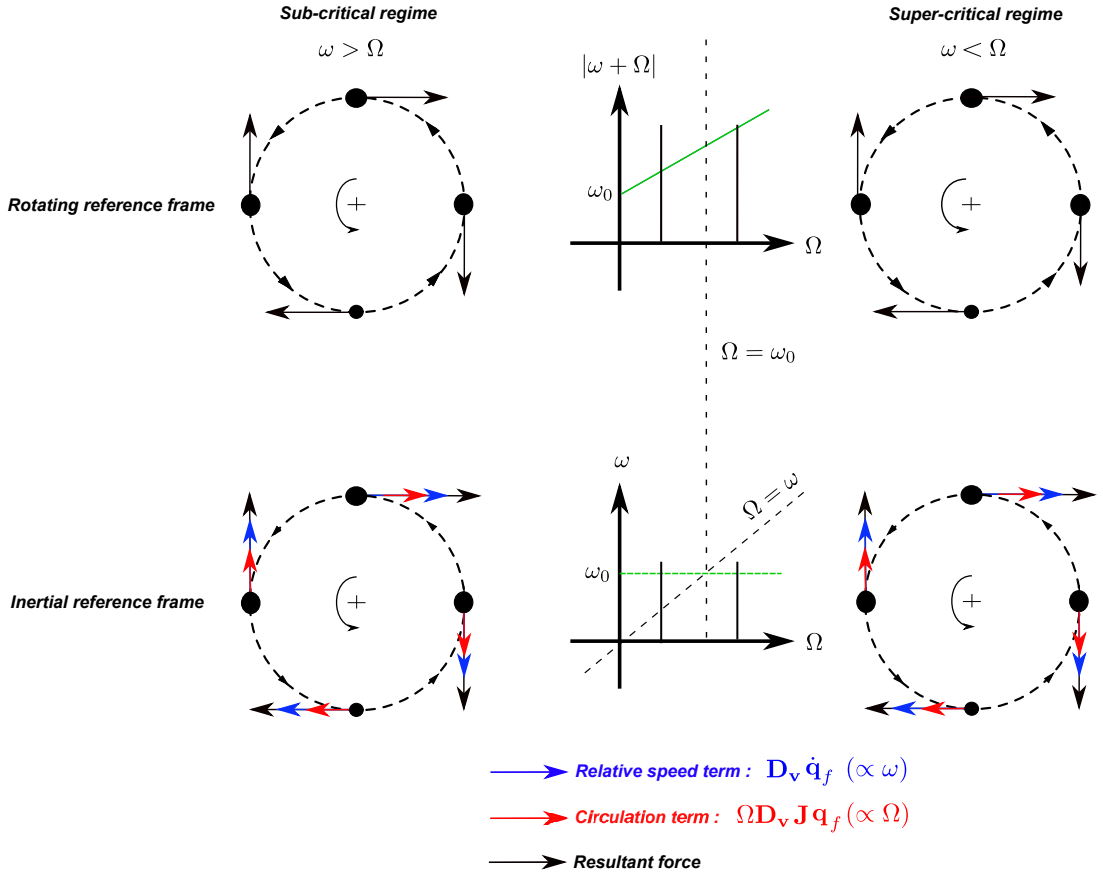

Figure 3.5: Viscous damping force representation in inertial and rotating reference frames, backward (inverse) whirling case.

4 Focus on hysteretic damping theory

The elementary hysteretic damping force $\mathbf{f_{dh}}$ is naturally evaluated in $\mathcal{R}_m$ as proportional to the relative displacements but out of phase:

$$\{\hat{\mathbf{f}}_{\mathbf{dh}}\}_{\mathcal{R}_m} = j\mathbf{D_h}\hat{\mathbf{q}}_m = j\eta_h\mathbf{K}\hat{\mathbf{q}}_m \tag{3.20}$$

The hysteretic damping model is employed to simulate a dissipation which is not dependent on the frequency, representing the energy loss during the hysteresis cycles of the elastic deformation. Crandall in 1970 and then Genta in 2004 proposed a formulation of the hysteretic damping equivalent to the viscous damping [Crandall, 1970; Genta, 2010]. In this approach, the hysteretic damping force is produced combining the *equivalent hysteretic damping* matrix $\mathbf{D_h}$ with the instantaneous speed of the system expressed in $\mathcal{R}_m$:

$$\{\mathbf{f_{dh}}\}_{\mathcal{R}_m} = \mathbf{D_h}\dot{\mathbf{q}}_m = \frac{1}{|\omega_m|}\eta_h\mathbf{K}\dot{\mathbf{q}}_m \tag{3.21}$$

ω_m is the frequency at which the hysteresis cycle is perceived by the rotating shaft and is considered to be positive in non rotating structures because the excitation frequencies are always positive. This is not the case in rotor-dynamics because of the whirling motion: the sign of ω_m depends on the relation between the whirling speed ω and the rotational speed Ω and it must not be neglected. The omission of this sign in the past gave rise to some misunderstanding on the destabilising effect of the hysteretic damping force in rotating systems [Zorzi, 1977; Melanson, 1998; Genta, 2004].

In the case of an harmonic motion, the displacements of a point P in the fixed reference frame $\mathcal{R}_f$ can be written through harmonic functions along the directions $\mathbf{Y}_f$ and $\mathbf{Z}_f$:

$$\{\mathbf{OP}\}_{\mathcal{R}_f} = \mathbf{q}_f = \begin{bmatrix} v_f\ cos(\omega t + \phi_v) \\ w_f\ cos(\omega t + \phi_w) \end{bmatrix} \tag{3.22}$$

Where (v_f, w_f, ϕ_v, ϕ_w) are respectively the amplitudes (in $\mathbb{R}^+$ and phases (in the range $[-\pi, \pi]$) of the displacements. The hysteretic damping force is naturally expressed in the rotating reference frame $\mathcal{R}_m$, so we have to write the displacements in the $\mathcal{R}_m$.

$$\{\mathbf{OP}\}_{\mathcal{R}_m} = \mathbf{q}_m = \mathbf{R}^T\mathbf{q}_f \tag{3.23}$$

After development and linearization of the expression, the equation becomes:

$$\mathbf{q}_m = \frac{1}{2}\begin{bmatrix} v_f\ cos((\omega-\Omega)t+\phi_v) - w_f\ sin((\omega-\Omega)t+\phi_w) \\ v_f\ sin((\omega-\Omega)t+\phi_v) + w_f\ cos((\omega-\Omega)t+\phi_w) \end{bmatrix} + \frac{1}{2}\begin{bmatrix} v_f\ cos((\omega+\Omega)t+\phi_v) + w_f\ sin((\omega+\Omega)t+\phi_w) \\ v_f\ sin((\omega+\Omega)t+\phi_v) + w_f\ cos((\omega+\Omega)t+\phi_w) \end{bmatrix} \tag{3.24}$$

The transformation of the displacements from $\mathcal{R}_f$ to $\mathcal{R}_m$ reveals two different harmonic components at frequencies $(\omega+\Omega)$ and $(\omega-\Omega)$. The employment of the Fourier's expansion wouldn't allow to simplify the expression of these displacements. For this reason, the following developments are presented at first in the time domain and then reported in the frequency domain.
Deriving equation 3.24, the instantaneous velocity is given by:

$$\dot{\mathbf{q}}_m = \frac{1}{2}(\omega-\Omega)\begin{bmatrix} -v_f\ sin((\omega-\Omega)t+\phi_v) - w_f\ cos((\omega-\Omega)t+\phi_w) \\ v_f\ cos((\omega-\Omega)t+\phi_v) - w_f\ sin((\omega-\Omega)t+\phi_w) \end{bmatrix} + \frac{1}{2}(\omega+\Omega)\begin{bmatrix} -v_f\ sin((\omega+\Omega)t+\phi_v) + w_f\ cos((\omega+\Omega)t+\phi_w) \\ -v_f\ cos((\omega+\Omega)t+\phi_v) - w_f\ sin((\omega+\Omega)t+\phi_w) \end{bmatrix} \tag{3.25}$$

This relationship can be grouped as follows by the identification of terms:

$$\dot{\mathbf{q}}_m = \frac{1}{2}(\omega-\Omega)\mathbf{dq}_m^- + \frac{1}{2}(\omega+\Omega)\mathbf{dq}_m^+ \tag{3.26}$$

with:

$$\mathbf{dq}_f^- = \begin{bmatrix} -v_f\ sin(\omega t+\phi_v) - w_f\ cos(\omega t+\phi_w) \\ v_f\ cos(\omega t+\phi_v) - w_f\ sin(\omega t+\phi_w) \end{bmatrix} \tag{3.27}$$

and:

$$\mathbf{dq}_f^+ = \begin{bmatrix} -v_f\ sin(\omega t+\phi_v) + w_f\ cos(\omega t+\phi_w) \\ -v_f\ cos(\omega t+\phi_v) - w_f\ sin(\omega t+\phi_w) \end{bmatrix} \tag{3.28}$$

The hysteretic damping force expressed in the rotating reference frame can be evaluated using equations 3.26 in 3.20, obtaining:

$$\{\mathbf{f_{dh}}\}_{\mathcal{R}_m} = \frac{1}{2}\frac{(\omega-\Omega)}{|\omega-\Omega|}\eta_h\mathbf{K}\mathbf{dq}_m^- + \frac{1}{2}\frac{(\omega+\Omega)}{|\omega+\Omega|}\eta_h\mathbf{K}\mathbf{dq}_m^+ \tag{3.29}$$

Considering that $\omega+\Omega$ is positive, the previous equation is simplified to:

$$\{\mathbf{f_{dh}}\}_{\mathcal{R}_m} = \frac{1}{2} sign(\omega - \Omega)\eta_h \mathbf{K}\mathbf{dq}_m^- + \frac{1}{2}\eta_h \mathbf{K}\mathbf{dq}_m^+ \tag{3.30}$$

Finally, the hysteretic damping force is reported in the inertial reference frame using the relation $\{\mathbf{f_{dh}}\}_{\mathcal{R}_f} = \mathbf{r}\{\mathbf{f_{dh}}\}_{\mathcal{R}_m}$.
The complete development of this operation is reported in Appendix 3 and its result is expressed in equation 3.31.

$$\{\mathbf{f_{dh}}\}_{\mathcal{R}_f} = \frac{\eta_h \mathbf{K}}{2}\left[sign(\omega-\Omega)\begin{bmatrix} -2\ v_f\ sin(\omega t+\phi_v) - 2\ w_f\ cos(\omega t+\phi_w) \\ 2\ v_f\ cos(\omega t+\phi_v) - 2\ w_f\ sin(\omega t+\phi_w)\end{bmatrix} + \right. \\ \left. + \begin{bmatrix} -2\ v_f\ sin(\omega t+\phi_v) + 2\ w_f\ cos(\omega t+\phi_w) \\ -2\ v_f\ cos(\omega t+\phi_v) - 2\ w_f\ sin(\omega t+\phi_w)\end{bmatrix}\right] \tag{3.31}$$

Two cases have to be be studied, if the system is in a sub-critical regime ($\omega > \Omega$), equation 3.31 becomes:

$$\{\mathbf{f_{dh}}\}_{\mathcal{R}_f} = \eta_h \mathbf{K}\begin{bmatrix} -v_f\ sin(\omega t+\phi_v) \\ -w_f\ sin(\omega t+\phi_w)\end{bmatrix} = \Re(j\eta_h \mathbf{K}\begin{bmatrix} v_f\ e^{j\phi_v} \\ w_f\ e^{j\phi_w}\end{bmatrix} e^{j\omega t}) \rightarrow$$

$$\rightarrow \{\hat{\mathbf{f}}_{\mathbf{dh}}\}_{\mathcal{R}_f} = j\eta_h \mathbf{K}\hat{\mathbf{q}}_f \tag{3.32}$$

If the system is in a super-critical regime ($\omega < \Omega$):

$$\{\mathbf{f_{dh}}\}_{\mathcal{R}_f} = \eta_h \mathbf{K}\begin{bmatrix} w_f\ cos(\omega t+\phi_w) \\ -v_f\ cos(\omega t+\phi_v)\end{bmatrix} = \Re(\eta_h \mathbf{K}\begin{bmatrix} 0 & 1 \\ -1 & 0\end{bmatrix}\begin{bmatrix} v_f\ e^{j\phi_v} \\ w_f\ e^{j\phi_w}\end{bmatrix} e^{j\omega t}) \rightarrow$$

$$\rightarrow \{\hat{\mathbf{f}}_{\mathbf{dh}}\}_{\mathcal{R}_f} = \eta_h \mathbf{K}\mathbf{J}\hat{\mathbf{q}}_f \tag{3.33}$$

Since the force $j\eta_h \mathbf{K}\hat{\mathbf{q}}_f$ is in phase lag with the elasticity and inertial forces, the hysteretic damping force makes a stabilizing contribution in subcritical regimes (see left side of Figure 3.6). On the contrary, the force $\eta_h \mathbf{K}\mathbf{J}\hat{\mathbf{q}}_f$ is in phase advance with the elasticity and inertial forces and due to its space direction, it has a destabilising effect in supercritical regimes. This is depicted on the right of Figure 3.6.

Until now, the damping force has not been defined for the critical speed: $\omega = \Omega$. This situation is not described in Genta's papers either. This represents a limitation for the computation of the synchronous response of an unbalanced rotor in the frequency domain.

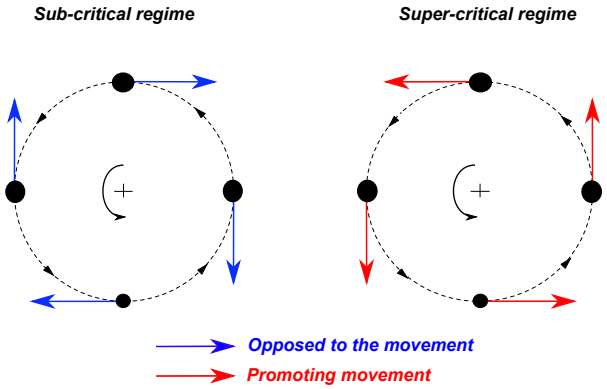

Figure 3.6: Hysteretic damping force in a rotating shaft in forward whirling motion.

To overcome this limitation, the authors propose here a definition of damping at the critical speed described as the mean value of the damping force from the left and the right of the discontinuity ($\omega = \Omega$). The model written in the $\mathcal{R}_f$ frame is singular with respect to $\omega = \Omega$; it must therefore be first written in $\mathcal{R}_m$ and then transformed back into $\mathcal{R}_f$, leading to:

$$\{\hat{\mathbf{f}}_{\mathbf{dh}}\}_{\mathcal{R}_f}(\omega = \Omega) = \frac{1}{2} j\eta_h \mathbf{K}\hat{\mathbf{q}}_f + \frac{1}{2}\eta_h \mathbf{J}\mathbf{K}\hat{\mathbf{q}}_f \tag{3.34}$$

This formulation shows two interesting features. First of all, it defines the hysteretic damping force as equal to zero in the case of a forward motion with circular centred orbit at critical speed (i.e. $j\hat{\mathbf{q}}_f = \mathbf{J}\hat{\mathbf{q}}_f$). The rotor is static at the critical speed from the point of view of the rotating reference frame, which means that there is no hysteretic damping force. Moreover, it agrees with the formulation of the hysteretic damping force in backward whirling motions with centered circular orbits that guarantees the continuity of the force in the frequency domain.
To summarize, the hysteretic damping can be written in three different ways as a function of the frequency vs the rotational speed:

$$\{\hat{\mathbf{f}}_{\mathbf{dh}}\}_{\mathcal{R}_f} = \begin{cases} j\eta_h \mathbf{K}\hat{\mathbf{q}}_f & \text{subcritical regime} : \omega > \Omega \\ \frac{1}{2} j\eta_h \mathbf{K}\hat{\mathbf{q}}_f + \frac{1}{2}\eta_h \mathbf{J}\mathbf{K}\hat{\mathbf{q}}_f & \text{synchronous regime} : \omega = \Omega \\ \eta_h \mathbf{J}\mathbf{K}\hat{\mathbf{q}}_f & \text{supercritical regime} : \omega < \Omega \end{cases} \tag{3.35}$$

Taking into account the most recent formulation of the hysteretic damping modeling in rotors proposed by Genta [Genta, 2004], a new model has been proposed, based on the combination of the displacements and the stiffness matrix.

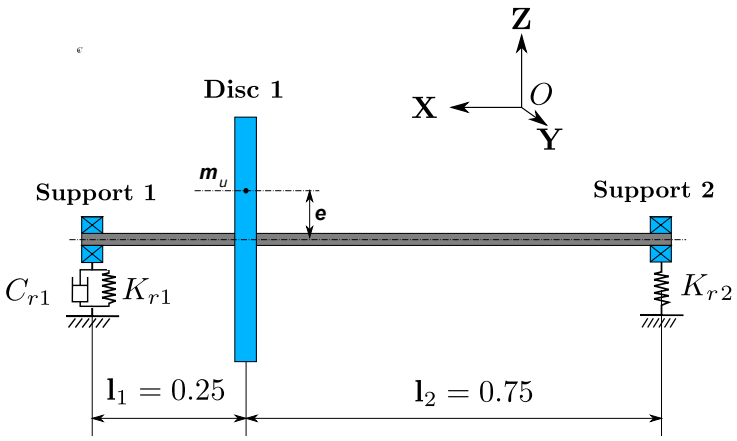

Figure 3.7: Modified Jeffcott-Laval rotor.

5 Numerical applications

In this section a modified Jeffcott-Laval rotor is studied using a FE approach and adopting both viscous and hysteretic damping. The considered model is defined in an orthogonal inertial reference frame $\mathcal{R}_f$. Since in this study there is no interest in torsional dynamics, the displacements field is defined in any node of the model by 4 DOFs as in Section 2.1. The structure is characterised by a rigid disc positioned on an elastic shaft with two radial supports at the extremities (see Figure 3.7). Twenty-four Timoshenko beams (96 DOFs) have been used to model the whole shaft. The elastic radial supports are symmetrical and only the one on the left is damped. A hysteretic damping ratio of $\eta_h = 10\%$ is adopted in the whole shaft. The disc is modelled using a lumped mass with inertial properties (see Figure 3.7). The operators representing the system are given in Appendix 1. The free motion of the system is controlled by the following relation expressed in the inertial reference frame and in the frequency domain:

$$\{-\omega^2\mathbf{M} + j\omega(\Omega\mathbf{G}_f + \mathbf{D}_\mathbf{v}) + \mathbf{K} + j\eta_h\mathbf{K}\}\hat{\mathbf{q}}_f = 0 \tag{3.36}$$

A study on the damping ratio of the first 4 vibration modes of the structure is performed at first without taking into account the effect of the circulatory damping force: the model proposed in equation 3.35 is not applied and the damping ratios are evaluated classically. The Campbell analysis and the damping ratios are reported in Figure 3.8. One can notice that the decay rates of the backward and forward modes are always positive since the circulatory effect of the hysteretic damping is not taken into account in the performed simulation. In this case, both viscous and hystretic damping present in the structure are always stabilising the system.

It is now interesting to perform the same study as before including the circulatory effect of the hysteretic damping present in the beam elements of the shaft, equation 3.35 is taken

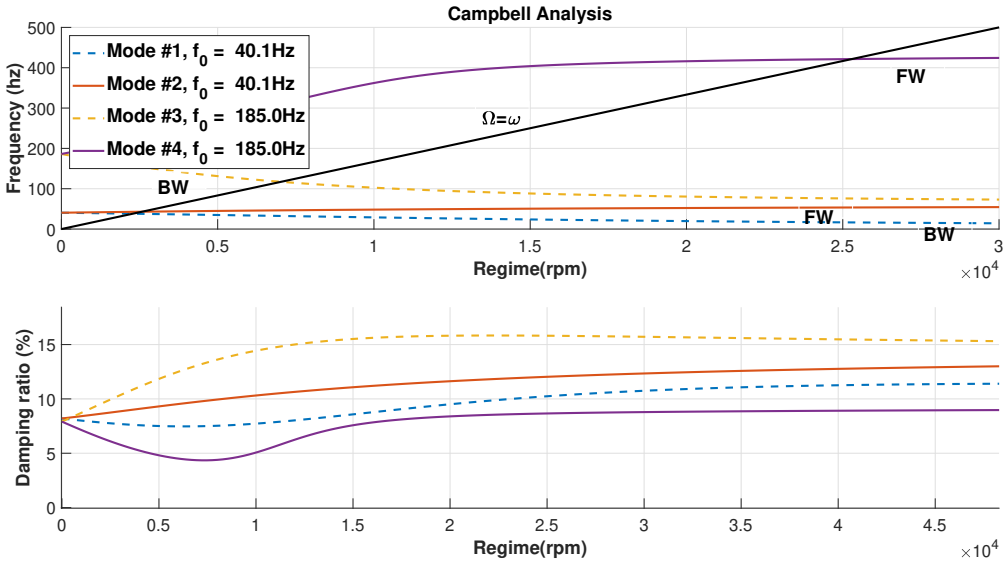

Figure 3.8: FE Jeffcott-Laval rotor with damped supports (viscous) **without** hysteretic damping in the shaft.

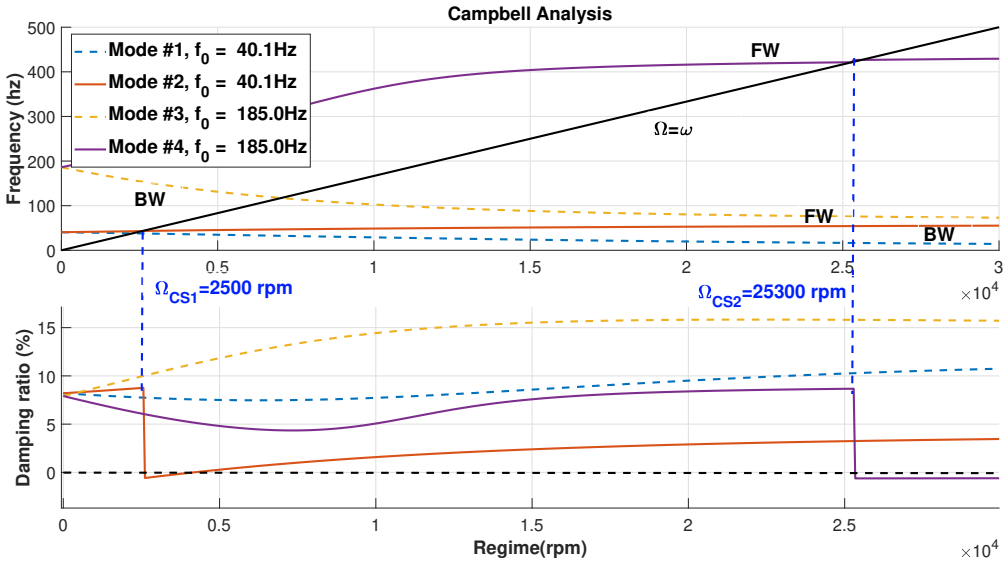

Figure 3.9: FE Jeffcott-Laval rotor with damped supports (viscous) and **with** hysteretic damping in the shaft.

into account in the Campbell analysis reported in Figure 3.9. As introduced before, the circulation of the damping force can make the system unstable in certain situations. The stability of the forward modes of the structure is affected: any forward mode, displays a discontinuity in the decay rate at the critical speed, the whirling mode is indeed stable before the critical speed and unstable after. In particular, the vibration mode #4 has the most important variation of the decay rate. As showed in Section 4, the backward modes are always stable even taking into account the circulatory effect of hysteretic damping.

6 Conclusions

The objective of this chapter is to discuss the impact of different options for modeling damping in rotating machines. Historically, viscous damping has been associated with bearings and shaft behaviors. However, for more realism, the damping of structural parts should be modeled by hysteretic models. Nevertheless, viscous damping approaches can be adapted with some modifications to simulate the structural damping as well [Crandall, 1991; Genta, 2004].

The main objective of this chapter is to make clear the effect of the damping forces in rotating shafts. The main differences between viscous and hysteretic damping have been highlighted, reporting the conditions in which these damping forces generate a stabilising or a destabilising effect. In stability simulations, on the one hand, it is shown that the decay rate is linearly dependent on the rotating speed in the case of viscous damping for both forward and backward whirling motions. On the other hand, the decay rate is constant with a discontinuity in the critical speed for the case of hysteretic damping with forward whirling motion and constant (positive) in the case of hysteretic damping with backward whirling motion. Figure 3.10 reports a resuming table containing the main elements presented in the above sections.
In regard of the hysteretic damping, the model proposed by Genta in 2004 [Genta, 2004] has been considered in the beginning and then a new formulation of this model has been developed and analysed. The proposed model can be employed in frequency and time domain. This new formulation is characterised by a proportionality with the displacements and not anymore with the instantaneous speed. The model has been proposed theoretically and then extended to a finite element formulation of a Jeffcott-Laval rotor. The extension of this practice in more complex cases is direct.

	Viscous damping	**Hysteretic damping**
Mathematical Formulation	$\{\mathbf{f_{dh}}\}_{\mathcal{R}_f} = \mathbf{D_v}\dot{\mathbf{q}}_f + \Omega\mathbf{D_v}\mathbf{J}_u\mathbf{q}_f$	$\{\hat{\mathbf{f}}_{\mathbf{dvh}}\} = \begin{cases} j\eta_h\mathbf{K}\hat{\mathbf{q}}_f & \text{subcritical} : \omega < \Omega \\ \frac{1}{2}j\eta_h\mathbf{K}\hat{\mathbf{q}}_f + \frac{1}{2}\mathbf{J}\eta_h\mathbf{K}\hat{\mathbf{q}}_f & \text{synchronous} : \omega = \Omega \\ \mathbf{J}\eta_h\mathbf{K}\hat{\mathbf{q}}_f & \text{supercritical} : \omega > \Omega \end{cases}$
Physical interpretation of damping forces	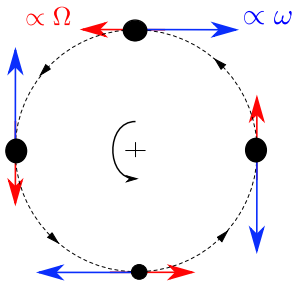	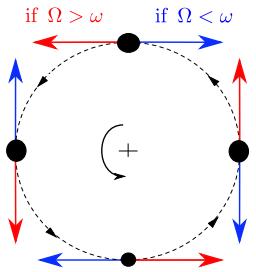
Modal damping FW and BW modes	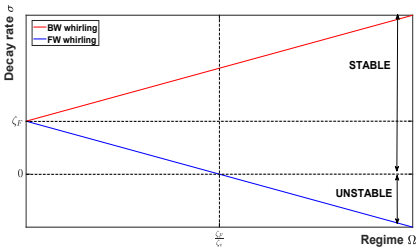	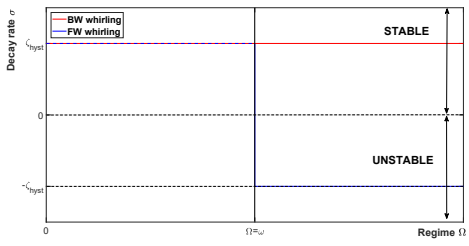

Figure 3.10: Resuming table of the viscous and hysteretic damping in rotating shafts.

Chapter 4

Numerical methods for nonlinear rotordynamics

"If you wish to understand the universe, think of energy frequency and vibration."

Nikola Tesla: Serbian-American inventor, engineer, physicist (1856-1943)

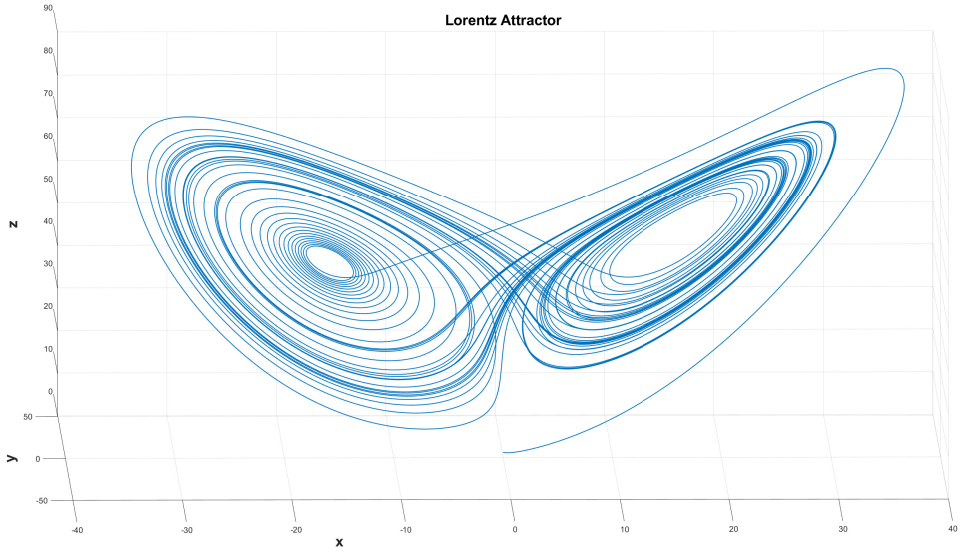

Objectives

This chapter seeks to introduce multiple numerical methods to study the nonlinear responses of rotating systems, such as the time marching approach or the harmonic balance method which is investigated in deep.

Contents

1 Solvers for nonlinear dynamics

First nonlinear effects affecting rotating shaft on bearings have been observed by Yamamoto from 1955 [Yamamoto, 1955], pointing at non-synchronous excitation coming from fluid film journals. Multiple works have been published concerning the experimental observation of nonlinear effects due to rotor-stator rub/impact, resumed in the following overviews [Muszynska, 1989; Ahmad, 2010; Jacquet-Richardet, 2013].

Classically, the solution of linear and nonlinear problems, in analytical and *Finite Element* (FE) formulations, were performed through the *direct Time Integration (TI)* [Robert, 1972], based on the *time finite differences* [Young, 1968]. Time marching solvers can be grouped into *implicit* and *explicit* types:

- Implicit solvers: if the state vector in the next time integration step t_{n+1} is dependent on the state vector at the time t_n, its derivative at the time t_n and its derivative at the time t_{n+1} [Robert, 1972; Choy, 1987; Festjens, 2013]. These methods are **unconditionally** stable and generally employed in nonlinear dynamics, seismic engineering etc.
- Explicit solvers: if the state vector in the next time integration step t_{n+1} depends only on the on the state vector at the time t_n [Carpenter, 1991; Legrand, 2009; Roques, 2010]. These methods are **conditionally** stable, their convergence depend on the step-size chosen and they are classically applied in *fast dynamics* [Bouaziz, 2014].

Especially in FE modeling, the direct time integration is performed using the *Newmark method* proposed in 1959 [Newmark, 1959], or the *Runge-Kutta* algorithm [Butcher, 1996; Butcher, 1976].

It seems essential now to introduce the major works reporting the time-integration methods in rotordynamics. First relevant works in computational rotor-dynamics have been proposed by Kirk et al. and by Shen et al. [Shen, 1972; Kirk, 1974] in the beginning of seventies. Childs in 1975 study the dynamical behaviour of the space shuttle main engine *High Pressure Oxygen Turbopump* (HPOTP), modeled with FE approach and using a time integration solver and including journal bearing nonlinearities [Childs, 1975; Childs, 1985]. A transient simulation like this allows to identify the unbalance response of the system and its dynamical behaviour working through the critical speeds. In 1980, Adams used the time-transient analysis to identify the dynamical behaviour of a nonlinear multi-bearing rotor [Adams, 1980]. In 1986, Muszynska [Muszynska, 1986] proposed a first numerical study of a simple rotor with a fluid film journal, observing sub-harmonic phenomena due to the nonlinear effect of the support.

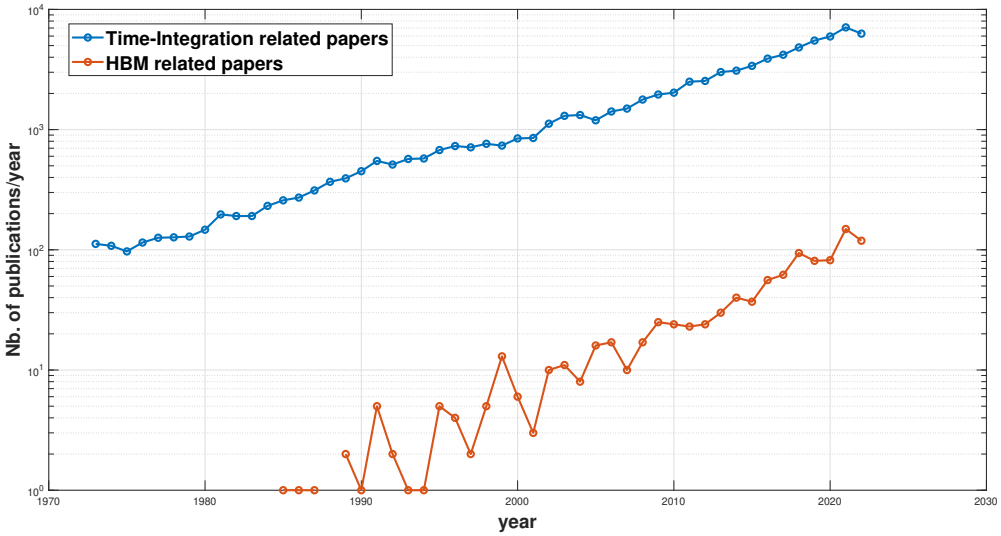

Figure 4.1: Steady state with TI related publications vs HBM related publications over the last 50 years. Data available at [DimensionsAIti, 2023; DimensionsAIhbm, 2023].

Untill the early nineties, the time integration is the only robust simulation method adopted for nonlinear periodic responses of mechanical systems. First computationally efficient frequency-based approaches are seen in the eighties: Chua et al. [Chua, 1981] proposed for the first time a new algorithm based on the Galerkin method to solve nonlinear multi-frequency electrical circuits, the nonlinear terms have been studied with the trigonometric collocation. A variant of this method has been proposed by Lau et al. [Lau, 1981] at the same time, adopting an *Incremental Harmonic Balance* (IHB) approach using a path-continuation technique and a cubic extrapolation for the computation of the nonlinear terms, this approach is nevertheless rigid and limited to polynomial nonlinear forces. In 1987, Choi and Noah [Choi, 1987] proposed a new method based on the *Fast Fourier Transformation* (FFT) to evaluate the steady state response of a nonlinear rotating system with deadbands and rubs, also including super and subharmonics components. At the same time Ling et al. [Ling, 1987] proposes a paper reporting the father of the modern *Harmonic Balance Method* (HBM), using the Galerkin weighted residual method [Galerkin, 1915], the FFT and the Newton-Raphson algorithm. Urabe in 1964 [Urabe, 1964] already proposed something similar but less efficient than Ling's variant with a classical Fourier expansion. In 1989, Nataraj and Nelson [Nataraj, 1989] proposed another approach to identify the steady state response of a nonlinear rotor without the direct time integration, adopting again the weighted residual method associated with the trigonometric collocation. Hwang et al. in 1991 [Hwang, 1991] proposed the trigono-

metric expansion to study a rotor suspended on nonlinear bearings, with the polynomial expansion instead of the FE approach, defining it less expensive in terms of computational effort and with no loss in accuracy if compared with the time marching approaches. Kim and Noah in 1990 [Kim, 1990] firstly study the stability of a Jeffcott rotor and proved a bifurcation analysis using the HBM, then in 1991 introduced the dynamical condensation for the study of larger systems [Kim, 1991a; Kim, 1991b]. The model reduction technique proposed by Kim and Noah performs the condensation of the structure on the nonlinear DOFs, avoiding useless numerical iterations (see [Peletan, 2012a; Peletan, 2013] for more examples). Yamauchi [Yamauchi, 1983] in 1983 and then Saito et al. in 1985 [Saito, 1985] use the HBM in rotor-dynamics with the numerical differentiation for the Newton-Raphson algorithm. The HBM is applied in modern times with an improved Newton-Raphson algorithm known as *continuation* and with the AFT algorithms [Seydel, 2009; Krack, 2019; Guskov, 2007]. Some alternatives to the HB approaches can be seen in wavelet-Galerkin variant [Pernot, 2001; Peletan, 2013] using wavelet functions instead of Fourier or discrete Fourier expansions or the trigonometric and the orthogonal collocation [Karkar, 2014; Krack, 2019]. The HB has been used for rotordynamics by multiple research teams, some examples are given: Groll and Edwins [Von Groll, 2001], Thouverez et al. [Guskov, 2007; Peletan, 2012a; Jacquet-Richardet, 2013; Peletan, 2013] and Bonello et al. [Bonello, 2002; Hai, 2008; Bonello, 2009].

Another relevant frequency-based approach for the evaluation of nonlinear steady-state responses of mechanical systems can be identified in the *shooting method*, proposed for the first time in the early eighties [Bock, 1984; Ascher, 1995]. Sundararajan and Noah applied successfully the shooting method in rotordynamics with a path continuation algorithm [Sundararajan, 1997; Sundararajan, 1998]. The shooting method has been coupled with the HBM in 2016 [Schreyer, 2016]. Krack et al. in 2015 [Krack, 2015] compared the shooting and the HBM in terms of computational efficiency for the evaluation of nonlinear normal modes and for the FRFs in 2019 [Krack, 2019].
Time-integration solvers are the most used for the evaluation of the steady-state response of dynamical systems, this type of solver has been used from the seventies and is generally available in any commercial FEM software. On the the contrary, the *Harmonic Balance* (HB) arrived lately, with an increasing interest because of its efficiency in terms of computational effort (see Figure 4.1) and is still not implemented efficiently in some established FEM commercial softwares.

This chapter seeks to present in detail the nonlinear framework of the rotor-stator interaction in rotating machines and the solver employed in the further parts of this work to deal with this problem.

2 The Harmonic Balance method

In this section an overview on the HBM is given, identifying its origins and the elements characterising the most recent variants of this method. The main elements of the modern HBM are presented in detail: the Galerkin method for the approximation of differential equations, the continuation algorithm for the solution of the numerical problem and the AFT algorithm for the treatment of the nonlinear force.

2.1 On the Harmonic Balance Method, an overview

The equation governing the nonlinear unbalance response of a rotating system in the time domain has been written in Chapter 2 as:

$$\mathbf{M}\ddot{\mathbf{q}}_f + (\mathbf{D_v} + \Omega\mathbf{G})\dot{\mathbf{q}}_f + \mathbf{K}\mathbf{q}_f + \mathbf{f_{nl}}(\mathbf{q}_f, t) = m \cdot e \cdot \Omega^2 \mathbf{f}(t) \tag{4.1}$$

In this equation, the term $\mathbf{f_{nl}}(\mathbf{q}_f, t)$ depends on the displacements field $\mathbf{q}_f(t)$, which is undetermined, hence the problem has to be solved using an iterative algorithm. The solution of this equation can only be approximated with an error more or less relevant, the exact mathematical solutions cannot be identified iteratively. The HBM can be employed to calculate the approximated solution of this equation. The whole solution technique is commonly referred as *harmonic balance algorithm* [Luongo, 2012], *harmonic balance method* [Sanliturk, 1996; Grolet, 2012] or simply *the harmonic balance* [Guskov, 2007; Krack, 2019], but in fact, the *Harmonic Balance* (HB) is an operation consisting in the application of the *Galerkin method* (also referred as the *weighted residual method*) [Galerkin, 1915] on a differential-algebraic systems of equations.

As described by Ling, [Ling, 1987] *"The Galerkin method is an approximate method which is often applied to solve differential equations and integral equations numerically. The basic idea is to seek a solution in terms of a series of characteristic functions which satisfy the boundary conditions"*. This method shares some elements with the Ritz approximation. A short focus on Galerkin and Ritz methods has been written in Appendix 4 to make clear the difference between these two approximation methods, the first applied on differential equations in strong form, the second applied on the weak form minimising the potential energy.

In the specific case of the HBM, the Galerkin method is applied using the *Fourier expansion* [Kim, 2003] as "*series of characteristics functions*". The first time this method was used by Urabe in 1965 [Urabe, 1964] with the classical Fourier expansion since the FFT still had to be popularised. The *fast Galerkin method* is proposed for the first time by Ling et al. in 1987 [Ling, 1987].

Once the problem formulated using this variant of the Galerkin method, it can be solved through an iterative algorithm such as the Newton-Raphson algorithm as done in [Ling, 1987]. In FE frameworks, this numerical problem is commonly solved using an improved variant of the Newton-Raphson algorithm known as *continuation* [Seydel, 2009].

The computation of the nonlinear force can be performed in multiple ways, in this work we only cite the classical Fourier expansion of the nonlinear force if it has a simple formulation (e.g. duffing [Kovacic, 2011]) or more generally through the algorithm known as AFT [Cameron, 1989]. For more methods concerning the evaluation of the nonlinear forces one can see [Krack, 2019].

To sum up, the modern HBM described in literature nowadays (e.g. [Guskov, 2007; Grolet, 2012; Krack, 2019]), is characterised by:

- The application of the Galerkin method with the *Fast Fourier Transformation* (FFT) on a differential-algebraic systems of Equations [Ling, 1987].
- The employment of the continuation algorithm (e.g.[Seydel, 2009]).
- The employment of the AFT algorithm [Cameron, 1989].

2.2 Fourier-Galerkin method (Harmonic Balance)

The HB formulation is based on the assumption that the displacement field $\boldsymbol{q}(\mathrm{t})$ has a periodic behaviour. This term can be expressed as reported in Equation 4.2 through the Fourier expansion in trigonometric or complex representations:

$$\mathbf{q}_f(t) \approx \hat{\mathbf{q}}_0 + \sum_{h=0}^{H} \hat{\mathbf{q}}_{2h-1} cos(m_h \omega t)) + \hat{\mathbf{q}}_{2h} sin(m_h \omega t) = \sum_{h=0}^{H} \hat{\mathbf{q}}_h e^{ih\omega t} \tag{4.2}$$

The Fourier expansion allows to approximate a periodic signal using a finite number H of harmonics function. The term m_h represents the Fourier harmonic coefficients, the term $\hat{\mathbf{q}}_0$ represents the constant contribution of the signal, the terms $\hat{\mathbf{q}}_{2h-1}$ and $\hat{\mathbf{q}}_{2h}$ represent respectively the harmonic amplitude of the $(2h-1)-th$ and $2h-th$ terms. Equation 4.2 can be expressed in matrix as well as reported in Equation 4.3.

$$\mathbf{q}_f(t) \approx \mathbf{A}(\omega, t)\, \hat{\mathbf{q}} \tag{4.3}$$

Using the trigonometric formulation we have:

$$\mathbf{A}(\omega,t) = \begin{bmatrix} \mathbf{I}_N & \mathbf{I}_N cos(\omega t) & \mathbf{I}_N sin(\omega t) & \dots & \mathbf{I}_N cos(H\omega t) & \mathbf{I}_N sin(H\omega t) \end{bmatrix}_{N\times(2H+1)}$$
$$\hat{\mathbf{q}} = \begin{bmatrix} \hat{\mathbf{q}}_0 & \hat{\mathbf{q}}_1 & \hat{\mathbf{q}}_2 & \dots & \hat{\mathbf{q}}_{2H-1} & \hat{\mathbf{q}}_{2H} \end{bmatrix}^T_{1\times(2H+1)}$$

or using the complex formulation:

$$\mathbf{A}(\omega,t) = \begin{bmatrix} \mathbf{I}_N & \mathbf{I}_N e^{j\omega t} & \dots & \mathbf{I}_N e^{jH\omega t} \end{bmatrix}_{N\times(H+1)}$$
$$\hat{\mathbf{q}} = \begin{bmatrix} \hat{\mathbf{q}}_0 & \hat{\mathbf{q}}_1 & \dots & \hat{\mathbf{q}}_H \end{bmatrix}^T_{1\times(H+1)}$$

with $\mathbf{I}_N$ representing an identity matrix of size N (size of the model in terms of DOFs). The problem can be thus expressed in complex or in real form with no loss of generality, its size depends on this choice. For the rest of this work, the complex representation will be preferred for its compact form. As well, the matrix $\mathbf{A}(\omega,t)$ in complex form can be decomposed in a constant and in a time-dependent parts through the Kronecker product ($\otimes$) as showed in Equation 4.4.

$$\mathbf{A}(\omega,t) = \begin{bmatrix} 1 & e^{j\omega t} & \dots & e^{jH\omega t} \end{bmatrix} \otimes \mathbf{I}_N = \mathbf{a}(\omega,t) \otimes \mathbf{I}_N \tag{4.4}$$

Finally, we can write:

$$\mathbf{q}_f(t) \approx \mathbf{a}(\omega,t) \otimes \mathbf{I}_N\, \hat{\mathbf{q}} \tag{4.5}$$

This representation allows to evaluate directly the derivative of the displacement field in matrix form.

$$\dot{\mathbf{q}}(t) \approx \dot{\mathbf{a}}(\omega,t) \otimes \mathbf{I}_N\, \hat{\mathbf{q}} = \omega\ \mathbf{a}(\omega,t)\ \Gamma \otimes \mathbf{I}_N\ \hat{\mathbf{q}} \tag{4.6}$$

$$\ddot{\mathbf{q}}(t) \approx \ddot{\mathbf{a}}(\omega,t) \otimes \mathbf{I}_N\, \hat{\mathbf{q}} = \omega^2\ \mathbf{a}(\omega,t)\ \Gamma^2_{\cdot} \otimes \mathbf{I}_N\ \hat{\mathbf{q}} \tag{4.7}$$

with:

$$\Gamma = \begin{bmatrix} 0 & 0 & \dots & 0 \\ 0 & jh & & \vdots \\ \vdots & & \ddots & \vdots \\ 0 & & \dots & jH \end{bmatrix}_{(H+1)\times(H+1)}$$

For the dynamic loading and the nonlinear term, the following developments are true if they are periodic functions. This assumption is generally true for the linear excitation but is not in the case of nonlinear force. Nevertheless, even if the nonlinear force has a non-periodical form it can be expanded using Fourier assuming that the whole length of

the signal represents a period [Krack, 2019].

$$\mathbf{f}(t) \approx \hat{\mathbf{f}}_0 + \sum_{j=1}^{H} \hat{\mathbf{f}}_{2j-1} cos(m_j \omega t)) + \hat{\mathbf{f}}_{2j} sin(m_j \omega t) = \mathbf{a}(\omega, t) \otimes \mathbf{I}_N \, \hat{\mathbf{f}} \tag{4.8}$$

$$\mathbf{f_{nl}}(t) \approx \hat{\mathbf{n}}_0 + \sum_{j=1}^{H} \hat{\mathbf{n}}_{2j-1} cos(m_j \omega t)) + \hat{\mathbf{n}}_{2j} sin(m_j \omega t) = \mathbf{a}(\omega, t) \otimes \mathbf{I}_N \, \hat{\mathbf{n}} \tag{4.9}$$

Substituting Equations 4.5, 4.6, 4.7, 4.8 and 4.9 in Equation 4.1, we can obtain:

$$\begin{aligned} \Big[\Big(\omega^2 \, \mathbf{a}(\omega t) \, \Gamma_{\cdot}^{2} \, \otimes \mathbf{M}\Big) + (\omega \, \mathbf{a}(\omega, t) \, \Gamma \otimes (\mathbf{B} + \mathbf{G}\Omega]) + \mathbf{a}(\omega, t) \otimes (\mathbf{K} + j\mathbf{K}\eta_h)\Big) \, \hat{\mathbf{q}} + \\ + \mathbf{a}(\omega, t) \otimes \mathbf{I}_N \hat{\mathbf{n}} \, (\hat{\mathbf{q}}) - \mathbf{a}(\omega, t) \otimes \mathbf{I}_N \hat{\mathbf{f}} - \mathbf{R} \, (\hat{\mathbf{q}}, \omega, H) = \boldsymbol{0} \end{aligned} \tag{4.10}$$

Using the Fourier expansion one can only approximate periodical functions, thus, Equation 4.10 is equal to zero adding the residual term $\mathbf{R} \, (\hat{\mathbf{q}}, \omega, H)$, expressed in the Fourier form (Fourier approximation residual).
In Equations 4.1 and 4.10 we consider the hypothesis of nonlinear force $\mathbf{f_{nl}}(\mathbf{q}_f, t)$ only dependent on the displacements field $\mathbf{q}_f(t)$ and the time t:

$$\mathbf{f_{nl}} = \mathcal{F}(\mathbf{q}_f, t) \rightarrow \hat{\mathbf{n}} = \mathcal{G} \, (\hat{\mathbf{q}}) \tag{4.11}$$

Developing Equation 4.10:

$$\begin{aligned} \mathbf{R} \, (\hat{\mathbf{q}}, \omega, H) = \mathbf{a}(\omega, t) \Bigg\{ \Big[\omega^2 (\Gamma_{\cdot}^{\mathbf{2}} \otimes \mathbf{M}) + \omega \, (\Gamma \otimes (\mathbf{B} + \mathbf{G}\Omega)) + (\Gamma^0 \otimes (\mathbf{K} + j\mathbf{K}\eta_h))\Big] \, \hat{\mathbf{q}} + \\ + \Gamma^0 \otimes \hat{\mathbf{n}} \, (\hat{\mathbf{q}}) - \Gamma^0 \otimes \hat{\mathbf{f}} \Bigg\} \end{aligned} \tag{4.12}$$

The Galerkin method assumes that the Fourier coefficients of the residual $\mathbf{R} \, (\hat{\mathbf{q}}, \omega, H)$ vanish up, balancing the harmonic terms:

$$\begin{aligned} \mathbf{R} \, (\hat{\mathbf{q}}, \omega, H) = \Big[\omega^2 (\Gamma_{\cdot}^{\mathbf{2}} \otimes \mathbf{M}) + \omega \, (\Gamma \otimes (\mathbf{B} + \mathbf{G}\Omega)) + (\Gamma^0 \otimes (\mathbf{K} + j\mathbf{K}\eta_h))\Big] \, \hat{\mathbf{q}} + \\ + \Gamma^0 \otimes \hat{\mathbf{n}} \, (\hat{\mathbf{q}}) - \Gamma^0 \otimes \hat{\mathbf{f}} = \boldsymbol{0} \end{aligned} \tag{4.13}$$

In a short form :

$$\mathbf{R} \, (\hat{\mathbf{q}}, \omega, H) = \boldsymbol{\Xi}_h(\omega, H) \hat{\mathbf{q}} + \hat{\mathbf{N}}_h \, (\hat{\mathbf{q}}) - \hat{\mathbf{F}}_h = \boldsymbol{0} \tag{4.14}$$

With:

$$\boldsymbol{\Xi}_h(\omega, H) = \Big[\omega^2 (\Gamma_{\cdot}^{\mathbf{2}} \otimes \mathbf{M}) + \omega \, (\Gamma \otimes (\mathbf{B} + \mathbf{G}\Omega)) + (\Gamma^0 \otimes (\mathbf{K} + j\mathbf{K}\eta_h))\Big] \tag{4.15}$$

$$\hat{\mathbf{N}}_h = \Gamma^0 \otimes \hat{\mathbf{n}}\left(\hat{\mathbf{q}}\right) \tag{4.16}$$

$$\hat{\mathbf{F}}_h = \Gamma^0 \otimes \hat{\mathbf{f}} \tag{4.17}$$

Equation 4.14 is the one to solve and represents the Problem 4.1 expressed in the HB formulation. The Galerkin method allowed to move from a differential problem to an algebraic one. Equation 4.14 is still nonlinear and the solution of this equation is not trivial, an iterative method for the evaluation of the response must be employed.

3 Nonlinear force treatment

Once Equation 4.14 has been expressed in the HB formulation, it is important to compute the nonlinear terms. Usually, the nonlinear forces are expressed as mathematical functions in the time domain. A classical example of nonlinear force is the Duffing spring [Kovacic, 2011]:

$$f_{nl}(q(t)) = k_{nl} \cdot q(t)^3 \tag{4.18}$$

Where the k_{nl} represents the *nonlinear stiffness* of the oscillator. On the contrary, during the solution of a problem expressed in the HB formulation, the generalised displacements are treated in the frequency domain. It is thus necessary to compute the nonlinear force in the frequency domain.
Classically, one can transform the analytic form of the nonlinear force from the time domain to the frequency domain using the Fourier expansions. Nevertheless, this approach is valid only for elementary forms of nonlinearity (e.g. polynomial, Duffing, etc.), its generalisation is not trivial.
A more general approach to evaluate the nonlinear force is the AFT algorithm, allowing to evaluate the nonlinear force in the time domain with no need to express it in the frequency domain. This approach is flexible and the introduction of new sources of nonlinearity is direct.

3.1 Alternating frequency-time (AFT) algorithm

The AFT algorithm allows to transform the generalised displacements $\hat{\mathbf{q}}$ from the frequency to time domain using an inverse Fourier transformation *Inverse Fast Fourier Transformation* (iFFT). In this way, the nonlinear force, which is generally expressed mathematically in the time domain, can be evaluated directly. The nonlinear force and its derivatives are finally approximated in the frequency domain using a FFT [Cameron,

1989; Krack, 2019]. The nonlinear force so calculated can be used in the dynamical Equation 4.14. With this approach, the introduction of new sources of nonlinearities is direct because there is no need to express them analytically in the frequency domain. A schematic representation of this algorithm is reported in Figure 6.5.

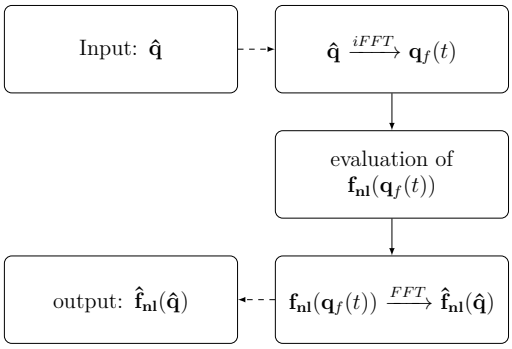

Figure 4.2: AFT cycle algorithm.

The AFT algorithm is applied on a simple problem with nonlinear contact in Figure 4.3 to show how it works practically. The displacements and the nonlinear force are approximated with the first harmonic only.

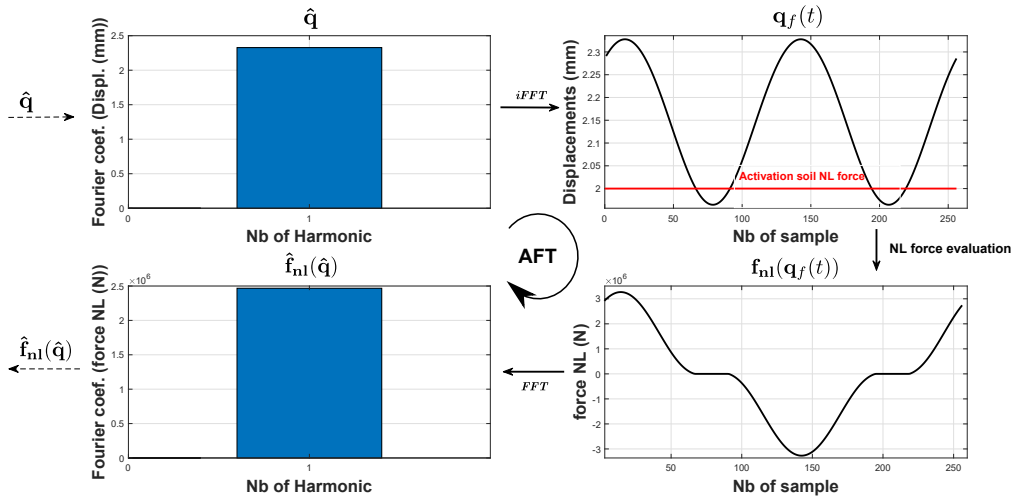

Figure 4.3: AFT approximation on the first (fundamental) harmonic for a nonlinear contact problem.

3.2 Rotor-stator contact: the full annular rub case

In the AFT algorithm, it is essential to have a mathematical representation of the nonlinear terms in the time domain. Since we are mainly interested in the rotor-stator

interaction, in this section we describe the mathematical model employed to simulate this type of nonlinear effect.

As already seen in Section 4.3.2, multiple forms of rotor-stator interactions can be established in rotating machines, in this work we are interested in the rotor-stator contact established between smooth surfaces such as shaft-support. This phenomenon can be described taking into account a node of the model representing the section of the shaft which is in relation with a certain shaft supports (see Figure 4.4). The displacements of this node can be described in the plan perpendicular to the rotating axis as:

$$\mathbf{q}_f(t) = \Big[q_1, q_2\Big]^T_{\mathcal{R}_f} \tag{4.19}$$

Thus:

$$\mathbf{q}_f(t) = q_1\vec{\mathbf{e}_1} + q_2\vec{\mathbf{e}_2} \tag{4.20}$$

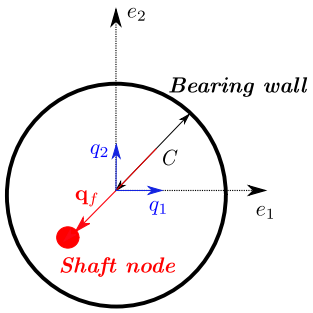

Figure 4.4: Rotor-stator interaction.

Where q_1 represents the displacements along the direction e_1 and q_2 the displacements along e_2. As shown in Figure 4.4, the absolute value of the displacements of the rotor in the displacements plan is Q:

$$Q = |\mathbf{q}_f| = \sqrt{q_1^2 + q_2^2} \tag{4.21}$$

thus:

$$\vec{\mathbf{n}} = \frac{\mathbf{q}_f}{Q} \qquad \rightarrow \qquad \vec{\mathbf{n}_1} = \frac{q_1\vec{\mathbf{e}_1}}{Q} \qquad and \qquad \vec{\mathbf{n}_2} = \frac{q_2\vec{\mathbf{e}_2}}{Q} \tag{4.22}$$

The contact condition depends on the value of Q(t):

$$\begin{cases} f_{nl}(\mathbf{q}_f(t)) = K_c \cdot (Q(t) - C) & if \quad Q(t) \geq C \\ f_{nl}(\mathbf{q}_f(t)) = 0 & if \quad Q(t) < C \end{cases} \tag{4.23}$$

Where C represents the clearance (max. displacement allowed) and K_c the contact stiffness.

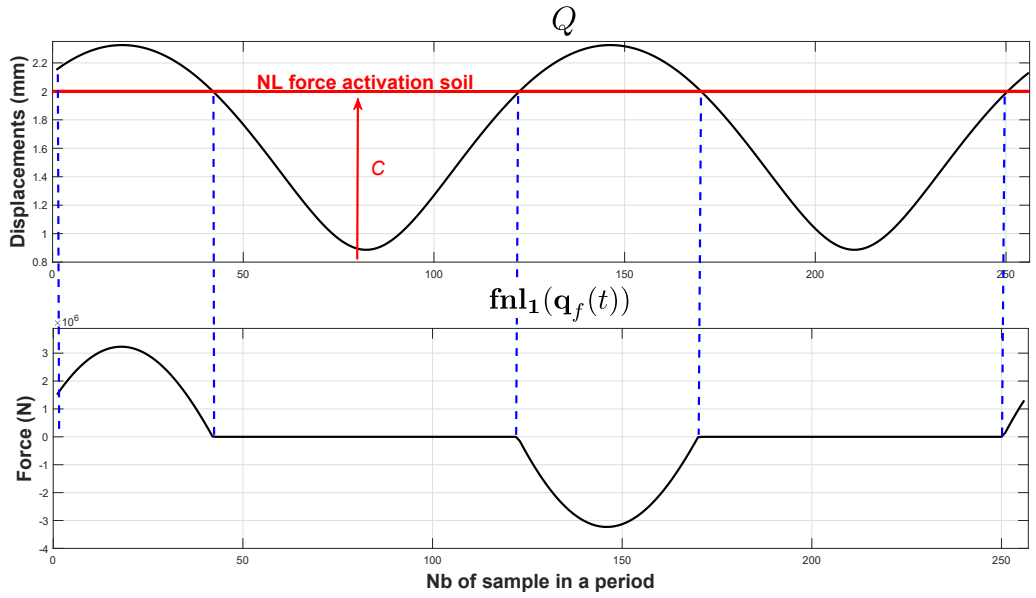

Figure 4.5: Example of nonlinear force controlled by the radial displacements Q.

Developing the expressions of the nonlinear force in the vectorial form:

$$\mathbf{f_{nl}}_1(\mathbf{q}_f(t)) = f_{nl} \cdot \vec{\mathbf{n}_1} = f_{nl} \cdot \frac{q_1 \vec{\mathbf{e}_1}}{Q} \qquad and \qquad \mathbf{f_{nl}}_2(\mathbf{q}_f(t)) = f_{nl} \cdot \vec{\mathbf{n}_2} = f_{nl} \cdot \frac{q_2 \vec{\mathbf{e}_2}}{Q} \quad (4.24)$$

Equations 4.24 express the value of nonlinear force along directions $\mathbf{n}_1$ and $\mathbf{n}_2$. As example, in Figure 4.5 is reported the radial displacement Q and the nonlinear force generated in a simple nonlinear rotor along the direction $\mathbf{n}_1$. Observing Figure 4.5, it is interesting to notice that the nonlinear force is not equal to zero only if the radial displacements Q are higher than the clearance C.

It is now necessary to introduce the Jacobian matrix of the nonlinear force $\frac{\partial \mathbf{f_{nl}}}{\partial \mathbf{q}_f}$ which is necessary to evaluate the Jacobian matrix of the residual $\mathbf{R}(\hat{\mathbf{q}}, \omega, H)$ demanded for the Newton-Raphson algorithm. Assuming that the nonlinear force is strictly dependent on the displacements $\mathbf{q}_f(t)$ and not on the excitation frequency ω, the Jacobian matrix of the nonlinear force is given in Equation 4.25.

$$\frac{\partial \mathbf{f_{nl}}}{\partial \mathbf{q}_f} = \begin{bmatrix} \frac{\partial \mathbf{f}_{nl1}}{\partial \boldsymbol{q}_{f1}} & \frac{\partial \mathbf{f}_{nl1}}{\partial \boldsymbol{q}_{f2}} & \frac{\partial \mathbf{f}_{nl2}}{\partial \boldsymbol{q}_{f1}} & \frac{\partial \mathbf{f}_{nl2}}{\partial \boldsymbol{q}_{f2}} \end{bmatrix} \quad (4.25)$$

This assumption is nevertheless too rough for sources of nonlinearities dependent on the excitation frequency (e.g. SFDs), in these cases the dependency of the nonlinear terms on the frequency has to be taken into account too.
Nowadays, it is common in large finite element models to use rigid or flexible connection elements to relate the displacements of any node of an annular section (e.g. see [De Gae-

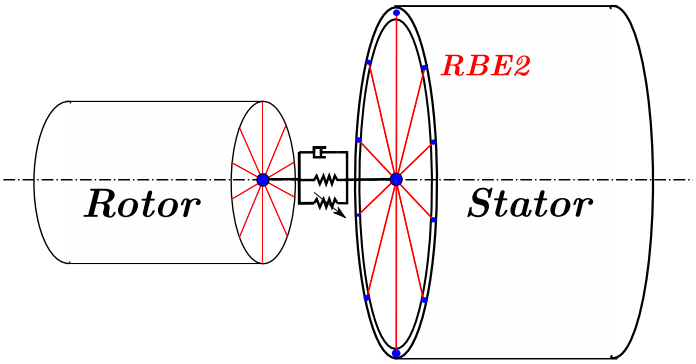

Figure 4.6: Roto-stator connection in whole engine dynamics.

tano, 2014]) with only one independent grid point positioned in the center of the annular section, as shown in Figure 4.6, the nodes of the annular sections are now dependent on the motion of the central grid point generated. In the FE software MSC NASTRAN, this type of connection can be generated using RBE2 or RBE3 elements [MSC, 2018]. It is important to keep in mind that the introduction of this sort of elements make the considered annular section stiffer. Once this rigid connection is generated, the shaft and the independent grid node of the annular section of the stator can be connected with the desired mechanical elements (see Figure 4.6), in this case a lumped stiffness, a lumped damping and a generic form of nonlinearity are represented.

To also take into account the stator's displacements into the model presented in Equation 4.23, the generalised displacements field becomes:

$$\mathbf{q}_f(t) = \left[q_{1r} - q_{1s}, q_{2r} - q_{2s}\right]^T_{\mathcal{R}_f} \tag{4.26}$$

The new generalised displacements are obtained from the difference $(q_{1r} - q_{1s})$ on the direction $\mathbf{n}_1$ and $(q_{2r} - q_{2s})$ on the direction $\mathbf{n}_2$, where the r index stands for rotor and s index stands for stator. These generalised DOFs represent the gap between the rotor and the stator projected on the direction $\mathbf{n}_1$ and $\mathbf{n}_2$.

To conclude, it is important to state that this model is particularly adapted to simulate the full annular rub phenomenon since the nonlinear force acts only in the direction perpendicular to the contact point. The proposed model is not adapted to simulate rotor-stator interaction in which sliding contact appears (e.g. *dry whip* phenomenon [Ehrich, 1992]) since the tangential sliding force, generated by the friction due to the sliding motion of the shaft on the contact surface is not taken into account in this work.
It is possible to take into account the friction force in full annular rub too as shown by Pelentan [Peletan, 2012b; Peletan, 2014]. Nevertheless, he concludes that the friction force can be neglected in full annular rub. This assumption is adopted as well in the

rotordynamics module of the FE software MSC NASTRAN with the nonlinear contact associated to the command NLRGAP [MSC, 2018]. On the contrary, the tangential force is fundamental and non-negligible in sliding or non-regular form of contacts.

4 Continuation algorithms

The solution of Equation 4.14 cannot be evaluated in a mathematical closed form, since the nonlinear force is dependent on displacements $\mathbf{q}_f$ which is unknown. To solve this nonlinear problem, a variant of the Newton-Raphson algorithm [Ypma, 1995] known as *continuation algorithm* is adopted. This algorithm introduces a *prediction step* into a classical Newton-Raphson loop, making it more efficient by providing an initial guess aiming to improve the convergence of the Newton-Raphson loop [Seydel, 2009]. After the prediction step, the Newton-Raphson algorithm is applied to approximate the actual solution, this second step is commonly called *correction*. The prediction-correction loops are applied continuously until the approximated solution is identified over the whole interesting frequency range.
In Figure 4.7a is reported a flux diagram representing the main elements of the continuation path algorithm in the HB framework. In relation to the flux diagram, a graphical example of the algorithm is applied on a Duffing oscillator response to highlight the phases of prediction and correction (see Figure 4.7b).

For clarity, in the following sections, the Fourier's coefficients of the displacements of the system $\hat{\mathbf{q}}_h$ approximated with the first h harmonics at a specific frequency ω is defined by the vector $\hat{\mathbf{y}}_h$:

$$\hat{\mathbf{y}}_h = [\hat{\mathbf{q}}_h, \omega]^T \tag{4.27}$$

4.1 The Newton-Raphson method

The Newton-Raphson algorithm can be applied in the HB framework to find the vetor $\hat{\mathbf{y}}_h$ that cancels the module of the residual function $\mathbf{R}(\hat{\mathbf{y}}_h)$:

$$|\mathbf{R}\left(\hat{\mathbf{y}}_h\right)| \approx \boldsymbol{0} \tag{4.28}$$

Since it is theoretically impossible to make this function equal to zero, one can state that the Newton-Raphson algorithm *has converged* when the module of the residual function is smaller than a specified value ϵ:

$$|\mathbf{R}\left(\hat{\mathbf{y}}_h\right)| < \epsilon \tag{4.29}$$

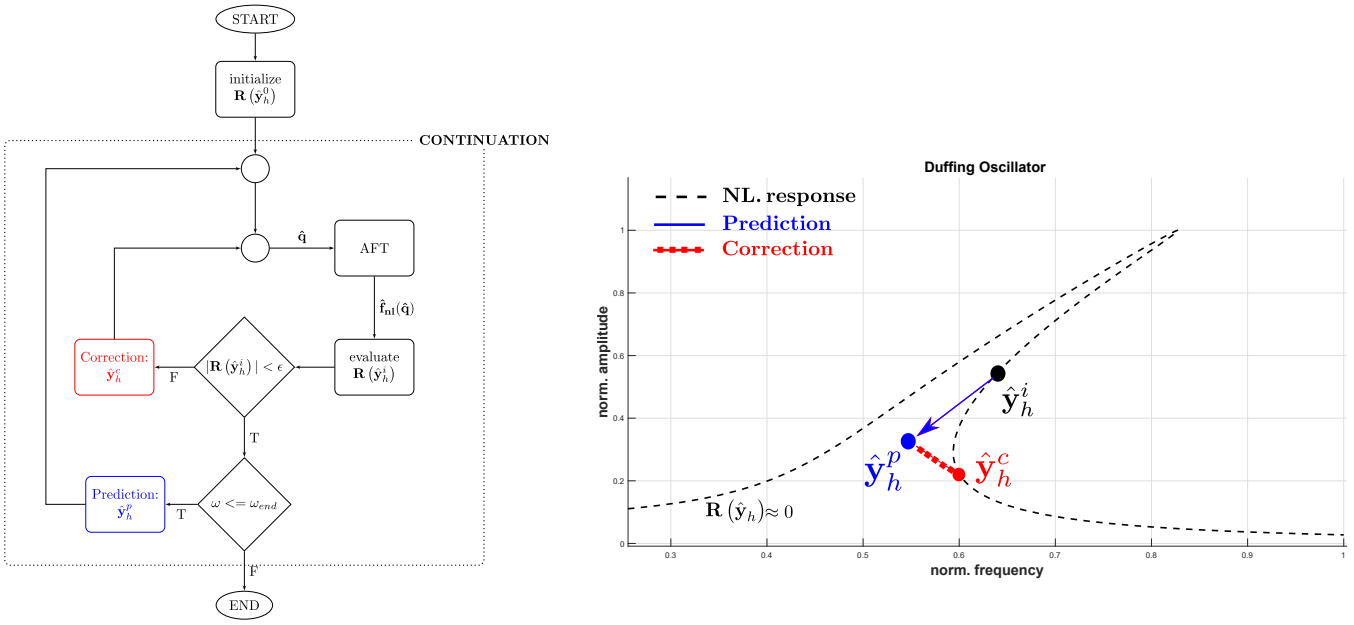

(a) Continuation algorithm applied to the Harmonic Balance.

(b) Duffing's oscillator response.

Figure 4.7: Application of the HB on a Duffing's oscillator.

The Newton-Raphson method is based on the expansion in Taylor series first order approximation of the residual function around a current estimation $\hat{\mathbf{y}}_h^i$:

$$\mathbf{R}(\hat{\mathbf{y}}_h^{i+1}) \approx \mathbf{R}(\hat{\mathbf{y}}_h^i) + \left.\frac{\partial \mathbf{R}}{\partial \hat{\mathbf{y}}_h}\right|_{\hat{\mathbf{y}}_h^i} \left(\hat{\mathbf{y}}_h^{i+1} - \hat{\mathbf{y}}_h^i\right) = \boldsymbol{0} \tag{4.30}$$

Thus:

$$\left.\frac{\partial \mathbf{R}}{\partial \hat{\mathbf{y}}_h}\right|_{\hat{\mathbf{y}}_h^i} \left(\hat{\mathbf{y}}_h^{i+1} - \hat{\mathbf{y}}_h^i\right) = -\mathbf{R}(\hat{\mathbf{y}}_h^i) \tag{4.31}$$

The algorithm must be initialised with an initial guess in $\mathbf{R}(\hat{\mathbf{y}}_h^0)$. The convergence of the algorithm depends on the choice of the initial guess: the closer to the actual solution is the initial guess, the faster the algorithm converges. On the contrary, if the initial guess is not close enough to the actual solution or badly chosen, the algorithm could not converge. As shown in Equation 4.31, it is necessary to evaluate the Jacobian matrix $\left.\frac{\partial \mathbf{R}}{\partial \hat{\mathbf{y}}_h}\right|_{\hat{\mathbf{y}}_h^i}$ at any step of the solution. The evaluation of the Jacobian matrix can be performed analytically or through the finite differences. The first approach is faster and more efficient than the second one, but the finite differences approach doesn't demand to express analytically the Jacobian matrix, which is an advantage if the source of nonlinearity is mathematically complex. The Jacobian matrix contains the directions of minimisation or maximisation allowing the algorithm to reach the convergence, for this reason it is defined as a *gradient based* method [Smale, 1986; Ozban, 2004]. The two discussed variants are known as *Full-*

Newton methods. A cheaper alternative are *Quasi-Newton* methods approximating the Jacobian matrix or using the same Jacobian matrix for multiple iterations ([Gill, 1972]).

4.2 The Jacobian Matrix: analytical formulation in rotordynamics

As seen in the last section, the Jacobian matrix has a fundamental role in gradient based methods. In this section we want to express analytically the Jacobian matrix of the residual function for the problem of rotordyanmics under exam and taking into account an unbalance excitation. The Jacobian matrix of the residual function is defined as:

$$\frac{\partial \mathbf{R}}{\partial \hat{\mathbf{y}}_h}(\hat{\mathbf{y}}_h) = \frac{\partial \mathbf{R}}{\partial \hat{\mathbf{q}}_h}\frac{\partial \hat{\mathbf{q}}_h}{\partial \hat{\mathbf{y}}_h} + \frac{\partial \mathbf{R}}{\partial \omega}\frac{\partial \omega}{\partial \hat{\mathbf{y}}_h} \tag{4.32}$$

Thus:

$$\frac{\partial \mathbf{R}}{\partial \hat{\mathbf{y}}_h}(\hat{\mathbf{y}}_h) = \left(\boldsymbol{\Xi}_h(\omega, H) + \frac{\partial \hat{\mathbf{N}}_h(\hat{\mathbf{q}}_h)}{\partial \hat{\mathbf{q}}_h} - \frac{\partial \hat{\mathbf{F}}_h(\omega)}{\partial \hat{\mathbf{q}}_h}\right)\frac{\partial \hat{\mathbf{q}}_h}{\partial \hat{\mathbf{y}}_h} + \left(\frac{\partial \boldsymbol{\Xi}_h(\omega,H)}{\partial \omega}\hat{\mathbf{q}}_h + \frac{\partial \hat{\mathbf{N}}_h(\hat{\mathbf{q}}_h)}{\partial \omega} - \frac{\partial \hat{\mathbf{F}}_h(\omega)}{\partial \omega}\right)\frac{\partial \omega}{\partial \hat{\mathbf{y}}_h} \tag{4.33}$$

Since the unbalance excitation $\hat{\mathbf{F}}_h(\omega)$ (see eq. 4.1) is purely frequency dependent, its derivative with respect to the generalised displacements $\hat{\mathbf{q}}_h$ is equal to zero:

$$\frac{\partial \hat{\mathbf{F}}_h(\omega)}{\partial \hat{\mathbf{q}}_h} = \boldsymbol{0} \tag{4.34}$$

As well, since the nonlinear force $\hat{\mathbf{N}}_h$ is purely dependent on the displacements $\hat{\mathbf{q}}_h$, it is possible to consider its derivative with respect to the frequency ω equal to zero.

$$\frac{\partial \hat{\mathbf{N}}_h(\omega)}{\partial \omega} = \boldsymbol{0} \tag{4.35}$$

In frequency dependent nonlinear loadings, this last derivative must not be neglected. Finally Equation 4.33 is written:

$$\frac{\partial \mathbf{R}}{\partial \hat{\mathbf{y}}_h}(\hat{\mathbf{y}}_h) = \left(\boldsymbol{\Xi}_h(\omega, H) + \frac{\partial \hat{\mathbf{N}}_h(\hat{\mathbf{q}}_h)}{\partial \hat{\mathbf{q}}_h}\right)\frac{\partial \hat{\mathbf{q}}_h}{\partial \hat{\mathbf{y}}_h} + \left(\frac{\partial \boldsymbol{\Xi}_h(\omega,H)}{\partial \omega}\cdot\hat{\mathbf{q}}_h - \frac{\partial \hat{\mathbf{F}}_h(\omega)}{\partial \omega}\right)\frac{\partial \omega}{\partial \hat{\mathbf{y}}_h} \tag{4.36}$$

With:

$$\begin{aligned}\frac{\partial \boldsymbol{\Xi}_h(\omega, H)}{\partial \omega} = \frac{\partial}{\partial \omega}\left[\omega^2(\Gamma_{\cdot}^{\mathbf{2}} \otimes \mathbf{M}) + \omega\left(\Gamma \otimes (\mathbf{B} + \mathbf{G}\cdot\Omega)\right) + (\Gamma^0 \otimes (\mathbf{K} + j\mathbf{K}\eta_h))\right] = \\ = \left[-2\omega\cdot(\Gamma_{\cdot}^2 \otimes \mathbf{M}) + \Gamma \otimes [\mathbf{B} + \mathbf{G}\Omega(\omega)]\right]\end{aligned} \tag{4.37}$$

Considering the unbalance excitation:

$$\frac{\partial \hat{\mathbf{F}}_h(\omega)}{\partial \omega} = 2\,\omega\, m\, e\hat{\mathbf{F}}_h \tag{4.38}$$

The Jacobian matrix proposed in Equation 4.37 is valid for any problem of rotordyanmics, with one or multiple punctual nonlinear forces strictly dependent on the displacements $\hat{\mathbf{q}}_h$ and under a synchronous excitation.

4.3 The Jacobian Matrix: finite differences formulation

Sometimes, the Jacobian matrix can be tedious to evaluate analytically, in small problems a valid option to evaluate numerically the Jacobian matrix in any gradient-based algorithm is the approximation by finite differences. This approach doesn't demand to express analytically the Jacobian matrix, making the algorithm more flexible in relation to the variation of the form of nonlinearity. Considering an initial guess $\hat{\mathbf{y}}_h^0$, one can define the perturbation $d\hat{\mathbf{y}}_h$ as:

$$d\hat{\mathbf{y}}_h = \epsilon \cdot \hat{\mathbf{y}}_h^0; \tag{4.39}$$

With ϵ defined as little as possible. It is then possible to evaluate a perturbed status following the forward or backward finite differences approximation, respectively:

$$\hat{\mathbf{y}}_h^F = \hat{\mathbf{y}}_h^0 + d\hat{\mathbf{y}}_h \;\; (Forward); \tag{4.40}$$

$$\hat{\mathbf{y}}_h^B = \hat{\mathbf{y}}_h^0 - d\hat{\mathbf{y}}_h \;\; (Backward); \tag{4.41}$$

From these status is possible to evaluate the residuals vectors $\mathbf{R}(\hat{\mathbf{y}}_h^0)$, $\mathbf{R}(\hat{\mathbf{y}}_h^F)$ and $\mathbf{R}(\hat{\mathbf{y}}_h^B)$. The Jacobian in $\hat{\mathbf{y}}_h^0$ is then numerically evaluated as:

$$\frac{\partial \mathbf{R}}{\partial \hat{\mathbf{y}}_h} = \frac{\mathbf{R}(\hat{\mathbf{y}}_h^F) - \mathbf{R}(\hat{\mathbf{y}}_h^0)}{d\hat{\mathbf{y}}_h} \;\; (Forward) \tag{4.42}$$

$$\frac{\partial \mathbf{R}}{\partial \hat{\mathbf{y}}_h} = \frac{\mathbf{R}(\hat{\mathbf{y}}_h^0) - \mathbf{R}(\hat{\mathbf{y}}_h^B)}{d\hat{\mathbf{y}}_h} \;\; (Backward) \tag{4.43}$$

Another classical approach in finite differences approximation is the central finite differences approximation. In this case, the perturbations defined in Equations 4.40 and 4.41 are both employed to define a smaller perturbation:

$$d\hat{\mathbf{y}}_h^C = (\hat{\mathbf{y}}_h^F - \hat{\mathbf{y}}_h^B)/2 \tag{4.44}$$

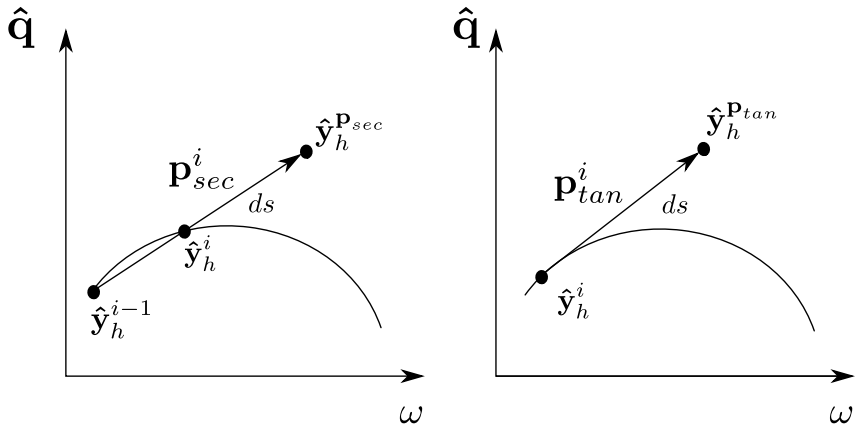

Figure 4.8: Secant(a) and Tangent(b) prediction strategies.

The Jacobian matrix is then evaluated as:

$$\frac{\partial \mathbf{R}}{\partial \hat{\mathbf{y}}_h} = \frac{(\mathbf{R}(\hat{\mathbf{y}}_h^F) - \mathbf{R}(\hat{\mathbf{y}}_h^B))}{2d\hat{\mathbf{y}}_h^c} \tag{4.45}$$

The method of the finite differences is always less efficient then the analytical representation of the Jacobian. First of all this approach is more time demanding because it needs several iterations for the evaluation of the integral Jacobian matrix. Moreover, only an approximation of the Jacobian matrix can be evaluated, introducing in this way a systematic error. The only advantage of this method is that the mathematical representation of the Jacobian matrix is not necessary.
If the residual function is smooth enough in a particular region, the Jacobian matrix doesn't change much. In this situation, to make this approach cheaper in terms of computational time, it is possible to re-use the same Jacobian matrix for several iterations. Nevertheless, when the Jacobian is not re-evaluated at any iteration, a larger number of iterations has to be expected to reach the convergence soil.

4.4 Parametric solver: prediction algorithms

The prediction step is employed in continuation path algorithm to find a well positioned initial guess $\hat{\mathbf{y}}_h^p$ allowing to improve the Newton-Raphson algorithm convergence. Multiple prediction strategies are described in literature [Nayfeh, 2008a; Seydel, 2009], the most diffused ones are the *secant* (see Figure 4.8a) and the *tangent* (see Figure 4.8b) predictions [Peletan, 2012a; Detroux, 2015], which are adopted in this work as well. Other predictions strategies can be cited: *polynomial* and *Lagrange* prediction [Jaumouille, 2010; Detroux, 2015].

4.4.1 Secant prediction strategy

The secant predictor uses the secant line passing through the last two evaluated points of the curve. The secant direction is defined by the following equation:

$$\mathbf{p}_{sec}^{i} = \frac{(\hat{\mathbf{y}}_h^i - \hat{\mathbf{y}}_h^{i-1})}{|(\hat{\mathbf{y}}_h^i - \hat{\mathbf{y}}_h^{i-1}|} \tag{4.46}$$

The vector $\mathbf{p}_{sec}^{i}$ represents the direction of the secant passing through the points $\hat{\mathbf{y}}_h^i$ and $\hat{\mathbf{y}}_h^{i-1}$. The initial guess is finally written as:

$$\hat{\mathbf{y}}_h^{\mathbf{p}_{sec}} = \hat{\mathbf{y}}_h^i + \Delta \cdot ds \cdot \mathbf{p}_{sec}^{i} \tag{4.47}$$

where Δ can be +1 or -1 to move forward or backward on the curve and ds is employed to measure the step-size. This prediction strategy needs at least 2 points to be used, thus for the first and second points of the path, an initialisation is needed if this strategy has to be used. A common initialisation strategy is to start with the linear response in the first and second frequency points: $\hat{\mathbf{y}}_h^0 = \hat{\mathbf{y}}_h^{lin.}(\omega_0)$ and $\hat{\mathbf{y}}_h^1 = \hat{\mathbf{y}}_h^{lin.}(\omega_1)$.

4.4.2 Tangent prediction strategy

The tangent prediction strategy uses the Jacobian matrix to identify the tangent line to the curve in the last evaluated point $\hat{\mathbf{y}}_h^i$. Considering the first order approximation of the Taylor series expansion of the residual function $\mathbf{R}(\hat{\mathbf{y}}_h^i)$ around the point $\hat{\mathbf{y}}_h^i$:

$$\mathbf{R}(\hat{\mathbf{y}}_h^{i+1}) \approx \mathbf{R}(\hat{\mathbf{y}}_h^i) + \left.\frac{\partial \mathbf{R}}{\partial \hat{\mathbf{y}}_h}\right|_{\hat{\mathbf{y}}_h^i} \left(\hat{\mathbf{y}}_h^{i+1} - \hat{\mathbf{y}}_h^i\right) = \boldsymbol{0} \tag{4.48}$$

Since the residual function $\mathbf{R}(\hat{\mathbf{y}}_h^i)$ has to be almost equal to zero: $\mathbf{R}(\hat{\mathbf{y}}_h^i) \approx 0$, Equation 4.48 becomes:

$$\left.\frac{\partial \mathbf{R}}{\partial \hat{\mathbf{y}}_h}\right|_{\hat{\mathbf{y}}_h^i} \left(\hat{\mathbf{y}}_h^{i+1} - \hat{\mathbf{y}}_h^i\right) = \boldsymbol{0} \rightarrow \left.\frac{\partial \mathbf{R}}{\partial \hat{\mathbf{y}}_h}\right|_{\hat{\mathbf{y}}_h^i} \mathbf{p}_{tan}^{i} = \boldsymbol{0} \tag{4.49}$$

With $\mathbf{p}_{tan}^{i} = (\hat{\mathbf{y}}_h^{i+1} - \hat{\mathbf{y}}_h^i)$ representing the tangent vector in the point $\hat{\mathbf{y}}_h^i$. This equation only constrains the tangent direction but not the tangent vector length. The system in Equation 4.49 is under-determined. Another equation have to be added in order to fix the tangent vector length, one can write generally:

$$\mathbf{x}^T \cdot \mathbf{p}_{tan}^{i} \neq \boldsymbol{0} \tag{4.50}$$

With the arbitrary vector $\mathbf{x}^T$. One possibility is to use the vector tangent to the curve in the last evaluated point $\mathbf{p}_{tan}^{i-1}$. Peletan [Peletan, 2012a] and Kuznetsov [Kuznetsov, 1998] propose this approach, assuming that two sequential tangent vectors are probably not

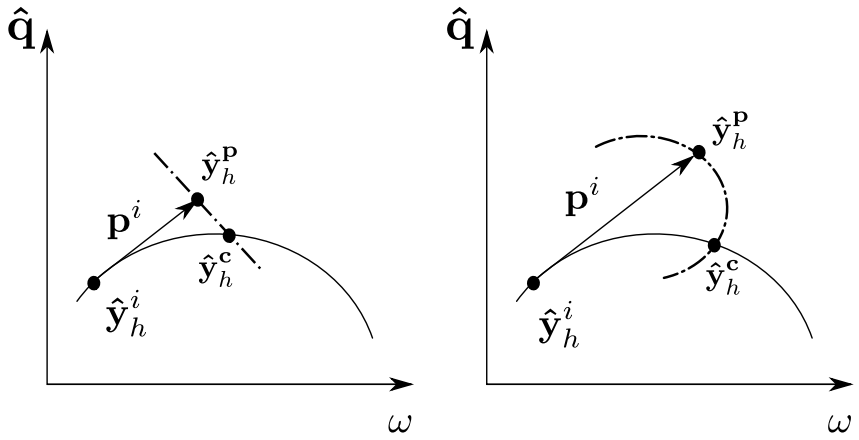

Figure 4.9: Orthogonal(a) and arch-length(b) correction strategies.

perpendicular to each other:

$$\mathbf{p}_{tan}^{i-1} \cdot \mathbf{p}_{tan}^{i} = 1 \tag{4.51}$$

The system to solve is then:

$$\begin{cases} \left.\frac{d\mathbf{R}}{d\hat{\mathbf{y}}_h}\right|_{\hat{\mathbf{y}}_h^i} \mathbf{p}_{tan}^{i} = \boldsymbol{0} \\ \mathbf{p}_{tan}^{i-1} \cdot \mathbf{p}_{tan}^{i} = 1 \end{cases} \tag{4.52}$$

Numerically:

$$\begin{bmatrix} \left.\frac{d\mathbf{R}}{d\hat{\mathbf{y}}_h}\right|_{\hat{\mathbf{y}}_h^i} \\ \mathbf{p}_{tan}^{i-1} \end{bmatrix} \cdot \mathbf{p}_{tan}^{i} = \begin{pmatrix} \boldsymbol{0} \\ 1 \end{pmatrix} \tag{4.53}$$

Another common choice for the arbitrary vector $\mathbf{x}^T$ is to use a unitary vector with all elements equal to zero except the one corresponding to the coordinate of $\hat{\mathbf{y}}_h$ which varying the most, as shown by [Seydel, 2009]. Equation 4.53 returns $\mathbf{p}_{tan}^{i}$. The prediction can be finally done as:

$$\hat{\mathbf{y}}_h^{\mathbf{p}_{tan}} = \hat{\mathbf{y}}_h^i + \Delta \cdot ds \cdot \mathbf{p}_{tan}^{i} \tag{4.54}$$

Differently from the secant prediction strategy, this one only needs one evaluated point to be initialised. A common initialisation strategy is to start with the linear response in the first frequency point: $\hat{\mathbf{y}}_h^0 = \hat{\mathbf{y}}_h^{linear}(\omega_0)$.

4.5 Parametric solver: correction algorithms

After the prediction of a good initial guess, the Newton-Raphson algorithm is employed to find the approximated solution. As already mentioned, the Newton-Raphson algorithm in the case of the HB applications, allows to approximate the solution of Equation 4.14. One can notice that the residual function in Equation 4.14 has the same dimension as the displacements in Fourier space $dim(\hat{\mathbf{q}})$, but the generic state s of the system is defined

by the vector $\hat{\mathbf{q}}_h^s$ and the frequency ω^s. The Newton-Raphson problem is thus underdetermined ($dim(\hat{\mathbf{q}}) + 1$ unknowns and only $dim(\hat{\mathbf{q}})$ equations), an additive equation $\mathbf{C}(\hat{\mathbf{y}}_h)$ has to be introduced to solve it:

$$\mathbf{R}_{par}(\hat{\mathbf{y}}_h) = \begin{bmatrix} \mathbf{R}^T(\hat{\mathbf{y}}_h) & \mathbf{C}(\hat{\mathbf{y}}_h) \end{bmatrix}^T \approx \mathbf{0} \tag{4.55}$$

The additive equation forces the Newton-Raphson algorithm to find a solution on a specific hyper-surface or hyper-curve, this type of Newton-Raphson algorithm is known as well as *Parametrised Newton-Raphson* as reported by Ajjarapu et al. [Ajjarapu, 1992]. The Jacobian matrix in the parameterised framework can be evaluated directly by:

$$\frac{\partial \mathbf{R}_{par}(\hat{\mathbf{y}}_h)}{\partial(\hat{\mathbf{y}}_h)} = \begin{bmatrix} \frac{\partial \mathbf{R}(\hat{\mathbf{y}}_h)}{\partial(\hat{\mathbf{y}}_h)} & \frac{\partial \mathbf{C}(\hat{\mathbf{y}}_h)}{\partial(\hat{\mathbf{y}}_h)} \end{bmatrix}^T \tag{4.56}$$

Multiple parametrisation choices are described in literature and they can influence the convergence history of the algorithm, we can cite the *orthogonal* corrector and the arc-length corrector [Nayfeh, 2008b], both illustrated in Figure 4.9. Other variants are popular in literature too: the fixed frequency Newton-Raphson loop or the Moore-Penrose correction [Jaumouille, 2010]) but in this work only the first two are directly employed.

4.5.1 Orthogonal correction

The orthogonal correction strategy imposes that the solution of the Newton-Raphson loop lies on the hyper-plan defined by the predicted point $\hat{\mathbf{y}}_h^p$ and the direction orthogonal to the prediction direction $\mathbf{p}^i$ (secant or tangent):

$$\mathbf{C}(\hat{\mathbf{y}}_h) = \mathbf{p}^i \cdot (\hat{\mathbf{y}}_h - \hat{\mathbf{y}}_h^p) = \mathbf{0} \tag{4.57}$$

4.5.2 Arch-length correction

The arch-length correction is one of the most diffused correction strategy. As suggested by the name, this correction strategy constraints the solver to find the solution on the arch of an hyper-sphere, centered in the predicted point $\hat{\mathbf{y}}_h^p$ and having as ray the step-size ds:

$$\mathbf{C}(\hat{\mathbf{y}}_h) = (\hat{\mathbf{y}}_h - \hat{\mathbf{y}}_h^p)^T(\hat{\mathbf{y}}_h - \hat{\mathbf{y}}_h^p) - ds^2 = \mathbf{0} \tag{4.58}$$

5 Multi-Harmonic Harmonic Balance in Rotordynamics

Even in simple FE model with nonlinearities (e.g. Duffing oscillator), it is possible to find sub- and super- harmonic resonances [Yang, 2016], not observable studying dynamical systems using the fundamental harmonic only. Complex FE models are very likely to generate phenomena from the combination of multiple harmonics due to the nonlinear modal interaction. For these reasons in HB simulations it is important to study the impact of the number of harmonics taken into account in the simulation on the response of the system.
In this section, we examine the nonlinear behaviour of the modified Jeffcott-Laval rotor presented in Chapter 2 with two different forms of nonlinearity:

- First of all a double-Duffing spring positioned on DOFs representing the disc, allowing to prove the need of multi-harmonic HB to study the dynamics of the system.
- The rotor-stator contact is studied simulating the full annular rub on the modified Jeffcott-Laval rotor first of all in a configuration with symmetrical supports and then with non-symmetrical supports.

In further sections considerations about the type of prediction and correction (Pre-Co) strategies adopted are presented.

5.1 Symmetrical Jeffcott-Laval simulation with double-Duffing spring

The nonlinearity adopted in this study case is the classical Duffing spring applied on the two degrees of freedom representing the displacements of the disc in the plan perpendicular to the rotation axis (double-Duffing). The Kinematic model adopted in this section is the same presented in Section 3.2. The nonlinear force is not conditional, applied on the disc at any moment and mathematically defined as:

$$\mathbf{f_{nl}}_1(\boldsymbol{q}(t)) = K_d \cdot \mathbf{q}_1^3 \tag{4.59}$$

$$\mathbf{f_{nl}}_2(\boldsymbol{q}(t)) = K_d \cdot \mathbf{q}_2^3 \tag{4.60}$$

The response of the proposed system along the n_1 direction is reported in Figure 4.10a, on the disc, support #1 and support #2. In Figure 4.10b one can see the 3-dimensional displacements of the rotating system at a specific frequency point of the response. The Duffing spring generates a third super-harmonics resonance [Hassan, 1994] and this is observable only taking into account higher order harmonics (e.g 3 or more) in the HB

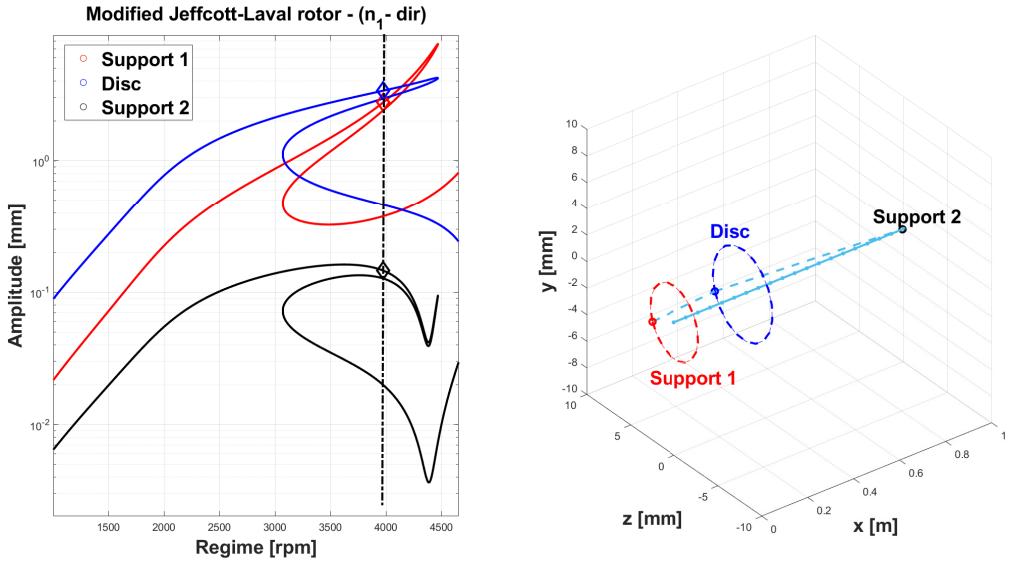

Figure 4.10: Jeffcott-Laval rotor with double-Duffing spring dynamical response, $K_d = 1e6$, 1st harmonic only: a) System's response observed on n_1 direction of the support #1, disc and support #2. b) Graphical representation of the system's displacements in three-dimensional space at $\Omega = 3973rpm$.

	1H	**2H**	**3H**
CPU time (norm.)	0.145	0.25	1 (220s)

Table 4.1: Normalised CPU times of the HB solution with respectively 1, 2 and 3 harmonics taken into account in the simulation.

simulations. In Figure 4.11 one can see on the left, the nonlinear response of the considered system taking into account only the first harmonic (blue line), the first two harmonics (black line) and finally, the first three harmonics (red line). On the right of Figure 4.11 the AFT algorithms at $\approx 3285rpm$ for the case with the fundamental harmonic only (blue line) and the first three harmonics (red line). One can see that the second harmonic doesn't introduce any relevant information, on the other hand the introduction of the third harmonic allows to observe a super-harmonic resonance highlighted at $\approx 3285rpm$. The computational time is strongly dependent on the number of harmonics, Table 4.1 reports the CPU times in the three studied cases. One can notice that the simulation performed taking into account the first three harmonics is more expensive than other cases. Super-harmonic and sub-harmonic resonances are observable only if higher order harmonics are taken into account in the simulation. Nevertheless, increasing the harmonic order of the HB algorithm is not always beneficial: as observed in Figure 4.11 and Table 4.1, the introduction of the second harmonics doesn't change radically the accuracy of the results but yield to double the CPU time. It is thus necessary to be able to optimise the number of harmonics to observe interesting phenomena obtained from the interaction of

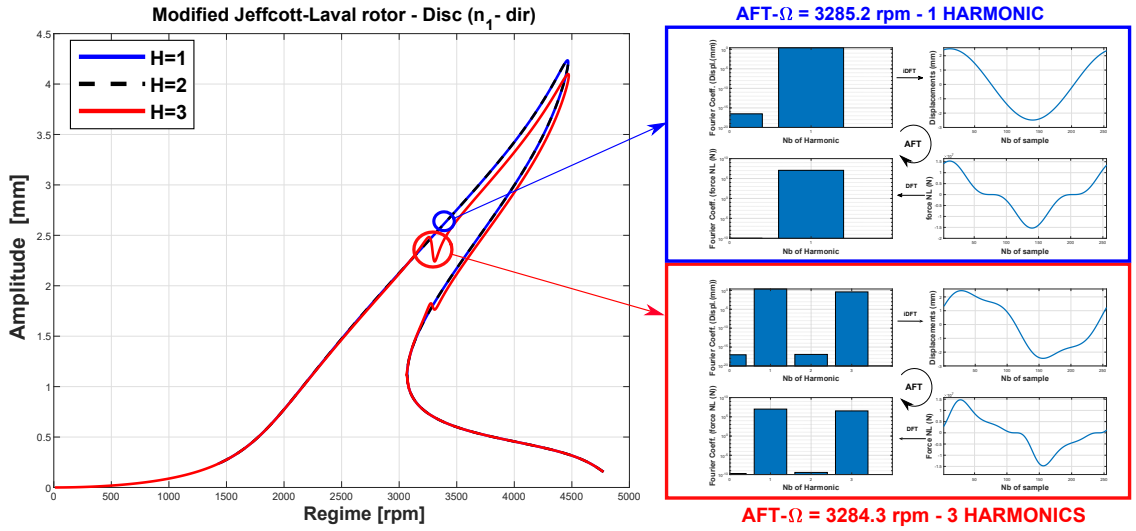

Figure 4.11: Influence of the number of harmonics in the nonlinear response of the Jeffcott-Laval rotor with Duffing springs.

different order harmonics and minimising computational effort.

5.2 Symmetrical Jeffcott-Laval with full annular rub non linearity

The modified Jeffcott-Laval rotor proposed in the previous section is now studied to simulate the rotor-stator contact with the contact model proposed in Equation 4.23, the nonlinear force is applied with a nonlinear gap of 2mm on the disc's displacements. First of all, it is interesting to observe Figure 4.12, reporting the impact of the nonlinear contact coefficient K_c on the nonlinear response of the system. Observing the response with $K_c = 1e5$ one can notice a very soft impact of the nonlinearity, on the contraty, observing the response with $K_c = 1e9$ (brown line) one can notice a response which is completely capped by the effect of the nonlinear force.

The physics of the system with the nonlinear force applied on the disc is reported in Figure 4.13. One can notice that the disc (blue curve) has its displacements capped by the presence of the nonlinear forces. As the support #1 is more flexible than the support #2, at $\Omega = 4589rpm$ the displacements of support #1 are higher than the displacements of the disc.

The influence of the number of harmonics in the evaluation of the nonlinear response is now discussed with the full annular rub type of nonlinearity. In Figure 4.14 one can compare the response of the system on the disc, along the n_1 direction, simulated respec-

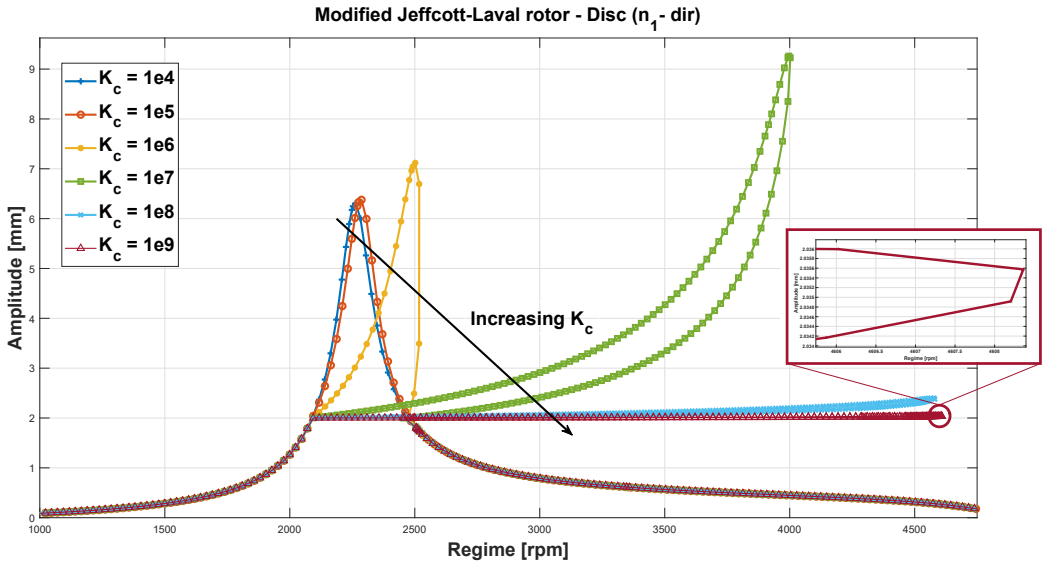

Figure 4.12: Impact of the nonlinear contact coefficient K_c on the nonlinear response of the modified Jeffcott-Laval rotor. $K_c = [1e4 - 1e9]$, $NLgap = 2mm$.

tively taking into account only the first harmonic (blue line) and the first 10 harmonics (red line). On the right of Figure 4.14 the AFT algorithms displayed at $\Omega \approx 4217rpm$: in blue approximating the response with the first harmonic only and in red with the first 10 harmonics. It is interesting to notice that even if a stiff nonlinearity is applied and high order harmonics are taking part into displacements and the nonlinear forces, their contribution is negligible when compared to the contribution of the first harmonic. The full annular rub with no friction, no impacts or other non-regular phenomena can be simulated with a good accuracy taking into account only the first harmonic. This practice allows to reduce the computational effort (see Table 4.2). On the other hand, if much complex phenomena have to be taken into account, super-harmonics excitation is likely to happen and higher order harmonics have to be taken into account.

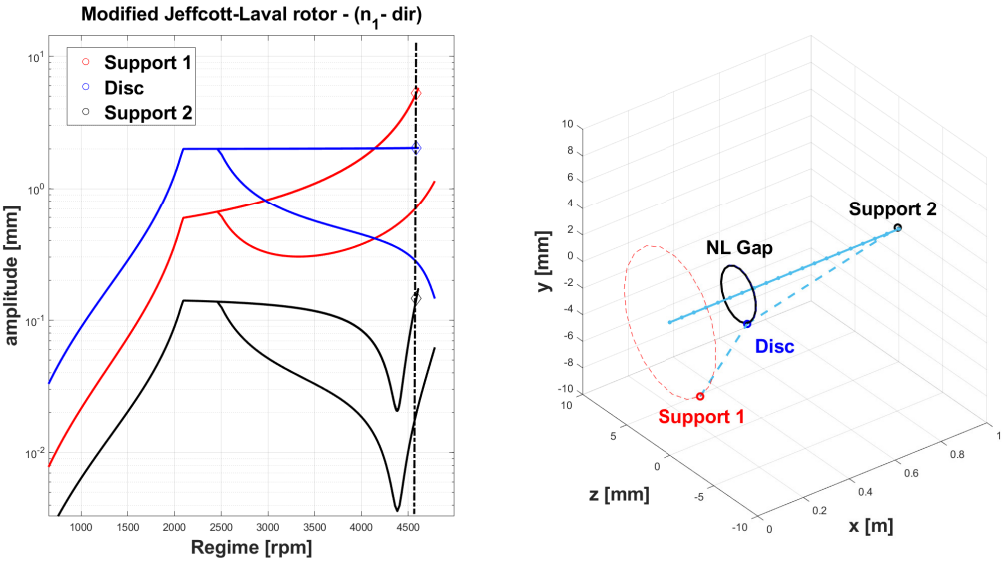

Figure 4.13: Jeffcott-Laval rotor with rotor-stator contact dynamical response, $K_c = 1e9$, 1st harmonic only: a) System's response observed on n_1 direction of the support #1, disc and support #2. b) Graphical representation of the system's displacements in the three-dimensional space at $\Omega = 4589rpm$.

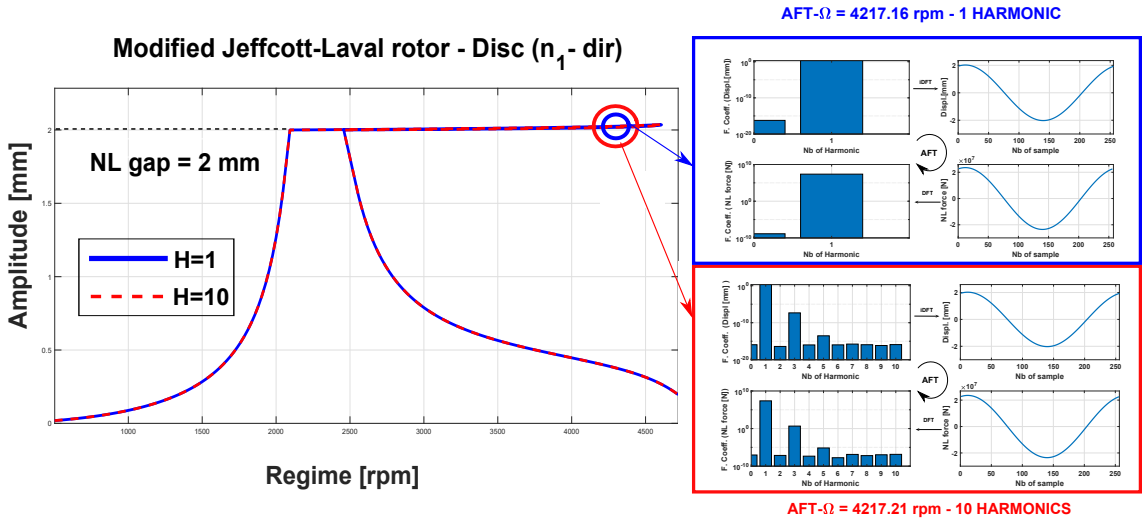

Figure 4.14: Influence of the number of harmonics in the nonlinear response of the Jeffcott-Laval rotor with full annular rub.

	1H	10H
CPU time (norm.)	0.075	1 (400s)

Table 4.2: Normalised CPU times of the HB solution with respectively 1 and 10 harmonics taken into account in the simulation.

5.3 Pre-Co strategies influence on the solution of nonlinear full annular rub

Step size(ds)	Pre/ Co	**CPU time(s)**	nb. function evaluated
0.01	**Sec. / Ortho.**	64.5	13106
	Sec. / A-Len.	NC	//
	Tan. / Ortho.	49	9209
	Tan. / A-Len.	55s	10701
0.05	**Sec. / Ortho.**	10.46	2221
	Sec. / A-Len.	12.30	2489
	Tan. / Ortho.	13.2	2271
	Tan. / A-Len.	13.5	2615

Table 4.3: Impact on the type of Pre-Co strategy on the solution and the CPU time.

In this section the proposed prediction (secant and tangent referred respectively as *Sec.* and *Tan.*) and correction strategies (Orthogonal and arc-length, referred respectively as *Ortho.* and *A-Len.*) are studied singularly to evaluate the impact of the Pre-Co strategies on the solution and on the CPU time. The Modified Jeffcott-Laval rotor observed in the previous section is studied here with the full annular rub nonlineairty with $K_c = 1e9$ and taking into account the first harmonic only. In table 4.3 are reported the CPU times of performed simulations with several Pre-Co strategies.

It is important to highlight that the convergence of the continuation algorithm is dependent on the minimum step size and the Pre-Co strategy. In the proposed analysis two minimum step sizes are taken into account: $ds_1 = 0.01$ and $ds_2 = 0.05$. We have to keep in mind that reducing the minimum step size more points will be evaluated on the continuation path, but a smaller amount of iterations is performed to reach the convergence.

From table 4.3 one can observe at first the study with a minimum step size of 0.01: the Sec./A-Len. doesn't converge at all, while the CPU time of the Sec./Ortho. is higher than the two cases performed using the tangent prediction with more evaluated points, which means that the convergence was not immediate to reach at any iteration and that the step size has been kept small during the whole solution. Concerning the tangent prediction one can notice that the two proposed strategies are similar in terms of computational effort and result's accuracy (see Figure 4.15) and more efficient than the converged case with the secant predictor.
Concerning the second study with the larger minimum step size of 0.05 one can notice that the four study cases have converged. Nevertheless the continuation path is not the same changing the prediction strategy: using a secant prediction the turning point of

the nonlinear response is not identified, the continuation path *jumps* from the nonlinear branch to the linear branch as reported in Figure 4.16. On the contrary, the tangent predictor allows to identify correctly the whole nonlinear branch. The CPU time of the secant strategies and the number of evaluated functions with these strategies are smaller than the tangent one but it is important to keep in mind that the evaluated responses are not complete.

One can conclude that the tangent prediction has to be preferred to the secant one for a better convergence of the continuation algorithm observed in the presented results. Concerning the correction strategy, the orthogonal correction seems to be more efficient in terms of computational effort and number of function evaluated but there is no relevant gap between these two strategies in terms of accuracy. The presented results concerning the Pre-Co strategy are very case-dependent and they represent a recommendation for similar nonlinear responses, a general conclusion about the Pre-Co strategy is difficult to draw.

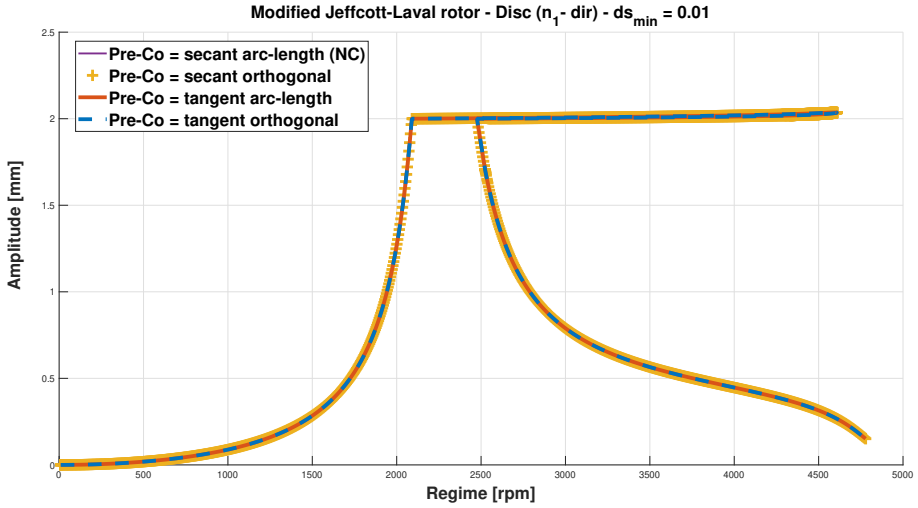

Figure 4.15: Pre-Co strategy influence on the system's response: modified Jeffcott-Laval rotor with nonlinear contact $K_c = 1e9$, NLgap = 2mm , $ds_{min} = 0.01$.

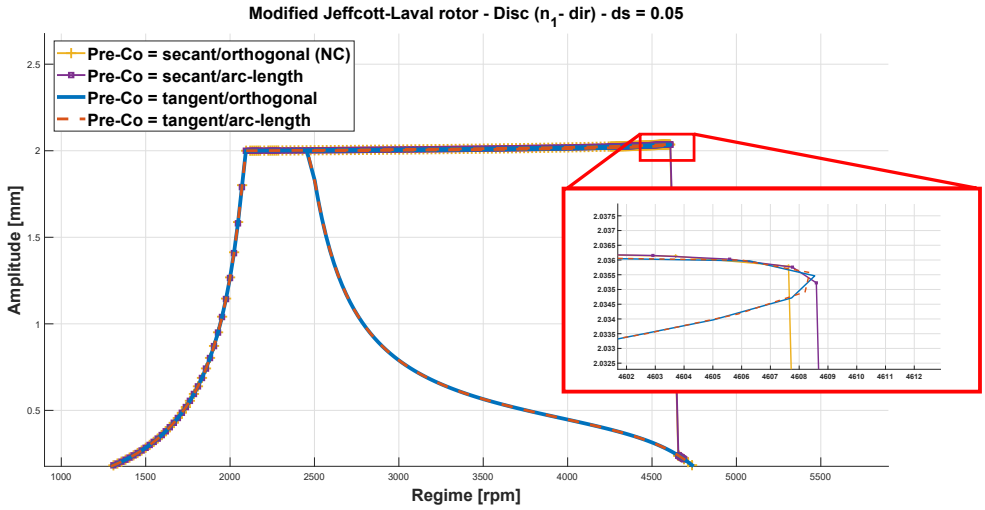

Figure 4.16: Pre-Co strategy influence on the system's response: modified Jeffcott-Laval rotor with nonlinear contact $K_c = 1e9$, NLgap = 2mm , $ds_{min} = 0.05$.

5.4 Conclusions

In this chapter the *Harmonic Balance* (HB) algorithm employed in the following sections has been presented and applied on the academical study case representing the modified Jeffcott-Laval rotor, with 2 different forms of lumped nonlinearities: double-duffing springs and nonlinear rotor-stator contact to simulate a full annular rub phenomenon.
Multiple numerical aspects regarding the algorithm are not discussed explicitly in this thesis such as the auto-adaptive step-size, the rejection or acceptance of an evaluated point etc.

The presented algorithm and the reported numerical study cases are employed to demonstrate that the full annular rub phenomenon can be simulated in the HB framework taking into account only the first harmonic of a Fourier expansion.
It has been seen as well that the prediction strategy has a very relevant role in the continuation path algorithm, the tangent prediction allows to reduce the computational effort of the simulation and conducts the algorithm to converge better than the secant prediction. On the contrary, the choice of the correction strategy seems to impact the CPU time but not the stability of the algorithm.

In further chapters, the full annular rub is simulated using the nonlinear force presented in this chapter on the more complex industrial scale model, the simulations are performed taking into account the first harmonic only and using the tangent/orthogonal Pre-Co strategy.

Chapter 5

A Ritz pure-modal reduction method for linear and non–linear rotating systems based on a critical speed subspace

"La perfection est atteinte, non pas lorsqu'il n'y a plus rien à ajouter, mais lorsqu'il n'y a plus rien à retirer."

"Perfection is reached, not when there is no longer anything to add, but when there is no longer anything to take away."

Antoine de Saint-Exupery: French writer, poet, journalist and aviator (1900-1944)

Objectives

Finite element models representing industrial scale rotating-machines have reached today a very large number of degrees of freedom. The large size of these models requires the use of model reduction to make the simulations computationally affordable. However, the physical characteristics (i.e. modes shapes and natural frequencies) of a rotating machine depend on the rotating speed of the system and classical modal reduction approaches could be not efficient in this case.

In this chapter a method is proposed to evaluate a reduction basis composed only by the modes excited when the system runs through its own critical speeds. This method produces a natural and essential basis of modes which is optimal for the identification of the main components of the unbalance response of a rotating system.

Contents

1 Classical model order reduction in structural dynamics

In industrial applications it is common to study *Finite Element* (FE) models composed by a large number of (DOFs) (1-100 $\cdot 1e6$ DOFs). In these situations it is essential to reduce the size of the model in order to be able to perform the simulation and compute the desired responses.
A lot of recent approaches based on data are proposed for model reduction in numerical simulations [Daniel, 2022; Quarteroni, 2014]. In structural dynamics, the approaches based on the employment of a *Ritz* projection are still widely employed [Wilson, 1982; Klerk, 2008; Lalanne M, 1998]. The *Full Order Model* (FOM) displacement field $\mathbf{q}_f(x,t)$ is projected and reduced on a set of independent vectors Ψ verifying the system's kinematic conditions:

$$\mathbf{q}_f(x,t) = [\Psi(x)]\ \mathbf{u}(t) \tag{5.1}$$

Many model reduction approaches employed in structure dynamics can be seen as extensions of the Ritz method. Among these methods, it is possible to identify two main classes of model reduction techniques:

- **Purely modal subspace reduction**: these methods are based on the projection of the large scale numerical model in a reduced subspace purely described by modal coordinates [Schilders, 2008a; Barbone, 2003]. This approach is widely employed for the reduction of large models representing a single component or assemblies studied from a global point of view.

- **Mixed modal and physical subspace reduction**: this is the case of reduction methods known as *Component Mode Synthesis* (CMS). These methods are more employed to reduce components that have to be assembled or to simulate the behavior of nonlinear systems with localized nonlinearities. Some classical methods composing this class are : Guyan Reduction, Craig-Bamtpon Reduction, Mac-Neal Reduction, Rubin Reduction or Dual Craig-Bampton [Allen, 2020].

These Ritz-based approaches are commonly employed in structure and rotor-dynamics and well documented [Wagner, 2010; Lund, 1974; Chevallier, 2011; Khulief, 1997]. This work is positioned in the domain of rotor-dynamics since the methods proposed are a form of Ritz projection based on specific properties of rotating machines.
A singular characteristic of the rotating machines is that they can trigger instabilities and resonance phenomena at some specific working regimes known as *critical speeds* [Greenhill, 1995; Swanson, 2005; Genta, 2007]. Lalanne [Lalanne M, 1998], investigates these phenomena showing that a rotating system presents two groups of mode shapes: forward

and backward whirling modes, excited differently depending on the type of driving force (synchronous and asynchronous). Since only the direct modes are excited in symmetrical rotating machines under synchronous excitations, this differentiation can be employed to identify an essential and restricted set of modes excited at critical speeds. This set of modes can be employed to reduce efficiently the size of the system [DAlessandro, 2022a]. Following the same philosophy, it will be shown that this approach is efficient even in the cases of non-symmetrical rotors with both forward and backward whirling modes excited.

In rotor dynamics, the rotational speed, via the gyroscopic effect, induces variations in physical properties of the system (i.e. natural frequencies and mode shapes). This variation of physical properties is not taken into account by the classical Ritz-type reduction approaches [Wagner, 2010]. Balmes et al. proposed several works taking into account the state variation of the system combining several modal basis evaluated in different states of the system [Balmes, 1997; Bobillot, 2002; Sternchüss, 2006]. These methods produce highly detailed *Reduced Order Model* (ROM) but they demand an important *offline work* before running the simulation. The Ritz approach proposed in this work can be evaluated in a singular operation and the family of modes composing the reduction basis is evaluated at different rotating speeds of the systems, taking into account the properties modification due to the variation of the rotating speed.

The main objective of this work is to show the efficiency of the reduction based on critical speeds modes in linear and nonlinear frameworks. Festjens et al. [Festjens, 2014] already proposed a Ritz modal approach to reduce a nonlinear mechanical system. This approach will be extended in the case of a rotating system working in a rub/contact condition [Adiletta, 1996; Choy, 1987; Jacquet-Richardet, 2011].
Two families of numerical methods are commonly employed to simulate these type of phenomena: the direct numerical integration with different integration schemes [Hua, 2005; Geradin, 2014] and the frequency based methods such as the *Harmonic Balance Method* (HBM) or the shooting method. These lasts have been widely developed in the last 10 years being particularly efficient in terms of computational effort [Guskov, 2007; Krack, 2019; Peeters, 2009]. The frequency-based methods are commonly solved using a continuation algorithm and adopting an AFT algorithm to for the evaluation of the nonlinear force [Woiwode, 2020; Adams, 1986].
Commonly the HBM solvers are associated with CMS-type reduction [Peletan, 2012a; Joannin, 2017; Mitra, 2016], considering the nonlinear DOFs as master nodes. In this configuration it is indeed possible to evaluate directly the nonlinear force on these nodes since they are expressed in the physical representation. In this work is proposed a less classical approach based on a full modal Ritz projection, for the evaluation of the nonlinear force and its derivative, the physical displacements of the nonlinear DOFs are rebuilt

from the modal space.

The efficiency of the proposed reduction method will be evaluated in linear and non-linear framework using an HBM algorithm, simulating the FOM and several types of ROMs. The critical speed reduction is compared with more classical approaches on an academical study case representing a Jeffcott rotor with rotor/stator contact and on an industrial size FE model representing an aeronautic fan/booster major module with the same form on nonlinearity.

2 Critical speed basis evaluation

The force produced by the unbalance of the rotor can be described as a vector rotating with the same angular speed as the rotor. The unbalance response of a rotating system is expressed in the frequency domain as [Dimarogonas, 2013]:

$$(-\omega^2\mathbf{M} + j\omega(\mathbf{D_v} + \sum_{i=1}^{r}\Omega_i\mathbf{G}_i) + \mathbf{K} + j\mathbf{K}\eta_h)\hat{\mathbf{q}}_f = m\,e\,\Omega^2\,\hat{\mathbf{f}} \tag{5.2}$$

The gyroscopic effect ($\Omega_i\mathbf{G}_i$) is expressed on the i-th rotor of the system. This work aims to develop a method to reduce the size of this dynamical problem.
The eigenvalues and eigenvectors of the system in a specific state s ($\Omega_i^s = const.$) are evaluated using the following equation of motion:

$$(-\omega^2\mathbf{M} + j\omega(\mathbf{D_v} + \sum_{i=1}^{r}\Omega_i\mathbf{G}_i) + \mathbf{K} + j\mathbf{K}\eta_h)\hat{\mathbf{q}}_f = \boldsymbol{0} \tag{5.3}$$

The passage to the state space is employed to solve this problem, yielding:

$$j\omega\,\mathbf{U}\,\hat{\mathbf{z}}_f - \mathbf{A}(\Omega^s)\,\hat{\mathbf{z}}_f = 0 \tag{5.4}$$

with :

$$\begin{aligned}
\mathbf{U} &= \begin{pmatrix} \mathbf{M} & 0 \\ 0 & -\mathbf{K} - j\mathbf{K}\eta_h \end{pmatrix} \\
\mathbf{A}(\Omega^s) &= \begin{pmatrix} -\mathbf{D_v} - \sum_{i=1}^{r}\Omega_i^s\mathbf{G}_i & -\mathbf{K} - j\mathbf{K}\eta_h \\ -\mathbf{K} - j\mathbf{K}\eta_h & 0 \end{pmatrix} \\
\hat{\mathbf{z}}_f &= \begin{pmatrix} j\omega\,\hat{\mathbf{q}}_f \\ \hat{\mathbf{q}}_f \end{pmatrix}
\end{aligned} \tag{5.5}$$

Other formulations are possible, producing the same results [Genta, 2007]. The eigenvectors and the corresponding eigenvalues of the problem in state s are (λ^s,Ψ^s):

$$[\lambda^s \mathbf{U} - \mathbf{A}(\Omega^s)]\,\Psi^s = 0, \qquad with \qquad \Psi^s = \begin{bmatrix} \Phi^s \\ \lambda^s \Phi^s \end{bmatrix} \tag{5.6}$$

The basis Φ^s can be employed to decompose the response or to reduce the system, nevertheless this modal basis is representative only for the state s and not for an arbitrary regime of the system because the modal features of the system depend on the rotating speed. Since in an unbalance response the resonances appear at the critical speeds, a natural basis to decompose an unbalance response would be a modal basis composed only by the modes excited at critical speeds.
For instance, the critical speeds are excited by the unbalance force, which has an angular frequency equal to the rotational speed of the system : $\Omega = \omega$. It is possible to generalize this relation in order to include more complex acceleration laws:

$$\Omega_i = \omega\ a_i + b_i \tag{5.7}$$

Using Equation 5.7 in Equation 5.3, the eigenvalues problem 5.8 becomes:

$$j\omega \cdot \mathbf{U}_{cs} \cdot \hat{\mathbf{z}}_f - \mathbf{A}_{cs} \cdot \hat{\mathbf{z}}_f = 0 \tag{5.8}$$

with :

$$\begin{aligned} \mathbf{U}_{cs} &= \begin{pmatrix} \mathbf{M} - \sum_i^r j\,\mathbf{G}_i\ a_i & 0 \\ 0 & -\mathbf{K} - j\mathbf{K}\eta_h \end{pmatrix} \\ \mathbf{A}_{cs} &= \begin{pmatrix} -\mathbf{D_v} - \sum_i^r \mathbf{G}_i\, b_i & -\mathbf{K} - j\mathbf{K}\eta_h \\ -\mathbf{K} - j\mathbf{K}\eta_h & 0 \end{pmatrix} \\ \hat{\mathbf{z}}_f &= \begin{pmatrix} j\omega\,\hat{\mathbf{q}}_f \\ \hat{\mathbf{q}}_f \end{pmatrix} \end{aligned} \tag{5.9}$$

The solution of the eigenvalues problem expressed in Equation 5.8 produces the critical speeds of the system λ_{cs} and a basis Φ_{cs} of complex modes corresponding to these critical speeds. This basis is invariant with the variation of the rotating speed of the system, while a classical modal basis depends on the rotational speed of the system. The response of the system is projected on this basis of modes using the following equation:

$$(-\omega^2 \mathbf{M}_r + j\omega(\mathbf{D_v}_r + \sum_{i=1}^{r} \Omega_i \mathbf{G}_{ir}) + \mathbf{K}_r + j\mathbf{K}_r\eta_h)\hat{\mathbf{u}} = m\,e\,\Omega^2\,\hat{\mathbf{f}}_r \tag{5.10}$$

With :

$$\begin{aligned} \mathbf{W}_r &= \Phi_{cs}^T\ \mathbf{W}\ \Phi_{cs} \quad \forall\ \mathbf{W} &&= \mathbf{M}, \mathbf{D_v}, \mathbf{G}, \mathbf{K} \\ \mathbf{F}_r &= \Phi_{cs}^T\ \mathbf{F} \quad \forall\ \mathbf{F} &&= \hat{\mathbf{f}} \\ \hat{\mathbf{q}}_f &= \Phi_{cs}\ \hat{\mathbf{u}} \end{aligned} \tag{5.11}$$

To avoid using a complex modal basis (i.e. in time integration simulations), it is possible to decompose it into its real and imaginary parts. Indeed, a complex three-dimensional mode is composed by two phase-shifted real modes. Considering the general complex modal basis Φ, containing $\boldsymbol{m}$ complex vectors:

$$\Phi = [\phi_1, ..., \phi_i, ..., \phi_m]_{n \times m}, \tag{5.12}$$

the i-th complex vector is:

$$\phi_i = \begin{bmatrix} a_{1i}e^{j\theta_{1i}} \\ \vdots \\ a_{li}e^{j\theta_{li}} \\ \vdots \\ a_{ni}e^{j\theta_{ni}} \end{bmatrix} = \begin{bmatrix} a_{1i}cos(\theta_{1i}) \\ \vdots \\ a_{li}cos(\theta_{li}) \\ \vdots \\ a_{ni}cos(\theta_{ni}) \end{bmatrix} + j \begin{bmatrix} a_{1i}sin(\theta_{1i}) \\ \vdots \\ a_{li}sin(\theta_{li}) \\ \vdots \\ a_{ni}sin(\theta_{ni}) \end{bmatrix} = \Re(\phi_i) + \Im(\phi_i). \tag{5.13}$$

Thus, the basis Φ expressed in the decomposed representation Φ_D is:

$$\Phi_D = [\Re(\phi_1), \Im(\phi_1), ..., \Re(\phi_m), \Im(\phi_m)]_{n \times 2m} \tag{5.14}$$

In this work, this representation is employed for the time integration simulations in the section dedicated to the nonlinear analyses.

3 Critical speeds subspace reduction : modified Jeffcott Laval rotor

The model reduction approach presented in the previous section is applied in this section on a modified Jeffcott-Laval rotor, in multiple frameworks: linear and nonlinear configurations of the system are considered in time and frequency domain in order to assure the efficiency of the considered method in any possible environment. Moreover the academical study case of a Jeffcott-Laval rotor is interesting because it allows to produce results easy to reproduce.

3.1 Harmonic study of the modified Jeffcott-Laval rotor with symmetrical supports

In this section, the critical speed basis Φ_{cs} presented in the above section is employed to reduce a rotating system with symmetrical supports as shown in Figure 5.1. The physical details of the system are reported in Table 5.1. This system is composed by a rigid

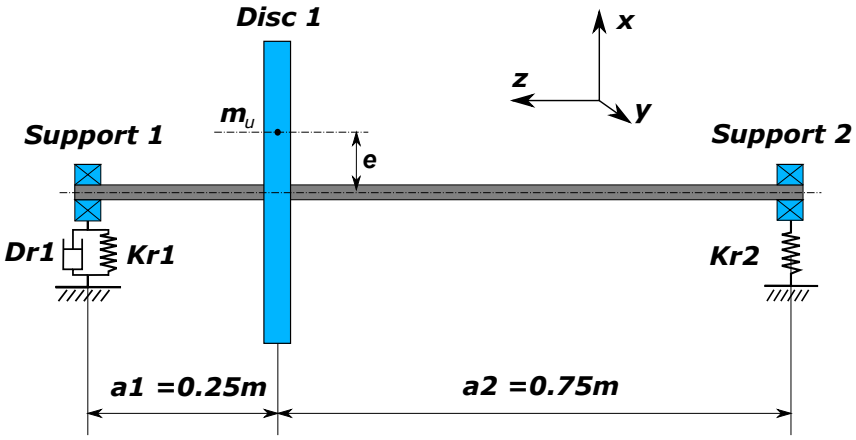

Figure 5.1: Mono-rotor system.

Mass disc #1	50 kg
Planar M. of inertia disc #1	0.5 $kg \cdot m^2$
Polar M. of inertia disc #1	1 $kg \cdot m^2$
Rad. stiffness of support #1	1e7 $N \cdot m$
Damping support #1	1e5 $N \cdot s/m$
Rad. stiffness of support #2	1e7 $N \cdot m$
Hysteretic damping factor	0.333
Beam external radius	0.03 m
Beam internal radius	0.027 m
Beam length	0.05 m
Beam density	7900 kg/m^3
Beam Poisson ratio	0.3
Shaft length	1 m

Table 5.1: Physical properties of the rotating system.

rotor, a flexible shaft (constituted by 20 'beam' elements) and symmetric supports, with an operational range of 0-40 000 rpm. The response of the system is simulated with an unbalance of 0.1kg*m applied on the disc #1. The physical response of support #2 is reported in figures 5.3 and 5.4 with a dotted black line. Only the response of the system along the X-direction (perpendicular to the rotation axis) is reported since the system has a symmetrical behavior. Only the first 9 modes of the system are taken into account for the following considerations.

The Campbell diagram is reported in Figure 5.2 to display the evolution of the natural frequency of the first 9 modes of the system and to identify the position of the first 9 critical speeds.

A conventional complex modal analysis performed at $\Omega^s = 0$ rpm (or generally $\Omega^s = const.$), solving the classical eigenvalues problem expressed in Equation 5.8, produces a basis of normal modes which describes the physics of the system in a fixed state s. This

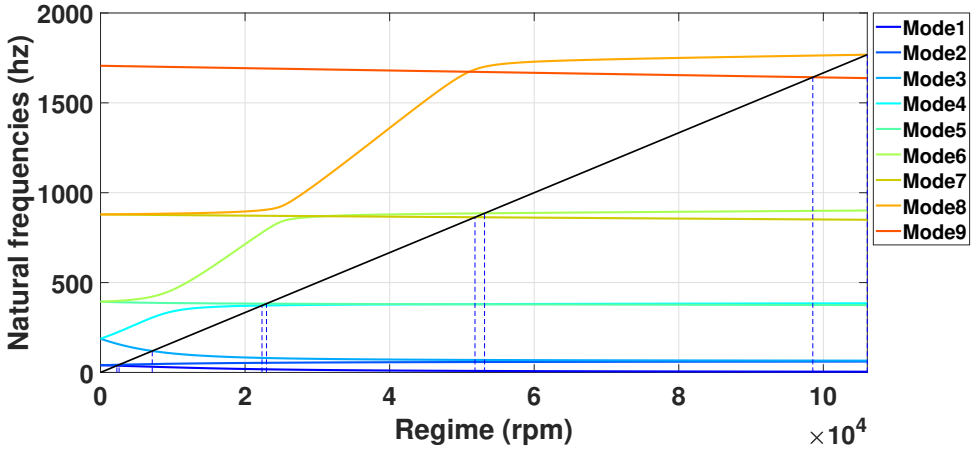

Figure 5.2: Campbell diagram.

modal basis cannot be employed to decompose the unbalance response of the system into independent modal contributions. Figure 5.3 reports the unbalance response of the system on support #2, decomposed using the classical normal modes evaluated at $\Omega^s = 0$. Any of the modes excited by the unbalance is seen to be coupled with the others (see Figure 5.3). This effect is produced by the presence of gyroscopic matrix in the mathematical problem.

On the contrary, it is possible to decompose the unbalance response of the system using the critical speed basis produced by the solution of the eigenvalues problem 5.9. The unbalance response of the system on support #2 decomposed using the critical speed modes is reported in Figure 5.4. The critical speed basis allows the response to be decomposed into independent contributions of the unbalance response of the system, which is fundamental to identify the most relevant modes for the response. The whirling direction of the modes and their critical speeds are reported in Table 5.2. It is interesting to notice that only the forward modes (2, 4, 7 and 9) have a relevant contribution on the response. The backward modes of the system have a marginal role.

Similar results are obtained calculating the participation factors [Nieto, 2018] of the modes composing the critical speed basis. The participation factor γ is defined by Equation 5.15:

$$\gamma = \Phi_{cs}^T \ \mathbf{M} \ \mathbf{d} \tag{5.15}$$

Where $\mathbf{d}$ is an assumed unitary displacement vector and depends on the direction of excitation. The participation factors of the first 9 critical speed modes are reported in Figure 5.5. One can notice that only the forward modes (2, 4, 7 and 9) have a non negligible participation factor.

For the purpose of model reduction, it is worthwhile to develop a reduction basis of the system containing only the critical speed modes associated to the forward modes (2, 4, 7

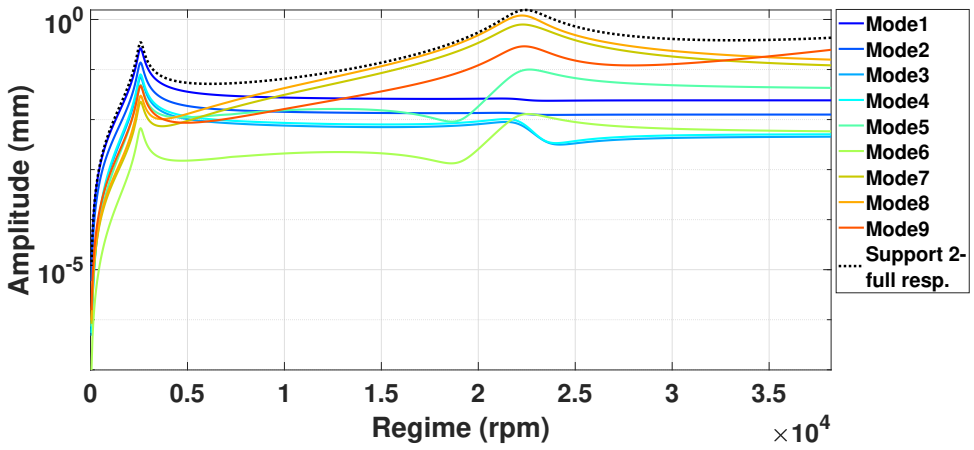

Figure 5.3: Unbalance response of support #2 on x direction decomposed using the first 9 normal modes ($\Omega = 0$) .

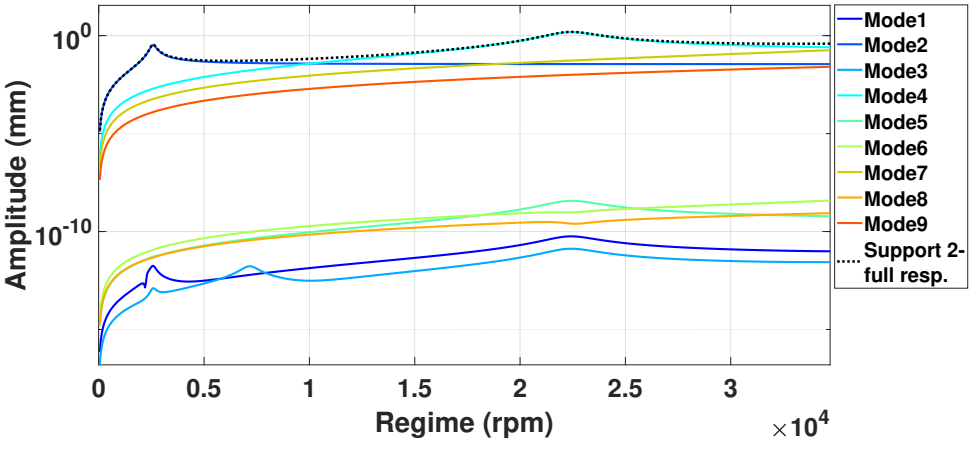

Figure 5.4: Unbalance response of support #2 on x direction decomposed using the first 9 critical speed modes.

Mode	Whirling direction	Critical speed (rpm)
1	Backward	2262
2	Forward	2568
3	Backward	7157
4	Forward	22339
5	Backward	22960
6	Backward	53132
7	Forward	51808
8	Backward	106080
9	Forward	98544

Table 5.2: Critical speed and whirling direction.

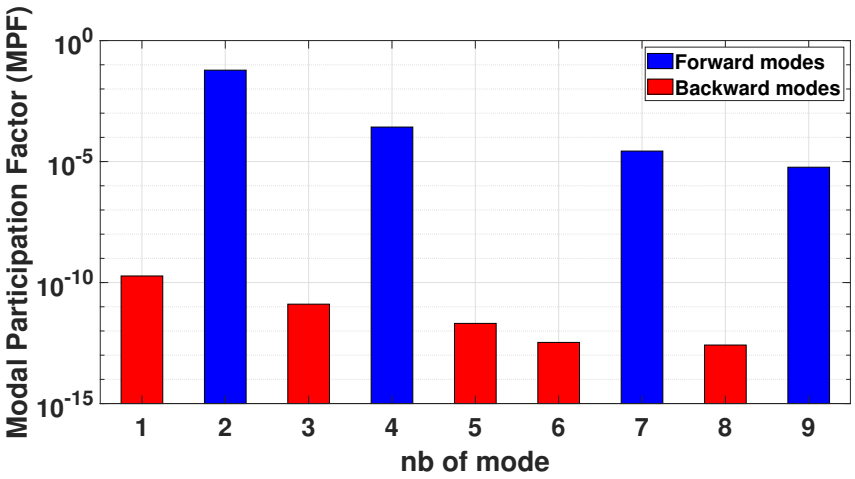

Figure 5.5: Modal participation factors.

and 9):

$$\Phi_{ROM1} = [\phi_2 \quad \phi_4 \quad \phi_7 \quad \phi_9] \tag{5.16}$$

The reduced order model, named ROM1, only has 4 analytical DOFs (vs 98 DOFs in the full model, 97% of size reduction). Moreover, a second ROM has been proposed adopting the first 4 normal modes of the system evaluated at $\Omega = 0$, it is known as ROM1M. The ROM1 is compared with the full system and with the ROM1M in figures 5.6a and 5.6b. Since the system is symmetrical and excited by a synchronous driving force, only the second (2568 rpm) and the fourth critical speed (22389 rpm) generate important resonance phenomena in the operational frequency range. Note that the ROM1M does not correctly represent the fourth critical speed of the system.

The first four normal modes of the structure are related to the first two critical speed modes of the system and there is a conjugate pair of normal vectors for each critical speed mode. Of these modes pairs, only the forward one is excited by the unbalance. Hence, the first four normal modes contain the principal information related to the second critical

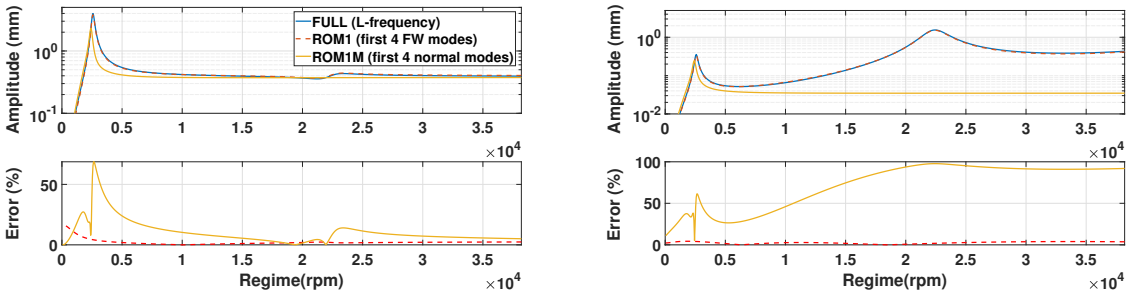

(a) Disc #1 displacements X

(b) support #2 displacements X

Figure 5.6: Harmonic response FOM vs ROM1 (4 critical speed modes) vs ROM1m (4 normal modes).

speed mode of the system. Meanwhile, Figure 5.3 shows that the contributions of the first four modes to the fourth critical speed of the system are negligible. To ensure that the ROM1M is able to correctly represent the fourth critical speed of the system, the modes five to nine must be included.

It is seen that with the same number of modes (4 critical speed modes in ROM1 and 4 normal modes in ROM1M), it is possible to produce a more accurate ROM with the critical speed basis than one composed of normal modes. The same level of precision is produced on the other DOFs of the system.

3.2 Time marching study of the reduced modified Jeffcott-Laval rotor with symmetrical supports

The model presented in the previous section, reduced using a critical speed basis, can be effectively used to solve linear problems as shown in Figures 5.6a and 5.6b. In this section, the proposed reduction method will be applied in a nonlinear framework. The reduced model ROM1 is employed here to simulate the dynamic behavior of the system in the presence of a rotor-stator contact. The nonlinear problem is solved via a time integration, simulating 2 seconds of the transient response of the system excited by the unbalance. To simplify the numerical simulations, the study is restrained to a frequency window positioned around the first critical speed (forward) of the system (1800-3000 rpm).

The transient response of the full model is reported and compared with several ROMs in order to evaluate the precision of the proposed reduction method under nonlinear operating conditions. Three ROMs are proposed in order to evaluate as well the impact of the backward modes on the response: ROM1 contains the first 4 forward modes, ROM2 employs the first 5 backward modes, and ROM3 contains the first 9 critical speed modes (including forward and backward modes of ROM1 and ROM2). A linear harmonic analysis of the full system is performed as well and reported in the results.

The nonlinear problem for the FOM is given by:

$$\mathbf{M}\ddot{\mathbf{q}}_f + (\mathbf{D_v} + \Omega\mathbf{G})\dot{\mathbf{q}}_f + \mathbf{K}\mathbf{q}_f + \mathbf{f_{nl}}(\mathbf{q}_f, t) = m \cdot e \cdot \Omega^2 \mathbf{f}(t) \tag{5.17}$$

with :

$$\begin{cases} \mathbf{f_{nl}}(\mathbf{q}_f(t)) = K_c \cdot (|\mathbf{q}_f^{disc1}| - C) \cdot \vec{\mathbf{n}} & if \quad ||\mathbf{q}_f^{disc1}|| \geq C \\ \mathbf{f_{nl}}(\mathbf{q}_f(t)) = \boldsymbol{0} & if \quad ||\mathbf{q}_f^{disc1}|| < C \end{cases} \tag{5.18}$$

For the reduced model, the nonlinear problem is given by:

$$\mathbf{M}_r\ddot{\boldsymbol{u}} + \left(\mathbf{D_{v}}_r + \sum_{i=1}^{r} \Omega_i \mathbf{G}_{ir}\right)\dot{\boldsymbol{u}} + (\mathbf{K}_r) \cdot \boldsymbol{u} + \mathbf{f_{nl}}_r(\boldsymbol{u}(t)) = m_u \cdot e \cdot \Omega^2 \cdot \mathbf{f}_r(t) \tag{5.19}$$

The nonlinear force must be evaluated in the physical space and then re-projected in the reduced space:

$$\mathbf{f_{nl}}_r(\boldsymbol{u}(t)) = \Phi_{cs}^T \cdot \mathbf{f_{nl}}(\Phi_{cs} \cdot \boldsymbol{u}(t)) \tag{5.20}$$

The simulations are performed applying an unbalance of $0.1kg \cdot m$ on disc #1. The nonlinear force is applied on disc #1 if the radial displacements exceed the threshold value of C = 1.6mm. In the nonlinear force, the term K_c represents the contact stiffness, which is

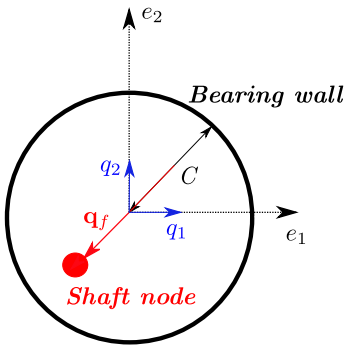

Figure 5.7: Contact representation.

fixed at $1e11N \cdot m$ and C represents the clearance between the rotor and the stator. The response of the system can be divided into a linear zone and a nonlinear zone. The disc #1 reaches the contact condition at approximately ≈2400 rpm. After that, the contact between the rotor and the stator is established and the nonlinear force, reported in Equation 6.2, is applied on the rotor. The response of the system is then nonlinear until the end of the simulation (3000 rpm). Figures 5.8a and 5.8b report the transient response of the system in full and reduced configurations, on disc #1 and support #2.
In order to obtain a global measure of precision and to estimate the error due to the model reduction, the minimum angle α between the exact displacement field $\mathbf{q}_f(t)$ of the system at time t and the displacement field $\mathbf{u}(t)$ of the system produced by the ROMs

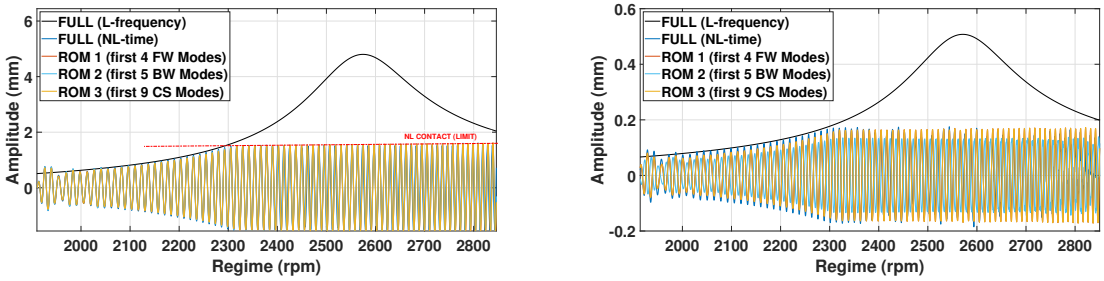

(a) disc #1 displacements along X

(b) support #2 displacements along X

Figure 5.8: Transient response full model (98 DOFs) vs ROM1 (4 fw modes) vs ROM2 (5 bw modes) vs ROM3 (9 cs modes).

is evaluated [Festjens, 2013]. If this angle is small, the compared subspaces are almost linearly dependent, which means that the two compared vectorial subspaces contain almost the same modal information. The evaluation of the angle α is performed using the MATLAB function `subspace`, returning the following function:

$$\alpha(t) = min\left\{arccos\left(\frac{\langle \mathbf{q}_f(t), \mathbf{u}(t)\rangle}{||\mathbf{q}_f(t)|| \cdot ||\mathbf{u}(t)||}\right)\right\} \tag{5.21}$$

The transient responses produced by these three ROMs are compared to the response of the full system in Figure 5.9, evaluating the minimum angle $\alpha(t)$. The error is then evaluated by:

$$err(t) = sin(\alpha(t)) \cdot 100 \tag{5.22}$$

The computational effort associated to the performed simulations are reported in Table 5.3. It is interesting to notice that even while ROM1 contains less modes than ROM2,

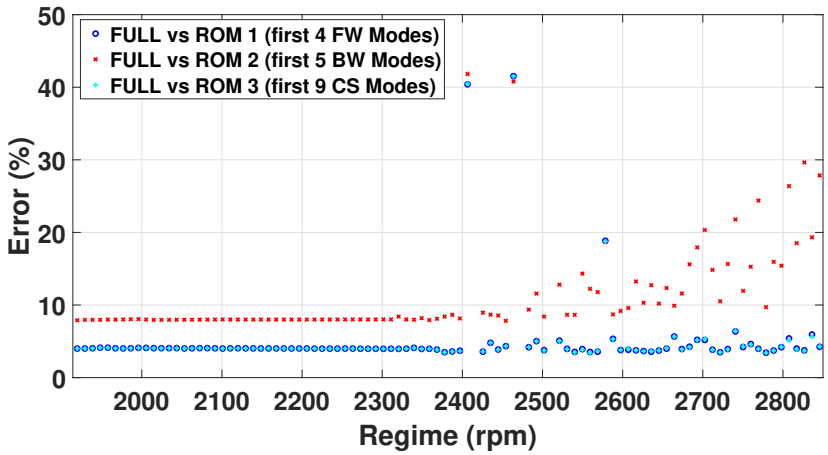

Figure 5.9: Minimum angle between the exact deformation field, the subspace generated by ROM1, ROM2 and ROM3.

the former is always more accurate than the latter. The error associated with ROM3 is always superposed to the error associated with ROM1, even if the computational effort associated to ROM3 is much larger than ROM1. There is thus no improvement in the ROM's accuracy when the forward and the backward modes are coupled. ROM3 shows that there is no value in including the backward modes in the reduction basis. The optimal ROM, in terms of accuracy and computational effort, is ROM1. Even in a nonlinear framework, the direct modes allow to represent the dynamical behavior of the system with an acceptable error.

Simulation	Norm. CPU time
Transient Analysis - FOM (97 DOFs)	1
Transient Analysis - ROM1 (4 DOFs)	0.006
Transient Analysis - ROM2 (5 DOFs)	0.007
Transient Analysis - ROM3 (9 DOFs)	0.123

Table 5.3: Computational effort of the simulations performed.

3.3 Harmonic study of the modified Jeffcott rotor with non-symmetrical supports

It is interesting to observe as well the proposed method in the case of a non-symmetrical system. The modified Jeffcott-Laval rotor proposed in the above section is now modified introducing non-symmetrical supports, their properties are reported in Table 5.4. In this case the backward modes are excited at the same level as the forward modes, (see Figure 5.11). It is important to notice that the critical speed basis allows in any case to obtain a decomposition of the response into independent components. The Campbell diagram of this modified Jeffcott-Laval rotor is reported in Figure 5.10 to display the evolution of the natural frequencies of the first 9 modes of the system and to identify the position of the first 9 critical speeds. The physical response of support #2 is reported in figures 5.11 with a dotted black line. Only the response of the system along the X-direction is displayed.

It is now interesting to compare the performances of a classical modal basis and the

Rad. stiffness of support #1 - dir X	1e7 $N \cdot m$
Rad. stiffness of support #1 - dir Y	2e7 $N \cdot m$
Rad. stiffness of support #2 - dir X	1e7 $N \cdot m$
Rad. stiffness of support #2 - dir Y	2e7 $N \cdot m$

Table 5.4: Elastic properties of the supports in a non-symmetrical case.

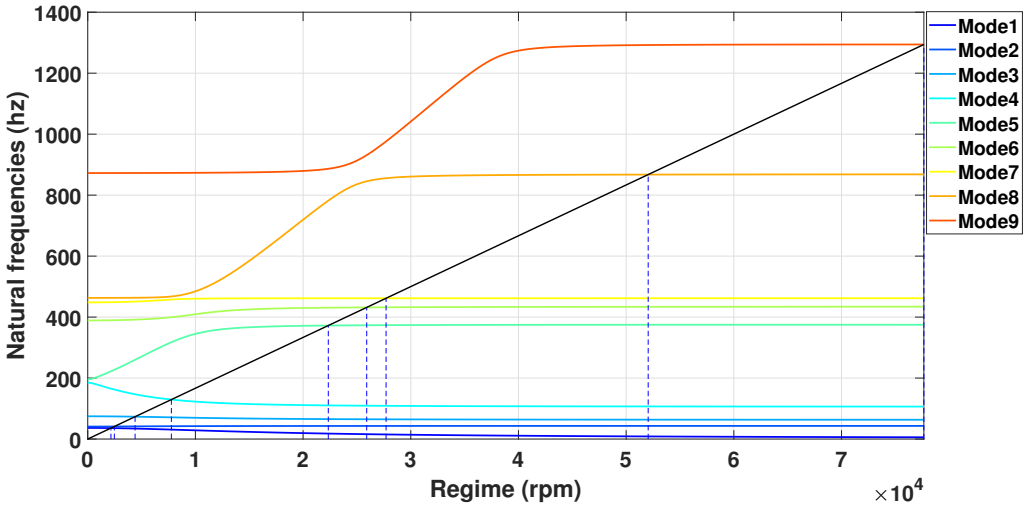

Figure 5.10: Campbell diagram of the modified Jeffcott-Laval rotor with non-symmetrical supports.

critical speed bases of the same size, in the case of a system with non-symmetrical supports. In order to obtain a global measure of the capacity of these two bases to generate the complete response of the system, is evaluated the minimum angle α_{mod} and α_{cs} between the exact displacement field $\hat{\mathbf{q}}_f(\omega)$ at the frequency ω and respectively, the classical modal basis Φ (9 modes) and the critical speed basis Φ_{cs} (9 critical speed modes) [Festjens, 2013]. The evaluation of the angle α_{mod} and α_{cs} are performed using the MATLAB function `subspace`, the results are reported in Figure 5.12.

$$\alpha_{mod}(\omega) = min\left\{arccos\left(\frac{\langle \hat{\mathbf{q}}_f(\omega), \Phi \rangle}{||\hat{\mathbf{q}}_f(\omega)|| \cdot ||\Phi||}\right)\right\} \tag{5.23}$$

$$\alpha_{cs}(\omega) = min\left\{arccos\left(\frac{\langle \hat{\mathbf{q}}_f(\omega), \Phi_{cs} \rangle}{||\hat{\mathbf{q}}_f(\omega)|| \cdot ||\Phi_{cs}||}\right)\right\} \tag{5.24}$$

A conventional complex modal analysis performed at $\Omega^s = 0$ rpm (or generally $\Omega^s = const.$), solving the classical eigenvalues problem expressed in Equation 5.8, produces a basis of normal modes which describes the physics of the system in a fixed state s. This modal basis cannot be employed to decompose the unbalance response of the system into independent modal contributions because it changes with the rotational speed variation. It is important to keep in mind that if this angle α is small, the compared vectorial sub-spaces are almost linearly dependent. The error is then evaluated by:

$$err(\omega) = sin(\alpha(\omega)) \cdot 100 \tag{5.25}$$

Observing Figure 5.12, one can notice that the minimum angle between the full response and the critical speeds basis is at any frequency lower than the one evaluated using the classical modal basis. The critical speed basis represents the full response better than a

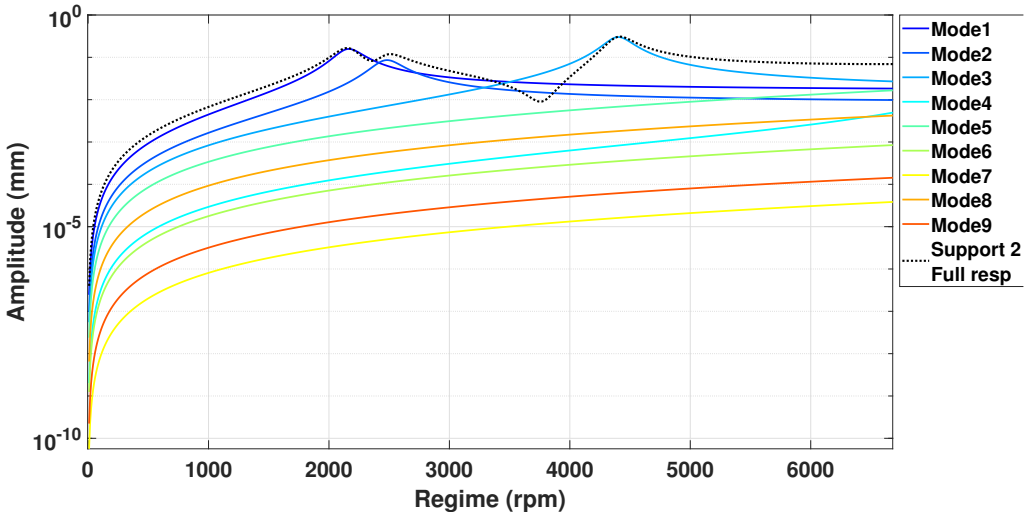

Figure 5.11: Unbalance response of support #2 along X direction decomposed using the first 9 critical speed modes.

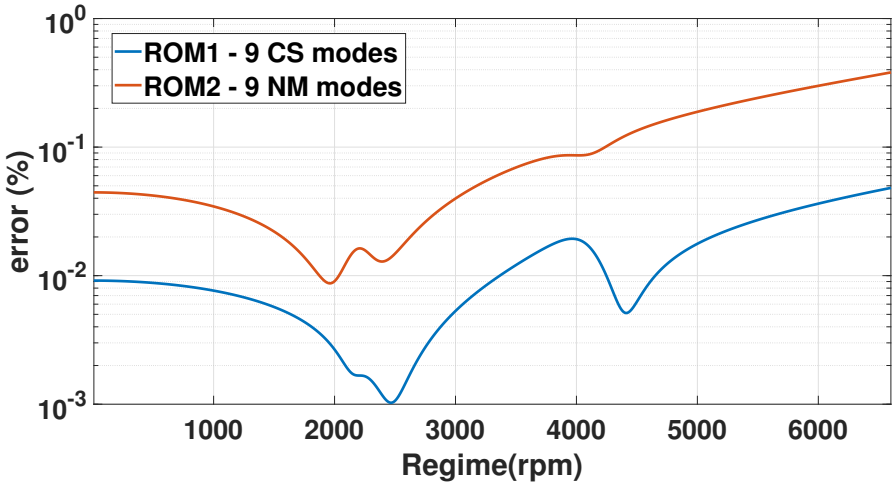

Figure 5.12: Minimum angle between the full response of the system frequency per frequency and ROMs: 9 critical speed (CS) modes and 9 normal modes (NM).

classical modal basis with the same amount of modes.

3.4 Nonlinear HB study of the modified Jeffcott-Laval rotor with non-symmetrical supports

The non-symmetrical system is now studied in a nonlinear framework using the HBM algorithm, adopting the same type of modal reductions proposed in previous sections. The rotor/stator contact is simulated adopting the contact formulation proposed in Equation 5.18, with a gap $C = 2mm$, a nonlinear stiffness $K_c = 1e8N.mm$ and an unbalance of $0.02kg.m$ positioned on the Disc #1.

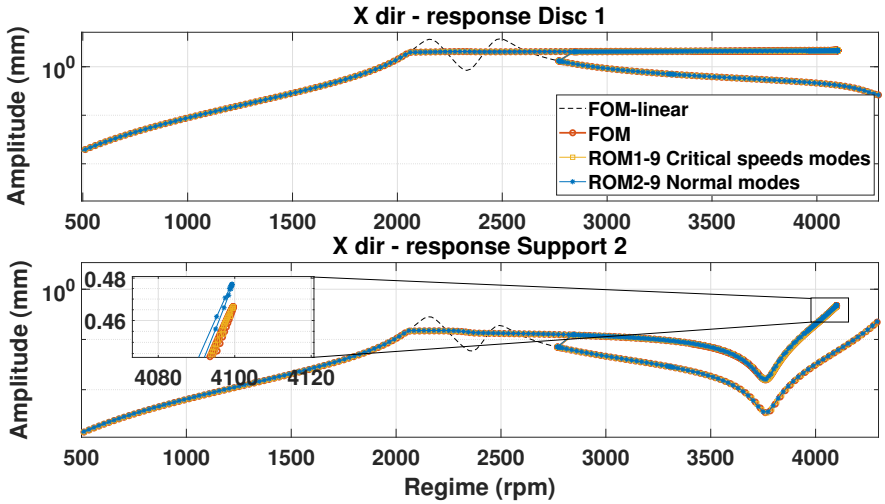

Figure 5.13: Nonlinear response of the Jeffcott rotor with rotor/stator rub.

The response of the nonlinear system are reported in Figure 5.13. To evaluate the global quality of a ROM on the whole displacements field $\hat{\mathbf{q}}_f(\omega)$ in nonlinear applications, the following *Root Mean Square Error* (RMSE) has been evaluated and reported in Figure 5.14:

$$RMSE(\omega) = \frac{\sqrt{\sum_{k=1}^{NDOFs}(\hat{\mathbf{q}}_f^k(\omega) - (\Phi_k \cdot \hat{\mathbf{u}}(\omega)))^2}}{\sqrt{\sum_{k=1}^{NDOFs}(\hat{\mathbf{q}}_f^k(\omega))^2}} \cdot 100 \tag{5.26}$$

The comparison between the FOM and the ROMs is proposed on the branch of the solution in the range of $[0 - 4100]$ rpm , before reaching the turning point at ≈ 4100 rpm. Results of the same order are produced after the turning point. Moreover, since the HBM algorithm employs an auto-adaptative step-size, the solution has been interpolated to be compared in the same exact frequency points and to produce Figure 5.14. Some noise is located in the frequency range of 2000 to 2500 rpm, related to an error due to the interpolation of the nonlinear curves.

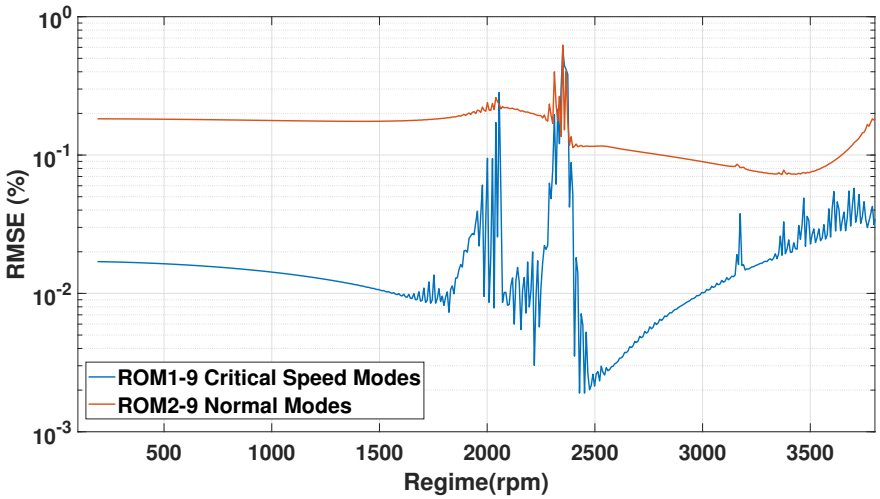

Figure 5.14: Root-mean-square error (RMSE) on the whole displacements field : FOM vs ROMs.

One can notice that even in a nonlinear working condition, a critical speed basis allows to represent the the response of the system with a higher precision than a classical modal basis with the same amount of modes.
Defining the *Offline time* as the time demanded to evaluate the reduction basis and the *Online time* as the nonlinear simulation time, is interesting to compare them in the cases of ROM1, ROM2 and FOM. This data is reported in Table 5.5. One can conclude that the critical speed basis take more time than a classical modal basis with the same amount of modes to be evaluated.

	FOM	ROM1 - 9 CS	ROM2 - 9 NM
Offline time (norm. Time)	0	5e-4	1e-4
Online time (norm. Time)	1	0.28	0.26

Table 5.5: Computational effort related to the simulations of the Jeffcott rotor.

4 Critical speed subspace reduction : whole aero-engine study case

The critical speed reduction has been applied on an academical model in previous sections, it is now interesting to estimate the efficiency in terms of precision and computational burden of the presented method on an industrial scale FE model. The considered FE model is the one representing a whole aeroengine reported in Section 3.2 (see Figure 5.15). As already said, the details of the considered model are not given explicitly in this work for

confidentiality reasons, the results are normalised too.
The considered model is studied at first in a linear framework, to display the efficiency of the technique investigated in this section in comparison to more classical methods. Then a study in nonlinear framework is conducted as well.

The considered system is a twin-spool engine with a low pressure rotor working in the frequency range of $[Idle1 - Redline1]$ $rpms$ (the value $Redline1$ is referred as *Redline* (RL) in the following sections of this work), the high pressure module works in $[Idle2 - Redline2]$ $rpms$. Figure 5.16 reports the normalised working regimes of the low and high pressure shafts with respect to the low pressure module regimes.

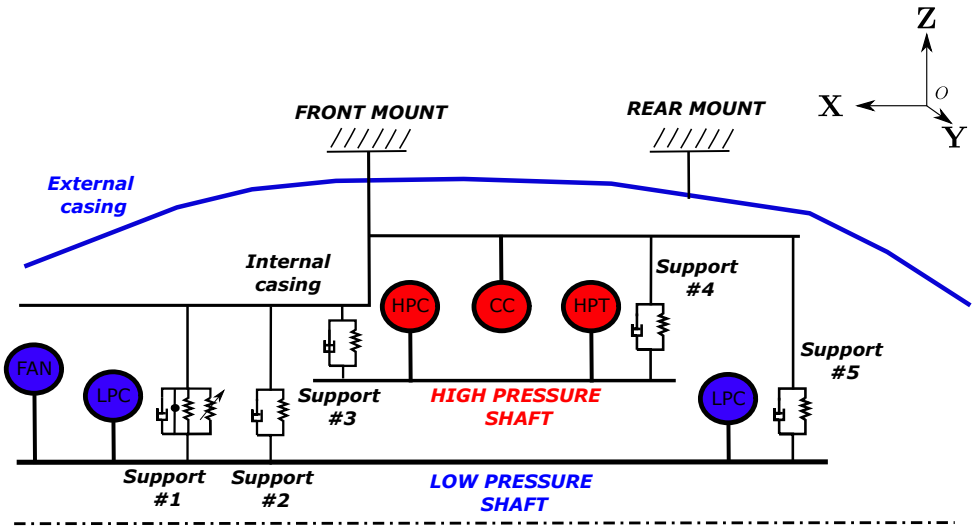

Figure 5.15: Simplified representation of a commercial aeroengine.

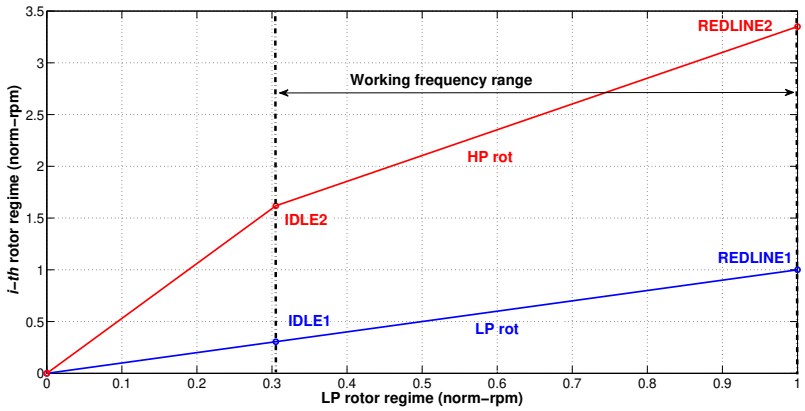

Figure 5.16: Normalised working regimes of the considered aeroengine.

4.1 Numerical model treatment

FE models in this work are generated and managed using NASTRAN 2018, as well as simulations in frequency and time domain on the FOMs. The FOM is then exported to MATLAB environment in order to perform model reduction operations and any sort of analysis on the ROM (see Figure 5.17). With no loss of generality, the results obtained in this work can be reproduced using any another combination of software, nevertheless it seems essential to use a commercial FE software to manage large scale FE models.

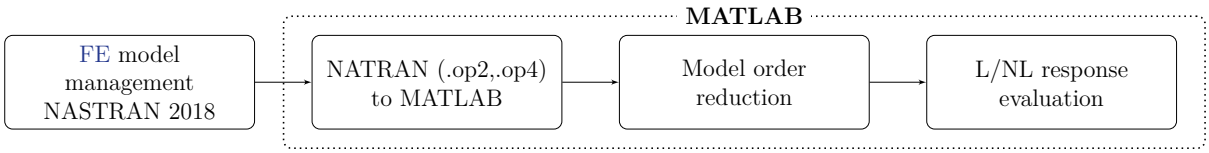

Figure 5.17: CM simulation chain.

4.2 Linear framework - Frequency response

In this section multiple classical model order reduction approaches are presented and compared using a criterion based on the aeroengine's *Redline* (RL). Only linear frequency responses are taken into account, solving Equation 5.10 in a linear framework and using different ROMs.

As already said, we are interested in the dynamical response of the engine in the working frequency range (see Figure 5.16), dynamical phenomena out of this frequency band are out of the scope of the analysis. Since this work is oriented toward the linear and nonlinear unbalance response and considering that the unbalance is a synchronous excitation, one can use the reduced sets of modes included into the frequency band to reduce the size of the problem through a Ritz Reduction (see Equation 5.11). Generally, the frequency range considered for the model reduction goes until $1.5 \cdot RL$ or $2 \cdot RL$ in order to take into account vibration modes arriving immediately after the RL, these modes can impact the response of the system in the working frequency range and produce a more accurate approximated response.

In structural dynamics this modal reduction is very similar to the *modal truncation* [Dickens, 1997], modal reduction using normal modes is adopted in this section comparing three different bases of modes : ROM1 containing any normal modes with frequency included into the range $[0 - RL]$, ROM2 and ROM3 contain normal modes with frequency included respectively in $[0 - 2 \cdot RL]$ and $[0 - 3 \cdot RL]$.

It is usual in structural dynamics to enrich modal bases with static residuals [Ben Smida, 2012] or to use multi-model approaches [Sternchüss, 2009a] in order to improve the accuracy of ROMs. Static residuals are calculated using the relation reported in Equation

5.27.

$$\tilde{\mathbf{q}} = \Phi \cdot (\Phi^T \cdot \mathbf{K}_{dyn} \cdot \Phi)^{-1} \cdot \Phi^T \cdot \mathbf{f}_{res} \tag{5.27}$$

The residual displacement is:

$$\mathbf{q}_{res} = \tilde{\mathbf{q}} - \mathbf{K}_{dyn}^{-1} \cdot \mathbf{f}_{res} \tag{5.28}$$

with:

$$\mathbf{K}_{dyn} = \mathbf{K} \tag{5.29}$$

$\mathbf{f}_{res}$ is a unitary vector with ones corresponding to the DOFs of the unbalanced nodes. This enrichment technique is classical and efficient in cases of non rotating systems. For rotating machines, one can take into account dynamical terms too (gyroscopic, etc.) as seen in Equation 5.30, relevant in the case of rotating shafts. In this case $\mathbf{K}_{dyn}$ is:

$$\mathbf{K}_{dyn} = -\Omega_d^2\, \mathbf{M} + j\Omega_d \left(\mathbf{D_v} + \textstyle\sum_{i=1}^{r} \Omega_i \mathbf{G}_i\right) + \mathbf{K} + j\mathbf{K}\eta_h \tag{5.30}$$

Residual vectors can be evaluated at multiple rotational speeds Ω_d. The residual vector $\boldsymbol{u}_{res}$ have to be orthonormalized with respect to the basis Φ using a *Singular Values Decomposition* (SVD) or with a Graham-Smith algorithm, obtaining $\boldsymbol{u}_{res}^{\perp\Phi}$. The enriched basis is finally expressed in Equation 5.31.

$$\Phi_{rich} = [\Phi \quad \mathbf{q}_{res}^{\perp\Phi}] \tag{5.31}$$

The ROM4 is obtained using this procedure, enriching the ROM3 with multiple residual dynamical vectors evaluated at $\Omega_d = [0\ , \frac{\Omega_{RL}}{2}\ , \Omega_{RL}]$. Finally, two ROMs are presented using the critical speed approach introduced in the above sections: the ROM5 and the ROM6 contain respectively critical speed modes with frequency included into the frequency range $[0 - RL]$ and $[0 - 1.5 \cdot RL]$. Table 5.6 summarises the ROMs presented in this section.

Name of ROM	Type of ROM	Frequency Criterion
$ROM1$	Normal modes	$[0 - RL]$
$ROM2$	Normal modes	$[0 - 2 \cdot RL]$
$ROM3$	Normal modes	$[0 - 3 \cdot RL]$
$ROM4$	Normal modes + Dynamical enrichement	$[0 - 3 \cdot RL]$ + Dynamical enrichment
$ROM5$	Critical speed modes	$[0 - RL]$
$ROM6$	Critical speed modes	$[0 - 1.5 \cdot RL]$

Table 5.6: ROMs for the study in linear framework.

All the presented ROMs are used to evaluate the unbalance response of the aeroengine with an unbalance of $1000\, cm \cdot g$ applied on the fan. The unbalance responses evaluated

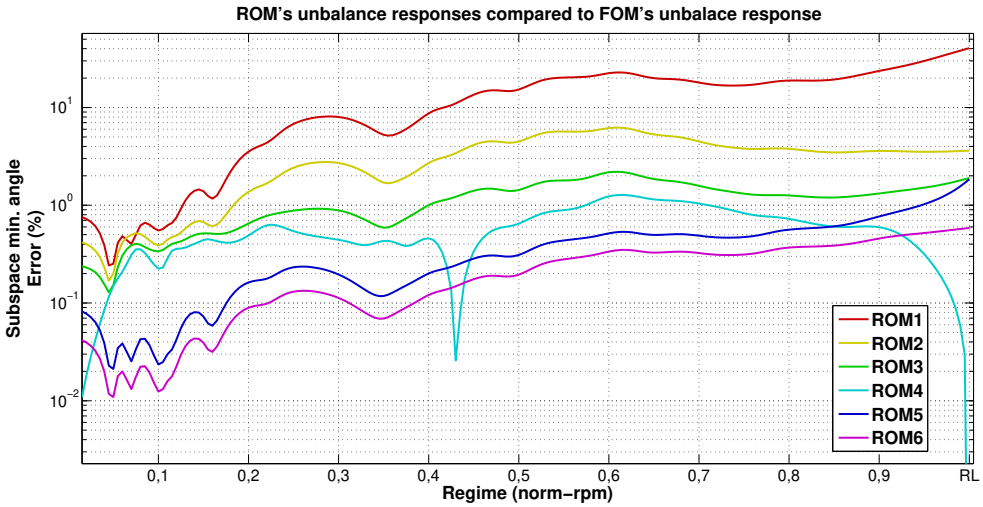

Figure 5.18: ROM's unbalance response vs FOM's unbalance response.

with the ROMs are compared with the unbalance response of FOM using the minimum angle between responses at any frequency point as seen in equations 5.23 and 5.24. Comparisons are reported in Figure 5.18. One can notice that increasing the number of modes in modal basis there is a consequent reduction of the error (one can see ROM1 vs ROM2 vs ROM3). The dynamical enrichment allows to improve locally the quality of responses, around the enrichment points $\Omega_d = [0\ ,\ \frac{\Omega_{RL}}{2}\ ,\Omega_{RL}]$ (see ROM3 vs ROM4). Critical speed reductions are always better in terms of accuracy than the classical normal modes reduction at any frequency range. It is interesting to notice that the ROM5 is even better than the ROM3 (which contains an higher amount of modes than the ROM5).
Any of the presented ROM displays the most important error around the RL, which is a very sensitive zone because the higher stress and displacements in the machine are produced at these working regimes as the excitation is maximal at this regime. It is thus interesting to enrich ROMs around the RL.

In order to better understand the error generated using the produced ROMs we consider the ROM3 and the ROM6. First of all we focus on ROM3: we can compare the difference between the maximum displacement on any DOF of the system. We decided to observe the maximum value to perform this comparison because it has a relevant role in engineering design. The first graphic on the left of Figure 5.19 shows a direct comparison between the maximum values of the unbalance response of the FOM and the ROM3 on any DOF of the system. In the second and third graphic on the left of Figure 5.19 the absolute and relative error between the maximum values of the FOM and ROM3 on any DOF. In this analysis a mean error on the maximum values of 0.56% and a maximum error of 7.46% on a specific node (worst case reported in Figure 5.19b) have been measured (see Figure

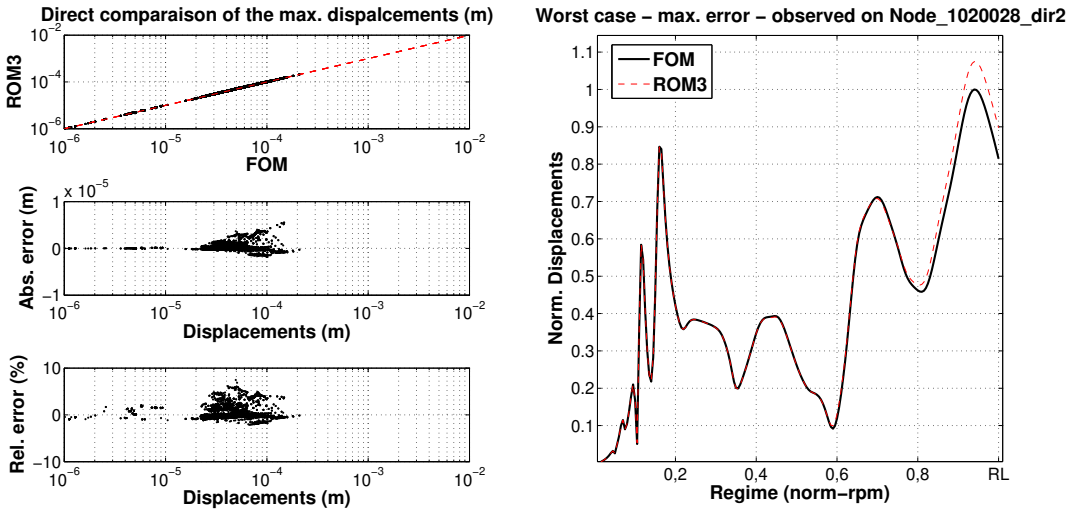

Figure 5.19: a) Comparison between the maximum FOM vs ROM3. b) Worst case produced with ROM3.

5.19).

The same analysis is also presented using the ROM6. In this case we have a mean error on maximum values of 0.03% and and a maximum error of 4.87% on a specific node reported in Figure 5.20. Even if the performance are improved using the ROM6, responses display

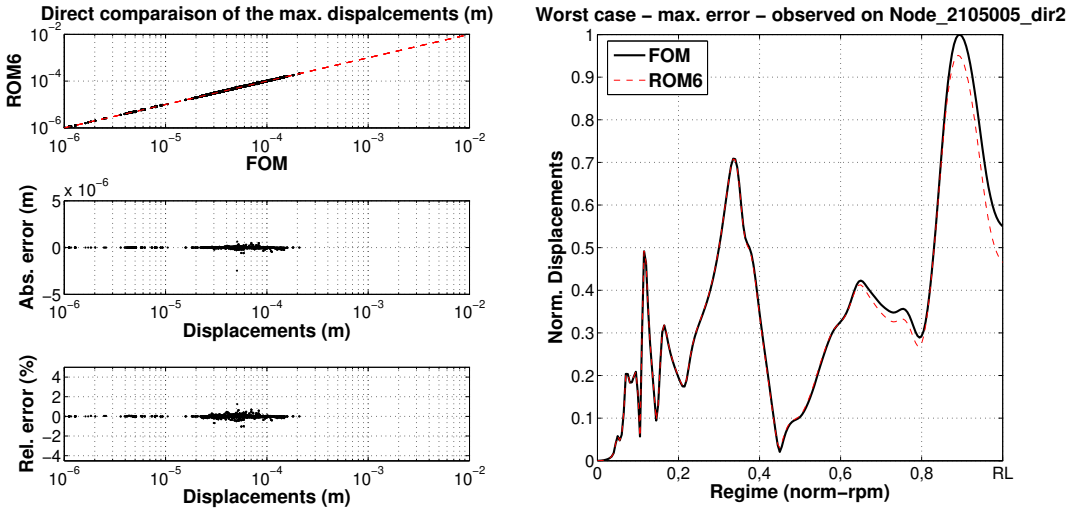

Figure 5.20: a) Comparison between the maximum FOM vs ROM6. b)Worst case produced with ROM6.

always a non negligible gap around the RL (see Figure 5.20b). It seems thus essential to enrich the reduction basis with a dynamical residual evaluated at $\Omega_d = \Omega_{RL}$, obtaining a relevant improvement of the ROM's accuracy around the RL (see Figure 5.21). This enriched ROM6 produces a mean error of 0.2% and a maximum error of 0.19% (see Figure

5.21 b).

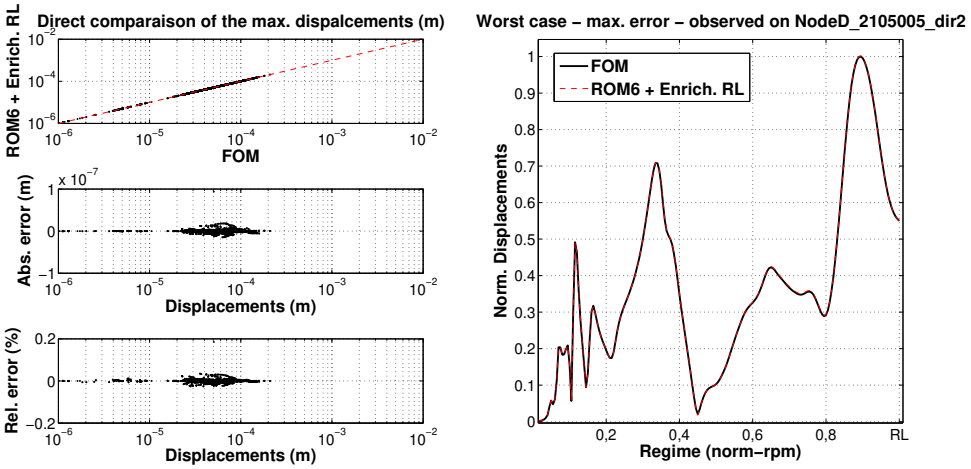

Figure 5.21: a) Comparison between the maximum FOM vs ROM6 enriched with res $\Omega_d = \Omega_{RL}$. b)Worst case produced with ROM6 enriched with res $\Omega_d = \Omega_{RL}$.

Table 5.7 reports the performances of the produced ROMs. Two CPU times are relevant in this study: the CPU time relative to the evaluation of the reduction basis and the CPU time relative to the unbalance response. The mean and maximum error are reported on any observed ROM. The total CPU time and the mean error are reported graphically in Figure 5.22. From Figure 5.22 one can notice that the classical modal reduction is cheaper than the critical speed one in terms of computational effort, but the accuracy of the critical speed approaches produce more accurate ROMs. The ROM4 (normal modes enriched with residual vectors) is almost equivalent in terms of mean error and maximum error to ROM6 which is evaluated using the critical speed approach and contains more dynamical modes than this last one, thus more expensive in terms of computational effort. From Figure 5.22, one can conclude that the ROM5 is the optimal choice in terms of computational effort and accuracy, for this reason, this last ROM is adopted in the further sections of this work.

Model	Nb. of Modes	CPU time Basis evaluation +Unb.Resp. (norm.)	CPU time Tot. (norm.)	Mean error (%)	Max error (%)
FOM	//	0.000+1.0	1.000 (ref.)	0% (ref.)	0% (ref.)
ROM1	95	0.007+0.084	0.091	5.7%	76.8%
ROM2	323	0.026+0.082	0.108	1.03%	12.3%
ROM3	616	0.063+0.087	0.150	0.56%	7.46%
ROM4	622	0.063+0.093	0.156	0.03%	4.87%
ROM5	194	0.032+0.084	0.116	0.17%	13.3%
ROM6	406	0.098+0.086	0.183	0.03%	3.6%
ROM6 + Enrich. RL	408	0.098+0.086	0.184	0.0021%	0.2%

Table 5.7: ROM's performances in linear framework.

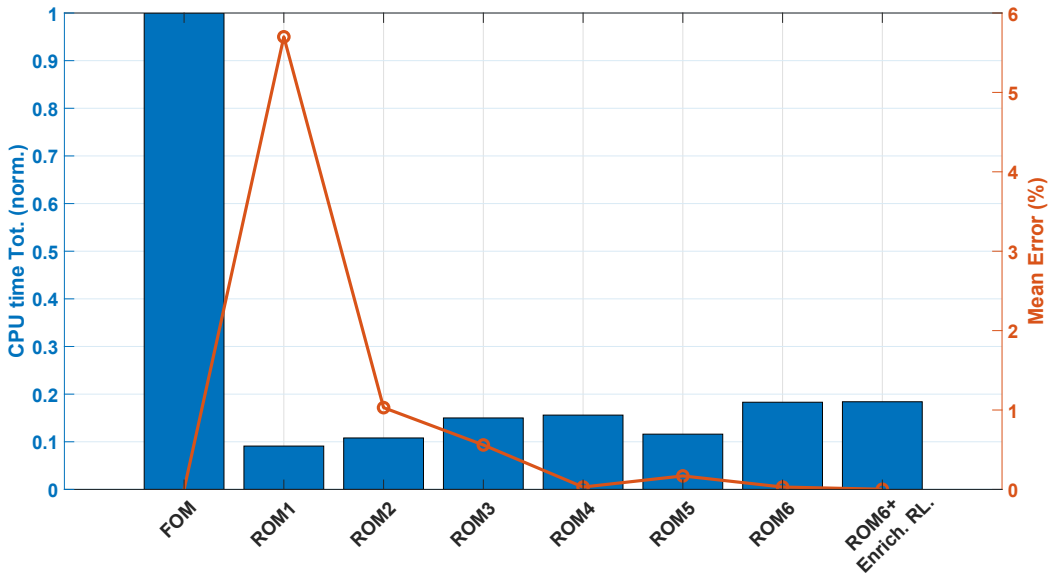

Figure 5.22: Unbalance response's mean accuracy vs CPU time.

4.3 Nonlinear framework study - Time marching

It is now interesting to observe the efficiency of the numerical reduction method described in this chapter in a nonlinear framework using a time marching algorithm. In this section the system under exam includes a nonlinear effect on the support #1: a nonlinear contact generating a full annular rub phenomenon in the aeroengine. The nonlinear force

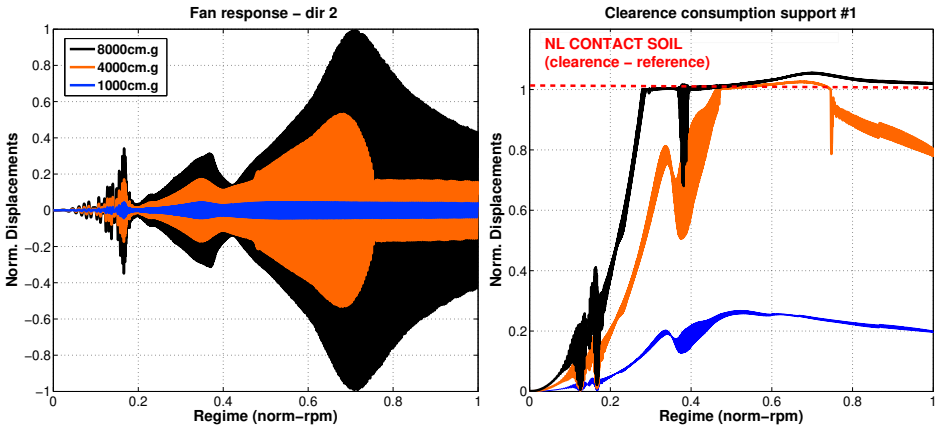

Figure 5.23: a) Fan response , b) Clearance consumption of the support #1.

is managed once again by Equation 5.18, with a nonlinear stiffness of $1e10N.m$ and a normalized clearance consumption of 1.

In this study the ROM5 is used and the nonlinear response evaluated with this ROM is compared with the FOM's response taking into account the nonlinear contact. Three different load cases are considered, using an unbalance load of $1000cm.g$, $4000cm.g$ and $8000cm.g$.
Simulations are performed on one hand in NASTRAN 2018, using the NASTRAN's solver known as `SOL129` for the transient analysis of the FOM. On the other hand, simulations are performed in MATLAB using the explicit time integration solver `ODE15s`, specially adapted to stiff nonlinear problems with an adaptive time step.

Figure 5.23 reports the time response of the fan and the shaft's support #1 evaluated with the FOM. One can notice that in the simulation with unbalance $1000cm.g$, the nonlinear contact is not established while it is in the two other cases. The response of the fan is reported for the three load cases in Figure 5.23a and nonlinear effect is managed by the clearance consumption of the support #1 reported in Figure 5.23b. The results reported in Figure 5.23 are evaluated using the FOM. As example the response of the fan along the Y axis evaluated with the FOM and the ROM are compared directly in Figures 5.24a and 5.24b, with a maximum error of approximately 7%.

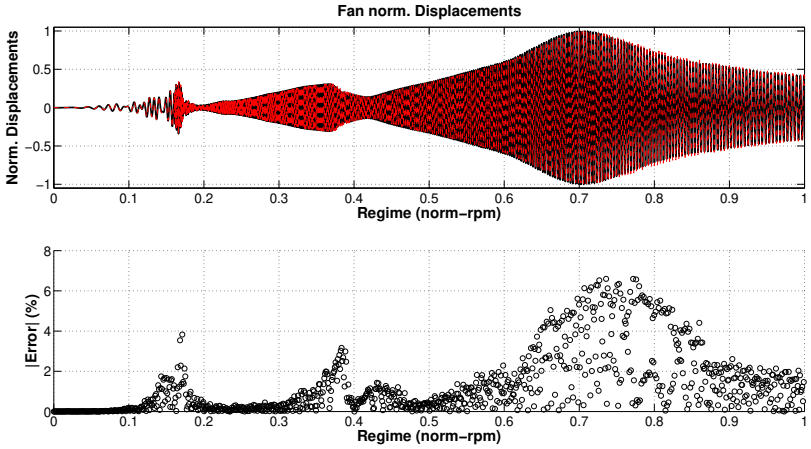

Figure 5.24: Fan response evaluated with ROM5 and FOM.

To have a global point of view on the accuracy of ROM5, the maximum displacements of any DOF are compared on the whole displacement fields evaluated respectively with ROM5 and FOM (see Figure 5.25a). The ROM5 produces a mean maximum error of 1.5%, in the worst case the error is 10.3% (see Figure 5.25b).

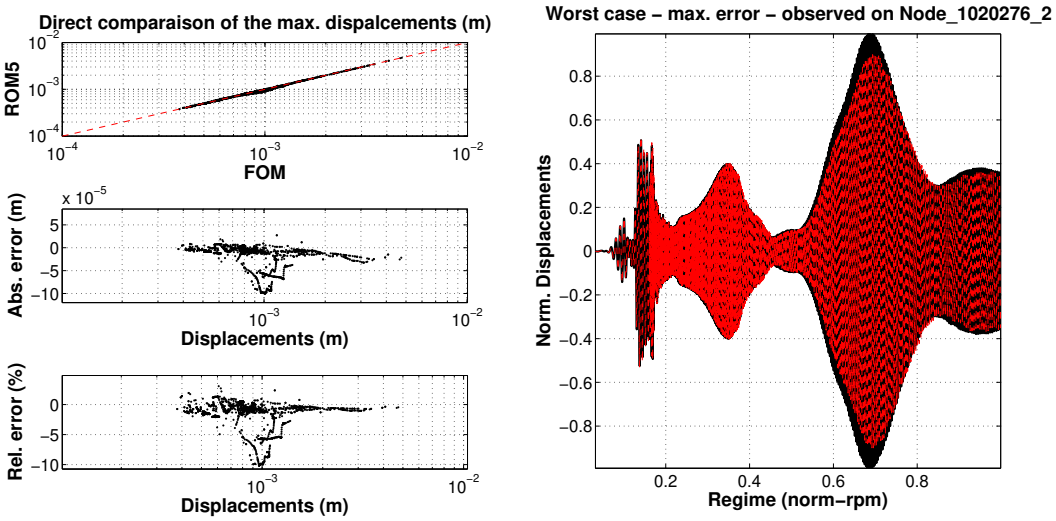

Figure 5.25: a) Comparison between the maximum FOM vs ROM5. b)Worst case produced with ROM5.

The same study is performed on the two other load cases: unbalance load of $1000cm.g$ and $4000cm.g$ the results are summarized in Table 5.8.

Load case	CPU time FOM	CPU time ROM	CPU Time Reduction (ratio)	Mean error (%)	Max error (%)
1000 cm.g	0.288	0.011	26	1.3%	8.02%
4000 cm.g	0.56	0.023	25	2.0%	10.4%
8000 cm.g	1 (ref.)	0.045	22	1.5%	10.3

Table 5.8: ROM5 performances in nonlinear framework.

From Table 5.8 one can observe a relevant reduction in computational effort with a relatively low mean error. The error and the time reduction produced with the model reduction is almost the same for the three load cases. This model reduction approach is proven to be efficient in time marching simulations too thanks to the results presented in this section.

5 Conclusions and perspectives

The Ritz reduction dedicated to rotating machines observed in this section has been evaluated in linear and a nonlinear frameworks proving its efficiency compared to more classical model reduction methods. This model reduction approach represents the natural equivalence of the classical modal reduction for non-rotating structures.

The first study presented with the simplified model, allows to validate the reduction technique in a controlled environment. On the other hand, the second study case, presented on the industrial scale FE model, allows to prove the scalability of the presented technique and its efficiency in multiple frameworks.
The critical speed basis is more demanding than a classical modal basis to be evaluated, but the increase in offline time is compensated by more accurate ROMs than the ones produced using more classical methods.

Model reduction approaches as presented in this section are classical and well known in the field of structure dynamics. In this work we want to introduce a new paradigm of model reduction allowing to push forward the classical definition of model reduction using surrogate modeling in order to produce SM-ROMs accurate enough for industrial purposes and faster to interrogate than a classical CM ROM in order to work efficiently in many-query frameworks.

Chapter 6

Surrogate modeling approaches for nonlinear rotating systems

"The only source of knowledge is experience."

Albert Einstein: German-born, theoretical physicist, Nobel prize (1879-1955)

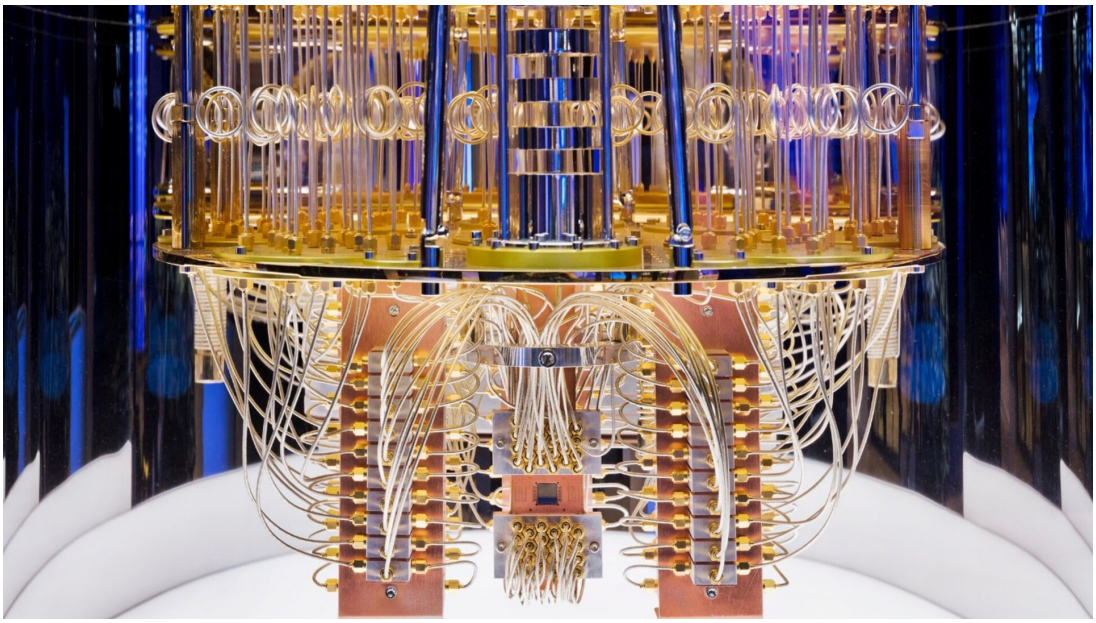

Objectives

Finite element models become more and more advanced and complex thanks to improvement of computational means. The numerical simulations for industrial scale applications are nevertheless expensive in terms of computational effort, it is quite hard today to use a detailed FE model to study a large number of variants of the same system. In many-query frameworks (sensitivity or robustness analysis, model updating, etc.) the FE models are simplified or strongly reduced with a consequent loss of accuracy.

Recent machine learning methods can be employed to obtain surrogates of the original model extremely faster in simulation and that can be employed for the High-Performance Computing (HPC). These surrogate models are based on the experience obtained from a set of numerical (or physical) experiments: Design of Experiments (DoE). To train an affordable surrogate model it is essential to keep low the DoE evaluation time.

This work wants to explore multiple surrogate modeling (SM) techniques and identify the best option in terms of computational effort and accuracy to reproduce the nonlinear unbalance responses of industrial scale aeronautical turbo machines. Two different surrogate modeling approaches will be examined in this work: firstly a punctual prediction of the most critical points of the unbalance responses using *Radial Basis Neural Networks* (RBNNs) or Kriging method, then a more challenging approach which aims to reproduce the whole frequency response on a set of strategical DOFs using a POD-based surrogate modeling technique known as POD-SM.

Contents

1 Introduction

Despite recent improvements in *High Performance Computing* (HPC), the increase of complexity of industrial *Finite Element* (FE) models (large size of the FE model, nonlinear, reliability analysis etc.) makes their use extremely time consuming for many-query frameworks such as sensitivity analysis, reliability analysis or *Finite Element* (FE) model calibration. In order to be able to deal with such complex FE models and to reduce the computational burden, alternative methods are being continuously proposed in a large range of applications. These novel approaches are based on a large number of simulations or experimental data and derive from developments in the field of *Machine Learning or Artificial Intelligence*. In this work, several methods of machine learning are adopted to predict the nonlinear dynamical response of complex rotating systems excited by a synchronous driving force (e.g. unbalance) in order to reduce the simulation time and better understand the impact of the scalar parameters on the dynamical behaviour of the rotating machine (such as support stiffness, damping, mass, nonlinear properties, etc.).
We are interested in *Surrogate Model* (SM) able to reproduce the evolution of the linear or nonlinear *Frequency Response Function* (FRF) of a rotating system in different dynamical configurations [Sobester, 2008; De Munck, 2009; Wang, 2017] with a focus on the phenomenon of rotor-stator contact.
Typical analyses in rotordynamics are the unbalance responses, linear and nonlinear, to study the response of rotating systems at any working regime and the critical speeds analyses to identify its own most dangerous rotational speeds [Lalanne M, 1998; Genta, 2007]. Sinou et al. in 2018 used the Kriging surrogate modeling technique to predict critical speeds and vibrations of a flexible rotor [Sinou, 2018]. Denimal et al. proposed a novel surrogate modeling approach to study the dynamics of rotating machines: combining the Kriging formulation with the generalised polynomial chaos theory [Denimal, 2021]. Several works are focused on the study of the stability of rotating systems with friction induced or squeal instabilities [Denimal, 2016; Denimal, 2018; Denimal, 2022b]. As well, Denimal et al. adopt this approach to study the evolution of the critical speeds with parametric uncertainties and the associated displacements amplitudes without taking into account contact or journal's nonlinearities, the observed system behaves linearly [Denimal, 2022a]. Ma et al. adopt the classical Kriging approach to predict the nonlinear response of a rotor with rub/impact nonlinearity [Ma, 2022]. In their work, Kriging models replace the FE model to perform a reliability analysis, with a comparison between numerical and experimental data. Nevertheless, the proposed model is limited to only one dynamical nonlinear mode within the frequency range of interest, simplifying the inference. Moreover, the surrogate model predicts the evolution of the nonlinear response of the *Degree Of Freedom* (DOF) in contact with the stator and nowhere else. The Kriging method seems to be very efficient for the prediction of this type of nonlinear response but

it becomes costly when expanded to multiple DOFs.
Other types of surrogate models exist and are adopted in rotordynamics, such as *Radial Basis Neural Networks* (RBNN)s or *Polynomial Response Surfaces* [Glaz, 2009; Karayiannis, 1997; Spooner, 1999; Chen, 2020]. These methods are employed and compared to perform parametric optimisations and they are widely used in mechanical engineering for their simplicity and efficiency [Jin, 2001].

Another family of techniques widely applied in structural dynamics are based on the *Proper Orthogonal Decomposition* (POD), also known as *Karhunen-Loève Method* (KLM) [Kim, 1998; Kim, 2015; Lu, 2019; Liang, 2002], and can be coupled with RBNN (POD-RBNN) or other forms of surrogate models (POD-SM, *non-intrustive-POD* (niPOD) [Benamara, 2017b], PODi etc.) to obtain a vectorial predictor which can be very efficient in problems of linear and nonlinear dynamics when a whole FRF must be predicted. POD is applied to identify the essential elements of the dynamics of a physical phenomenon from a set of full-field simulations defined by Sirovich as *Snapshots* [Sirovich, 1987]. This technique identifies a few dominant but independent modes defining the dynamics of the system, strongly reducing the computational effort of the simulation with a negligible loss in accuracy. Classical POD reduction has already been applied in rotordynamics in several works to reduce the size of the model in linear and nonlinear cases, with no coupling of the POD method with surrogate modeling techniques [Meyer, 2003; Jin, 2019; Aguirre, 2019; Balmaseda, 2020]. POD-SM methods are widely applied in fluid-mechanics [Benamara, 2017a; Benamara, 2017b; Hinze, 2005; Braconnier, 2011] and other mechanical fields (fracture mechanics, solid mechanics, etc.) [Hamim, 2017; Lu, 2016; Benaissa, 2016; Sampaio, 2007]. However, to the author's best knowledge, the POD-SM techniques have not been used for the identification of linear and nonlinear frequency responses of rotating machines at the industrial scale.

It is interesting to cite another machine learning approach for structural dynamics, proposed by Gibanica et al. [Gibanica, 2021], consisting in modeling the linear response of a complex structure by predicting the evolution of the system's principal modes with respect to the design parameters to quantify the uncertainty on these parameters. In this case a *Gaussian process* surrogate is trained on the modes shapes of the system. A limitation of this approach appears in the treatment of nonlinear problems. Cenedese et al. proposed an innovating machine learning approach to predict the response of weakly nonlinear systems through the study of the *spectral submanifolds* [Cenedese, 2022a; Cenedese, 2022b]. The extension of this approach to industrial scale FE models appears expensive in terms of computational effort.

The present work compares several methods to develop an efficient surrogate model-

ing technique to predict the nonlinear frequency response of a rotating system with rub/contact nonlinearities. In particular, this work is focused on three types of surrogate modeling approaches: RBNN, Kriging and POD-RBNN. These approaches are applied on nonlinear industrial scale rotating systems ($\approx 1e6 - 1e7$ DOFs). The responses of the system are predicted on 20 DOFs carefully chosen, the extension to a higher number of DOFs is direct and doesn't represent a limitation. The RBNN and Kriging approaches are employed to predict the positions of maximum displacement and the relative frequency of several DOFs. The POD-RBNN approach is employed to predict the whole response of the system of the DOFs of interest.
This chapter is structured as follows. After this introduction, the mathematical background is proposed in Section 2. The third section is dedicated to the presentation of the simulation chain. The fourth section presents an original method to accelerate the model reduction procedure and to reduce the computational effort of the whole surrogate modeling process. The fifth section is dedicated to apply the proposed surrogate modeling techniques to an industrial FE model. Finally, in the last section, our conclusions are drawn and future perspectives are given.

2 Mathematical background

One of the most important numerical operations performed in rotordynamics is the unbalance response. Rotating systems are naturally unbalanced and it is physically impossible to perfectly balance a rotating machine. It is thus essential to be able to identify the unbalance response of the rotating system over the whole operational frequency range. In the most general case, the unbalance response is evaluated using Equation 6.1, taking

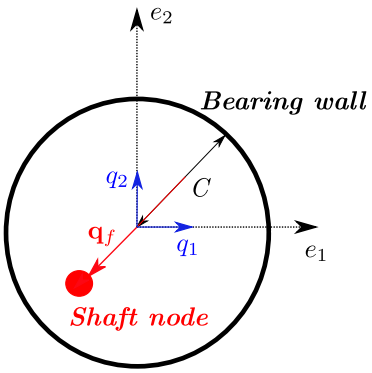

Figure 6.1: Rotor/stator interaction representation.

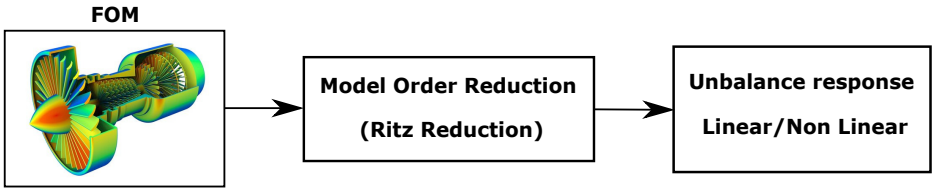

Figure 6.2: Classical workflow in structural dynamics.

into account nonlinear phenomena as well.

$$(-\omega^2\mathbf{M} + j\omega(\mathbf{D_v} + \sum_{i=1}^{r}\Omega_i\mathbf{G}_i) + \mathbf{K} + j\mathbf{K}\eta_h)\,\hat{\mathbf{q}}_f + \hat{\mathbf{f}}_{\mathbf{nl}}(\hat{\mathbf{q}}_f) = m\,e\,\Omega^2\,\hat{\mathbf{f}} \tag{6.1}$$

The physical properties of the system are described in matrix form using a FE formulation: the mass ($\mathbf{M}$), the viscous damping ($\mathbf{D_v}$), the gyroscopic effect of the *i-th* rotor ($\mathbf{G}_i$), the stiffness ($\mathbf{K}$), the hysteretic damping ($\mathbf{K}\eta_h$). In Equation 6.1 the term $\hat{\mathbf{f}}_{\mathbf{nl}}(\hat{\mathbf{q}}_f)$ represents the effect of nonlinear forces, assumed as purely dependent of the displacements $\hat{\mathbf{q}}_f$. The unbalance force is a centrifugal load defined by the term $me\,\Omega^2$, where m is the value of the unbalance mass, e is the distance of this mass from the rotation axis and Ω is the rotational speed of the unbalanced rotor. The excitation frequency is equal to the rotational speed of the rotor and for this reason, this type of excitation is defined as *synchronous driving force*. Nevertheless, linear behaviours are exceptions in the real world, they are usually perturbed by nonlinear phenomena acting on the system (nonlinear geometries, nonlinear contacts, nonlinear materials, etc.). This type of nonlinear problem is classically solved in the time domain with direct time integration methods [Hilber, 1977]. More recently, frequency domain solvers for the evaluation of the steady-state response of nonlinear systems have been proposed: we can cite the *Harmonic Balance Method* (HBM), the *shooting method* and others [Guskov, 2007; Krack, 2019]. The HBM is employed in this work for the solution of nonlinear problems. To highlight the influence of nonlinear phenomena in rotordynamics, a comparison between a linear and a nonlinear response is reported in the study case section (see Figure 6.12).

The nonlinear force considered in this work is generated by the rotor-stator contact. While rotating, if the rotor's displacements exceed a specific limit (see Figure 6.1) the system starts working in contact with the stator introducing additional forces. This type of nonlinear force is described by Equation 6.2.

$$\begin{cases} \mathbf{f}_{\mathbf{nl}}(\mathbf{q}_f(t)) = K_c \cdot (|\mathbf{q}_f^{cont.}| - C) \cdot \vec{\mathbf{n}} & if \quad ||\mathbf{q}_f^{disc1}|| \geq C \\ \mathbf{f}_{\mathbf{nl}}(\mathbf{q}_f(t)) = \boldsymbol{0} & if \quad ||\mathbf{q}_f^{disc1}|| < C \end{cases} \tag{6.2}$$

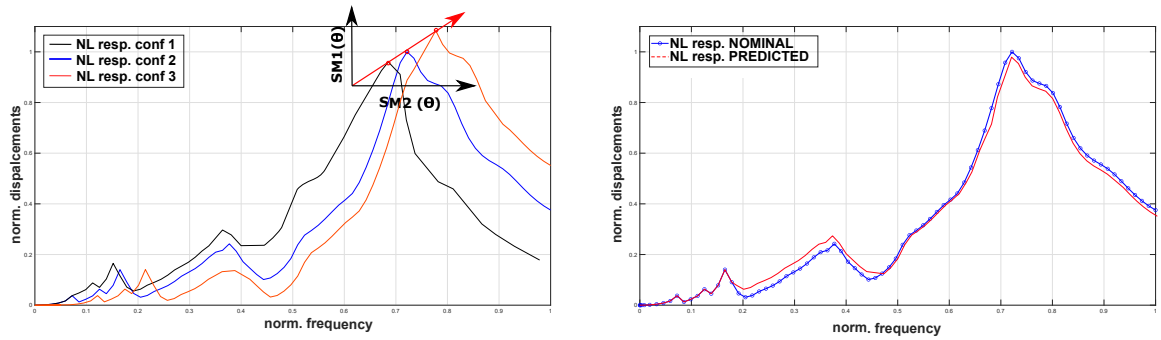

Figure 6.3: Surrogate modeling approaches: a) Surrogate modeling of the maximum amplitude and its frequency position, b) Surrogate modeling of the whole dynamical response of the system.

In structural dynamics, it is usual to reduce the complexity of the system using an approach based on the projection of the dynamical matrices on a *Ritz basis*. This principle has been derived in a large number of model reduction approaches [Schilders, 2008a; Wagner, 2010; Kumar, 2017]. The Ritz reduction in all its variants is performed employing the group of equations 6.3. In these equations, Φ is commonly called the *reduction basis* and contains the essential subspace of modes shapes able to span almost the full space of the solution in a specific frequency range. Generally, the modes shapes excited in a frequency range which is out of the scope of the analysis are removed from the reduction basis, in this way $dim(\mathbf{W}_r) << dim(\mathbf{W})$.

$$\begin{aligned} \mathbf{W}_r &= \Phi^T\ \mathbf{W}\ \Phi \quad \forall\ \mathbf{W} &&= \mathbf{M}, \mathbf{D_v}, \mathbf{G}_i, \mathbf{K} \\ \mathbf{F}_r &= \Phi^T\ \mathbf{F} \quad \forall\ \mathbf{F} &&= \hat{\mathbf{f}} \\ \hat{\mathbf{q}}_f &= \Phi\ \hat{\mathbf{u}} \end{aligned} \tag{6.3}$$

The model reduction method adopted in this work is dedicated to rotating structures and it is based on the employment of the modes shapes of the system excited when it runs through its own critical speeds [DAlessandro, 2022b; DAlessandro, 2022a].

The classical workflow used in the field of structural dynamics consists first of all in a model order reduction operation to reduce the size and complexity of the *Full Order Model* (FOM). Once the model reduced, Equation 6.1 can be solved with a reduced computational effort and an acceptable loss of precision (see Figure 6.2.
This simulation procedure can be expensive in both model reduction and unbalance response calculation phases and this is a severe limit if multiple variants of the system have to be studied (e.g. many-query applications).

In this work, several surrogate modeling approaches are compared to study the evolution

of the dynamical response of the system on a limited number of DOFs with dynamical parameters change. Two approaches have been identified to predict the dynamical behaviour of the system:

- Prediction of the evolution of the maximum response amplitude and the relative frequency considering these two quantities independently. This approach is referred as the *scalar approach* (see Figure 6.3a)).
- Prediction of the entire response. Referred as the *vectorial approach* (see Figure 6.3b)).

Concerning the scalar approach, several nonlinear data-fitting modeling techniques can be used to build the surrogates of the amplitude ($SM1(\theta)$) and frequency ($SM2(\theta)$) (see Figure 6.3a)):

- *Neural Networks* (NN);
- *Radial Basis Functions* (RBF);
- *Kriging*;
- *Support Vector Regression* (SVR);

More information concerning these methods are available in the literature [Bishop, 1995; Rippa, 1999; Jin, 2001; Sobester, 2008]. In order to obtain both an accurate and computationally efficient surrogate model for approximating in high dimensions, the RBNN and the Kriging approaches have been favoured in this work [Jin, 2001].

The RBNN develops a surrogate model $\tilde{\boldsymbol{y}}(\theta)$ of the nominal function $\boldsymbol{y}(\theta)$ combining linearly n radial basis functions $h(\theta, \sigma)$, as shown in Equation 6.4.

$$\tilde{\boldsymbol{y}}(\theta) = \sum_{i}^{n} w_i \cdot h(||\theta - c_i||, \sigma_i) \rightarrow \tilde{\boldsymbol{Y}}(\theta) = \nabla \boldsymbol{H}(\theta, \sigma) \tag{6.4}$$

Where w_i is a weight coefficient associated to the *i-th* RB function. Each RB function is defined by a centre c_i and a width σ_i. The training process of this type of surrogate model consists in finding the weights w_i minimising the error between the real outputs and those predicted by the model on the training points. Firstly the centre of the RB functions are positioned in the training points θ_{tr} ($c_i = \theta_{tr}^i$) in order to build the matrix $\boldsymbol{H}$. The weight vector is then evaluated directly during the training process as shown in Equation 6.5. The tuned RBNN interpolates always the training points. On the contrary, the quality of the predicted points (excluding training points) depends on the quality and quantity of the training data.

$$\nabla = \boldsymbol{H}^{-1}(\theta, \sigma)\ \boldsymbol{Y}(\theta_{tr}) \tag{6.5}$$

Different types of RB functions can be employed as *kernels* of the surrogate model: exponential, rational-quadratic, wave, Gaussian, multi-quadratic [Sobester, 2008; Bishop, 1995]. In this work, an algorithm to identify the optimum type of RB function is employed (Gaussian or multi-quadratic), this type of RBNN is referred to *Tuned Radial Basis Functions* (TRBF) by Sainvitu et al., for more details see [Sainvitu, 2010; Beaucaire, 2019]. The result of the prediction is a couple of scalar quantities (maximum amplitude and relative frequency) per DOF.

Concerning the vectorial approach, the Kriging method or RBNN could be employed to predict the evolution of an entire response using several surrogate models: one surrogate model per frequency point in the response. The SM must reproduce the evolution of the amplitude of the response in a specific frequency position. That would be expensive in terms of computational effort, in both training and prediction phases. Moreover, multiple sets of surrogate models must be developed if several DOFs are tracked. A more efficient approach is to have one surrogate model for the entire response of any DOF of interest. A POD-SM technique allows to predict the whole response of a DOF with a singular surrogate model [Benamara, 2017a; Kerschen, 2005]. The result of the prediction in this type of approach is no longer a scalar value but a vector representing the response amplitudes in multiple frequency points. For this reason, we decided to use this approach to predict the whole responses of the interesting DOFs.
POD-SM approaches are based on the full-field dynamical response of the system $\boldsymbol{y}(\theta_i)$ in a specific parametric condition θ_i, also known as Snapshot. The snapshots evaluated in several parametric conditions are assembled in a matrix $\mathbf{Y}$:

$$\mathbf{Y} = [\boldsymbol{y}(\theta_1), \ldots, \boldsymbol{y}(\theta_n)] \tag{6.6}$$

The POD basis Φ_{POD} is evaluated from the snapshot matrix through a *Singular Values Decomposition* (SVD) [Liang, 2002], as shown in Equation 6.7.

$$\mathbf{Y} \cdot \mathbf{Y}^T \cdot \Phi_{POD} = \Lambda \cdot \Phi_{POD} \tag{6.7}$$

The predicted response is described in Equation 6.8.

$$\tilde{\boldsymbol{y}}(\theta) = \sum_{i}^{m} \Phi_{POD-i} \cdot \alpha_i(\theta) \rightarrow \tilde{\boldsymbol{Y}}(\theta) = \Phi_{POD} \cdot \alpha(\theta) \quad with \quad m << n \tag{6.8}$$

The $\alpha(\theta)$ vector defines the weight of any POD vector on the response. The training process of this type of surrogate model consists in the evaluation of the $\alpha(\theta_i)$ vector in the training points $\boldsymbol{y}(\theta_i)$. Using an RBNN (or similar), it is possible to define the $\alpha(\theta)$ vector continuously in the design space, in order to predict the response of the system in

any possible configuration θ. The main POD modes are identified a posteriori using the snapshots of the response in multiple configurations.

3 Simulation procedure

As specified in the previous section, the aim of this work is to study the behaviour of nonlinear aeronautical rotating machines with uncertainties coming from dynamical parameters (support stiffness, support damping, nonlinear gap, etc.) using surrogate models. DoE to train the surrogate model requires to run multiple simulations on the system in multiple configurations.
In this work, while the components are not changing, the links between them are variable, influencing the dynamics of the system with local modifications in the dynamical matrices. It is possible to parameterise the system's matrices to generate multiple configurations of the original system (see Figure 6.4). In Figure 6.4 the generic matrix $\mathbf{W}(\theta)$ represents one of the dynamical matrix $\mathbf{M}(\theta), \mathbf{D_v}(\theta), \mathbf{G}_i(\theta)$ or $\mathbf{K}(\theta)$. The matrix $\mathbf{W}$ is parameterised with respect to the vector θ, the i-th substructure is represented by the generic matrix $\mathbf{W}_i$, which is not dependent on the vector θ as in this work we only consider uncertainty in the supports.

The simulation procedure is composed of three steps: (1) the FE model is built, (2) the full order model is reduced using an approach based on the critical speeds of the system [DAlessandro, 2022b; DAlessandro, 2022a], (3) the nonlinear frequency response is finally simulated in the frequency domain using the HBM (see Figure 6.5).
In this simulation procedure, since the intermediate step of model order reduction is still expensive, an accelerated procedure is developed and applied to reduce the computational effort of the reduction phase. This method is presented and discussed in the next section.

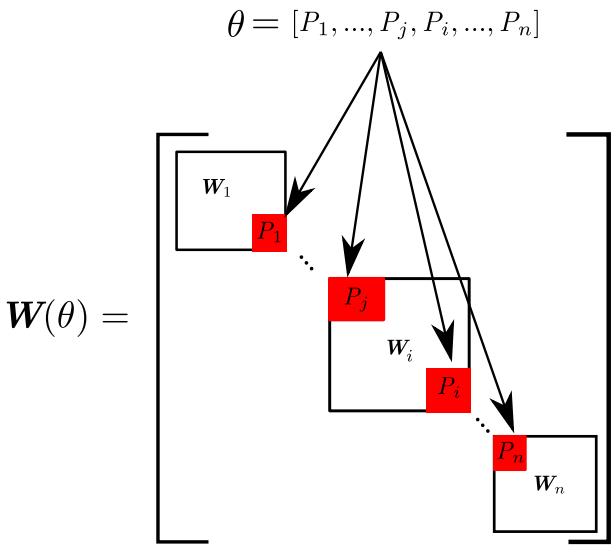

Figure 6.4: System matrix parametrisation.

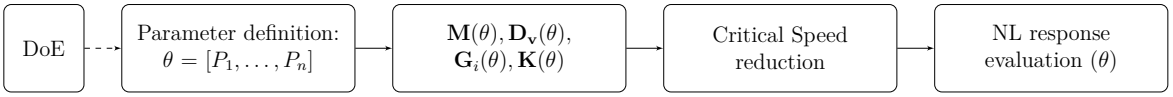

Figure 6.5: Mechanical simulation chain

4 Acceleration of the model order reduction procedure

The reduction of the system on the critical speed basis requires the solution of an eigenvalues problem which is expensive on an industrial scale model [DAlessandro, 2022b; DAlessandro, 2022a]. Since this operation has to be repeated once per new configuration, it is important to reduce this computational effort. In this section, a method to speed up the model reduction operation is presented.

4.1 Theoretical elements

Classically, after the generation of the FOM(θ) in configuration θ the critical speed basis Φ_{cs} is directly evaluated as shown by D'Alessandro et al. [DAlessandro, 2022b; DAlessandro, 2022a] and finally the FOM(θ) is reduced using this basis (Equations 6.9) to produce the ROM-CS(θ) (see Algorithm 1).

$$\begin{aligned} \mathbf{W}_{cs} &= \Phi_{cs}^T\ \mathbf{W}\ \Phi_{cs} \quad \forall\ \mathbf{W} &&= [\mathbf{M}, \mathbf{D_v}, \mathbf{G}_i, \mathbf{K}]_{FOM} \\ \mathbf{F}_{cs} &= \Phi_{cs}^T\ \mathbf{F} \quad\quad \forall\ \mathbf{F} &&= \hat{\mathbf{f}} \\ \hat{\mathbf{q}}_f &= \Phi_{cs}\ \hat{\mathbf{u}} \end{aligned} \tag{6.9}$$

Considering that multiple model reductions have to be performed in the DoE evaluation

Algorithm 1 Classical model reduction approach

1: *Build* FOM(θ)
2: *Evaluate Critical speeds basis of the* FOM(θ) : $\Phi_{cs}(\theta)$
3: *Reduce* FOM(θ) using the critical speeds basis $\Phi_{cs}(\theta)$ (Equation 6.9) $\rightarrow$ ROM-CS (θ)

phase, we propose to add an intermediate a priori model reduction based on a *global enriched basis* Φ_{rich} obtained from several bases computed in the extreme configurations of the design space. This model reduction approach is detailed in Equation 6.10 and in Algorithm 2.

$$\begin{aligned} \mathbf{W}_{rich} &= \Phi_{rich}^T \, \mathbf{W} \, \Phi_{rich} \quad \forall \; \mathbf{W} = [\mathbf{M}, \mathbf{D_v}, \mathbf{G}_i, \mathbf{K}]_{FOM} \\ \mathbf{F}_{rich} &= \Phi_{rich}^T \, \mathbf{F} \quad \forall \; \mathbf{F} = \hat{\mathbf{f}} \\ \hat{\mathbf{q}}_f &= \Phi_{rich} \, \hat{\mathbf{u}} \end{aligned} \tag{6.10}$$

Algorithm 2 Accelerated model reduction approach

1: *Get the enriched basis* : Φ_{rich}
2: Build FOM(θ)
3: *Reduce* FOM(θ) using the enriched basis (Equation 6.10)$\rightarrow$ ROM-RICH (θ)
4: *Evaluate Critical speeds basis of the* ROM-RICH (θ) : $\Phi_{r-cs}(\theta)$
5: *Reduce* ROM-RICH(θ) using the critical speeds basis (Equation 6.9) $\rightarrow$ ROM-RCS (θ)

This operation allows to reduce the full order model using the enriched basis developed a priori by evaluating the critical speeds basis on the reduced order model ROM-RICH(θ) and no longer on the FOM(θ), which is less expensive. The ROM-RICH(θ) is finally reduced on the critical speed basis producing the ROM-RCS(θ).

4.2 Evaluation of the Φ_{rich} basis

The $\Phi_{rich}(\theta)$ basis must be able to span any subspace generated in the design space of the system. To develop this enriched basis, several critical speed bases of the system in multiple configurations are evaluated. In particular, the critical speed bases of the system in the corners of the design space can be evaluated and assembled to build a unique global basis Φ_{glob}. An example of this procedure on a system with two variables is reported in Figure 6.6.

$$\Phi_{glob} = [\Phi_1, \Phi_2, \Phi_3, \Phi_4] \tag{6.11}$$

This global basis is likely to contain redundant modes. To reduce the size of this basis and to remove correlated information, a SVD is performed.

$$SVD(\Phi_{glob}) \rightarrow \Phi_{rich} \tag{6.12}$$

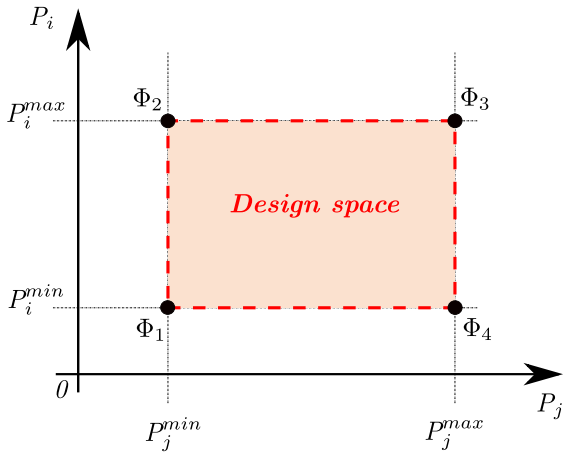

Figure 6.6: Φ_{rich} in a 2 dimensions example.

This approach could be applied in multiple fields. In the specific case of structural dynamics, since the stiffness, mass and damping matrices define the shapes and the frequency position of the vibration modes it seems interesting to apply this approach only on mass, stiffness and damping parameters.

4.3 Discussion on the size of the Φ_{rich} basis for an industrial scale application

In this section the proposed acceleration method is examined for an industrial scale rotating system. In this model, two variable radial stiffnesses related to two different supports are considered. The design space is defined in Table 6.1.

Parameter name	Parameter symbol	Range
Support #1 Stiffness	$P_1 = K_1$	$[0.5,2] \cdot K_1^{nom}$
Support #2 Stiffness	$P_2 = K_2$	$[0.5,2] \cdot K_2^{nom}$

Table 6.1: Parametric design space for model reduction acceleration.

The dynamics of the system in the desired frequency range can be defined by the first 400 critical speed modes in any configuration. The design space is represented by its 4 corner points (Figure 6.6), yielding a basis Φ_{glob} composed of 1600 modes. It is necessary to identify the minimal size of Φ_{rich} after the SVD. Three variants of Φ_{rich} are proposed: with 500, 1000 and 1600 modes as shown in Figure 6.7. The unbalance response of the nominal ROM-CS(θ) are compared with the unbalance response of the ROM-RCS(θ) developed using the three variants of Φ_{rich}: Φ_{rich}^{500}, Φ_{rich}^{1000} and Φ_{rich}^{1600}. The responses are compared in the following design points:

- P1 : $K1 = 1 \cdot K_1^{nom}, K2 = 1 \cdot K_2^{nom}$ (see Figure 6.8).

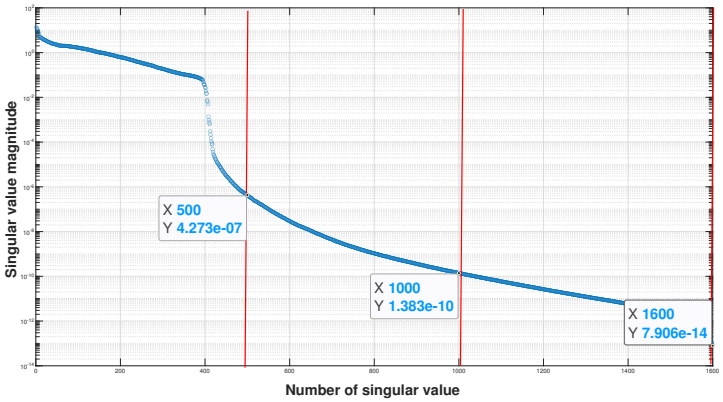

Figure 6.7: Singular values decomposition of Φ_{glob}

- P2 : $K1 = 1.5 \cdot K_1^{nom}, K2 = 1.5 \cdot K_2^{nom}$ (see Figures 6.9).

In order to obtain a global measurement of the error between the nominal ROM-CS(θ) $\rightarrow$ $u_{cs}(\omega)$ and the three accelerated ROM-RCS(θ) $\rightarrow$ $u_{r-cs}(\omega)$ responses, the minimum angle α expressed in Equation 6.13 is evaluated using the MATLAB function `subspace`.

$$\alpha(\omega) = min\left\{arccos\left(\frac{\langle \boldsymbol{u}_{cs}(\omega), \boldsymbol{u}_{r-cs}(\omega)\rangle}{||\boldsymbol{u}_{cs}(\omega)|| \cdot ||\boldsymbol{u}_{r-cs}(\omega)||}\right)\right\} \tag{6.13}$$

It is important to remember that if this angle α is small, the compared vectorial subspaces are almost linearly dependent. The error is then evaluated by:

$$err(\omega) = sin(\alpha(\omega)) \cdot 100 \tag{6.14}$$

This error compares the entire displacements fields (nominal ROM-CS and accelerated ROM-RCSs) at any frequency. The error between the nominal and the accelerated bases are reported in Figures 6.8A) and 6.9A). In Figures 6.8B) and 6.9B) the computational efforts of the different configurations are displayed. In Figures 6.8C) and 6.9C) the position of the examined points in the design space are shown. First of all, observing the errors committed by the different accelerated ROM-RCSs with respect to the nominal ROM-CS it is possible to conclude that the error is negligible and almost the same for the three variants of the Φ_{rich} basis at any regime. It appears unnecessary to include more than 500 modes into the Φ_{rich} basis. Observing the calculation time including the evaluation of the critical speed basis and the unbalance response, one can notice that the basis Φ_{rich}^{500} is always associated with the least computational effort. This time reduction is mainly due to the calculation of the critical speed basis, which is cheaper when performed on a smaller system. Similar results are obtained in the rest of the design space. The error is minimal if the design point is positioned closer to the training points (extremities of the domain).

One can conclude that this approach allows to reduce the computational effort of the model reduction step by a factor of 5 to 10, with an estimated ROM comparable to the nominal one. It is difficult to give a general recommendation concerning the size of Φ_{rich} basis, the optimal amount of modes included in this basis should be case dependent. This same approach is employed in the coming sections, allowing to strongly reduce the time demanded to evaluate the DoEs.

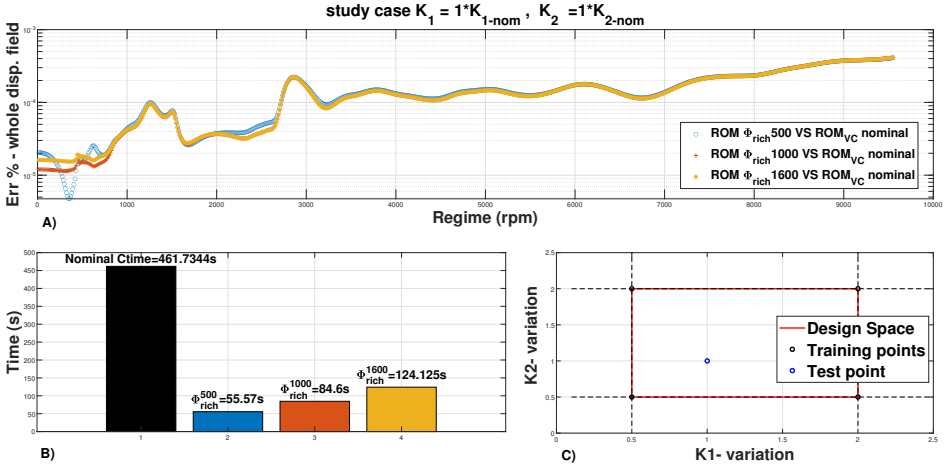

Figure 6.8: Validation of the procedure in the design point P1 : $[K1 = 1 \cdot K_1^{nom}, K2 = 1 \cdot K_2^{nom}]$. A) Error ROM-CS($\theta_{P1}$) vs ROM-RCSs($\theta_{P1}$). B) CPU time (s) - Basis evaluation + linear unbalance response. C) Position of the test point P1 in the design space.

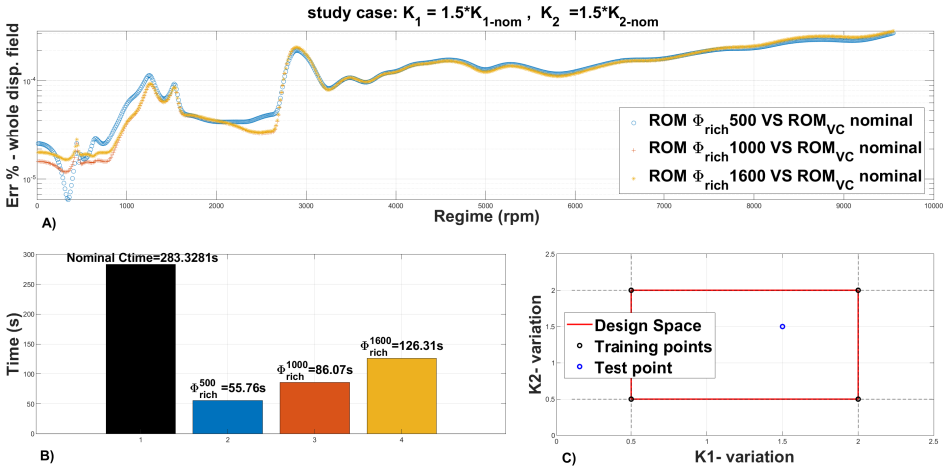

Figure 6.9: Validation of the procedure in the design points P2 : $[K1 = 1.5 \cdot K_1^{nom}, K2 = 1.5 \cdot K_2^{nom}]$. A) Error ROM-CS($\theta_{P2}$) vs ROM-RCSs($\theta_{P2}$). B) CPU time (s) - Basis evaluation + linear unbalance response. C) Position of the test point P2 in the design space.

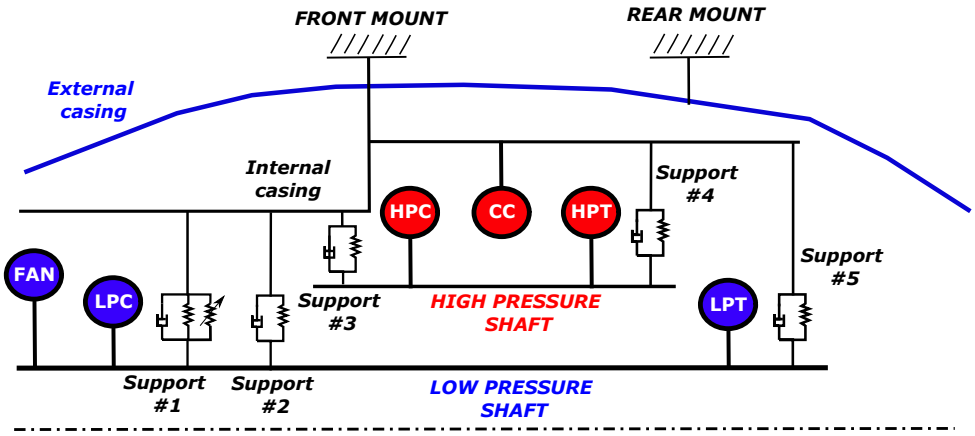

Figure 6.10: Simplified representation of the industrial system employed in this study.

5 Study case: industrial scale whole engine dynamics

In this section, the aforementioned RBNN, Kriging and POD-RBNN approaches are applied to an industrial FE model representing a whole aircraft engine modeled by $\approx 5e6$ DOFs and submitted to a synchronous excitation generated by an unbalance mass positioned on the fan. A nonlinear contact is applied on the support #1 (see Equation 6.2), the nonlinear force is activated if the support #1 bearing comes in contact with its casing. It is important to mention that the support #1 is a *Squeeze Film Dampers* (SFD), it is modeled using a lumped mass, a damping element and a spring [San Andres, 2010].
A simplified representation of the industrial system examined in this study is reported in Figure 6.10. The dynamical parameters defining the design space are reported in Table 6.2, six parameters have been studied at the same time in this work. The design space is defined by the uncertainty on the parameters associated to the support #1 in order to study their impact on the responses.

A detailed representation of the industrial system is impossible for confidentiality reasons and the response amplitudes, frequencies and numerical values of the dynamical parameters are therefore normalised.

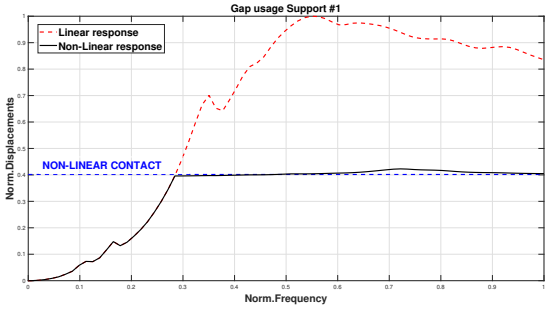

Figure 6.11: Gap usage support #1.

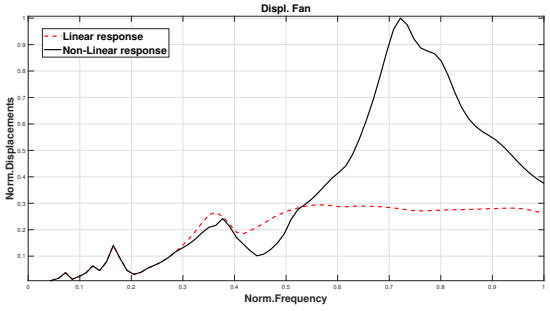

Figure 6.12: Fan nonlinear response.

Parameter name	Par. symbol	Values
support #1 SFD Stiffness	K_{s1}	[0.9-1.1] $\cdot K_{s1}^{nom}$
support #1 SFD Damping	B_{s1}	[0.5-2] $\cdot B_{s1}^{nom}$
support #1 SFD lumped Mass	M_{s1}	[0.1-1] $\cdot M_{s1}^{nom}$
support #1 NL gap	C_{s1}	[0.8-1.2] $\cdot C_{s1}^{nom}$
Hysteretic Damping Factor	Q	[0.5-2] $\cdot Q^{nom}$
Unbalance	M_u	[1-2] $\cdot M_u{}^{nom}$

Table 6.2: Parametric design space for the industrial study case allowing to quantify the impact of the uncertainty on the parameters of the support #1 on the system's dynamics.

Name of DoE	Type of DoE	Nb. of experiments	CPU Time (norm)
Θ_{L-c}	LCVT (cheap)	20	≈ 0.31
Θ_{L-r}	LCVT (rich)	40	≈ 0.66
Θ_{FAC}	Factorial	64	≈ 1 (32450s)

Table 6.3: DoEs properties.

In this study, unbalance response simulations are performed and two types of data are extracted: the displacements of multiple DOFs of the system with respect to the rotational speed and another type of response known in the aeronautical domain as *Gap Usage* (GU). The gap usage represents the euclidean distance still available between the rotor and the stator in the plane perpendicular to the rotation axis at any point of the system. If the gap usage cancels the rotor-to-stator clearance at a specific point of the axis, a nonlinear contact is established and new forces are introduced in the system.
The nonlinear force is controlled by the gap usage of support #1. In Figure 6.11, is reported the evolution of the gap usage at the support #1 in a generic configuration of the aeroengine, one can notice that the gap usage increases until reaching the clearance value (≈ 0.4 norm.) at normalised frequency ≈ 0.3. When the contact is established, a nonlinear force is applied on the rotor capping the displacements. As well, it is reported in Figure 6.12, the response of the fan with and without the application of the nonlinear force. One can notice from Figures 6.11 and 6.12 that the linear and nonlinear responses are superposed before the establishment of the nonlinear contact, remaining linear before the establishment of the contact. Moreover, it is important to highlight the importance of the nonlinear effect on the system's response: from Figure 6.12, one can notice that the fan's displacements increased by about 3 times in comparison with the linear configuration, and this is the case of the other DOFs too.

In this work 12 DOFs displacements amplitude and 8 gap usages are identified strategically to be observed as they are particularly relevant.

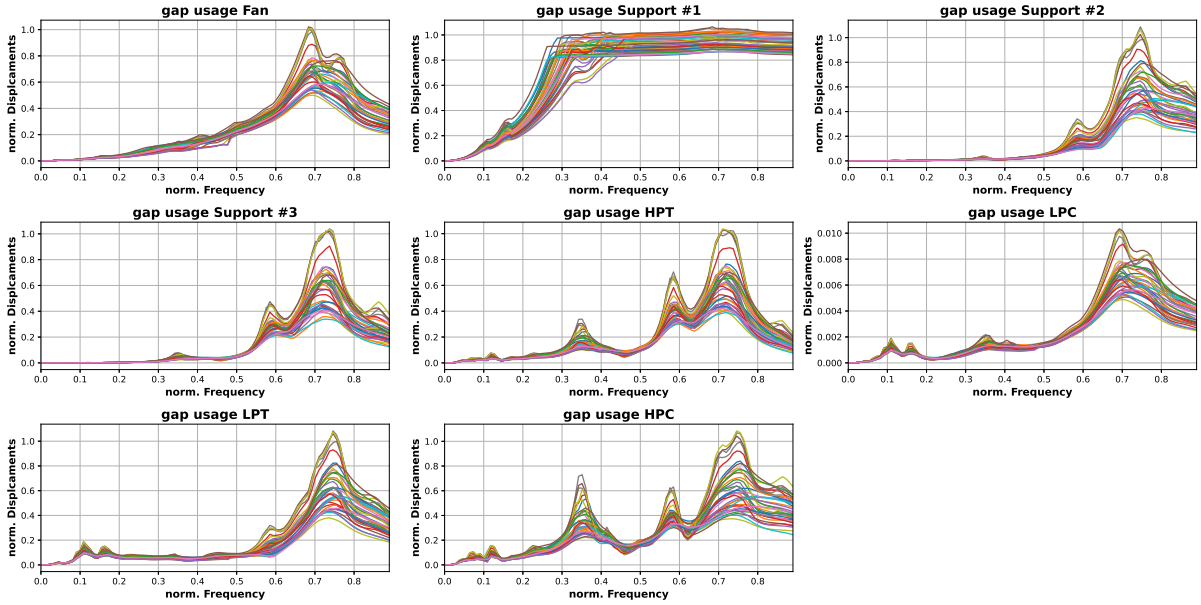

Figure 6.13: Evolution of the **normalised gap usage responses** in 40 training points

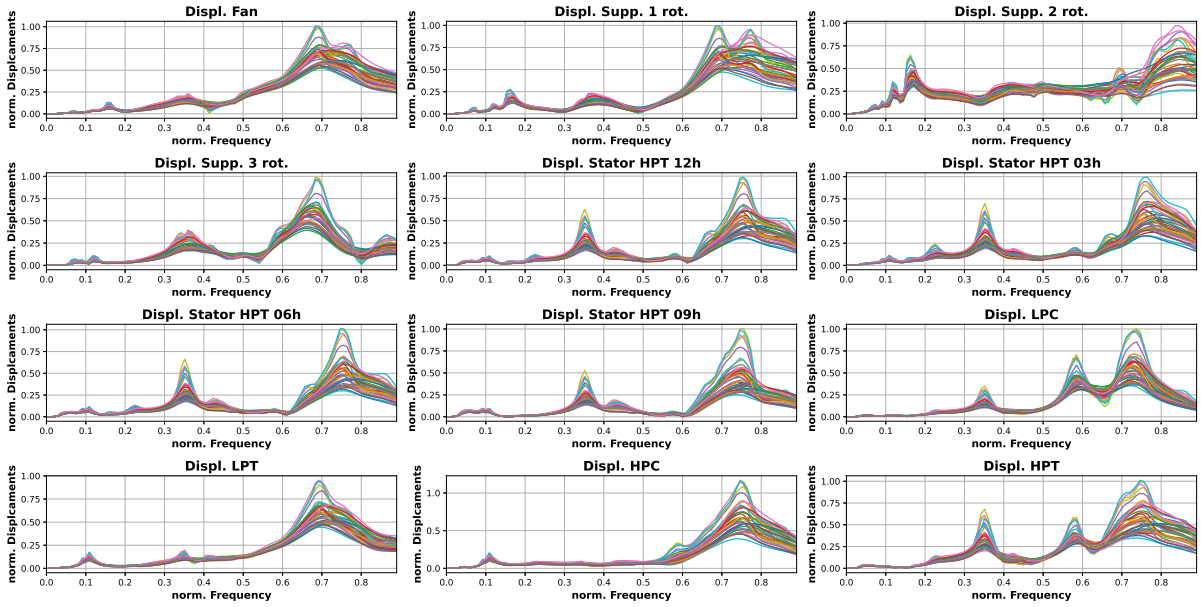

Figure 6.14: Evolution of the **normalised displacements responses** in 40 training points

5.1 Design of Experiments and validation plan

Three different DoEs have been investigated in this study. Two of them have been developed using a *Latin Centroidal Voronoi Tessellations* (LCVT) algorithm [Romero, 2006; Saka, 2007]. The remaining one has been developed using a two-level factorial sampling. The details on the DoEs are reported in Table 6.3. Since the time demanded to perform a single simulation is nearly constant, we can ensure that the overall DoE evaluation cost is almost linearly dependent on its size.
Figures 6.13 and 6.14 report the evolution of the normalised gap usages and DOFs responses of the system in the 40 experiments of the DoE Θ_{L-r}, one can notice that these 20 nonlinear responses have a non negligible evolution with the variation of the parameters in the design space.
The trained surrogate models are compared using a direct validation procedure with respect to the nominal responses computed for all configurations of a 18 random points validation plan.

5.2 Scalar surrogate modeling approaches

In this section the RBNN and Kriging surrogate modeling techniques are employed to predict the maximum amplitudes of the system's nonlinear frequency responses on the DOFs under exam. The position of the maximum point is decomposed into two components predicted by two independent surrogate models (RBNN or Kriging) per response (yielding 40 scalar surrogates to model the 20 responses at hand): one of them predicts the maximum amplitude and the other one predicts the relative frequency. Four different sets of 40 scalar surrogates are trained and compared using the validation plan, 3 of them adopt the RBNN approach while the other one employs the Kriging method, both available in MINAMO platform [CENAERO, 2023]. The details on the development of the 4 sets of surrogates are reported in Table 6.4.
One can notice that the training time of the Kriging surrogate model is approximately 20 times higher than of RBNNs. All these training times are negligible when compared to the time required for the evaluation of the DoEs but this could represent a limitation for the Kriging approach if more training points are necessary or if more input parameters have to be considered [Bouhlel, 2019]. It is important to observe that the extension of these techniques in terms of observed number of DOFs is direct because it only impacts the training time which is negligible if compared with the DoE evaluation time.
Once the surrogate models are trained, they are compared with nominal responses using a scalar criterion which takes into account both the frequency shift and magnitude error, as shown in Equation 6.15:

$$Err = \left(\frac{|u_{max} - \tilde{u}_{max}|}{u_{max}} + \frac{|\omega_{max} - \tilde{\omega}_{max}|}{\omega_{max}}\right) \cdot 0.5 = (Err_{mag} + Err_{freq}) \cdot 0.5 \tag{6.15}$$

Name of SM	Type of SM	DoE	Training Time (norm.)
$\mathbb{S}^{Krig}_{\Theta_{L-r}}$	Kriging	Θ_{L-r}	≈ 1 $(20s)$
$\mathbb{S}^{RBNN}_{\Theta_{L-r}}$	RBNN	Θ_{L-r}	≈ 0.05
$\mathbb{S}^{RBNN}_{\Theta_{L-c}}$	RBNN	Θ_{L-c}	≈ 0.044
$\mathbb{S}^{RBNN}_{\Theta_{FAC}}$	RBNN	Θ_{FAC}	≈ 0.053

Table 6.4: Scalar surrogate models training details.

with u_{max} representing the nominal maximum displacement, ω_{max} the frequency of the nominal maximum displacement, $\tilde{u}_{max}$ and $\tilde{\omega}_{max}$ their respective predictions.
Figure 6.15 illustrates the predictions of the 8 gap consumptions for the validation experiment #16. In any graphic of Figure 6.15 are reported the nominal responses and the relative predictions:

- black dot: nominal maximum displacement.
- blue triangle: prediction performed with $\mathbb{S}^{RBNN}_{\Theta_{L-r}}$,
- cyan pentagon: prediction performed with $\mathbb{S}^{Krig}_{\Theta_{L-r}}$,
- red triangle: prediction performed with $\mathbb{S}^{RBNN}_{\Theta_{L-c}}$,
- green square: prediction performed with $\mathbb{S}^{RBNN}_{\Theta_{FAC}}$,

At the top of Figure 6.15 is reported the mean error per surrogate model for the considered validation experiment. This last information represents the mean quality of the surrogate on the validation experiment and it is interesting to compare surrogates and DoEs. In validation experiment #16 the $\mathbb{S}^{Krig}_{\Theta_{L-r}}$ and $\mathbb{S}^{RBNN}_{\Theta_{L-r}}$ produce the best results in terms of global accuracy, with respectively a mean error of 1.04% and 1.59%.

It is now worthwhile to move to more critical cases identified in the validation experiments #1 and #16, reported respectively in Figures 6.16 and 6.17. Globally the responses are predicted with an acceptable precision with $\mathbb{S}^{Krig}_{\Theta_{L-r}}$ and $\mathbb{S}^{RBNN}_{\Theta_{L-r}}$ but there is a problem for support #2 rotor side responses. This response (top-right graphics in Figures 6.16 and 6.17) is characterised by a competition between the two maximum amplitudes positioned respectively around frequency 0.2 and 0.85. In these cases the frequency position of the maximum amplitude can move dramatically from the one mode positioned at frequency ≈ 0.2 to another one positioned at frequency ≈ 0.85 producing a set of training data presenting a non-continuous evolution and generating non-predictive surrogate models.

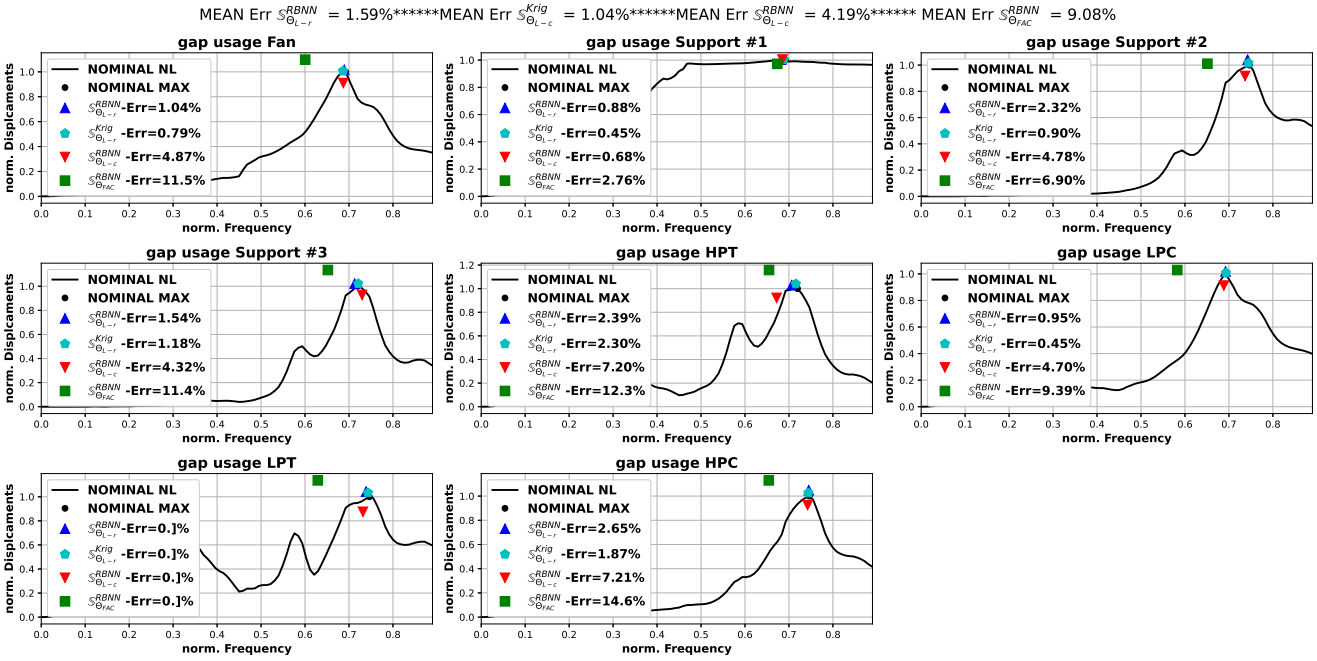

Figure 6.15: Prediction of the maximum gap usage responses and relative frequencies in **experiment 16**.

Both types of surrogate approaches (Kriging and RBNN) are subject to increased prediction error when responses have constant-like evolution. In this study, this situation is isolated to a singular DOF (support #2 rotor side) and reproduced only 2 times on the 18 experiments of the validation plan. A regular prediction is reported in Figure 6.18 and similar performances are produced on the other 16 validation points. Nevertheless, it is important to keep this example in mind because it reveals a conceptual limitation of this scalar approach that the enrichment of the surrogates barely overcomes.

In Figure 6.19, the mean error per surrogate model is reported for any validation experiment: in blue the mean error of $\mathbb{S}^{RBNN}_{\Theta_{L-r}}$ on the 18 validation experiments, in cyan the mean error of $\mathbb{S}^{Krig}_{\Theta_{L-r}}$, in red the mean error of $\mathbb{S}^{RBNN}_{\Theta_{L-c}}$ and in green the mean error of $\mathbb{S}^{RBNN}_{\Theta_{FAC}}$. The $\mathbb{S}^{Krig}_{\Theta_{L-r}}$ and $\mathbb{S}^{RBNN}_{\Theta_{L-r}}$ produce the best results with respectively a global mean error among the validation plan of $\approx 2.5\%$ and $\approx 4.5\%$. The Kriging approach could generate a more accurate set of surrogate models if compared with the RBNN approach but it demands a higher effort in the training phase. The $\mathbb{S}^{RBNN}_{\Theta_{L-c}}$ produces a mean error on the whole validation plan of $\approx 6\%$, this last surrogate is a good compromise between accuracy and computational effort. It is indeed developed on the Θ_{L-c} DoE which was the one evaluated with the lowest computational effort. The $\mathbb{S}^{RBNN}_{\Theta_{FAC}}$ is the least accurate SM with the most important computational effort.

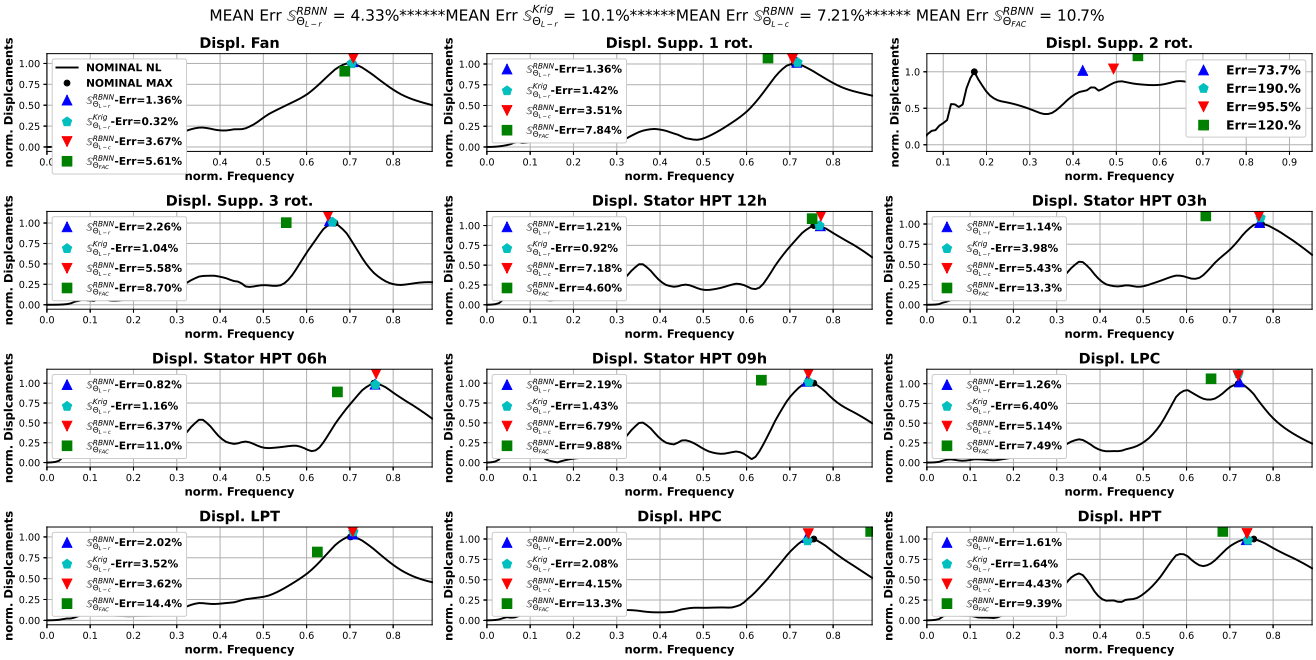

Figure 6.16: Prediction of the maximum responses amplitude and relative frequencies in **experiment 1**.

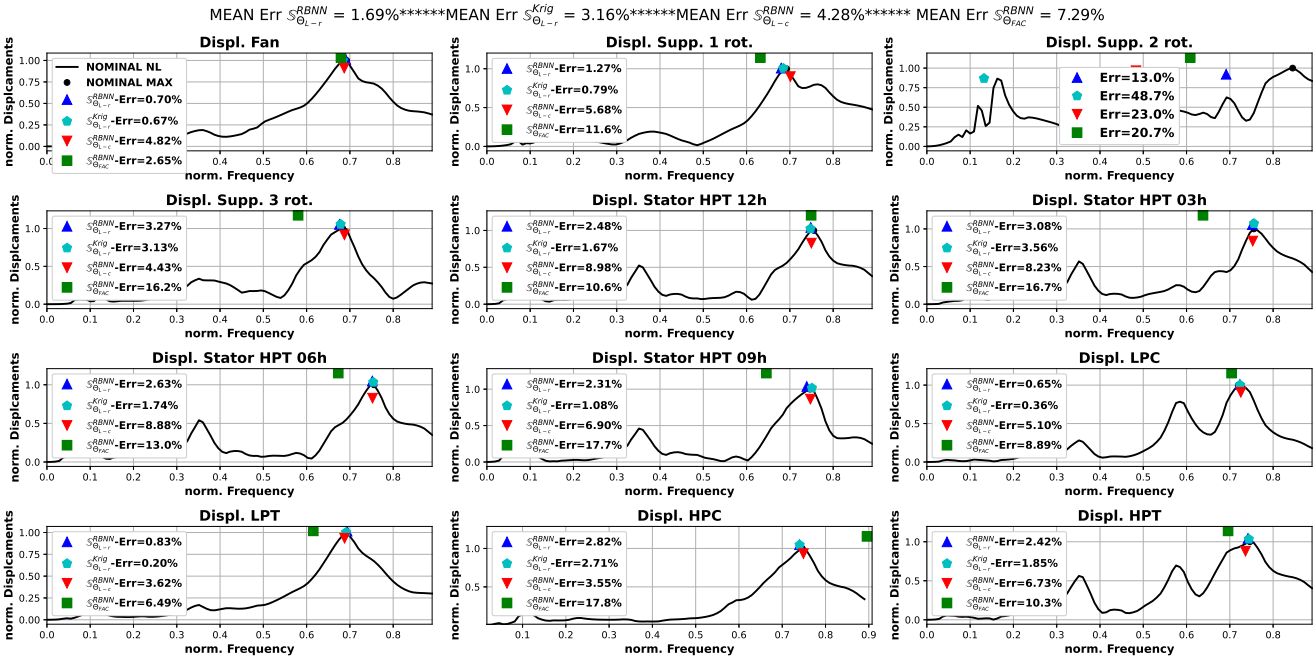

Figure 6.17: Prediction of the maximum responses amplitude and relative frequencies in **experiment 16**.

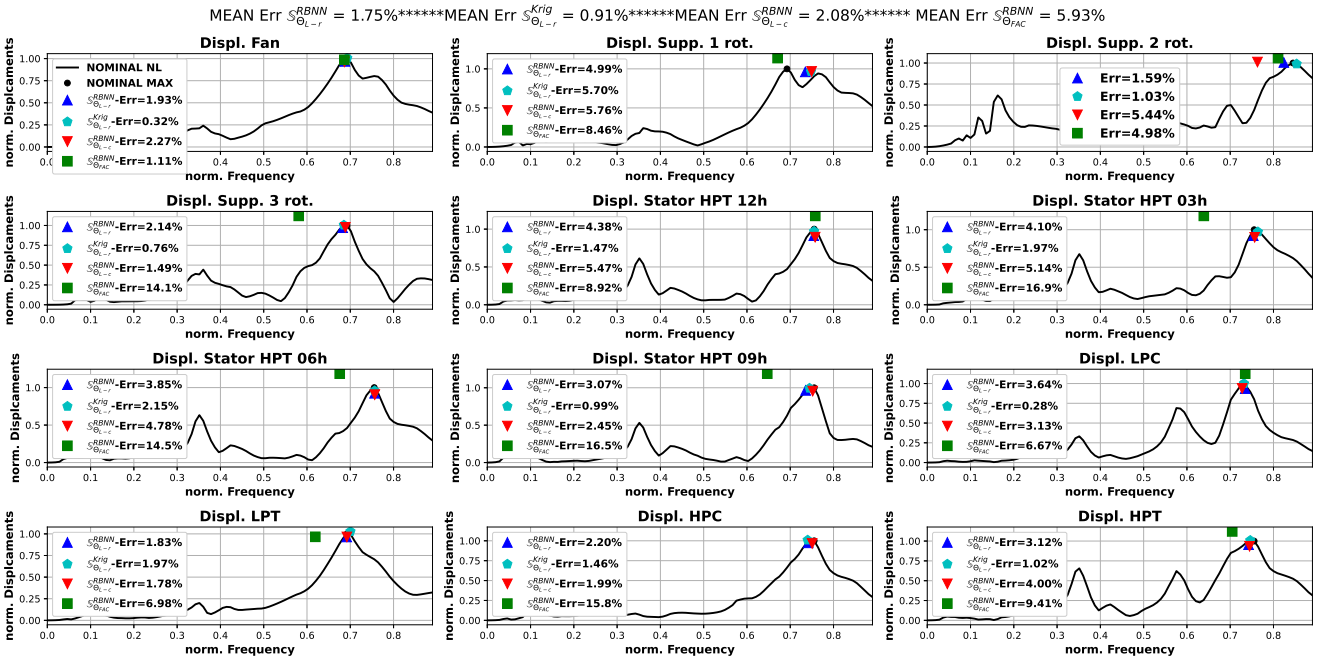

Figure 6.18: Prediction of the maximum responses amplitude and relative frequencies in **experiment 15**.

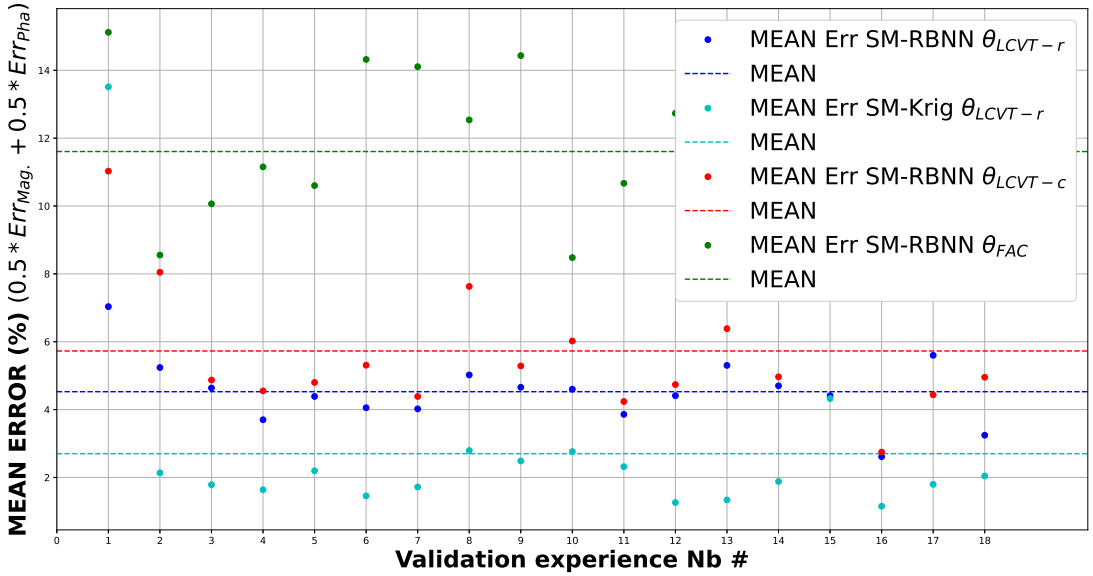

Figure 6.19: Mean Error $(0.5 \cdot Err_{mag.} + 0.5 \cdot Err_{freq.})$ per surrogate model on the validation plan.

5.3 Vectorial surrogate modeling approaches

In this section the POD-RBNN surrogate models are employed to predict the evolution of the system's nonlinear response on the interesting DOFs. A set of 20 surrogates are trained to predict the whole responses and no longer a single point of the response as in the scalar approach.
It is essential to emphasise that the harmonic balance algorithm adopts an auto-adaptive step-size [Krack, 2019] which depends on the convergence of the solution. For this reason, the responses produced with this algorithm are evaluated on non-regular frequency grids. In order to fix a unique frequency vector for any response and any training point the responses have been interpolated on a fixed frequency discretisation. In this way, there is no longer a need to develop a surrogate model to predict the frequency because the frequency vector is already known and unique.

Three surrogate models are proposed: $\mathbb{S}_{\Theta_{L-r}}, \mathbb{S}_{\Theta_{L-c}}$ and $\mathbb{S}_{\Theta_{FAC}}$. The training details concerning these surrogates are reported in Table 6.5. The training time of the three surrogates is negligible if compared with the time demanded for the DoEs evaluation. It is important to mention that the number of predicted DOFs (20 in this study) impacts the training time and not DoEs evaluation time. For this reason, since the training time is negligible if compared with the DoEs evaluation time, the extension to a larger number of observed DOFs is direct. In order to compare nominal and predicted frequency re-

Name of SM	Type of SM	DoE	Training Time (norm.)
$\mathbb{S}_{\Theta_{L-c}}$	POD-RBNN	Θ_{L-c}	≈ 0.4
$\mathbb{S}_{\Theta_{L-r}}$	POD-RBNN	Θ_{L-r}	≈ 0.7
$\mathbb{S}_{\Theta_{FAC}}$	POD-RBNN	Θ_{FAC}	≈ 1 (10s)

Table 6.5: *Vectorial* surrogate models training details.

sponses, a correlation coefficient known as *Enhanced Error Assessment of Response Time Histories* (EEARTH) [Zhan, 2011] is employed. This coefficient has been developed to compare signals in time domain but it can be extended to frequency response with no loss of efficiency. It defines the correlation between two responses taking into account the error on magnitude, frequency shift and slope gradient as reported in Equation 6.16. The errors are weighted by the three factors $\alpha_{freq}, \alpha_{mag}$ and α_{slope}, the values of the three errors are varying between 0 and 1 and so is the EEARTH coefficient being equal to 0 in the case of no correlation at all and to 1 if the responses are superposable. In this work the weight factors are set to $\alpha_{freq} = 0.333, \alpha_{mag} = 0.333$ and $\alpha_{slope} = 0.333$, in order to give the same importance to any of the three error considered. More details on the

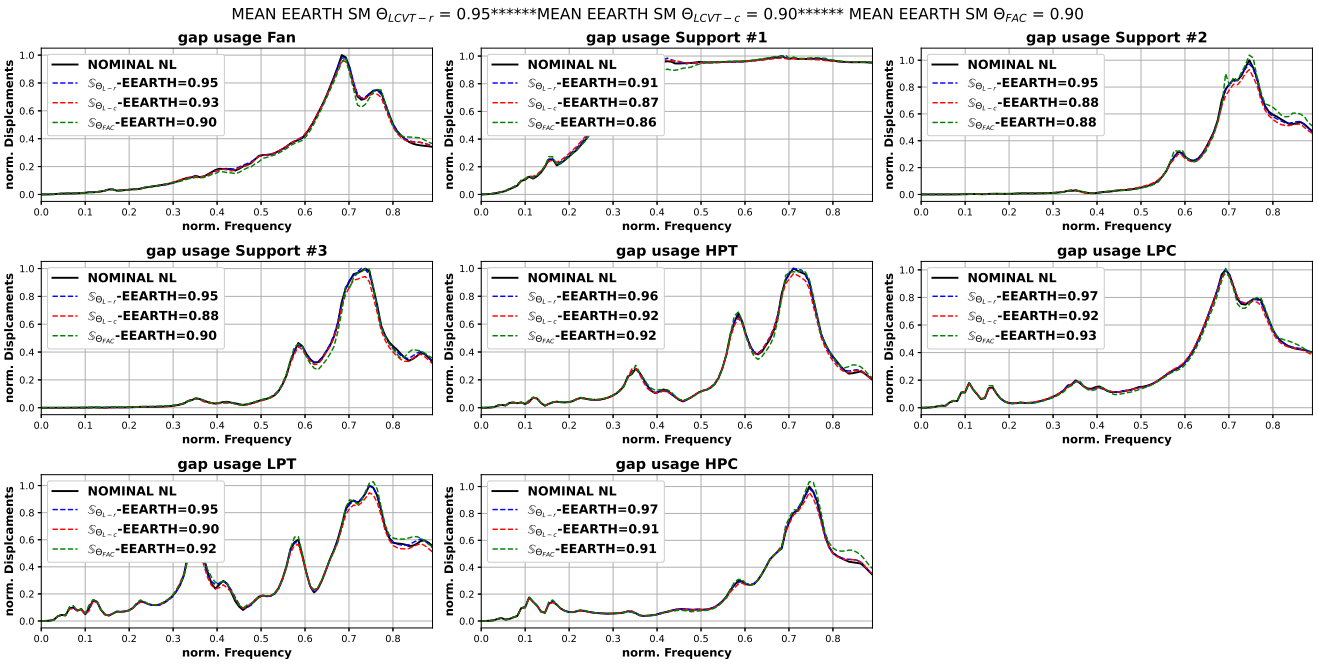

Figure 6.20: POD-RBNN SM: prediction of the gap usage responses in **experiment 18**.

calculation of the three errors are available in literature [Zhan, 2011]:

$$EEARTH = \alpha_{freq} \cdot Err_{freq} + \alpha_{mag} \cdot Err_{mag} + \alpha_{slope} \cdot Err_{slope} \tag{6.16}$$

Figures 6.20 and 6.21 report the predictions of the three proposed SMs for the validation experiment #18, respectively displaying the gap usages and the DOFs displacements. For any gap usage and DOF displacement the EEARTH coefficient is calculated between the nominal response and the three proposed surrogate models. As well, in the top of Figures 6.20 and 6.21 is reported the mean EEARTH coefficients for each surrogate model.
One can notice that the $\mathbb{S}_{\Theta_{FAC}}$ is the one presenting the worst performances in terms of accuracy despite being trained on the Θ_{FAC} DoE which is the most expensive one. The LCVT based surrogate models $\mathbb{S}_{\Theta_{L-r}}$ and $\mathbb{S}_{\Theta_{L-c}}$ yield a better performance in terms of accuracy and computational effort than the $\mathbb{S}_{\Theta_{FAC}}$ (respectively 24 and 44 training points less than Θ_{FAC}). Finally, the surrogate model $\mathbb{S}_{\Theta_{L-r}}$ produces less accurate results than the $\mathbb{S}_{\Theta_{L-c}}$ with the half of the training points, but still better than Θ_{FAC}. These performances can be observed on the mean EEARTHs of the experiment #18.
The same trend can be observed on the whole validation plan as reported in Figure 6.22 by the mean EEARTH per surrogate model. To sum up, the $\mathbb{S}_{\Theta_{L-r}}$ is the most accurate, then there is the $\mathbb{S}_{\Theta_{L-c}}$ and finally the $\mathbb{S}_{\Theta_{FAC}}$.

One can conclude that while both the surrogate models trained using the LCVT sampling

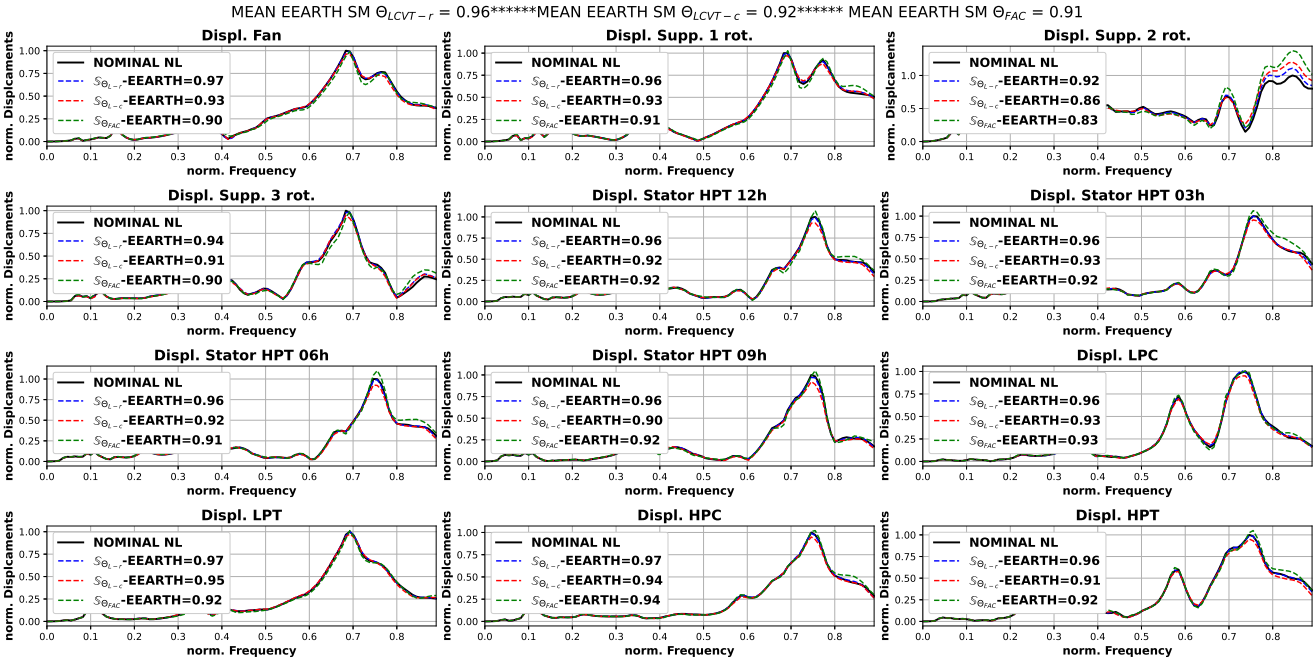

Figure 6.21: POD-RBNN SM: prediction of the responses in **experiment 18**.

algorithm are interesting, the $\mathbb{S}_{\Theta_{L-r}}$ is the one producing the best performances in terms of accuracy, the $\mathbb{S}_{\Theta_{L-c}}$ produces results globally less accurate than the $\mathbb{S}_{\Theta_{L-r}}$ but it is cheaper both to train and in terms of DoE evaluation. It could represent a good compromise between accuracy and computational effort. The factorial DoE is the most expensive in terms of computational effort and produces less accurate surrogates than the other two options. The POD-RBNN approach combined with an LCVT sampling algorithm allows to predict with good accuracy and with a relatively low computational effort the evolution of the nonlinear responses of rotating machines with nonlinear contacts.

5.4 Comparison between the scalar and vectorial approach

In Section 5.2 the limitation of the scalar approach has been illustrated in Figures 6.16 and 6.17, for experiments #1 and #16. This limitation is seen using both Kriging and RBNN approaches. In Figures 6.16 and 6.17 the experiments #1 and #16 are predicted using the vectorial approach. The scalar and vectorial approaches are directly compared on the responses of support #2 in Figure 6.23, highlighting the advantages of using the vectorial approach instead of the scalar one.

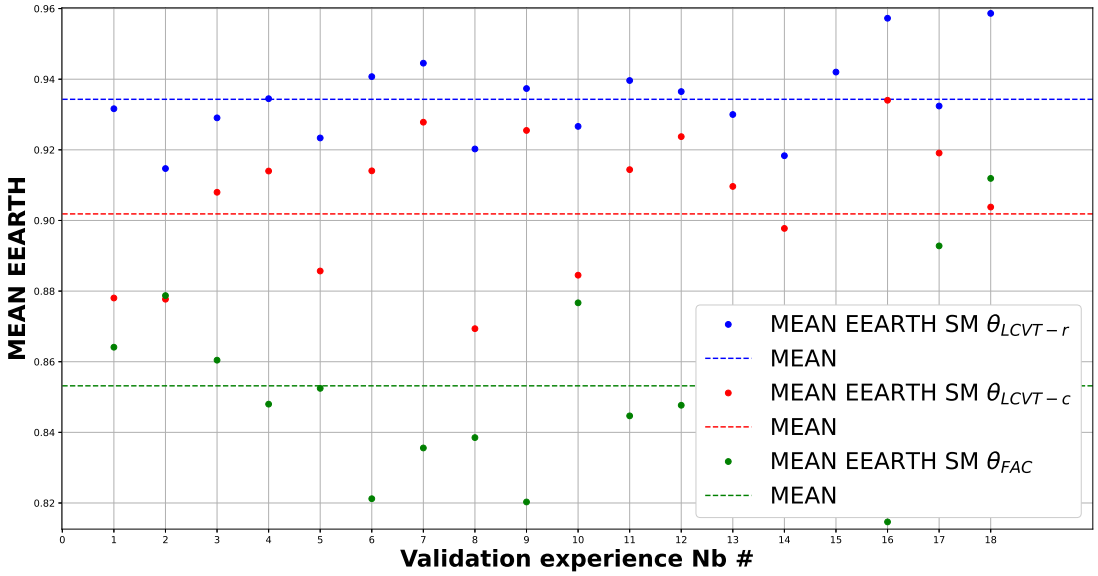

Figure 6.22: Mean EEARTH factor per surrogate model in any validation experiment.

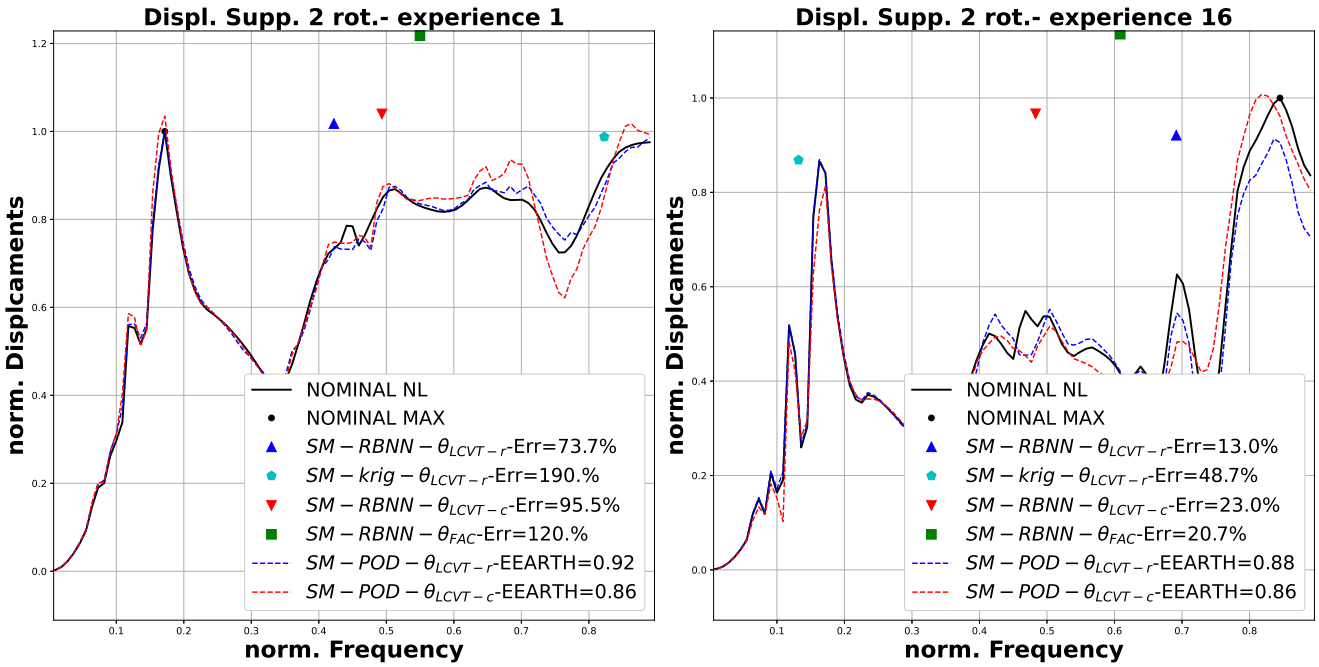

Figure 6.23: Direct comparison of the scalar and vectorial approaches on the responses of support #2 rotor side in validation experiments #1 and #16

6 Conclusions

In both scalar and vectorial approaches, the Θ_{L-c} and Θ_{L-r} DoEs yield more accurate surrogate models with a reduced computational effort in comparison with a factorial DoE. Even the Θ_{L-c}, which is the cheapest DoE composed only with 20 sampling points, allows in any circumstance to produce better surrogate models than the ones developed using the factorial DoE. The factorial DoE is inefficient in terms of accuracy and is computationally expensive.
Concerning the scalar approach, a limitation has been identified in the surrogate modeling of the responses having two or more pics in competition and a relatively *flat* evolution. This condition is generated when the maximum amplitude is positioned at different modes depending on the system's configuration. Both Kriging and RBNN surrogate modeling approaches are subject to this limitation. The points predicted with this error present an acceptable maximum amplitude and a major error in the associated frequency prediction. In addition, the Kriging method allows the development of a set of surrogates that are slightly more accurate than RBNNs trained on the same DoE. This approach could be preferable in case of a low number of parameters and a low number of training points. In high-dimensional problems with a large number of training points, the RBNNs are more efficient in terms of training time.
The vectorial approach based on POD-RBNN surrogate modeling technique has been employed to predict the response of a rotating machine with nonlinearities obtaining a marginal error and a relatively low computational effort. This approach produces predictions with acceptable accuracy in almost any validation experiment. The limitation identified in the scalar approach doesn't appear with the vectorial one. As observed in the scalar approach, the factorial design Θ_{FAC} is globally the one producing the least accurate surrogates. This type of DoE should be avoided for training purposes and only kept for surrogate models validation.

The surrogates produced with the vectorial approach could be employed in multiple scenarios for engineering purposes: design space exploration, sensitivity and reliability analysis and model calibration. An application of this method for these purposes will be proposed in future works.
Future work will also focus on the reduction of the computational effort required for the generation of the surrogate model. In order to reduce the evaluation time of the DoEs, multi-fidelity approaches will be considered and compared to more classical methods.

Chapter 7

Conclusions and perspectives

1 General conclusions

Aircraft engine design are nowadays going through a significant change in their mechanical architecture in order to deal with the environmental challenges imposed by regulators (e.g. Flightpath 2050 Europe's vision for aviation report [Darecki, 2011]). In over than 60 years, this is the first time that civil aircraft engines are experiencing such a drastic architecture change by moving from ducted to unducted fan architectures (also known as UDF) in order to increase their global efficiency. These new technologies come with multiple technological challenges impacting their mechanical design, and a large number of experiments and simulations must be performed to develop the knowledge necessary to efficiently design these new families of aeroengines. In this work the focus is on the dynamical simulation of turbomachines. The industrial context was exhaustively presented in Chapter 1. Considering the size of modern FE models and the complexity of numerical simulations (e.g. transient analyses, etc.), conventional methods lead to a CPU time ranging between 0.5-5 days. In the design, model updating, monitoring and diagnostic phases, an optimization process requiring hundreds or thousands of simulations must be performed. Considering the actual processing times, these operations are computationally unaffordable nowadays. The same limitation exists for the sensitivity and robustness analyses or for any other sort of many-query study.

This work develops and applies multiple techniques to drastically reduce the computational effort of numerical simulations on industrial scale FE models. These methods are positioned in an advanced design phase of the engine and while they don't claim to produce high accuracy results, they prove to be efficient and reliable enough to support decisions in the design space exploration and to allow sensitivity and robustness analyses to be performed efficiently. Within the scope of this study, we assume that a maximum

error of 10% on the nominal responses is considered acceptable.

In Chapter 3, we investigated the damping effect in rotating machines since it is necessary to control the sources of damping in mechanical systems to represent exhaustively their dynamical behaviour. Two sources of damping are classically studied in mechanical systems: viscous and structural. The first one is well known and the modeling techniques available in literature allow to correctly represent the viscous damping in mechanical systems. In contrast, structural damping is tedious and several papers have led in the past to misunderstandings about the role of hysteretic damping in rotating shafts [Genta, 2004]. In this chapter we develop an original mathematical model allowing to represent unequivocally the effect of hysteretic damping in rotating shafts in any working condition (sub or supercritical regimes), which is valid in both time and frequency domains. The role of hysteretic damping in rotating shafts is clarified by a graphic representation of the forces acting on rotors in forward and backward whirling motions. This model has been adopted in following chapters too. This chapter has been submitted for journal publication in the *Journal of Sound and Vibration (JSV)* and has been presented to the conference *SEM-IMAC XL* (Orlando, FL, USA, Feb 2021).

In Chapter 4, we present the numerical methods adopted to simulate the response of nonlinear rotating machines, the focus of this chapter is the HBM which is adapted to the case of rotating machines and used to simulate the rotor/stator interaction phenomenon known as *full annular rub*. We demonstrate that the first harmonic approximation is sufficient to represent correctly the nonlinear response of the system. This method is interesting for this work because it allows to solve nonlinear problems in frequency domain and it is generally less computationally demanding than time integration approaches.

In Chapter 5, we present a model reduction approach allowing to deal with industrial scale FE models of rotating machines and reduce their computational burden. In the literature it is common to use CMS-like reduction approaches (e.g. [Peletan, 2012a]) to deal with model order reduction of rotating shafts, nevertheless, to our best knowledge, a dedicated method seems lacking. In this chapter is developed a model reduction approach dedicated to the linear and nonlinear unbalance responses of rotating machines. It is based on the fact that rotating machines do not resonate at natural frequencies like non rotating systems but at critical speeds. Thus, we propose to build reduction bases using the mode shapes of the system at critical speeds. The ROMs developed with this approach are proven to be smaller and more accurate than ROMs developed using bases composed by normal modes. The computational effort on an industrial scale model is reduced by a factor $\approx$10 with a mean error on the maximum amplitudes smaller than 1% in linear FRF simulations. In nonlinear transient analyses we can have a mean error on

the maximum amplitudes of about 2% reducing the computational effort by a factor ≈ 22 to 26. Parts of this chapter have been published in the proceedings of *ASME TurboExpo 2022* [DAlessandro, 2022b].

In Chapter 6, we propose to use surrogate models for the dynamical responses of aero-engines in their design space to respond to the industrial requirements motivating this research. Surrogate models can be used efficiently in any sort of many-query study if trained with an acceptable computational burden and if they are accurate enough. The HB algorithm (Chapter 4) is used on ROMs produced with the critical speed reduction (Chapter 5) to efficiently build databases necessary to train the surrogate models. Two different surrogate modeling approaches are explored: a *scalar approach* (see Section 5.2) and a *vectorial approach* (see Section 5.3). The first one seeks to identify the maximum displacement of the response of a certain DOF and its frequency while, the second one reproduces the frequency response on the whole operational frequency range. The scalar approach is easier to implement than the vectorial one but it presents a severe limitation due to the fact that the maximum amplitude of the response can move discontinuously from a critical speed to another changing the mechanical configuration of the engine and surrogate models do not work efficiently with training data varying discontinuously. In contrast, this limitation does not affect the vectorial approach (POD-RBNN) as the whole frequency responses (snapshots) are taken into account and their variation is always smooth between two different configurations. These approaches are applied on 20 DOFs of an industrial scale FE model, the extension of these techniques to a higher amount of DOFs is direct and discussed in Chapter 6. This chapter has been presented for the conference *ASME TurboExpo 2023* [DAlessandro, 2023] and has been recommended for journal publication on *The Journal of Turbomachinery* (ASME).

The POD-RBNNs surrogates for the dynamical nonlinear responses represent the approach responding to the industrial demands motivating this research. Their application is discussed in the perspectives of this work.

2 Perspectives

Many potential research and developments can be carried out using surrogate models in the field of structural dynamics. Surrogate modeling can be adopted at two different points of the simulation chain in structural dynamic analyses:

1. **Low modeling level**: the development of the ROMs adopted in the classical structural dynamics simulation chain could be quite demanding on large scale FE models. Surrogate models can be used **to develop parametric ROMs** (pseudo-ROM) (see Figure 7.1), employed directly in the algorithm for the linear or nonlinear responses evaluation, reducing the global computational burden of the simulation chain. The whole displacement field would be produced in this case as the solver works on pseudo-ROM but the computational burden related to the solution of the linear/nonlinear problem remains. This option could be investigated in future.

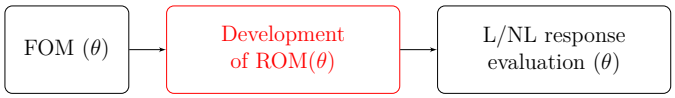

Figure 7.1: Surrogate modeling at low modeling level.

2. **High modeling level**: as proposed in this work, surrogate modeling can be employed **on the response of the system** (see Figure 7.2) allowing to produce a fast-to-evaluate function taking into account the whole simulation chain. Surrogate modeling at this level has been investigated in this work with scalar and vectorial approaches.

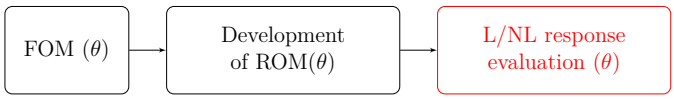

Figure 7.2: Surrogate modeling at high modeling level.

Multiple applications of vectorial surrogate models (POD-RBNN) are left for future works:

- Vectorial surrogate models can be adopted efficiently for **optimisation purposes**. The structural configuration of machines can be optimised in terms of structural and viscous damping, position and physical characteristics of elastic and viscoelastic shaft supports, in order to minimise the unbalance response of the system.
- Even if modern numerical models are accurate and highly detailed, multiple sources of uncertainty are still present (damping parameters, modeling systematic errors, etc.). Hence, the parameters of numerical models need to be

adjusted to correctly calibrate their responses.

Data-based surrogates can be employed for **model calibration purposes** using an optimisation algorithm allowing to identify the mechanical configuration minimising the gap between experimental responses of real machines and the response of numerical models. A dedicated research and optimisation algorithm should be developed for this task.

It is finally interesting to cite in this high modeling level approach, an axis of improvement of vectorial surrogate models, which has been taken into account at the beginning of this work but finally abandoned for lack of time: *Multi-Fidelity Surrogate Modeling* (MFSM) [Benamara, 2017a; Benamara, 2017b; Khatouri, 2022]. This surrogate modeling approach allows to develop cheap and reliable surrogate models integrating a high volume of *low fidelity data*, consisting in cheap degraded simulation results, and a low volume of *high fidelity data*, consisting in expensive numerical results or experimental data.

List of publications

Articles

F.D'Alessandro, H. Festjens, G. Chevallier, S. Cogan. "*Formulation and interpretation of hysteretic damping models for rotating machines*". Journal of sound and vibration. Available at SSRN 4533289. http://dx.doi.org/10.2139/ssrn.4533289.

F.D'Alessandro, H. Festjens, G. Chevallier, S. Cogan, T. Benamara, C. Sainvitu. "*Proper Orthogonal Decomposition-Based Surrogate Modeling Approximation for Aeroengines Nonlinear Unbalance Responses. Journal of Engineering for Gas Turbines and Power, 146(1). https://doi.org/10.1115/1.4063519*".

.

Communications in conferences

F.D'Alessandro, H. Festjens, G. Chevallier, S. Cogan, T. Benamara, C. Sainvitu. "*Metamodélisation multi-fidélité pour la simulation et le recalage en dynamique d'ensemble.*". JJCAB (Journées Jeunes Chercheuses et Chercheurs Acoustique, vibration et Bruit), Lyon, France, November, 2020.

F.D'Alessandro, H. Festjens, G. Chevallier, S. Cogan. "*Hysteretic damping in rotordynamics : A focus on damping induced instability*". SEM IMAC XL (International Modal Analysis Conference), Orlando, Florida, USA, February 7-10, 2021. Submission number 12320, Available at: https://hal.science/hal-04237791.

F.D'Alessandro, H. Festjens, G. Chevallier, S. Cogan, T. Benamara, C. Sainvitu. "*A Dedicated Model Reduction Method for Turbo-Machines Using a Critical Speed Subspace*". Turbo Expo 2022, Rotterdam, The Netherlands, June 13-17, 2022. In Turbo Expo : Power for Land, Sea, and Air (Vol. 86076, p. V08BT26A002). American Society of Mechanical Engineers (ASME). https://doi.org/10.1115/GT2022-79691.

F.D'Alessandro, H. Festjens, G. Chevallier, S. Cogan, T. Benamara, C. Sainvitu. "*POD-based surrogate modeling approximation for aeroengines nonlinear unbalance responses*". Turbo Expo 2023, Boston, USA, June 26-30, 2023. In Turbo Expo: Power for Land, Sea, and Air (Vol. 87066, p. V11BT26A002). American Society of Mechanical Engineers. https://doi.org/10.1115/GT2023-100656.

F.D'Alessandro, F.Garnier, D.Guivarch, A.Zutshi, W.Kang, M.Kunnil, P.Narayanan,

J.S.Kumar, J. Cao, T.Rose, M.Robinson. "*Damping Phenomena in Rotating Machines: A Focus on Rotor Damping With Synchronous and Asynchronous Excitation*". Turbo Expo 2024, London, United Kingdom, June 24-28, 2024. American Society of Mechanical.

Books only

[Allen, 2020] Matthew S Allen, Daniel Rixen, Maarten Van der Seijs, Paolo Tiso, Thomas Abrahamsson, and Randall L Mayes. *Substructuring in engineering dynamics*. Springer, 2020 (cit. on pp. 39, 40, 100).

[Ascher, 1995] Uri M Ascher, Robert MM Mattheij, and Robert D Russell. *Numerical solution of boundary value problems for ordinary differential equations*. SIAM, 1995 (cit. on p. 71).

[Bishop, 1995] Christopher M Bishop et al. *Neural networks for pattern recognition*. Oxford university press, 1995 (cit. on pp. 43, 135, 136).

[Chinesta, 2013] Francisco Chinesta, Roland Keunings, and Adrien Leygue. *The proper generalized decomposition for advanced numerical simulations: a primer*. Springer Science & Business Media, 2013 (cit. on p. 40).

[Dimarogonas, 2013] Andrew D Dimarogonas, Stefanos A Paipetis, and Thomas G Chondros. *Analytical methods in rotor dynamics*. Springer Science & Business Media, 2013 (cit. on pp. 48, 102).

[Ehrich, 1992] Fredric F Ehrich. *Handbook of rotordynamics*. McGraw-Hill Companies, 1992 (cit. on pp. 36, 80).

[Genta, 2007] Giancarlo Genta. *Dynamics of rotating systems*. Springer Science & Business Media, 2007 (cit. on pp. 15, 17, 19, 21, 32, 33, 100, 102, 130).

[Geradin, 2014] Michel Geradin and Daniel J Rixen. *Mechanical vibrations: theory and application to structural dynamics*. John Wiley & Sons, 2014 (cit. on p. 101).

[Gmür, 1997] Thomas Gmür. *Dynamique des structures: analyse modale numerique*. PPUR presses polytechniques, 1997 (cit. on pp. 50–52).

[Gorla, 2003] Rama SR Gorla and Aijaz A Khan. *Turbomachinery: design and theory*. CRC Press, 2003 (cit. on p. 4).

[Janes, 2022] Jane's. *All The World's Aircraft: Dev and Production 22/23 Yearbook*. Jane's, 2022 (cit. on p. 3).

[Kovacic, 2011] Ivana Kovacic and Michael J Brennan. *The Duffing equation: nonlinear oscillators and their behaviour*. John Wiley & Sons, 2011 (cit. on pp. 73, 76).

[Krack, 2019] Malte Krack and Johann Gross. *Harmonic balance for nonlinear vibration problems*. Vol. 1. Springer, 2019 (cit. on pp. 37, 71–73, 75, 77, 101, 133, 151).

[Kuznetsov, 1998] Yuri A Kuznetsov, Iu A Kuznetsov, and Y Kuznetsov. *Elements of applied bifurcation theory*. Vol. 112. Springer, 1998 (cit. on p. 86).

[Lalanne, 1996] Michel Lalanne and Guy Ferraris. *Dynamique des rotors en flexion*. Ed. Techniques Ingenieur, 1996 (cit. on p. 32).

[Lalanne M, 1998] Ferraris G. Lalanne M. *Rotordynamics Prediction in Engineering,2nd Edition*. Wiley, 1998 (cit. on pp. 15, 19, 100, 130).

[Muszynska, 2005] Agnieszka Muszynska. *Rotordynamics*. CRC press, 2005 (cit. on p. 36).

[Nayfeh, 2008a] Ali H Nayfeh and Dean T Mook. *Nonlinear oscillations*. John Wiley & Sons, 2008 (cit. on p. 85).

[Nayfeh, 2008b] Ali H Nayfeh and P Frank Pai. *Linear and nonlinear structural mechanics*. John Wiley & Sons, 2008 (cit. on p. 88).

[Quarteroni, 2014] Alfio Quarteroni, Gianluigi Rozza, et al. *Reduced order methods for modeling and computational reduction*. Vol. 9. Springer, 2014 (cit. on p. 100).

[Royce, 2015] Rolls Royce. *The jet engine*. John Wiley & Sons, 2015 (cit. on pp. 3, 4).

[Ruhl, 1970] Roland Luther Ruhl. *Dynamics of distributed parameter rotor systems: transfer matrix and finite element techniques*. Cornell University, 1970 (cit. on pp. 15, 18).

[Schilders, 2008b] Wilhelmus HA Schilders, Henk A Van der Vorst, and Joost Rommes. *Model order reduction: theory, research aspects and applications*. Vol. 13. Springer, 2008 (cit. on p. 40).

[Seydel, 2009] Rüdiger Seydel. *Practical bifurcation and stability analysis*. Vol. 5. Springer Science & Business Media, 2009 (cit. on pp. 71, 73, 81, 85, 87).

[Sforza, 2016] Pasquale M Sforza. *Theory of aerospace propulsion*. Butterworth-Heinemann, 2016 (cit. on pp. 5, 7).

[Sobester, 2008] András Sobester, Alexander Forrester, and Andy Keane. *Engineering design via surrogate modelling: a practical guide*. John Wiley & Sons, 2008 (cit. on pp. 42, 130, 135, 136).

[Stodola, 1927] Aurel Stodola. *Steam and gas turbines: with a supplement on the prospects of the thermal prime mover*. Vol. 2. McGraw-Hill, 1927 (cit. on p. 15).

[Vance, 1991] John M Vance. *Rotordynamics of turbomachinery*. John Wiley & Sons, 1991 (cit. on pp. 19, 23).

Articles only

[Adams, 1986] J Adams and Ting-Wei Tang. "A revised boundary condition for the numerical analysis of Schottky barrier diodes". *IEEE electron device letters* 7.9 (1986), pp. 525–527 (cit. on p. 101).

[Adams, 1980] ML Adams. "Non-linear dynamics of flexible multi-bearing rotors". *Journal of sound and vibration* 71.1 (1980), pp. 129–144 (cit. on pp. 15, 37, 69).

[Adhikari, 2006] Sondipon Adhikari. "Damping modelling using generalized proportional damping". *Journal of Sound and Vibration* 293.1-2 (2006), pp. 156–170 (cit. on p. 30).

[Adiletta, 2002] G Adiletta and L Della Pietra. "The squeeze film damper over four decades of investigations. Part II: Rotordynamic analyses with rigid and flexible rotors". *The Shock and vibration digest* 34.2 (2002), pp. 97–126 (cit. on pp. 15, 24).

[Adiletta, 1996] G Adiletta, AR Guido, and C Rossi. "Chaotic motions of a rigid rotor in short journal bearings". *Nonlinear dynamics* 10.3 (1996), pp. 251–269 (cit. on p. 101).

[Ahmad, 2010] Sagheer Ahmad. "Rotor casing contact phenomenon in rotor dynamics—literature survey". *Journal of Vibration and Control* 16.9 (2010), pp. 1369–1377 (cit. on pp. 15, 36, 69).

[Ajjarapu, 1992] Venkataramana Ajjarapu and Colin Christy. "The continuation power flow: a tool for steady state voltage stability analysis". *IEEE transactions on Power Systems* 7.1 (1992), pp. 416–423 (cit. on p. 88).

[Alves, 2020] Pedro Alves, Miguel Silvestre, and Pedro Gamboa. "Aircraft Propellers—Is There a Future?" *Energies* 13.16 (2020), p. 4157 (cit. on pp. 5, 7).

[Ammar, 2010] Amine Ammar. "The proper generalized decomposition: a powerful tool for model reduction". *International Journal of Material Forming* 3 (2010), pp. 89–102 (cit. on p. 40).

[Arab, 2018] Safa Ben Arab, Jose Dias Rodrigues, Slim Bouaziz, and Mohamed Haddar. "Stability analysis of internally damped rotating composite shafts using a finite element formulation". *Comptes Rendus Mecanique* 346.4 (2018), pp. 291–307 (cit. on p. 48).

[Atamturktur, 2015] Sez Atamturktur, Zhifeng Liu, Scott Cogan, and Hsein Juang. "Calibration of imprecise and inaccurate numerical models considering fidelity and robustness: a multi-objective optimization-based approach". *Structural and Multidisciplinary Optimization* 51.3 (2015), pp. 659–671 (cit. on p. 10).

[Ball, 1997] Linden J Ball, Jonathan St. BT Evans, Ian Dennis, and Thomas C Ormerod. "Problem-solving strategies and expertise in engineering design". *Thinking & Reasoning* 3.4 (1997), pp. 247–270 (cit. on p. 10).

[Balmaseda, 2020] Mikel Balmaseda, Georges Jacquet-Richardet, Antoine Placzek, and D-M Tran. "Reduced order models for nonlinear dynamic analysis with application to a fan blade". *Journal of Engineering for Gas Turbines and Power* 142.4 (2020) (cit. on p. 131).

[Balmes, 1997] Etienne Balmes. "Model reduction for systems with frequency dependent damping properties". *OFFICE NATIONAL D ETUDES ET DE RECHERCHES AEROSPATIALES ONERA-PUBLICATIONS-TP* (1997) (cit. on p. 101).

[Balmès, 1996a] Etienne Balmès et al. "Frequency domain identification of structural dynamics using the pole/residue parametrization". *OFFICE NATIONAL D ETUDES ET DE RECHERCHES AEROSPATIALES ONERA-PUBLICATIONS-TP* (1996) (cit. on p. 29).

[Balmès, 1996b] Etienne Balmès. "Parametric families of reduced finite element models. Theory and applications". *Mechanical systems and signal Processing* 10.4 (1996), pp. 381–394 (cit. on pp. 39, 40).

[Barbone, 2003] Paul E Barbone, Dan Givoli, and Igor Patlashenko. "Optimal modal reduction of vibrating substructures". *International Journal for Numerical Methods in Engineering* 57.3 (2003), pp. 341–369 (cit. on p. 100).

[Ben Smida, 2012] B Ben Smida, R Majed, Noureddine Bouhaddi, and Morvan Ouisse. "Investigations for a model reduction technique of fluid–structure coupled systems". *Proceedings of the Institution of Mechanical Engineers, Part C: Journal of Mechanical Engineering Science* 226.1 (2012), pp. 42–54 (cit. on p. 118).

[Benaissa, 2016] Brahim Benaissa, Nourredine Ait Hocine, Idir Belaidi, Abderrachid Hamrani, and Valeria Pettarin. "Crack identification using model reduction based on proper orthogonal decomposition coupled with radial basis functions". *Structural and Multidisciplinary Optimization* 54.2 (2016), pp. 265–274 (cit. on p. 131).

[Benamara, 2017b] Tariq Benamara, Piotr Breitkopf, Ingrid Lepot, Caroline Sainvitu, and Pierre Villon. "Multi-fidelity POD surrogate-assisted optimization: Concept and aero-design study". *Structural and Multidisciplinary Optimization* 56.6 (2017), pp. 1387–1412 (cit. on pp. 11, 43, 131, 161).

[Bently, 2002] Donald E Bently, John J Yu, Paul Goldman, and Agnes Muszynska. "Full annular rub in mechanical seals, Part I: experimental results". *International Journal of Rotating Machinery* 8.5 (2002), pp. 319–328 (cit. on p. 37).

[Bi, 2017] Sifeng Bi, Saurabh Prabhu, Scott Cogan, and Sez Atamturktur. "Uncertainty quantification metrics with varying statistical information in model calibration and validation". *AIAA journal* 55.10 (2017), pp. 3570–3583 (cit. on p. 10).

[Bock, 1984] Hans Georg Bock and Karl-Josef Plitt. "A multiple shooting algorithm for direct solution of optimal control problems". *IFAC Proceedings Volumes* 17.2 (1984), pp. 1603–1608 (cit. on p. 71).

[Bonello, 2002] P Bonello, MJ Brennan, and R Holmes. "Non-linear modelling of rotor dynamic systems with squeeze film dampers—an efficient integrated approach". *Journal of Sound and Vibration* 249.4 (2002), pp. 743–773 (cit. on pp. 24, 71).

[Bonello, 2009] Philip Bonello and Pham Minh Hai. "A receptance harmonic balance technique for the computation of the vibration of a whole aero-engine model with nonlinear bearings". *Journal of Sound and Vibration* 324.1-2 (2009), pp. 221–242 (cit. on pp. 16, 24, 71).

[Bonello, 2010] Philip Bonello and Pham Minh Hai. "Computational studies of the unbalance response of a whole aero-engine model with squeeze-film bearings". *Journal of engineering for gas turbines and power* 132.3 (2010) (cit. on pp. 18, 19).

[Bouaziz, 2014] Sofien Bouaziz, Sebastian Martin, Tiantian Liu, Ladislav Kavan, and Mark Pauly. "Projective dynamics: Fusing constraint projections for fast simulation". *ACM transactions on graphics (TOG)* 33.4 (2014), pp. 1–11 (cit. on p. 69).

[Bouhlel, 2019] Mohamed A Bouhlel and Joaquim RRA Martins. "Gradient-enhanced kriging for high-dimensional problems". *Engineering with Computers* 35.1 (2019), pp. 157–173 (cit. on p. 146).

[Bourquin, 1992] Frederic Bourquin. "Component mode synthesis and eigenvalues of second order operators: discretization and algorithm". *ESAIM: Mathematical Modelling and Numerical Analysis* 26.3 (1992), pp. 385–423 (cit. on p. 39).

[Braconnier, 2011] Thierry Braconnier, Marc Ferrier, J-C Jouhaud, Marc Montagnac, and Pierre Sagaut. "Towards an adaptive POD/SVD surrogate model for aeronautic design". *Computers & Fluids* 40.1 (2011), pp. 195–209 (cit. on p. 131).

[Butcher, 1976] John C Butcher. "On the implementation of implicit Runge-Kutta methods". *BIT Numerical Mathematics* 16.3 (1976), pp. 237–240 (cit. on p. 69).

[Butcher, 1996] John Charles Butcher. "A history of Runge-Kutta methods". *Applied numerical mathematics* 20.3 (1996), pp. 247–260 (cit. on p. 69).

[Cameron, 1989] TM Cameron and Jerry H Griffin. "An alternating frequency/time domain method for calculating the steady-state response of nonlinear dynamic systems" (1989) (cit. on pp. 73, 76).

[Carpenter, 1991] Nicholas J Carpenter, Robert L Taylor, and Michael G Katona. "Lagrange constraints for transient finite element surface contact". *International journal for numerical methods in engineering* 32.1 (1991), pp. 103–128 (cit. on p. 69).

[Caughey, 1965] TK Caughey and M EoJ O'Kelly. "Classical normal modes in damped linear dynamic systems" (1965) (cit. on pp. 30, 48).

[Cenedese, 2022a] Mattia Cenedese, Joar Axaas, Bastian Bauerlein, Kerstin Avila, and George Haller. "Data-driven modeling and prediction of non-linearizable dynamics via spectral submanifolds". *Nature communications* 13.1 (2022), pp. 1–13 (cit. on p. 131).

[Cenedese, 2022b] Mattia Cenedese, Joar Axaas, Haocheng Yang, Melih Eriten, and George Haller. "Data-driven nonlinear model reduction to spectral submanifolds in mechanical systems". *Philosophical Transactions of the Royal Society A* 380.2229 (2022), p. 20210194 (cit. on p. 131).

[Chen, 2015] G Chen. "Vibration modelling and verifications for whole aero-engine". *Journal of Sound and Vibration* 349 (2015), pp. 163–176 (cit. on p. 21).

[Chen, 2020] Xu Chen, Hao Zhang, Cunjian Zou, Jingyu Zhai, and Qingkai Han. "Research on the prediction method of unbalance responses of dual-rotor system based on surrogate models". *SN Applied Sciences* 2.1 (2020), pp. 1–13 (cit. on p. 131).

[Cheng, 1994] Bing Cheng and D Michael Titterington. "Neural networks: A review from a statistical perspective". *Statistical science* (1994), pp. 2–30 (cit. on p. 43).

[Childs, 1985] Dara W Childs and DS Moyer. "Vibration characteristics of the HPOTP (high-pressure oxygen turbopump) of the SSME (space shuttle main engine)" (1985) (cit. on p. 69).

[Chinesta, 2011a] Francisco Chinesta, Amine Ammar, Adrien Leygue, and Roland Keunings. "An overview of the proper generalized decomposition with applications in computational rheology". *Journal of Non-Newtonian Fluid Mechanics* 166.11 (2011), pp. 578–592 (cit. on p. 40).

[Chinesta, 2011b] Francisco Chinesta, Pierre Ladeveze, and Elias Cueto. "A short review on model order reduction based on proper generalized decomposition". *Archives of Computational Methods in Engineering* 18.4 (2011), pp. 395–404 (cit. on p. 40).

[Choi, 1994] Sang-Kyu Choi and Sherif T Noah. "Mode-locking and chaos in a Jeffcott rotor with bearing clearances" (1994) (cit. on p. 15).

[Choi, 2002] Y.S. Choi. "Investigation on the whirling motion of full annular rotor rub". *Journal of Sound and Vibration* 258.1 (2002), pp. 191–198 (cit. on pp. 36, 37).

[Choi, 1987] Yeon-Sun Choi and Sherif T Noah. "Nonlinear steady-state response of a rotor-support system" (1987) (cit. on pp. 15, 16, 70).

[Choy, 1987] FK Choy and J Padovan. "Non-linear transient analysis of rotor-casing rub events". *Journal of Sound and Vibration* 113.3 (1987), pp. 529–545 (cit. on pp. 36, 69, 101).

[Chu, 1998] Fulei Chu and Zhengsong Zhang. "Bifurcation and chaos in a rub-impact Jeffcott rotor system". *Journal of Sound and Vibration* 210.1 (1998), pp. 1–18 (cit. on p. 15).

[Chua, 1981] Leon Chua and Akio Ushida. "Algorithms for computing almost periodic steady-state response of nonlinear systems to multiple input frequencies". *IEEE Transactions on circuits and systems* 28.10 (1981), pp. 953–971 (cit. on p. 70).

[Chun, 1996] Sang-Bok Chun and Chong-Wen Lee. "Vibration analysis of shaft-bladed disk system by using substructure synthesis and assumed modes method". *Journal of Sound and Vibration* 189.5 (1996), pp. 587–608 (cit. on p. 22).

[Clarke, 2005] Stella M Clarke, Jan H Griebsch, and Timothy W Simpson. "Analysis of support vector regression for approximation of complex engineering analyses" (2005) (cit. on p. 43).

[Colaitis, 2021] Yann Colaitis and Alain Batailly. "The harmonic balance method with arc-length continuation in blade-tip/casing contact problems". *Journal of Sound and Vibration* 502 (2021), p. 116070 (cit. on p. 22).

[Cole, 2008] Matthew OT Cole. "On stability of rotordynamic systems with rotor–stator contact interaction". *Proceedings of the Royal Society A: Mathematical, Physical and Engineering Sciences* 464.2100 (2008), pp. 3353–3375 (cit. on p. 37).

[Combescure, 2008] Didier Combescure and Arnaud Lazarus. "Refined finite element modelling for the vibration analysis of large rotating machines: Application to the gas turbine modular helium reactor power conversion unit". *Journal of Sound and Vibration* 318.4-5 (2008), pp. 1262–1280 (cit. on p. 20).

[Craig Jr, 1968] Roy R Craig Jr and Mervyn CC Bampton. "Coupling of substructures for dynamic analyses." *AIAA journal* 6.7 (1968), pp. 1313–1319 (cit. on pp. 38, 41).

[Crandall, 1991] SH Crandall. "The hysteretic damping model in vibration theory". *Proceedings of the Institution of Mechanical Engineers, Part C: Mechanical Engineering Science* 205.1 (1991), pp. 23–28 (cit. on pp. 48, 64).

[Crandall, 1970] Stephen H Crandall. "The role of damping in vibration theory". *Journal of sound and vibration* 11.1 (1970), 3–IN1 (cit. on pp. 49, 58).

[Crawley, 1986] EF Crawley, EH Ducharme, and DR Mokadam. "Analytical and experimental investigation of the coupled bladed disk/shaft whirl of a cantilevered turbofan" (1986) (cit. on p. 22).

[Crawley, 1984] EF Crawley and DR Mokadam. "Stagger angle dependence of inertial and elastic coupling in bladed disks" (1984) (cit. on p. 22).

[Cressie, 1988] Noel Cressie. "Spatial prediction and ordinary kriging". *Mathematical geology* 20.4 (1988), pp. 405–421 (cit. on p. 43).

[Daniel, 2022] Thomas Daniel, Fabien Casenave, Nissrine Akkari, Ali Ketata, and David Ryckelynck. "Physics-informed cluster analysis and a priori efficiency criterion for the construction of local reduced-order bases". *Journal of Computational Physics* (2022), p. 111120 (cit. on p. 100).

[De Gaetano, 2014] Giovanni De Gaetano, Domenico Mundo, FI Cosco, Carmine Maletta, and Stijn Donders. "Concept modelling of vehicle joints and beam-like structures through dynamic FE-based methods". *Shock and Vibration* 2014 (2014) (cit. on p. 79).

[Defaye, 2006] Cyril Defaye, Mihai Arghir, Olivier Bonneau, Philippe Carpentier, Charles Debailleux, and Frederic Imbourg. "Experimental study of the radial and tangential forces in a whirling squeeze film damper". *Tribology transactions* 49.2 (2006), pp. 271–278 (cit. on p. 24).

[Della Pietra, 2002] L Della Pietra and G Adiletta. "The squeeze film damper over four decades of investigations. Part I: Characteristics and operating features". *The Shock and Vibration Digest* 34.1 (2002), pp. 3–26 (cit. on pp. 15, 24, 48).

[Denimal, 2016] E Denimal, L Nechak, J-J Sinou, and S Nacivet. "Kriging surrogate models for predicting the complex eigenvalues of mechanical systems subjected to friction-induced vibration". *Shock and vibration* 2016 (2016) (cit. on p. 130).

[Denimal, 2018] Enora Denimal, Lyes Nechak, Jean-Jacques Sinou, and Samuel Nacivet. "A novel hybrid surrogate model and its application on a mechanical system subjected to friction-induced vibration". *Journal of Sound and Vibration* 434 (2018), pp. 456–474 (cit. on p. 130).

[Denimal, 2021] Enora Denimal and Jean-Jacques Sinou. "Advanced kriging-based surrogate modelling and sensitivity analysis for rotordynamics with uncertainties". *European Journal of Mechanics - A/Solids* 90 (2021), pp. 1–20 (cit. on p. 130).

[Denimal, 2022b] Enora Denimal, Jean-Jacques Sinou, and Samuel Nacivet. "Prediction of Squeal Instabilities of a Finite Element Model Automotive Brake With Uncertain Structural and Environmental Parameters With a Hybrid Surrogate Model". *Journal of Vibration and Acoustics* 144.2 (2022) (cit. on p. 130).

[Detroux, 2015] Thibaut Detroux, Ludovic Renson, Luc Masset, and Gaetan Kerschen. "The harmonic balance method for bifurcation analysis of large-scale nonlinear mechanical systems". *Computer Methods in Applied Mechanics and Engineering* 296 (2015), pp. 18–38 (cit. on p. 85).

[Dickens, 1997] JM Dickens, JM Nakagawa, and MJ Wittbrodt. "A critique of mode acceleration and modal truncation augmentation methods for modal response analysis". *Computers & structures* 62.6 (1997), pp. 985–998 (cit. on pp. 41, 44, 118).

[Donders, 2010] Stijn Donders, Bert Pluymers, Patrik Ragnarsson, Rabah Hadjit, and Wim Desmet. "The wave-based substructuring approach for the efficient description of interface dynamics in substructuring". *Journal of Sound and Vibration* 329.8 (2010), pp. 1062–1080 (cit. on p. 42).

[Dubourg, 2014] V Dubourg and Bruno Sudret. "Meta-model-based importance sampling for reliability sensitivity analysis". *Structural Safety* 49 (2014), pp. 27–36 (cit. on p. 42).

[Dumon, 2011] Antoine Dumon, Cyrille Allery, and Amine Ammar. "Proper general decomposition (PGD) for the resolution of Navier–Stokes equations". *Journal of Computational Physics* 230.4 (2011), pp. 1387–1407 (cit. on p. 40).

[Dyn, 1986] Nira Dyn, David Levin, and Samuel Rippa. "Numerical procedures for surface fitting of scattered data by radial functions". *SIAM Journal on Scientific and Statistical Computing* 7.2 (1986), pp. 639–659 (cit. on p. 43).

[Festjens, 2014] H Festjens, G Chevallier, and JL Dion. "Nonlinear model order reduction of jointed structures for dynamic analysis". *Journal of Sound and Vibration* 333.7 (2014), pp. 2100–2113 (cit. on pp. 44, 101).

[Festjens, 2013] Hugo Festjens, Gaël Chevallier, and Jean-luc Dion. "A numerical tool for the design of assembled structures under dynamic loads". *International Journal of Mechanical Sciences* 75 (2013), pp. 170–177 (cit. on pp. 48, 69, 111, 113).

[Festjens, 2012] Hugo Festjens, Chevallier Gaël, Renaud Franck, Dion Jean-Luc, and Lemaire Remy. "Effectiveness of multilayer viscoelastic insulators to prevent occurrences of brake squeal: A numerical study". *Applied Acoustics* 73.11 (2012), pp. 1121–1128 (cit. on pp. 30, 48).

[Friedman, 1991] Jerome H Friedman. "Multivariate adaptive regression splines". *The annals of statistics* 19.1 (1991), pp. 1–67 (cit. on p. 43).

[Galerkin, 1915] Boris Grigoryevich Galerkin. "Series solution of some problems of elastic equilibrium of rods and plates". *Vestnik inzhenerov i tekhnikov* 19.7 (1915), pp. 897–908 (cit. on pp. 70, 72, 190).

[Gander, 2012] Martin J Gander and Gerhard Wanner. "From Euler, Ritz, and Galerkin to modern computing". *Siam Review* 54.4 (2012), pp. 627–666 (cit. on p. 189).

[Ganguly, 2022] Krishanu Ganguly, Saurabh Chandraker, and Haraprasad Roy. "A review on modelling and dynamic analysis of viscoelastic rotor systems". *Aircraft Engineering and Aerospace Technology* (2022) (cit. on p. 48).

[Gehannin, 2009a] Jerome Gehannin, Mihai Arghir, and Olivier Bonneau. "Evaluation of Rayleigh–Plesset equation based cavitation models for squeeze film dampers" (2009) (cit. on pp. 24, 27).

[Gehannin, 2009b] Jérôme Gehannin, Mihai Arghir, and Olivier Bonneau. "Complete squeeze-film damper analysis based on the "bulk flow" equations". *Tribology transactions* 53.1 (2009), pp. 84–96 (cit. on p. 24).

[Genta, 1988] G Genta. "Whirling of unsymmetrical rotors: a finite element approach based on complex co-ordinates". *Journal of Sound and Vibration* 124.1 (1988), pp. 27–53 (cit. on p. 17).

[Genta, 1996a] G Genta, C Delprete, and D Bassani. "DYNROT: a finite element code for rotordynamic analysis based on complex co-ordinates". *Engineering computations* 13.6 (1996), pp. 86–109 (cit. on p. 21).

[Genta, 1999] G Genta, C Delprete, and E Brusa. "Some considerations on the basic assumptions in rotordynamics". *Journal of Sound and Vibration* 227.3 (1999), pp. 611–645 (cit. on p. 49).

[Genta, 2004] Giancarlo Genta. "On a persistent misunderstanding of the role of hysteretic damping in rotordynamics". *J. Vib. Acoust.* 126.3 (2004), pp. 459–461 (cit. on pp. 28, 43, 47–49, 52, 58, 61, 64, 158).

[Genta, 2010] Giancarlo Genta and Nicola Amati. "Hysteretic damping in rotordynamics: An equivalent formulation". *Journal of Sound and Vibration* 329.22 (2010), pp. 4772–4784 (cit. on pp. 49, 58).

[Genta, 1996b] Giancarlo Genta and Andrea Tonoli. "A harmonic finite element for the analysis of flexural, torsional and axial rotordynamic behaviour of discs". *Journal of Sound and Vibration* 196.1 (1996), pp. 19–43 (cit. on p. 21).

[Geradin, 1984] M Geradin and N Kill. "A new approach to finite element modelling of flexible rotors". *Engineering Computations* (1984) (cit. on pp. 17, 19, 21).

[Gibanica, 2021] Mladen Gibanica and Thomas JS Abrahamsson. "Data-driven modal surrogate model for frequency response uncertainty propagation". *Probabilistic Engineering Mechanics* 66 (2021), p. 103142 (cit. on p. 131).

[Gill, 1972] Philip E Gill and Walter Murray. "Quasi-Newton methods for unconstrained optimization". *IMA Journal of Applied Mathematics* 9.1 (1972), pp. 91–108 (cit. on p. 83).

[Glaz, 2009] Bryan Glaz, Tushar Goel, Li Liu, Peretz P Friedmann, and Raphael T Haftka. "Multiple-surrogate approach to helicopter rotor blade vibration reduction". *AIAA journal* 47.1 (2009), pp. 271–282 (cit. on p. 131).

[Green, 1948] Robert Boyce Green. "Gyroscopic effects on the critical speeds of flexible rotors" (1948) (cit. on p. 15).

[Griffin, 1966] William S Griffin, Herbert H Richardson, and S Yamanami. "A study of fluid squeeze-film damping" (1966) (cit. on p. 23).

[Grolet, 2012] Aurélien Grolet and Fabrice Thouverez. "On a new harmonic selection technique for harmonic balance method". *Mechanical Systems and Signal Processing* 30 (2012), pp. 43–60 (cit. on pp. 72, 73).

[Guedri, 2012] Mohamed Guedri, Scott Cogan, and Noureddine Bouhaddi. "Robustness of structural reliability analyses to epistemic uncertainties". *Mechanical systems and signal processing* 28 (2012), pp. 458–469 (cit. on p. 10).

[Guenot, 2013] Marc Guenot, Ingrid Lepot, Caroline Sainvitu, Jordan Goblet, and Rajan Filomeno Coelho. "Adaptive sampling strategies for non-intrusive POD-based surrogates". *Engineering computations* (2013) (cit. on p. 40).

[Gunter, 1977] EJ Gunter, LE Barrett, and PE Allaire. "Design of nonlinear squeeze-film dampers for aircraft engines" (1977) (cit. on p. 24).

[Guo, 2005] Zenglin Guo, Toshio Hirano, and R Gordon Kirk. "Application of CFD analysis for rotating machinery—part I: hydrodynamic, hydrostatic bearings and squeeze film damper". *J. Eng. Gas Turbines Power* 127.2 (2005), pp. 445–451 (cit. on p. 24).

[Guskov, 2007] Mikhail Guskov, Jean-Jacques Sinou, and Fabrice Thouverez. "Multi-dimensional harmonic balance applied to rotor dynamics". 48027 (2007), pp. 1243–1249 (cit. on pp. 16, 21, 37, 71–73, 101, 133).

[Guyan, 1965] Robert J Guyan. "Reduction of stiffness and mass matrices". *AIAA journal* 3.2 (1965), pp. 380–380 (cit. on p. 38).

[Hai, 2008] Pham Minh Hai and Philip Bonello. "An impulsive receptance technique for the time domain computation of the vibration of a whole aero-engine model with nonlinear bearings". *Journal of Sound and Vibration* 318.3 (2008), pp. 592–605 (cit. on p. 71).

[Hall, 2006] John F Hall. "Problems encountered from the use (or misuse) of Rayleigh damping". *Earthquake engineering & structural dynamics* 35.5 (2006), pp. 525–545 (cit. on p. 48).

[Hamim, 2017] Salah U Hamim and Raman P Singh. "Taguchi-based design of experiments in training POD-RBF surrogate model for inverse material modelling using nanoindentation". *Inverse Problems in Science and Engineering* 25.3 (2017), pp. 363–381 (cit. on p. 131).

[Hassan, 1994] A Hassan. "On the third superharmonic resonance in the Duffing oscillator". *Journal of sound and vibration* 172.4 (1994), pp. 513–526 (cit. on p. 89).

[Hearst, 1998] Marti A. Hearst, Susan T Dumais, Edgar Osuna, John Platt, and Bernhard Scholkopf. "Support vector machines". *IEEE Intelligent Systems and their applications* 13.4 (1998), pp. 18–28 (cit. on p. 43).

[Hetzler, 2013] Hartmut Hetzler. "On the effect of non-smooth Coulomb damping on flutter-type self-excitation in a non-gyroscopic circulatory 2-DoF-system". *Nonlinear Dynamics* 73.3 (2013), pp. 1829–1847 (cit. on p. 55).

[Hilber, 1977] Hans M Hilber, Thomas JR Hughes, and Robert L Taylor. "Improved numerical dissipation for time integration algorithms in structural dynamics". *Earthquake Engineering & Structural Dynamics* 5.3 (1977), pp. 283–292 (cit. on p. 133).

[Hill, 2017] TL Hill, Andrea Cammarano, SA Neild, and DAW Barton. "Identifying the significance of nonlinear normal modes". *Proceedings of the Royal Society A: Mathematical, Physical and Engineering Sciences* 473.2199 (2017), p. 20160789 (cit. on p. 39).

[Hua, 2005] J Hua, S Swaddiwudhipong, ZS Liu, and QY Xu. "Numerical analysis of nonlinear rotor–seal system". *Journal of sound and vibration* 283.3-5 (2005), pp. 525–542 (cit. on p. 101).

[Hwang, 1991] Jon Li Hwang and Ting Nung Shiau. "An application of the generalized polynomial expansion method to nonlinear rotor bearing systems" (1991) (cit. on p. 70).

[Ilanko, 2009] Sinniah Ilanko. "Comments on the historical bases of the Rayleigh and Ritz methods". *Journal of Sound and Vibration* 319.1-2 (2009), pp. 731–733 (cit. on p. 38).

[Jacquet-Richardet, 1996] G Jacquet-Richardet, G Ferraris, and P Rieutord. "Frequencies and modes of rotating flexible bladed disc-shaft assemblies: a global cyclic symmetry approach". *Journal of sound and vibration* 191.5 (1996), pp. 901–915 (cit. on pp. 18, 22, 36).

[Jacquet-Richardet, 2013] Georges Jacquet-Richardet, Mohamed Torkhani, Patrice Cartraud, Fabrice Thouverez, T Nouri Baranger, Mathieu Herran, et al. "Rotor to stator contacts in turbomachines. Review and application". *Mechanical Systems and Signal Processing* 40.2 (2013), pp. 401–420 (cit. on pp. 15, 69, 71).

[Jaumouille, 2010] Vincent Jaumouille, J-J Sinou, and Benoit Petitjean. "An adaptive harmonic balance method for predicting the nonlinear dynamic responses of mechanical systems—application to bolted structures". *Journal of sound and vibration* 329.19 (2010), pp. 4048–4067 (cit. on pp. 85, 88).

[Jeffcott, 1919] Henry Homan Jeffcott. "XXVII. The lateral vibration of loaded shafts in the neighbourhood of a whirling speed.—The effect of want of balance". *The London, Edinburgh, and Dublin Philosophical Magazine and Journal of Science* 37.219 (1919), pp. 304–314 (cit. on p. 15).

[Jiang, 2009] Jun Jiang. "Determination of the global responses characteristics of a piecewise smooth dynamical system with contact". *Nonlinear Dynamics* 57.3 (2009), pp. 351–361 (cit. on p. 37).

[Jin, 2001] Ruichen Jin, Wei Chen, and Timothy W Simpson. "Comparative studies of metamodelling techniques under multiple modelling criteria". *Structural and multidisciplinary optimization* 23.1 (2001), pp. 1–13 (cit. on pp. 131, 135).

[Jin, 2019] Yulin Jin, Kuan Lu, Chongxiang Huang, Lei Hou, and Yushu Chen. "Nonlinear dynamic analysis of a complex dual rotor-bearing system based on a novel model reduction method". *Applied Mathematical Modelling* 75 (2019), pp. 553–571 (cit. on p. 131).

[Joannin, 2017] Colas Joannin, Benjamin Chouvion, Fabrice Thouverez, Jean-Philippe Ousty, and Moustapha Mbaye. "A nonlinear component mode synthesis method for the computation of steady-state vibrations in non-conservative systems". *Mechanical Systems and Signal Processing* 83 (2017), pp. 75–92 (cit. on pp. 44, 101).

[Jolliffe, 1990] Ian T Jolliffe. "Principal component analysis: a beginner's guide—I. Introduction and application". *Weather* 45.10 (1990), pp. 375–382 (cit. on p. 40).

[Junge, 2009] Michael Junge, Dominik Brunner, Jens Becker, and Lothar Gaul. "Interface-reduction for the Craig–Bampton and Rubin method applied to FE–BE coupling with a large fluid–structure interface". *International journal for numerical methods in engineering* 77.12 (2009), pp. 1731–1752 (cit. on pp. 41, 44).

[Kane, 1991] K Kane and BJ Torby. "The extended modal reduction method applied to rotor dynamic problems" (1991) (cit. on p. 44).

[Karayiannis, 1997] Nicolaos B Karayiannis and Glenn Weiqun Mi. "Growing radial basis neural networks: Merging supervised and unsupervised learning with network growth techniques". *IEEE Transactions on Neural networks* 8.6 (1997), pp. 1492–1506 (cit. on pp. 43, 131).

[Karkar, 2014] Sami Karkar, Bruno Cochelin, and Christophe Vergez. "A comparative study of the harmonic balance method and the orthogonal collocation method on stiff nonlinear systems". *Journal of Sound and Vibration* 333.12 (2014), pp. 2554–2567 (cit. on p. 71).

[Katz, 1988] R Katz, Chong-Won Lee, AG Ulsoy, and RA Scott. "The dynamic response of a rotating shaft subject to a moving load". *Journal of sound and vibration* 122.1 (1988), pp. 131–148 (cit. on p. 18).

[Kerschen, 2005] Gaetan Kerschen, Jean-claude Golinval, Alexander F Vakakis, and Lawrence A Bergman. "The method of proper orthogonal decomposition for dynamical characterization and order reduction of mechanical systems: an overview". *Nonlinear dynamics* 41.1 (2005), pp. 147–169 (cit. on p. 136).

[Kerschen, 2009] Gaëtan Kerschen, Maxime Peeters, Jean-Claude Golinval, and Alexander F Vakakis. "Nonlinear normal modes, Part I: A useful framework for the structural dynamicist". *Mechanical systems and signal processing* 23.1 (2009), pp. 170–194 (cit. on p. 39).

[Khader, 1990] N Khader and RG Loewy. "Shaft flexibility effects on the forced response of a bladed-disk assembly". *Journal of sound and vibration* 139.3 (1990), pp. 469–485 (cit. on p. 22).

[Khatouri, 2022] Hanane Khatouri, Tariq Benamara, Piotr Breitkopf, and Jean Demange. "Metamodeling techniques for CPU-intensive simulation-based design optimization: a survey". *Advanced Modeling and Simulation in Engineering Sciences* 9.1 (2022), pp. 1–31 (cit. on pp. 42–44, 161).

[Khulief, 1997] YA Khulief and MA Mohiuddin. "On the dynamic analysis of rotors using modal reduction". *Finite Elements in Analysis and Design* 26.1 (1997), pp. 41–55 (cit. on pp. 31, 100).

[Kim, 2015] T Kim. "Surrogate model reduction for linear dynamic systems based on a frequency domain modal analysis". *Computational Mechanics* 56.4 (2015), pp. 709–723 (cit. on pp. 40, 131).

[Kim, 1998] Taehyoun Kim. "Frequency-domain Karhunen-Loeve method and its application to linear dynamic systems". *AIAA journal* 36.11 (1998), pp. 2117–2123 (cit. on pp. 40, 131).

[Kim, 2003] W-J Kim and NC Perkins. "Harmonic balance/Galerkin method for non-smooth dynamic systems". *Journal of Sound and Vibration* 261.2 (2003), pp. 213–224 (cit. on p. 72).

[Kim, 1996] Y-B Kim and ST Noah. "Quasi-periodic response and stability analysis for a non-linear Jeffcott rotor". *Journal of Sound and Vibration* 190.2 (1996), pp. 239–253 (cit. on p. 16).

[Kim, 1990] YB Kim and ST Noah. "Bifurcation analysis for a modified Jeffcott rotor with bearing clearances". *Nonlinear Dynamics* 1.3 (1990), pp. 221–241 (cit. on pp. 16, 71).

[Kim, 1991a] YB Kim and ST Noah. "Stability and bifurcation analysis of oscillators with piecewise-linear characteristics: a general approach" (1991) (cit. on p. 71).

[Kim, 1991b] Young B Kim and Sherif T Noah. "Response and bifurcation analysis of a MDOF rotor system with a strong nonlinearity". *Nonlinear Dynamics* 2.3 (1991), pp. 215–234 (cit. on p. 71).

[Kirchgäßner, 2016] B Kirchgäßner. "Finite elements in rotordynamics". *Procedia Engineering* 144 (2016), pp. 736–750 (cit. on p. 17).

[Kirk, 1974] RG Kirk and EJ Gunter. "Transient response of rotor-bearing systems" (1974) (cit. on p. 69).

[Kleijnen, 2009] Jack PC Kleijnen. "Kriging metamodeling in simulation: A review". *European journal of operational research* 192.3 (2009), pp. 707–716 (cit. on p. 43).

[Klerk, 2008] Dennis de Klerk, Daniel J Rixen, and SN Voormeeren. "General framework for dynamic substructuring: history, review and classification of techniques". *AIAA journal* 46.5 (2008), pp. 1169–1181 (cit. on p. 100).

[Koch, 2002] Patrick N Koch, John P Evans, and David Powell. "Interdigitation for effective design space exploration using iSIGHT". *Structural and Multidisciplinary Optimization* 23.2 (2002), pp. 111–126 (cit. on p. 10).

[Koff, 1991] B Koff. "Spanning the globe with jet propulsion" (1991), p. 2987 (cit. on pp. 5, 6).

[Kounadis, 1992] AN Kounadis. "On the paradox of the destabilizing effect of damping in non-conservative systems". *International journal of non-linear mechanics* 27.4 (1992), pp. 597–609 (cit. on p. 48).

[Krack, 2015] Malte Krack. "Nonlinear modal analysis of nonconservative systems: Extension of the periodic motion concept". *Computers & Structures* 154 (2015), pp. 59–71 (cit. on p. 71).

[Krysl, 2001] Petr Krysl, Sanjay Lall, and Jerrold E Marsden. "Dimensional model reduction in non-linear finite element dynamics of solids and structures". *International Journal for numerical methods in engineering* 51.4 (2001), pp. 479–504 (cit. on p. 39).

[Kuczkowiak, 2020] Antoine Kuczkowiak, Scott Cogan, Morvan Ouisse, Emmanuel Foltête, and Mathieu Corus. "Experimental validation of an info-gap uncertainty model for a robustness analysis of structural responses". *ASCE-ASME J Risk and Uncert in Engrg Sys Part B Mech Engrg* 6.3 (2020) (cit. on p. 10).

[Kumar, 2019] Jha Abhishek Kumar and Dasgupta Sovan Sundar. "A numerical study on vibration control of a nonlinear Jeffcott rotor via Bouc-Wen model". *FME Transactions* 47.1 (2019), pp. 190–194 (cit. on p. 48).

[Langston, 2018] Lee S Langston. "Open rotor engines—still an open question?" *Mechanical Engineering* 140.12 (2018), S46–S48 (cit. on pp. 6, 7).

[Lau, 1981] SL Lau and YK Cheung. "Amplitude incremental variational principle for nonlinear vibration of elastic systems" (1981) (cit. on p. 70).

[Laxalde, 2007] Denis Laxalde, Jean-Pierre Lombard, and Fabrice Thouverez. "Dynamics of multistage bladed disks systems" (2007) (cit. on pp. 18, 21, 22).

[Lazarus, 2010] Arnaud Lazarus, Benoit Prabel, and Didier Combescure. "A 3D finite element model for the vibration analysis of asymmetric rotating machines". *Journal of Sound and Vibration* 329.18 (2010), pp. 3780–3797 (cit. on p. 50).

[Legrand, 2004] Mathias Legrand, Dongying Jiang, Christophe Pierre, and Steven W Shaw. "Nonlinear normal modes of a rotating shaft based on the invariant manifold method". *International Journal of Rotating Machinery* 10.4 (2004), pp. 319–335 (cit. on p. 39).

[Legrand, 2009] Mathias Legrand, Christophe Pierre, Patrice Cartraud, and Jean-Pierre Lombard. "Two-dimensional modeling of an aircraft engine structural bladed disk-casing modal interaction". *Journal of Sound and Vibration* 319.1-2 (2009), pp. 366–391 (cit. on p. 69).

[Leissa, 2005] Arthur W Leissa. "The historical bases of the Rayleigh and Ritz methods". *Journal of Sound and Vibration* 287.4-5 (2005), pp. 961–978 (cit. on p. 38).

[Liang, 2002] YC Liang, HP Lee, SP Lim, WZ Lin, KH Lee, and CG1237 Wu. "Proper orthogonal decomposition and its applications—Part I: Theory". *Journal of Sound and vibration* 252.3 (2002), pp. 527–544 (cit. on pp. 40, 131, 136).

[Ling, 1987] FH Ling and XX Wu. "Fast Galerkin method and its application to determine periodic solutions of non-linear oscillators". *International Journal of Non-Linear Mechanics* 22.2 (1987), pp. 89–98 (cit. on pp. 70, 72, 73).

[Loewy, 1984] RG Loewy and N Khader. "Structural dynamics of rotating bladed-disk assemblies coupled with flexible shaft motions". *AIAA journal* 22.9 (1984), pp. 1319–1327 (cit. on p. 22).

[Lord Rayleigh, 1877] JWS Lord Rayleigh. "The theory of sound". *Aufl. von 1894. Reprint: Dover Publications, New York 1945* (1877) (cit. on p. 38).

[Lu, 2019] Kuan Lu, Yulin Jin, Yushu Chen, Yongfeng Yang, Lei Hou, Zhiyong Zhang, et al. "Review for order reduction based on proper orthogonal decomposition and outlooks of applications in mechanical systems". *Mechanical Systems and Signal Processing* 123 (2019), pp. 264–297 (cit. on pp. 40, 131).

[Lu, 2016] Zhiwen Lu, Dawei Dong, Shancheng Cao, Huajiang Ouyang, and Chunrong Hua. "Multicrack localization in rotors based on proper orthogonal decomposition using fractal dimension and gapped smoothing method". *Shock and Vibration* 2016 (2016) (cit. on p. 131).

[Lumley, 1967] John Leask Lumley. "The structure of inhomogeneous turbulent flows". *Atmospheric turbulence and radio wave propagation* (1967), pp. 166–178 (cit. on p. 40).

[Lund, 1974] JW Lund. "Modal response of a flexible rotor in fluid-film bearings". *Journal of Engineering for Industry* 96.2 (1974), pp. 509–517 (cit. on pp. 43, 100).

[Luongo, 2012] Angelo Luongo and Daniele Zulli. "Dynamic analysis of externally excited NES-controlled systems via a mixed Multiple Scale/Harmonic Balance algorithm". *Nonlinear Dynamics* 70.3 (2012), pp. 2049–2061 (cit. on p. 72).

[Ma, 2022] Xinxing Ma, Zhenguo Zhang, and Hongxing Hua. "Uncertainty quantization and reliability analysis for rotor/stator rub-impact using advanced Kriging surrogate model". *Journal of Sound and Vibration* 525 (2022), p. 116800 (cit. on p. 130).

[MacNeal, 1971] Richard H MacNeal. "A hybrid method of component mode synthesis". *Computers & Structures* 1.4 (1971), pp. 581–601 (cit. on p. 42).

[Melanson, 1998] J Melanson and JW Zu. "Free vibration and stability analysis of internally damped rotating shafts with general boundary conditions" (1998) (cit. on pp. 43, 48, 58).

[Meyer, 2003] Marcus Meyer and Hermann G Matthies. "Efficient model reduction in non-linear dynamics using the Karhunen-Loeve expansion and dual-weighted-residual methods". *Computational Mechanics* 31.1 (2003), pp. 179–191 (cit. on p. 131).

[Mikota, 2017] G Mikota. "Modal analysis of rotors under special support conditions". *Technische Mechanik-European Journal of Engineering Mechanics* 37.2-5 (2017), pp. 250–257 (cit. on p. 31).

[Mitra, 2016] Mainak Mitra, Stefano Zucca, and Bogdan I Epureanu. "Adaptive microslip projection for reduction of frictional and contact nonlinearities in shrouded blisks". *Journal of Computational and Nonlinear Dynamics* 11.4 (2016) (cit. on pp. 44, 101).

[Montagnier, 2007] Olivier Montagnier and Ch Hochard. "Dynamic instability of supercritical driveshafts mounted on dissipative supports—effects of viscous and hysteretic internal damping". *Journal of Sound and Vibration* 305.3 (2007), pp. 378–400 (cit. on pp. 48, 49).

[Muszynska, 1989] A Muszynska. "Rotor-to-stationary element sub-related vibration phenomena in rotating machinery: literature survey". *The Shock and Vibration Digest* 21.3 (1989), pp. 3–11 (cit. on pp. 15, 69).

[Muszynska, 1995] Agnes Muszynska and Paul Goldman. "Chaotic responses of unbalanced rotor/bearing/stator systems with looseness or rubs". *Chaos, Solitons & Fractals* 5.9 (1995), pp. 1683–1704 (cit. on p. 36).

[Muszynska, 1986] Agnieszka Muszynska. "Whirl and whip—rotor/bearing stability problems". *Journal of Sound and vibration* 110.3 (1986), pp. 443–462 (cit. on pp. 48, 69).

[Nataraj, 1989] C1 Nataraj and HD Nelson. "Periodic solutions in rotor dynamic systems with nonlinear supports: a general approach" (1989) (cit. on pp. 15, 70).

[Nelson, 2007] Frederick C Nelson. "Rotor dynamics without equations". *International Journal of COMADEM* 10.3 (2007), p. 2 (cit. on p. 55).

[Nelson, 1980] HD Nelson. "A finite rotating shaft element using Timoshenko beam theory" (1980) (cit. on pp. 15, 18, 26).

[Nelson, 1976] HD Nelson and JM McVaugh. "The dynamics of rotor-bearing systems using finite elements" (1976) (cit. on pp. 15, 18).

[Newmark, 1959] Nathan M Newmark. "A method of computation for structural dynamics". *Journal of the engineering mechanics division* 85.3 (1959), pp. 67–94 (cit. on p. 69).

[Nieto, 2018] Michelle Nieto, Mostafa Elsayed, and Denis Walch. "Modal participation factors and their potential applications in aerospace: a review" (2018) (cit. on p. 106).

[Ouisse, 2011] Morvan Ouisse and Emmanuel Foltete. "On the properness condition for modal analysis of non-symmetric second-order systems". *Mechanical Systems and Signal Processing* 25.2 (2011), pp. 601–620 (cit. on p. 31).

[Ozban, 2004] Ahmet Yasar Ozban. "Some new variants of Newton's method". *Applied Mathematics Letters* 17.6 (2004), pp. 677–682 (cit. on p. 82).

[Papadrakakis, 2017] M Papadrakakis and M Fragiadakis. "MODAL ANALYSIS PROCEDURE USING COMPLEX LEFT AND RIGHT EIGENVECTORS OF NON-PROPORTIONALLY DAMPED STRUCTURES" (2017) (cit. on p. 31).

[Papadrakakis, 1998] Manolis Papadrakakis, Nikos D Lagaros, and Yiannis Tsompanakis. "Structural optimization using evolution strategies and neural networks". *Computer methods in applied mechanics and engineering* 156.1-4 (1998), pp. 309–333 (cit. on p. 43).

[Peeters, 2009] Maxime Peeters, Regis Viguie, Guillaume Serandour, Gaëtan Kerschen, and J-C Golinval. "Nonlinear normal modes, Part II: Toward a practical computation using numerical continuation techniques". *Mechanical systems and signal processing* 23.1 (2009), pp. 195–216 (cit. on p. 101).

[Peletan, 2012a] Loic Peletan. "Strategie de modelisation simplifiee et de resolution acceleree en dynamique non lineaire des machines tournantes: Application au contact rotor-stator" (2012) (cit. on pp. 37, 39, 44, 71, 85, 86, 101, 158).

[Peletan, 2012b] Loic Peletan, Sebastien Baguet, Georges Jacquet-Richardet, and Mohamed Torkhani. "Use and limitations of the harmonic balance method for rub-impact phenomena in rotor-stator dynamics". 44731 (2012), pp. 647–655 (cit. on p. 80).

[Peletan, 2013] Loic Peletan, Sebastien Baguet, Mohamed Torkhani, and Georges Jacquet-Richardet. "A comparison of stability computational methods for periodic solution of nonlinear problems with application to rotordynamics". *Nonlinear dynamics* 72.3 (2013), pp. 671–682 (cit. on p. 71).

[Peletan, 2014] Loic Peletan, Sebastien Baguet, Mohamed Torkhani, and Georges Jacquet-Richardet. "Quasi-periodic harmonic balance method for rubbing self-induced vibrations in rotor–stator dynamics". *Nonlinear Dynamics* 78.4 (2014), pp. 2501–2515 (cit. on pp. 37, 80).

[Pernot, 2001] Stéphane Pernot and C-H Lamarque. "A wavelet-Galerkin procedure to investigate time-periodic systems: transient vibration and stability analysis". *Journal of Sound and Vibration* 245.5 (2001), pp. 845–875 (cit. on p. 71).

[Petrov, 2004] EP Petrov. "A method for use of cyclic symmetry properties in analysis of nonlinear multiharmonic vibrations of bladed disks". *J. Turbomach.* 126.1 (2004), pp. 175–183 (cit. on p. 22).

[Petrov, 2006] EP Petrov and DJ Ewins. "Effects of damping and varying contact area at blade-disk joints in forced response analysis of bladed disk assemblies" (2006) (cit. on p. 22).

[Popprath, 2007] S Popprath and H Ecker. "Nonlinear dynamics of a rotor contacting an elastically suspended stator". *Journal of Sound and Vibration* 308.3-5 (2007), pp. 767–784 (cit. on p. 37).

[Ramasso, 2022] Emmanuel Ramasso, Thierry Denoeux, and Gael Chevallier. "Clustering acoustic emission data streams with sequentially appearing clusters using mixture models". *Mechanical Systems and Signal Processing* 181 (2022), p. 109504 (cit. on p. 42).

[Rayleigh, 1911] Lord Rayleigh. "XXIV. On the calculation of Chladni's figures for a square plate". *The London, Edinburgh, and Dublin Philosophical Magazine and Journal of Science* 22.128 (1911), pp. 225–229 (cit. on p. 38).

[Renaud, 2011] Franck Renaud, Jean-Luc Dion, Gaël Chevallier, Imad Tawfiq, and Remi Lemaire. "A new identification method of viscoelastic behavior: Application to the generalized Maxwell model". *Mechanical Systems and Signal Processing* 25.3 (2011), pp. 991–1010 (cit. on pp. 30, 48).

[Ri, 2020] Kwangchol Ri, Poknam Han, Inchol Kim, Wonchol Kim, and Hyonbok Cha. "Stability analysis of composite shafts considering internal damping and coupling Effect". *International Journal of Structural Stability and Dynamics* 20.11 (2020), p. 2050118 (cit. on p. 48).

[Rippa, 1999] Shmuel Rippa. "An algorithm for selecting a good value for the parameter c in radial basis function interpolation". *Advances in Computational Mathematics* 11.2 (1999), pp. 193–210 (cit. on p. 135).

[Ritz, 1909a] Walter Ritz. "Theorie der Transversalschwingungen einer quadratischen Platte mit freien Rändern". *Annalen der Physik* 333.4 (1909), pp. 737–786 (cit. on p. 38).

[Ritz, 1909b] Walter Ritz. "Über eine neue Methode zur Lösung gewisser Variationsprobleme der mathematischen Physik." (1909) (cit. on p. 38).

[Rixen, 2004] Daniel J Rixen. "A dual Craig–Bampton method for dynamic substructuring". *Journal of Computational and applied mathematics* 168.1-2 (2004), pp. 383–391 (cit. on p. 39).

[Robert, 1972] Andre Robert, John Henderson, and Colin Turnbull. "An implicit time integration scheme for baroclinic models of the atmosphere". *Monthly Weather Review* 100.5 (1972), pp. 329–335 (cit. on p. 69).

[Romero, 2006] Vicente J Romero, John V Burkardt, Max D Gunzburger, and Janet S Peterson. "Comparison of pure and "Latinized" centroidal Voronoi tessellation against various other statistical sampling methods". *Reliability Engineering & System Safety* 91.10-11 (2006), pp. 1266–1280 (cit. on p. 146).

[Roques, 2010] Sebastien Roques, Mathias Legrand, Patrice Cartraud, Carlo Stoisser, and Christophe Pierre. "Modeling of a rotor speed transient response with radial rubbing". *Journal of Sound and Vibration* 329.5 (2010), pp. 527–546 (cit. on p. 69).

[Roux, 1998] WJ Roux, Nielen Stander, and Raphael T Haftka. "Response surface approximations for structural optimization". *International journal for numerical methods in engineering* 42.3 (1998), pp. 517–534 (cit. on p. 10).

[Rowley, 2005] Clarence W Rowley. "Model reduction for fluids, using balanced proper orthogonal decomposition". *International Journal of Bifurcation and Chaos* 15.03 (2005), pp. 997–1013 (cit. on p. 40).

[Roy, 2019] Dipendra Kumar Roy and Rajiv Tiwari. "Development of identification procedure for the internal and external damping in a cracked rotor system undergoing forward and backward whirls". *Archive of Mechanical Engineering* (2019), pp. 229–255 (cit. on p. 48).

[Rubin, 1975] S Rubin. "Improved component-mode representation for structural dynamic analysis". *AIAA journal* 13.8 (1975), pp. 995–1006 (cit. on pp. 38, 41).

[Ruhl, 1972] Roland L Ruhl and JF Booker. "A finite element model for distributed parameter turborotor systems" (1972) (cit. on pp. 15, 18).

[Sacks, 1989] Jerome Sacks, William J Welch, Toby J Mitchell, and Henry P Wynn. "Design and analysis of computer experiments". *Statistical science* 4.4 (1989), pp. 409–423 (cit. on p. 43).

[Sainvitu, 2010] Caroline Sainvitu, Vicky Iliopoulou, and Ingrid Lepot. "Global optimization with expensive functions-sample turbomachinery design application" (2010), pp. 499–509 (cit. on pp. 11, 136).

[Saito, 1985] S Saito. "Calculation of nonlinear unbalance response of horizontal Jeffcott rotors supported by ball bearings with radial clearances" (1985) (cit. on p. 71).

[Saka, 2007] Yuki Saka, Max Gunzburger, and John Burkardt. "Latinized, improved LHS, and CVT point sets in hypercubes". *International Journal of Numerical Analysis and Modeling* 4.3-4 (2007), pp. 729–743 (cit. on p. 146).

[Sampaio, 2007] Rubens Sampaio and Christian Soize. "Remarks on the efficiency of POD for model reduction in non-linear dynamics of continuous elastic systems". *International Journal for numerical methods in Engineering* 72.1 (2007), pp. 22–45 (cit. on p. 131).

[San Andres, 1986] L San Andres and JM t Vance. "Effects of fluid inertia and turbulence on the force coefficients for squeeze film dampers" (1986) (cit. on p. 24).

[San Andres, 2010] L. San Andres. "Squeeze Film Dampers: Operation, Models and Technical Issues". *Modern Lubrication Theory, Note* 13 (2010) (cit. on p. 143).

[Sanliturk, 1996] KY Sanliturk and DJ Ewins. "Modelling two-dimensional friction contact and its application using harmonic balance method". *Journal of sound and vibration* 193.2 (1996), pp. 511–523 (cit. on p. 72).

[Schimming, 2003] Peter Schimming. "Counter rotating fans—An aircraft propulsion for the future?" *Journal of Thermal Science* 12.2 (2003), pp. 97–103 (cit. on p. 6).

[Schreyer, 2016] Frederic Schreyer and Remco I Leine. "A mixed shooting-harmonic balance method for unilaterally constrained mechanical systems". *Archive of mechanical engineering* 63.2 (2016), pp. 297–314 (cit. on p. 71).

[Seshu, 1997] P Seshu. "Substructuring and component mode synthesis". *Shock and Vibration* 4.3 (1997), pp. 199–210 (cit. on p. 39).

[Shaw, 1989] J Shaw and SW Shaw. "Instabilities and bifurcations in a rotating shaft". *Journal of Sound and Vibration* 132.2 (1989), pp. 227–244 (cit. on p. 33).

[Shen, 1972] FA Shen. "Transient Flexible-Rotor Dynamics Analysis: Part 1—Theory" (1972) (cit. on p. 69).

[Shen, 2021] Zihan Shen, Benjamin Chouvion, Fabrice Thouverez, and Aline Beley. "Enhanced 3D solid finite element formulation for rotor dynamics simulation". *Finite Elements in Analysis and Design* 195 (2021), p. 103584 (cit. on p. 49).

[Sinou, 2018] J-J Sinou, Lyes Nechak, and Sebastien Besset. "Kriging metamodeling in rotordynamics: Application for predicting critical speeds and vibrations of a flexible rotor". *Complexity* 2018 (2018) (cit. on p. 130).

[Sinou, 2005] J-J Sinou, Cristiano Villa, and Fabrice Thouverez. "Experimental and numerical investigations of a flexible rotor on flexible bearing supports". *International Journal of Rotating Machinery* 2005.3 (2005), pp. 179–189 (cit. on p. 19).

[Sirovich, 1987] Lawrence Sirovich. "Turbulence and the dynamics of coherent structures. I. Coherent structures". *Quarterly of applied mathematics* 45.3 (1987), pp. 561–571 (cit. on pp. 40, 131).

[Smola, 2004] Alex J Smola and Bernhard Schölkopf. "A tutorial on support vector regression". *Statistics and computing* 14.3 (2004), pp. 199–222 (cit. on p. 43).

[Spooner, 1999] Jeffrey T Spooner and Kevin M Passino. "Decentralized adaptive control of nonlinear systems using radial basis neural networks". *IEEE transactions on automatic control* 44.11 (1999), pp. 2050–2057 (cit. on pp. 43, 131).

[Stapelfeldt, 2016] Sina C Stapelfeldt, Anthony B Parry, and Mehdi Vahdati. "Investigation of flutter mechanisms of a contra-rotating open rotor". *Journal of Turbomachinery* 138.5 (2016), p. 051009 (cit. on p. 9).

[Sternchüss, 2009b] Arnaud Sternchüss, Etienne Balmès, Pierrick Jean, and Jean-Pierre Lombard. "Reduction of Multistage disk models: application to an industrial rotor". *Journal of Engineering for Gas Turbines and Power* 131.1 (2009) (cit. on p. 39).

[Sundararajan, 1997] P Sundararajan and ST Noah. "Dynamics of forced nonlinear systems using shooting/arc-length continuation method—application to rotor systems" (1997) (cit. on p. 71).

[Sundararajan, 1998] P Sundararajan and ST Noah. "An algorithm for response and stability of large order non-linear systems—application to rotor systems". *Journal of sound and vibration* 214.4 (1998), pp. 695–723 (cit. on p. 71).

[Swanson, 2005] Erik Swanson, Chris D Powell, and Sorin Weissman. "A practical review of rotating machinery critical speeds and modes". *Sound and vibration* 39.5 (2005), pp. 16–17 (cit. on p. 100).

[Tannous, 2015a] Mikhael Tannous, Patrice Cartraud, David Dureisseix, and Mohamed Torkhani. "A beam to 3D model switch for rotor dynamics applications". *Engineering Structures* 84 (2015), pp. 54–66 (cit. on p. 20).

[Tannous, 2015b] Mikhael Tannous, Patrice Cartraud, Mohamed Torkhani, and David Dureisseix. "Assessment of 3D modeling for rotor–stator contact simulations". *Journal of Sound and Vibration* 353 (2015), pp. 327–343 (cit. on p. 20).

[Tian, 2011] Li Tian, WJ Wang, and ZJ Peng. "Dynamic behaviours of a full floating ring bearing supported turbocharger rotor with engine excitation". *Journal of Sound and Vibration* 330.20 (2011), pp. 4851–4874 (cit. on p. 20).

[Turhan, 2006] Özgür Turhan and Gökhan Bulut. "Linearly coupled shaft-torsional and blade-bending vibrations in multi-stage rotor-blade systems". *Journal of Sound and Vibration* 296.1-2 (2006), pp. 292–318 (cit. on p. 22).

[Ullman, 2001] David G Ullman. "Robust decision-making for engineering design". *Journal of Engineering Design* 12.1 (2001), pp. 3–13 (cit. on p. 10).

[Vakakis, 1997] Alexander Vakakis. "Non-linear normal modes (NNMs) and their applications in vibration theory: an overview". *Mechanical systems and signal processing* 11.1 (1997), pp. 3–22 (cit. on p. 39).

[Van Zante, 2014] Dale E Van Zante, Fayette Collier, Arthur Orton, S Arif Khalid, John P Wojno, and Trevor H Wood. "Progress in open rotor propulsors: The FAA/GE/NASA open rotor test campaign". *The Aeronautical Journal* 118.1208 (2014), pp. 1181–1213 (cit. on p. 9).

[Vendhan, 1975] CP Vendhan and YC Das. "Application of Rayleigh-Ritz and Galerkin methods to non-linear vibration of plates". *Journal of Sound and Vibration* 39.2 (1975), pp. 147–157 (cit. on p. 189).

[Von Groll, 2001] Gotz Von Groll and David J Ewins. "The harmonic balance method with arc-length continuation in rotor/stator contact problems". *Journal of sound and vibration* 241.2 (2001), pp. 223–233 (cit. on pp. 16, 71).

[Wagner, 2010] Matthew B Wagner, Amir Younan, Paul Allaire, and Randy Cogill. "Model reduction methods for rotor dynamic analysis: a survey and review". *International Journal of Rotating Machinery* 2010 (2010) (cit. on pp. 30, 41, 100, 101, 134).

[Walczak, 1996] B Walczak and DL Massart. "The radial basis functions—partial least squares approach as a flexible non-linear regression technique". *Analytica Chimica Acta* 331.3 (1996), pp. 177–185 (cit. on p. 43).

[Wang, 2017] JT Wang, CJ Wang, and JP Zhao. "Frequency response function-based model updating using Kriging model". *Mechanical Systems and Signal Processing* 87 (2017), pp. 218–228 (cit. on p. 130).

[Wilson, 1982] Edward L Wilson, Ming-Wu Yuan, and John M Dickens. "Dynamic analysis by direct superposition of Ritz vectors". *Earthquake Engineering & Structural Dynamics* 10.6 (1982), pp. 813–821 (cit. on p. 100).

[Woiwode, 2020] Lukas Woiwode, Nidish Narayanaa Balaji, Jonas Kappauf, Fabia Tubita, Louis Guillot, Christophe Vergez, et al. "Comparison of two algorithms for harmonic balance and path continuation". *Mechanical Systems and Signal Processing* 136 (2020), p. 106503 (cit. on p. 101).

[Yamamoto, 1955] Toshio Yamamoto. "On the critical speeds of a shaft". *Memoirs of the faculty of engineering, Nagoya University* 6.2 (1955), pp. 106–174 (cit. on p. 69).

[Yamauchi, 1983] Shingo Yamauchi. "The nonlinear vibration of flexible rotors". *Transaction of JSME* 446.49 (1983), pp. 1862–1868 (cit. on pp. 15, 71).

[Yang, 2016] JH Yang, Miguel AF Sanjuán, and HG Liu. "Vibrational subharmonic and superharmonic resonances". *Communications in Nonlinear Science and Numerical Simulation* 30.1-3 (2016), pp. 362–372 (cit. on p. 89).

[Yin, 2020] Feijia Yin and Arvind Gangoli Rao. "A review of gas turbine engine with inter-stage turbine burner". *Progress in Aerospace Sciences* 121 (2020), p. 100695 (cit. on p. 5).

[Yokoyama, 1988] T Yokoyama. "Free vibration characteristics of rotating Timoshenko beams". *International Journal of Mechanical Sciences* 30.10 (1988), pp. 743–755 (cit. on p. 18).

[Yondo, 2018] Raul Yondo, Esther Andres, and Eusebio Valero. "A review on design of experiments and surrogate models in aircraft real-time and many-query aerodynamic analyses". *Progress in aerospace sciences* 96 (2018), pp. 23–61 (cit. on pp. 40, 42, 43).

[Young, 1968] John A Young. "Comparative properties of some time differencing schemes for linear and nonlinear oscillations". *Monthly Weather Review* 96.6 (1968), pp. 357–364 (cit. on p. 69).

[Ypma, 1995] Tjalling J Ypma. "Historical development of the Newton–Raphson method". *SIAM review* 37.4 (1995), pp. 531–551 (cit. on p. 81).

[Yuan, 2017] Jie Yuan, Fabrizio Scarpa, Giuliano Allegri, Branislav Titurus, Sophoclis Patsias, and Ramesh Rajasekaran. "Efficient computational techniques for mistuning analysis of bladed discs: a review". *Mechanical Systems and Signal Processing* 87 (2017), pp. 71–90 (cit. on pp. 18, 21, 22).

[Zeidan, 1989] Fouad Y Zeidan and John M Vance. "Cavitation leading to a two phase fluid in a squeeze film damper". *Tribology transactions* 32.1 (1989), pp. 100–104 (cit. on p. 24).

[Zeidan, 1990] Fouad Y Zeidan and John M Vance. "Cavitation regimes in squeeze film dampers and their effect on the pressure distribution". *Tribology transactions* 33.3 (1990), pp. 447–453 (cit. on p. 24).

[Zhang, 1988] Q Zhang, G Lallement, and R Fillod. "Relations between the right and left eigenvectors of non-symmetric structural models. Applications to rotors". *Mechanical Systems and Signal Processing* 2.1 (1988), pp. 97–103 (cit. on p. 31).

[Zorzi, 1977] E. S. Zorzi and H. D. Nelson. "Finite Element Simulation of Rotor-Bearing Systems With Internal Damping". *Journal of Engineering for Power* 99 (1977), pp. 71–76 (cit. on pp. 15, 18, 48, 58).

Online references and Patents

[CFM-ad, 2017] CFM-ad. *CFM LEAP 1A*. https://www.cfmaeroengines.com/wp-content/uploads/2017/09/Brochure_LEAPfiches_2017.pdf. 2017 (cit. on p. 9).

[CFM-LEAP-1A, 2022] CFM-LEAP-1A. *CFM LEAP 1A*. https://www.safran-group.com/fr/produits-services/leap-1a-moteur-nouvelle-generation-avions-civils-court-moyen-courriers. 2022 (cit. on p. 4).

[CFM-RISE, 2021] CFM-RISE. *RISE-rend*. https://www.cfmaeroengines.com/wp-content/uploads/2021/07/CFM_RISE_Whitepaper_Media.pdf. 2021 (cit. on p. 8).

[CFM-web, 2021] CFM-web. *CFM RISE*. https://www.flightglobal.com/engines/cfm-launches-open-rotor-demonstrator-promising-20-better-fuel-burn-for-mid-2030s-applications/144141.article. 2021 (cit. on p. 9).

[CROR, 2019] CROR. *CFM-CROR*. https://www.ainonline.com/aviation-news/air-transport/2017-10-04/safran-inaugurates-open-rotor-test-program. 2019 (cit. on p. 7).

[Darecki, 2011] M Darecki, C Edelstenne, T Enders, E Fernandez, P Hartman, JP Herteman, et al. *Flightpath 2050 Europe's vision for aviation (European Commission)*. 2011 (cit. on pp. 6, 157).

[DimensionsAIhbm, 2023] DimensionsAIhbm. *DimensionsAIhbm*. 2023 (cit. on p. 70).

[DimensionsAIti, 2023] DimensionsAIti. *DimensionsAIti*. 2023 (cit. on p. 70).

[PW-GTF, 2023] PW-GTF. *PeW-GTF*. https://prattwhitney.com/products-and-services/products/commercial-engines/pratt-and-whitney-gtf. 2023 (cit. on p. 4).

[Guillaume, 1921] Maxime Guillaume. *Thruster by reaction on air*. 1921 (cit. on p. 3).

[MIT, 2008] MIT. *Lecture 8: Energy Methods in Elasticity*. https://ocw.mit.edu/courses/2-080j-structural-mechanics-fall-2013/2d0cc95bd3556fdadc28226acabafa51_MIT2_080JF13_Lecture8.pdf. 2008 (cit. on p. 190).

[MSC, 2018] MSC. *NASTRAN2018 quick reference guide*. https://help.hexagonmi.com/fr-FR/bundle/MSC_Nastran_2020/page/Nastran_Combined_Book/refman/refmanpreface/TOC.List.of.MSC.Nastran.Books4.xhtml. 2018 (cit. on pp. 80, 81).

[RollsRoyce-Trent, 2022] RollsRoyce-Trent. *RR-TRENT*. https://www.behance.net/gallery/27888995/How-does-a-turbofan-engine-work?locale=ko_KR. 2022 (cit. on p. 17).

[SAE-carbon, 2021] SAE-carbon. *SAE-carbon*. https://www.safran-group.com/group/commitments/decarbonizing-aeronautics. 2021 (cit. on p. 6).

[SAE-GE, 2021] SAE-GE. *installation*. https://www.seattletimes.com/business/boeing-aerospace/ge-and-safran-tout-new-open-rotor-engine-future-for-sustainable-aviation. 2021 (cit. on p. 8).

[SAE-SP, 2019] SAE-SP. *Supportpalier*. https://www.safran-group.com/fr/produits-services/enceintes-paliers-turboreacteurs-civils. 2019 (cit. on p. 23).

[RR-Trent900, 2009] RR-Trent900. *RR-TRENT*. https://web.archive.org/web/20101205122456/http://www.rolls-royce.com/Images/brochure_Trent900_tcm92-11346.pdf. 2009 (cit. on pp. 3, 16).

Appendices

1 APPENDIX : Finite Element matrices for the modified Jeffcott-Laval rotor

The Timoshenko's beam element is defined by the following matrices:

$$\mathbf{M}_b = \frac{\rho S L_b}{420}\begin{bmatrix} 156 & 0 & 0 & -22L_b & 54 & 0 & 0 & 13L_b \\ & 156 & 22L_b & 0 & 0 & 54 & -13L_b & 0 \\ & & 4L_b^2 & 0 & 0 & 13L_b & -3L_b^2 & 0 \\ & & & 4L_b^2 & -13L_b & 0 & 0 & \\ & & & & 156 & 0 & 0 & 22L_b \\ & & & & & 156 & -22L_b & 0 \\ & & & & & & 4L_b^2 & 0 \\ sym. & & & & & & & 4L_b^2 \end{bmatrix}_{u_j} \tag{1}$$

$$\mathbf{G}_b = \frac{I_p b}{3}\begin{bmatrix} 0 & 0 & 0 & 0 & \dots & & \\ 0 & 0 & 0 & 0 & \dots & & \\ 0 & 0 & 0 & 1 & \dots & & \\ 0 & 0 & -1 & 0 & \dots & & \\ \vdots & \vdots & 0 & 0 & \ddots & & \\ & & & & & & 1 \\ & & & & & -1 & 0 \end{bmatrix} \tag{2}$$

$$\mathbf{K}_b = \frac{EI}{(1+\Phi)L_b^3}\begin{bmatrix} 12 & 0 & 0 & 6L_b & -12 & 0 & 0 & 6L_b \\ & 12 & -6L_b & 0 & 0 & -12 & -6L_b & 0 \\ & & (4+\Phi)L_b^2 & 0 & 0 & 6L_b & (2-\Phi)L_b^2 & 0 \\ & & & (4+\Phi)L_b^2 & -6L_b & 0 & 0 & (2-\Phi)L_b^2 \\ & & & & 12 & 0 & 0 & -6L_b \\ & & & & & 12 & 6L_b & 0 \\ & & & & & & (4+\Phi)L_b^2 & 0 \\ sym. & & & & & & & (4+\Phi)L_b^2 \end{bmatrix} \tag{3}$$

with $\Phi = \frac{12EI}{GSL_b^2}$ and $G = \frac{E}{2(1+\nu)}$, L_b is the beam's length, E is the Young's module, I is the diametral inertia, S the surface area and ν the Poisson's ratio. The beam's properties are defined in Table 2.1.

The disc is modelled using a singular node positioned on the shaft, with mass and inertial

properties :

$$\mathbf{M}_d = \begin{bmatrix} m & 0 & 0 & mL \\ & m & -mL & 0 \\ & & I_d + mL^2 & 0 \\ sym. & & & I_d + mL^2 \end{bmatrix} \qquad \mathbf{G}_d = \begin{bmatrix} 0 & 0 & 0 & 0 \\ 0 & 0 & 0 & 0 \\ 0 & 0 & 0 & I_p \\ 0 & 0 & -I_p & 0 \end{bmatrix} \tag{4}$$

At the extremities of the shaft, the visco-elastic support #1 introduces viscous damping into the system, with the following properties:

$$\mathbf{K}_{supp} = \begin{bmatrix} k_{rx} & 0 & 0 & 0 & -k_{rx} & 0 & 0 & 0 \\ & k_{ry} & 0 & 0 & 0 & -k_{ry} & 0 & 0 \\ & & k_\phi & 0 & 0 & 0 & -k_\phi & 0 \\ & & & k_\psi & 0 & 0 & 0 & -k_\psi \\ & & & & k_{rx} & 0 & 0 & 0 \\ & & & & & k_{ry} & 0 & 0 \\ & & & & & & k_\phi & 0 \\ sym. & & & & & & & k_\psi \end{bmatrix} \tag{5}$$

$$\mathbf{D}_{supp} = \begin{bmatrix} c_{rx} & 0 & 0 & 0 & -c_{rx} & 0 & 0 & 0 \\ & c_{ry} & 0 & 0 & 0 & -c_{ry} & 0 & 0 \\ & & 0 & 0 & 0 & 0 & 0 & 0 \\ & & & 0 & 0 & 0 & 0 & 0 \\ & & & & c_{rx} & 0 & 0 & 0 \\ & & & & & c_{ry} & 0 & 0 \\ & & & & & & 0 & 0 \\ sym. & & & & & & & 0 \end{bmatrix} \tag{6}$$

With : $k_{rx} = k_{ry} = 1e7N/m$ (symmetrical support) , $k_\phi = k_\psi = 0N/m$, $c_{rx} = c_{ry} = 1e5N/m * s$. The support #2 is undamped.

2 APPENDIX: Definition of the FEM operators

The FEM can be used to construct an approximation of the solution. First of all, the approximation is based on the use of a weak formulation of the problem. For each term $f(x)$ of the function:

$$\int_{\mathcal{D}} \delta \mathbf{u}^T f(x, \mathbf{u}, \dot{\mathbf{u}}, \ddot{\mathbf{u}}) dV \tag{7}$$

This approximation is of course based on the discretization of the domain with finite element.

$$\mathcal{D} = \cup_{h=1}^{N} \mathcal{D}_h \tag{8}$$

and the use of interpolation functions such as

$$\mathbf{u} = \mathbf{H}(\mathbf{x})\mathbf{q}_m \tag{9}$$

After processing the approximation, the Partial Differential Equations (PDEs) are transformed into a set of Ordinary Differential Equations (ODEs).

3 APPENDIX : Transformation of the Hysteretic damping force from $\mathcal{R}_m$ to $\mathcal{R}_f$

Here is reported the transformation of the hysteretic damping force from the rotating reference frame to the inertial reference frame.

$$\{\mathbf{f_{dh}}\}_{\mathcal{R}_f} = \mathbf{R}^T\{\mathbf{f_{dh}}\}_{\mathcal{R}_m} = \mathbf{R}^T\{\frac{1}{2}sign(\omega-\Omega)\eta_h\mathbf{K}\mathbf{dq}_f^- + \frac{1}{2}\eta_h\mathbf{K}\mathbf{dq}_f^+\} \tag{10}$$

Developing this equation :

$$\begin{aligned}\{\mathbf{f_{dh}}\}_{\mathcal{R}_f} = \frac{\eta_h\mathbf{K}}{2}\begin{bmatrix} cos(\theta) & sin(\theta) \\ -sin(\theta) & cos(\theta)\end{bmatrix}\cdot \\ \left[sign(\omega-\Omega)\begin{bmatrix}-v_f\ sin((\omega-\Omega)t+\phi_v) - w_f\ cos((\omega-\Omega)t+\phi_w) \\ v_f\ cos((\omega-\Omega)t+\phi_v) - w_f\ sin((\omega-\Omega)t+\phi_w)\end{bmatrix} + \right. \\ \left. + \begin{bmatrix}-v_f\ sin((\omega+\Omega)t+\phi_v) + w_f\ cos((\omega+\Omega)t+\phi_w) \\ -v_f\ cos((\omega+\Omega)t+\phi_v) - w_f\ sin((\omega+\Omega)t+\phi_w)\end{bmatrix}\right]\end{aligned} \tag{11}$$

Studying the first term of the sum :

$$\begin{aligned}&\begin{bmatrix} cos(\theta) & sin(\theta) \\ -sin(\theta) & cos(\theta)\end{bmatrix}\begin{Bmatrix}-v_f\ sin((\omega-\Omega)t+\phi_v) - w_f\ cos((\omega-\Omega)t+\phi_w) \\ v_f\ cos((\omega-\Omega)t+\phi_v) - w_f\ sin((\omega-\Omega)t+\phi_w)\end{Bmatrix} = \\ &= \begin{Bmatrix} -v_f\ cos(\theta)sin((\omega-\Omega)t+\phi_v) - w_f\ cos(\theta)cos((\omega-\Omega)t+\phi_w) - \\ -v_f\ sin(\Omega t)cos((\omega-\Omega)t+\phi_v) + w_f\ sin(\theta)sin((\omega-\Omega)t+\phi_w) \\ -v_f\ sin(\Omega t)sin((\omega-\Omega)t+\phi_v) - w_f\ sin(\theta)cos((\omega-\Omega)t+\phi_w) + \\ +v_f\ cos(\Omega t)cos((\omega-\Omega)t+\phi_v) - w_f\ cos(\theta)sin((\omega-\Omega)t+\phi_w) =\end{Bmatrix} \\ &= \begin{Bmatrix}-2\ v_f\ sin(\omega t+\phi_v) - 2\ w_f\ cos(\omega t+\phi_w) \\ 2\ v_f\ cos(\omega t+\phi_v) - 2\ w_f\ sin(\omega t+\phi_w)\end{Bmatrix}\end{aligned} \tag{12}$$

Studying the second term of the sum :

$$\begin{bmatrix} cos(\theta) & sin(\theta) \\ -sin(\theta) & cos(\theta) \end{bmatrix} \begin{Bmatrix} -v_f\ sin((\omega+\Omega)t+\phi_v) + w_f\ cos((\omega+\Omega)t+\phi_w) \\ -v_f\ cos((\omega+\Omega)t+\phi_v) - w_f\ sin((\omega+\Omega)t+\phi_w) \end{Bmatrix} =$$

$$= \begin{Bmatrix} -v_f\ cos(\theta)sin((\omega+\Omega)t+\phi_v) + w_f\ cos(\theta)cos((\omega+\Omega)t+\phi_w) + \\ +v_f\ sin(\Omega t)cos((\omega+\Omega)t+\phi_v) - w_f\ sin(\theta)sin((\omega+\Omega)t+\phi_w) \\ -v_f sin(\Omega t)sin((\omega+\Omega)t+\phi_v) + w_f\ sin(\theta)cos((\omega+\Omega)t+\phi_w) - \\ -v_f\ cos(\Omega t)cos((\omega+\Omega)t+\phi_v) - w_f\ cos(\theta)sin((\omega+\Omega)t+\phi_w) = \end{Bmatrix} \tag{13}$$

$$= \begin{Bmatrix} -2v_f\ sin(\omega t+\phi_v) + 2w_f\ cos(\omega t+\phi_w) \\ -2v_f\ cos(\omega t+\phi_v) - 2w_f\ sin(\omega t+\phi_w) \end{Bmatrix}$$

Resuming :

$$\{\mathbf{f_{dh}}\}_{\mathcal{R}_f} = \frac{\eta_h \boldsymbol{K}}{2} \left[sign(\omega-\Omega) \begin{bmatrix} -2\ v_f\ sin(\omega t+\phi_v) - 2\ w_f\ cos(\omega t+\phi_w) \\ 2\ v_f\ cos(\omega t+\phi_v) - 2\ w_f\ sin(\omega t+\phi_w) \end{bmatrix} + \right.$$
$$\left. + \begin{bmatrix} -2\ v_f\ sin(\omega t+\phi_v) + 2\ w_f\ cos(\omega t+\phi_w) \\ -2\ v_f\ cos(\omega t+\phi_v) - 2\ w_f\ sin(\omega t+\phi_w) \end{bmatrix} \right] \tag{14}$$

4 APPENDIX : A short focus on Galerkin and Ritz methods

Since the Galerkin method is a key element for the HB and since the Ritz method is widely employed in the further parts of this work for model reduction, it seems due to spend some words to the relation and the differences existing between these two methods. The Galerkin method is generally used to calculate approximated solutions of differential equation expressed in *strong form*. On the other hand, the Ritz method must be applied to the *weak form (variational)* of a differential equation and allows to obtain an approximated solution by minimising the potential energy of the system represented by the differential equations. Gander trace the historical development of the two cited methods [Gander, 2012]. Galerkin was inspired by the Ritz method (1909) and proposes its own method in 1915 citing multiple times the Swiss scientist. The Galerkin method has a wider applicability than the Ritz method because it can be applied directly on the strong form of the differential equations. Both cited methods allow to obtain an approximated solution of a differential problem, in the analytical framework, it is possible to see that using the same number of generalised coordinates it is possible to obtain exactly the same approximated solution for a generic differential problem using the two approaches. In the next subsection, an academical study is reported comparing the approximated solutions evaluated using the two proposed methods on a cantilever beam under traction load.
In numerical application the equivalence of this two methods is not trivial. Vandhan et al. in 1975 proposed a study on a nonlinear vibrating plate, solving the differential problem with both Ritz and Galerkin approaches, it shows that the two approximated solutions are similar but not exactly the same, the convergence path is not the same and on large models it can impact the solution [Vendhan, 1975].

Application of Galerkin and Ritz methods on a cantilever beam under traction load

It is considered a generic cantilever beam, with section S, Young's module E, length L. The only displacement considered is along the axial direction and it is expressed as x, the

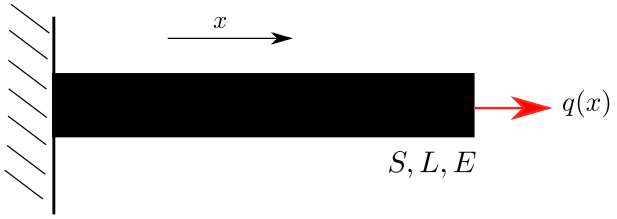

Figure 3: Cantilever beam under axial load.

beam's axial deformation is expressed as u(x) and the axial force is $q(x)$=kx (see Figure 3). The governing equation of the deformation is expressed by the following differential equation [MIT, 2008]:

$$SE\frac{d^2u}{dx^2} + q(x) = 0 \qquad with \qquad u(x=0) = 0 \tag{15}$$

The approximated solution of this differential problem is approximated through the Galerkin method and the Ritz methods.

Galerkin method

One can write the residual function after Galerkin [Galerkin, 1915] with the relative weight functions using the differential equation in the strong form (Equation 15):

$$R(u,x) = \int_0^L \left(SE\frac{d^2u}{dx^2} + q(x)\right) w(x)dx = 0 \tag{16}$$

with *w(x)* representing the Galerkin's weight functions. Integrating by parts Equation 16:

$$R(u,x) = \left[g(x)SE\frac{du}{dx}\right]_0^L - \int_0^L \left(SE\frac{du}{dx} + q(x)\right)\frac{dg}{dx}dx + \int_0^L q(x)g(x)dx = 0 \tag{17}$$

Since $g(x)$ has to respect the kinematic condition $g(x=0) = 0$ and since $SE\frac{du}{dx}|_{x=L} = 0$ because there is no load at the free extremity, the first term $\left[g(x)SE\frac{du}{dx}\right]_0^L = 0$. The Equation 16 is finally written as:

$$R(u,x) = -\int_0^L \left(SE\frac{du}{dx} + q(x)\right)\frac{dg}{dx}dx + \int_0^L q(x)g(x)dx = 0 \tag{18}$$

The general solution of this integral is in the form:

$$u(x) = c_0 + c_1x + c_2x^2 \tag{19}$$

Applying the boundary condition $u(x=0) = 0 \rightarrow c_0 = 0$.
The Galerkin function is $g_i(x) = \frac{du}{dc_i}$, thus:

$$g_1(x) = \frac{du}{dc_1} = x \tag{20}$$

$$g_2(x) = \frac{du}{dc_2} = x^2 \tag{21}$$

Substituting $(u(x), g_1(x))$ and $(u(x), g_2(x))$ in Equation 18 we can obtain the system of equations:

$$\begin{cases} \frac{KL^3}{3} - SLEc_1 - SL^2Ec_2 \\ \frac{KL^4}{4} - SL^2Ec_1 - \frac{4}{3}SL^3Ec_2 \end{cases} \rightarrow u(x) = \frac{7KL^2}{12SE}x - \frac{KL}{4SE}x^2 \tag{22}$$

Ritz method

The Ritz approximation is performed minimising the potential energy of the system. The weak form of the differential Equation15 is employed.

$$\mathcal{U}_p = \int_0^L \frac{1}{2}SE\left(\frac{du}{dx}\right)^2 dx - \int_0^L q(x)u(x)dx \tag{23}$$

As seen before, the general integral is in the form :

$$u(x) = c_1x + c_2x^2 \tag{24}$$

substituting $u(x)$ in Equation 23, one can write $\mathcal{U}_p(c_1, c_2)$:

$$\mathcal{U}_p = -\frac{1}{3}KL^3c_1 + \frac{1}{2}SLEc_1^2 - \frac{1}{4}KL^4c_2 + SL^2c_1c_2 + \frac{2}{3}SL^3Ec_2^2 \tag{25}$$

Minimising the potential energy $\frac{d\mathcal{U}_p}{dc_i} = 0$, one can obtain the system:

$$\begin{cases} \frac{d\mathcal{U}_p}{dc_1} = 0 \\ \frac{d\mathcal{U}_p}{dc_2} = 0 \end{cases} \rightarrow \begin{cases} \frac{KL^3}{3} - SLEc_1 - SL^2Ec_2 \\ \frac{KL^4}{4} - SL^2Ec_1 - \frac{4}{3}SL^3Ec_2 \end{cases} \rightarrow u(x) = \frac{7KL^2}{12SE}x - \frac{KL}{4SE}x^2 \tag{26}$$

Comments

Using a reduced number of generalised coordinates, both Ritz and Galerkin methods show that is it possible to approximate the solution of the differential problems, even if the hypothesis are not exactly the same for the two cases. In Ritz method, the generalised coordinates must respect only the kinematic boundary conditions of the system while in Galerkin this is often not enough, the coordinates should satisfy both kinematic and natural or force boundary conditions as seen in Equation 18. In model reduction point of view, the Ritz method is widely employed to approximate the full order displacements field of a FE model, using a basis of vectors respecting the kinematics constrains of the system (vibration modes) and a reduced number of generalised coordinates. The Galerkin method is mostly employed for the resolution of differential problem as will be seen in the HB method.